

2

**STUDY OF DYNAMIC BEHAVIOR AND HAZARDS OF VHBR,LOVA, AND
PSS PROPELLANTS UNDER RAPID IGNITION AND COMBUSTION
CONDITIONS BY REAL-TIME X-RAY RADIOGRAPHY**

FINAL REPORT

AD-A256 775



K. K. Kuo, W. H. Hsieh, and S. J. Ritchie

**Department of Mechanical Engineering
The Pennsylvania State University
University Park, PA 16802**

1991

SUBMITTED TO:

U.S. ARMY RESEARCH OFFICE



Contract No: DAALO3-87-K-0064

**THE VIEW, OPINIONS, AND/OR FINDINGS CONTAINED IN THIS REPORT ARE
THOSE OF THE AUTHOR(S) AND SHOULD NOT BE CONSTRUED AS AN
OFFICIAL DEPARTMENT OF THE ARMY POSITION, POLICY, OR DECISION,
UNLESS SO DESIGNATED BY OTHER DOCUMENTATION.**

**APPROVED FOR PUBLIC RELEASE;
DISTRIBUTION UNLIMITED.**

92 10

626105

92-27597



166088

REPORT DOCUMENTATION PAGE			Form Approved OMB No. 0704-0188	
Public reporting burden for this collection of information is estimated to average 1 hour per response, including the time for reviewing instructions, searching existing data sources, gathering and maintaining the data needed, and completing and reviewing the collection of information. Send comments regarding this burden estimate or any other aspect of this collection of information, including suggestions for reducing this burden, to Washington Headquarters Services, Directorate for Information Operations and Reports, 1215 Jefferson Davis Highway, Suite 1204, Arlington, VA 22202-4302, and to the Office of Management and Budget, Paperwork Reduction Project (0704-0188), Washington, DC 20503.				
1. AGENCY USE ONLY (Leave blank)		2. REPORT DATE December 9, 1991		3. REPORT TYPE AND DATES COVERED
4. TITLE AND SUBTITLE Study of Dynamic Behavior and Hazards of VHBR, LOVA, and PSS Propellants under Rapid Ignition and Combustion conditions by Real-Time X-Ray Radiography			5. FUNDING NUMBERS DAAL03-87-K-0064	
6. AUTHOR(S) K.K.Kuo, W.H.Hsieh, and S.J.Ritchie			8. PERFORMING ORGANIZATION REPORT NUMBER	
7. PERFORMING ORGANIZATION NAME(S) AND ADDRESS(ES) Department of Mechanical Engineering The Pennsylvania State University University Park, PA 16802			10. SPONSORING/MONITORING AGENCY REPORT NUMBER ARU 25121.9-EG	
9. SPONSORING/MONITORING AGENCY NAME(S) AND ADDRESS(ES) U. S. Army Research Office P. O. Box 12211 Research Triangle Park, NC 27709-2211			11. SUPPLEMENTARY NOTES The view, opinions and/or findings contained in this report are those of the author(s) and should not be construed as an official Department of the Army position, policy, or decision, unless so designated by other documentation.	
12a. DISTRIBUTION/AVAILABILITY STATEMENT Approved for public release; distribution unlimited.			12b. DISTRIBUTION CODE	
13. ABSTRACT (Maximum 200 words) The purpose of this work is to study the dynamic behavior in the combustion of three types of propellants used in artillery systems. These propellants include very high burning rate (VHBR), low vulnerability ammunition (LOVA), and programmed splitting stick (PSS) propellants. Several advanced nonintrusive diagnostic instruments were utilized in this study. These instruments include: a real-time X-ray radiography system, a digital image processing system, a multi-channel laser doppler velocimeter, and high-speed movie cameras. A shock tunnel and a high-powered CO ₂ laser were also employed for this investigation. This research project was divided into three major areas: (a) combustion behavior of VHBR propellants; (b) convective and radiative ignition processes of LOVA propellants; and (c) combustion and segregation phenomena of PSS propellants. The research motivation, program objectives, method of approach, results, and summary and conclusions of each are given in Chapters 1, 2, and 3, respectively. Results obtained from this study not only enhance the basic understanding of the complex phenomena and controlling mechanisms associated with ignition, combustion, and mechanical deformation of these propellants but also helps the design of future artillery systems with minimum hazards.				
14. SUBJECT TERMS Ignition, Combustion, Dynamic Behavior, LOVA propellants, VHBR propellants, PSS propellants, Real-Time X-ray Radiography			15. NUMBER OF PAGES	
17. SECURITY CLASSIFICATION OF REPORT UNCLASSIFIED			16. PRICE CODE	
18. SECURITY CLASSIFICATION OF THIS PAGE UNCLASSIFIED			19. SECURITY CLASSIFICATION OF ABSTRACT UNCLASSIFIED	
20. LIMITATION OF ABSTRACT UL				

TABLE OF CONTENTS

List of Appendices	1
List of Figures	ii
Summary	iii
Acknowledgement	v
CHAPTER 1	1
Combustion Behavior of Very High Burning Rate Propellants	
1.1 Introduction	1
1.1.1 Background	1
1.1.2 Objectives	1
1.2 Method of Approach	2
1.2.1 Real-Time X-Ray Radiography Study	2
1.2.1.1 X-Ray System	2
1.2.1.2 Medium-Pressure Test Rig	2
1.2.1.3 High-Pressure Double-Windowed Test Rig	2
1.2.2 Pressure and Temperature Controlled Optical Strand Burner	2
1.3 Discussion of Results	7
1.3.1 Results Obtained From Real-Time X-Ray Radiography Study	7
1.3.1.1 Results Obtained From the Medium-Pressure Test Rig	7
1.3.1.2 Results Obtained From the High-Pressure Double-Windowed Test Rig	7
1.3.2 Results Obtained From Temperature Sensitivity Measurements	8
1.4 Summary and Conclusions	9
1.5 References	10
CHAPTER 2	11
Convective and Radiative Ignition Processes of Low Vulnerability Ammunition Propellants	
2.1 Introduction	11
2.1.1 Background and Motivation	11
2.1.2 Problem Statement	11
2.1.3 Program Objectives	12
2.2 Experimental Approach	13
2.2.1 Convective Ignition Tests	13
2.2.1.1 HPCL Shock Tunnel Facility	13
2.2.1.2 Convective Ignition Test Section	13
2.2.1.3 Diagnostics for Convective Ignition Tests	14
2.2.1.4 Test Samples	14
2.2.2 Radiative Ignition Tests	14
2.2.2.1 CO ₂ Laser Ignition Test Facility	14
2.2.2.2 High Pressure Test Chamber	14
2.2.2.3 Diagnostics for Radiative CO ₂ Laser Ignition Tests	14
2.2.2.4 Test Samples	14
2.3 Experimental Results and Discussion	15
2.3.1 Convective Ignition Test Results	15
2.3.1.1 Freestream Oxygen Dependency	15
2.3.1.2 Ignition and Flame-Spread Observation	15
2.3.1.3 Ignition Delay Time	15
2.3.1.4 Microscopic Analysis of Propellant Surface Characteristics	16
2.3.2 Radiative Ignition Test Results	16
2.3.2.1 Test Conditions	16
2.3.2.2 Observed Ignition and Flame-Spreading	16

2.3.2.2	Observed Ignition and Flame-Spreading	16
2.3.2.3	Ignition Delay Time	16
2.3.2.4	Pressure Dependency	16
2.4	Comparative Analysis of Convective and Radiative Processes	17
2.4.1	General Description of Convective Ignition Process	17
2.4.2	General Description of the Radiative Ignition Process	18
2.4.3	Comparative Analysis of the Radiative and Convective Processes ...	18
2.5	Theoretical Approach	18
2.5.1	Chemical Model	20
2.5.2	Simplifying Assumptions Discussion	21
2.5.3	Governing Equations	21
2.5.4	Initial and Boundary Conditions	23
2.5	Summary and Conclusions	23
2.6	References of Chapter 2	25
CHAPTER 3		27
Combustion and Segregation of Programmed Splitting Stick Propellants		
3.1	Introduction	27
3.1.1	Motivation and Objectives	27
3.2	Method of Approach	30
3.2.1	Experimental Approach	30
3.2.2	Theoretical Approach	31
3.3	Discussion of Results	31
3.4	Summary and Conclusions	34
3.5	References of Chapter 3	35

DTIC QUALITY INSPECTED 1

Accession For	
NTIS GRA&I	<input checked="" type="checkbox"/>
DTIC TAB	<input type="checkbox"/>
Unannounced	<input type="checkbox"/>
Justification	
By	
Distribution/	
Availability Codes	
Dist	Avail and/or Special
A-1	

LIST OF APPENDICES

- Appendix A** Study of Combustion Behavior of Very High Burning Rate Propellants Using a Real-Time X-ray Radiography System
- Appendix B** Some High-Pressure Combustion Characteristics of VHBR Propellants
- Appendix C** Regression Behavior and Temperature Sensitivity Measurements of Very High Burning Rate Propellants
- Appendix D** Convective Ignition of LOVA Propellants Subjected to Crossflow Heating Conditions
- Appendix E** Convective Ignition Phenomena of LOVA Propellants
- Appendix F** Convective Ignition of LOVA Propellants
- Appendix G** An Experimental Ignition Study of RDX-Based Solid Propellant Grains Subjected to Crossflow Convective Heating
- Appendix H** A Comparative Analysis of the Convective and Radiative Ignition Processes of XM-39 Solid Propellant

LIST OF FIGURES

Figure 1.1	Layout of the Real-Time X-Ray Radiography System	3
Figure 1.2	Experimental Setup for X-Ray Radiography of VHBR Propellant Combustion	4
Figure 1.3	High Pressure Double Windowed Chamber	5
Figure 1.4	Pressure & Temperature Controlled Optical Strand Burner	6
Figure 2.1	Typical Large Caliber Ballistic Round with Granular Solid Propellant Bed	12
Figure 2.2	Important chemical and Physical Processes Which Characterize Thermal Ignition	19
Figure 2.3	Reaction Pathways for the Chemical Model of Ignition	20
Figure 3.1	Pressure-travel Curve and Elastic Strength of the Gun	28
Figure 3.2	Programmed Splitting Stick Propellants	29
Figure 3.3	Different Regions Considered in the Model	32

SUMMARY

The purpose of this work is to study the dynamic behavior in the combustion of three types of propellants used in artillery systems. These propellants include very high burning rate (VHBR), low vulnerability ammunition (LOVA), and programmed splitting sticks (PSS) propellants. Several advanced non-intrusive diagnostic instruments were utilized in this study. These instruments include: a real-time x-ray radiography system, a digital image processing system, a multi-channel laser Doppler velocimeter, and high-speed movie cameras. A shock tunnel and a high-powered CO₂ laser were also employed for this investigation.

This research project was divided into three major areas: a) combustion behavior of very high burning rate propellants, b) corrective and radiative ignition processes of low vulnerability ammunition propellants, and c) combustion and segregation phenomena of programmed objectives, method of approach, results, and summary and conclusion of each area is given in Chapter 1, 2, and 3 respectively. Results obtained from this study not only enhance the basic understanding of the complex phenomena and controlling mechanisms associated with ignition, combustion, and mechanical deformation of these propellants but also help the design of future artillery system with minimum hazards. A list of publications and paper presentations of the research findings of this project is given below. Some of these papers are attached as Appendices of this Final Report.

1. Salizzoni, R. M., Hsieh, W. H., Kuo, K.K., and Juhasz, A.A., "Study of Combustion Behavior of Very High Burning Rate Propellants Using a Real-Time X-Ray Radiography System," 25th JANNAF Combustion Meeting, NASA/Marshall Space Flight Center, October 1988, Huntsville, AL.
2. Field, R. and Kuo, K.K., "Observation of Multi-dimensional Flame Structures of LOVA Propellants," 25th JANNAF Combustion Meeting, NASA Marshall Space Flight Center, Huntsville, AL. CPIA Publication 498, Vol. 2, pp. 127-134, October, 1988.
3. Kuo, K.K., and Robbins, F.W., "Workshop Report: Combustion Characteristics of Stick Propellants," 25th JANNAF Combustion Meeting, NASA/Marshall Space Flight Center, Huntsville, AL, CPIA Publication 498, Vol. 2, pp. 281-288, October 1988.
4. Salizzoni, R. M., Hsieh, W. H., and Kuo, K. K., "Real-time X-Ray Radiography of VHBR Propellants," JANNAF Workshop on "Advanced Diagnostics for Propellant Combustion," June 1989, U.S.Army ARDEC, Picatinny Arsenal, NJ.
5. Ritchie, S. J., Hsieh, W. H., and Kuo, K. K., "Convective Ignition of LOVA Propellants Subjected to Crossflow Heating Conditions," 26th JANNAF Combustion Meeting, Pasadena, California, CPIA Publication 529, Vol. 1, October 1989.
6. Salizzoni, R. M., Hsieh, W. H., Peretz, A. and Kuo, K. K., "Some High-Pressure Combustion Characteristics of VHBR Propellants," 26th JANNAF Combustion Meeting, Pasadena, CA, CPIA Publication 529, Vol 1, October 1989.
7. Harris, L. E., and Kuo, K. K., "Workshop Report: Advanced Diagnostics for Propellant Combustion," 26th JANNAF Combustion Meeting, Pasadena, CA, CPIA Publication 529, Vol. 1, pp. 217-226, October, 1989.
8. Ritchie, S. J., Hsieh, W. H., and Kuo, K. K., "Convective Ignition Phenomena of LOVA Propellants," AIAA-90-2194, AIAA/ASME/SAE/ASEE 26th Joint Propulsion Conference, Orlando, FL., July 16-18, 1990.
9. Salizzoni, R. M., Hsieh, W. H., and Kuo, K. K., "Regression Behavior and Temperature Sensitivity Measurements of Very High Burning Rate Propellants," 27th JANNAF Combustion Meeting, Cheyenne, Wyoming, November 5-9, 1990.
10. Ritchie, S. J., Hsieh, W. H., and Kuo, K. K., "Convective Ignition of LOVA Propellants," 27th JANNAF Combustion Meeting, Cheyenne, Wyoming, November 5-9, 1990.

11. Rivera, J. D., Hsieh, W. H., and Kuo, K. K., "Experimental Study and Modeling of the Combustion of Programmed Splitting Stick Propellants," 27th JANNAF Combustion Meeting, Cheyenne, Wyoming, November 5-9, 1990.
12. Ritchie, S. J., Hsieh, W. H., and Kuo, K. K., "An Experimental Study of RDX-Based Solid Propellant Grains Subjected to Cross-Flow Convective Heating," accepted for publication in the *Journal of Propulsion and Power*, February 1991.
13. Rivera, J. D., Hsieh, W. H., and Kuo, K. K., "Experimental Study and Modeling of the Combustion of Programmed Splitting Stick Propellants," AIAA-90-2198, AIAA/ASME/SAE/ASEE 26th Joint Propulsion Conference, Orlando, FL, July 16-18, 1990.
14. Rivera, J.D., Hsieh, W. H., and Kuo, K. K., "Theoretical Modeling of the Combustion Processes of Programmed Splitting Stick Propellants," *Proceedings of the 13th International Colloquium on Dynamics of Explosions and Reactive Systems*, Nagoya, Japan, July 28 - August 2, 1991.
15. Ritchie, S. J., Hsieh, W. H., and Kuo, K. K., "An Experimental Study of RDX-Based Solid Propellant Grains Subjected to Crossflow Convective Heating," accepted for publication in *AIAA Journal of Propulsion and Power*, May 21, 1991.
16. Ritchie, S. J., Fetherolf, B. L., Hsieh, W. H., and Kuo, K. K., "A Comparative Analysis of the Convective and Radiative Ignition Processes of XM-39 Solid Propellants," 28th JANNAF Combustion Subcommittee Meeting, San Antonio, Texas, October 28 - November 1, 1991.
17. Salizzoni, R. M., Hsieh, W. H., and Kuo, K. K., "Temperature Sensitivity Measurements and Regression Behavior of a Family of Boron-Based Very High Burning Rate Propellants," accepted for publication in the *Proceedings of the Second International Symposium on Special Topics in Chemical Propulsion: Combustion of Boron-Based Solid Propellants and Solid Fuels.*, (Ed. K.K.Kuo and R. Pein) Hemisphere Publishing Corp., 1992.

ACKNOWLEDGEMENT

This report represents the research results obtained under Contract No. DAAL-03-83-K-0064 sponsored by the Army Research Office, Research Triangle Park, NC under the management of Dr. David M. Mann. The support and encouragement of Mr. A. Horst, Mr. D. Kruczynski, Mr. F. W. Robbins and Dr. A. A. Juhasz of BRL are also appreciated. The authors would like to thank Aerojet Propulsion Company for providing the VHBR propellants used in this study. The efforts of Mr. Robert Tompkins and Mr. Charles D. Bullock of BRL for the supply of fiberglass tubes and high-pressure seals are also acknowledged.

CHAPTER 1

COMBUSTION BEHAVIOR OF VERY HIGH BURNING RATE PROPELLANTS

1.1 INTRODUCTION

1.1.1 Background

The term very high burning rate (VHBR) propellant refers to a solid propellant that has exhibited apparent burning rates between 1 and 500 m/s (3 and 1600 ft/s) in closed vessel tests. Before VHBR propellants were developed in the early 1970's, the only solid propellants that burned faster than 0.5 m/s were explosives, and explosives burned much faster, i.e., above 2000 m/s. The burning rates for a VHBR propellant lie in the range between normal deflagration (subsonic combustion) and detonation (supersonic combustion). One of the possible explanations for this seemingly high burning rate is porous burning; the combustion does not occur only at the surface of the propellant (layer-by-layer burning) but actually penetrates the surface and propagates inside the propellant (volumetric burning)¹.

VHBR propellants are composite propellants, which, in general, contain two basic chemical constituents, an oxidizer and a binder. The oxidizer could be HMX, RDX, AN, TAGN, or KNO_3 or a combination of these. The binder could be comprised of CTBP, carbowax 4000, GAP, NC/DNT/A4, epoxy, or PNC. In addition to these basic constituents, VHBR propellants also contain a burning rate catalyst. Even a small amount of the burning rate catalyst can increase the burning rate of the propellant markedly².

The most prominent burning rate catalyst for VHBR propellants are the salts of boron hydrides, particularly the salts of the $\text{B}_{10}\text{H}_{10}^-$ and $\text{B}_{12}\text{H}_{12}^-$ anions. Researchers know that chemical reactions involving boron are highly exothermic; however, they do not know how the boron could affect the burning rate so dramatically. To make the problem worse, they do not even know if the catalytic effect occurs in the gas or the solid phase. Some researchers speculate that the abundance of loosely bound hydrogen atoms in boron hydride is partially responsible for the increased burning rate; they believe that the hydrogen atoms break away from the boron hydride easily and become highly reactive free radicals. This would enhance the combustion process in the gas phase, which would in turn, increase the heat transfer to the solid phase. The end result being an increase in burning surface temperature and burning rate.

Since the first applications of VHBR propellants in the early 1970's, interest in their combustion phenomena has continued to increase. This interest arises primarily because of VHBR propellants potential use in interior gun ballistics as a monolithic (stationary) or travelling charge. Determining the burning rate of a solid propellant as a function of pressure is the minimum amount of information needed to design any charge. This relationship between burning rate and pressure is often measured using a closed bomb apparatus.

In a conventional closed bomb test, a propellant sample is burned in a sturdy metal enclosure which retains all of the combustion products. As the propellant burns, the pressure inside the chamber increases, and from this pressure-time data, the gas generation rate can be calculated as a function of time and pressure. If the burning surface area of the propellant is also known, the burning rate can be deduced from the gas generation rate. Often times, however, the burning surface area is not known with great certainty and must be estimated. An error in this estimation would result in an error in the calculated burning rate. For this reason, this burning rate is often called an apparent burning rate. This research focussed on measuring the burning rate by using a series of X-ray images instead of deducing it from a pressure-time trace.

1.1.2 Objectives

The combustion behavior of three formulations of very high burning rate (VHBR) propellants was investigated. These formulations contain 0, 2, and 4% boron hydride, $\text{B}_{10}\text{H}_{10}$, the burning rate catalyst.

The first objective was to measure the burning rates of all three formulations using a real-time X-ray radiography (RT) system. In these tests, the RTR system was used to determine the instantaneous burning surface profile of the VHBR grains as they burned in a transient test with pressure levels reaching 330 MPa (48,000 psi). From the X-ray images obtained from these tests, the burning rates were deduced.

The second objective was to measure the burning rate of the 0% boron hydride formulation as a function of pressure and initial strand temperature. This was accomplished by using a temperature and pressure controlled optical strand burner (OSB). The temperature of the strand burner can be set from -40°C to $+70^{\circ}\text{C}$ (-40°F to $+158^{\circ}\text{F}$), and the pressure can be maintained at steady levels up to 41 MPa (6000 psi). The 0% boron hydride formulation was tested at -10, 20, and 70°C and to the maximum pressure.

1.2 METHOD OF APPROACH

Two major diagnostic tools were incorporated in this study: a real-time X-ray radiography (RTR) system and a pressure and temperature controlled optical strand burner (OSB). The RTR system allowed burning rates to be measured under dynamic pressurization up to 345 MPa (50,000 psi), and the OSB allowed for burning rate measurements at constant pressures up to 41.4 MPa (6000 psi).

1.2.1 Real-Time X-Ray Radiography Study

Two test rigs were designed and built for this portion of the study: a medium-pressure (MP) test rig and a high-pressure double-windowed (HPDW) test rig. The medium-pressure test rig reached a maximum pressure of 172 MPa (25,000 psi) and the HPDW reached 345 MPa (50,000 psi).

1.2.1.1 X-Ray System

The purpose of the real-time X-ray radiography system is to generate many instantaneous images of the propellant grain as it burns in a high-pressure chamber. A schematic diagram of the X-ray system is shown in Figure 1.1. The X-rays are produced in the X-ray head, pass through the test rig and are intercepted by the image intensifier. The image intensifier then transforms the X-ray image into a visible-light image with a time constant of less than 1 microsecond. This visible-light image is then recorded with a high-speed video camera (up to 12,000 pps) and later analyzed with the image processing system. A brief description of the X-ray system is given in Appendix A in the Method of Approach.

1.2.1.2 Medium-Pressure Test Rig

Figure 1.2 shows a diagram of the medium-pressure test rig. This test rig can reach a maximum pressure of 172 MPa (25,000 psi). The heart of this device is a fiberglass or carbon-fiber tube. Because of their relatively low X-ray attenuation and high strength, these two materials are suited for this particular application. The tubes had an inner diameter of 2.86 cm (1.125 in.) and an outer diameter of 4.13 or 4.76 cm (1.625 or 1.875 in.). In this chamber, X-ray images of an end-burning cylindrical grain were recorded at 4000 pictures per second. This test rig was also used to conduct interrupted burning tests of VHBR propellants. A more detailed description of this test rig is given in Appendix A.

1.2.1.3 High-Pressure Double-Windowed Test Rig

Figure 1.3 shows a diagram of the high-pressure double-windowed (HPDW) test rig used in conjunction with the X-ray system. This chamber was tested to a maximum pressure of 345 MPa (50,000 psi). The free volume of the chamber is 320 cc. As was the case with the medium-pressure rig, the heart of this chamber is the filament-wound fiberglass tube. The tube has an inner diameter of 6.99 cm (2.75 in.) and an outer diameter of 12.06 cm (4.75 in.). It can accommodate a cylindrical grain which has a diameter of 5.08 cm (2.0 in.) and a length of 5.08 cm (2.0 in.). In a typical test, the grain had a length of 3.38 cm (1.33 in.) and a perforation diameter of 0.63 cm (0.25 in.). It had a mass of 110 gm which created a loading density of 0.34 gm/cc. A description of this test rig is given in Appendix C.

1.2.2 Pressure and Temperature Controlled Optical Strand Burner

Figure 1.4 shows a schematic diagram of the strand burner. The design conditions of the strand burner are as follows: the temperature range is -40°C to $+70^{\circ}\text{C}$ (-40°F to 158°F), and the pressure level range is vacuum to 41.4 MPa (6000 psi). The size of the propellant strand was 6.3 mm (0.25 in.) in diameter by 5.08

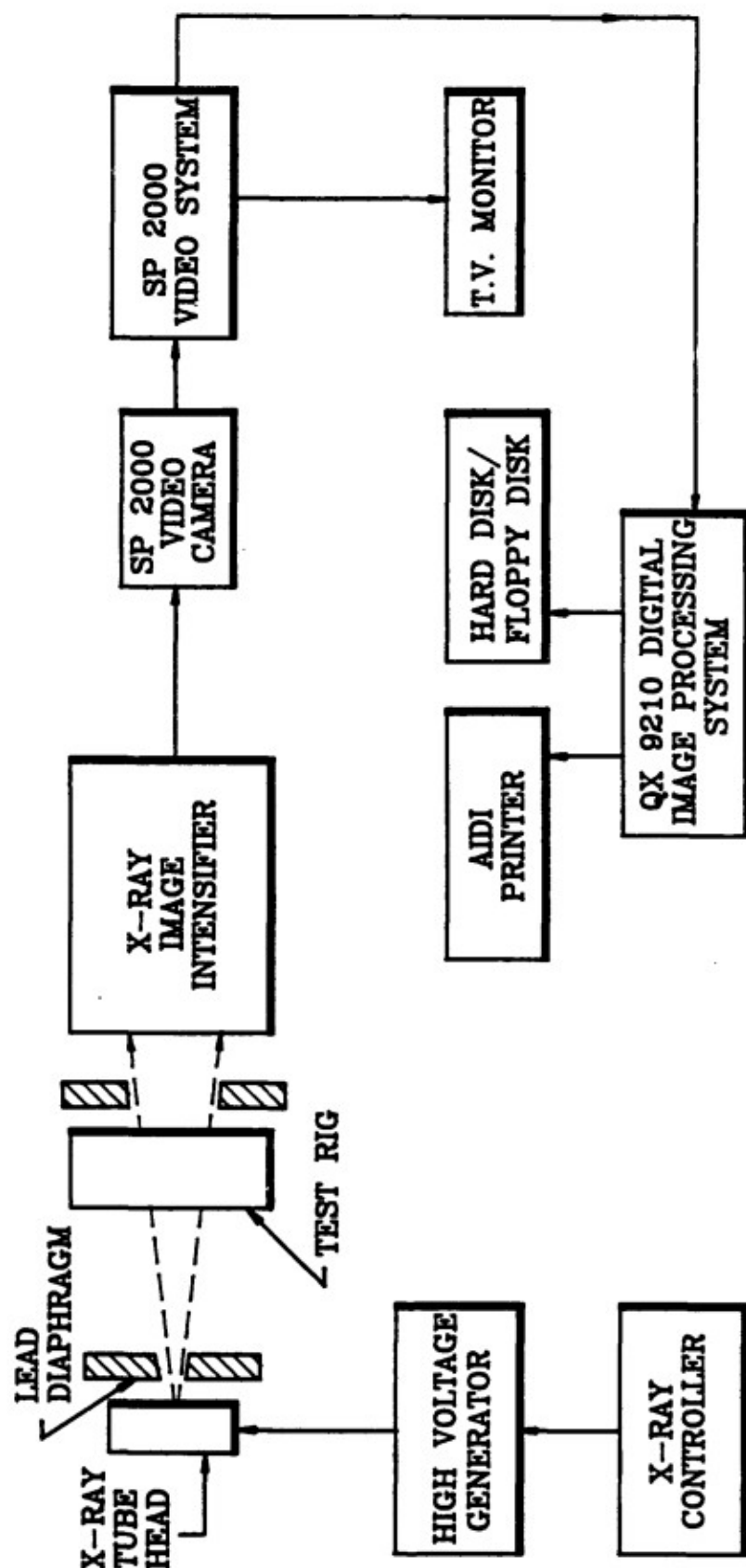


Figure 1.1 Layout of the Real-Time X-Ray Radiography System

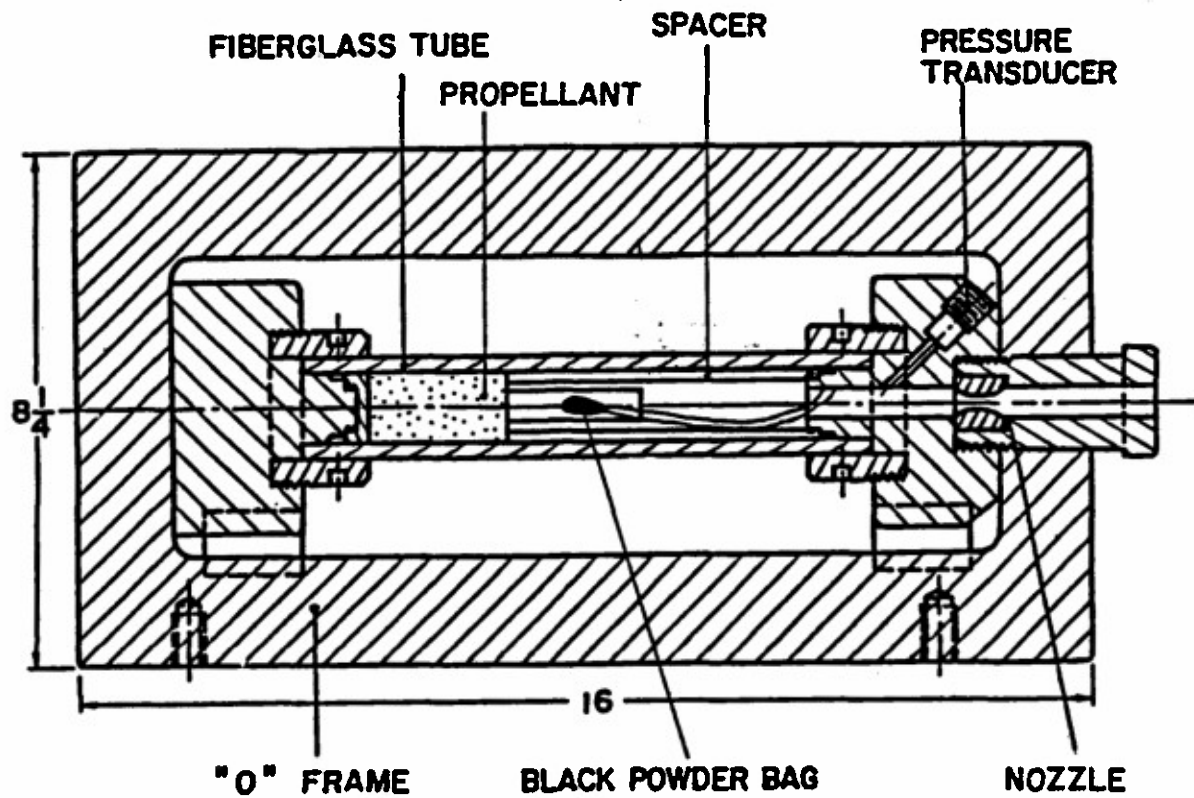
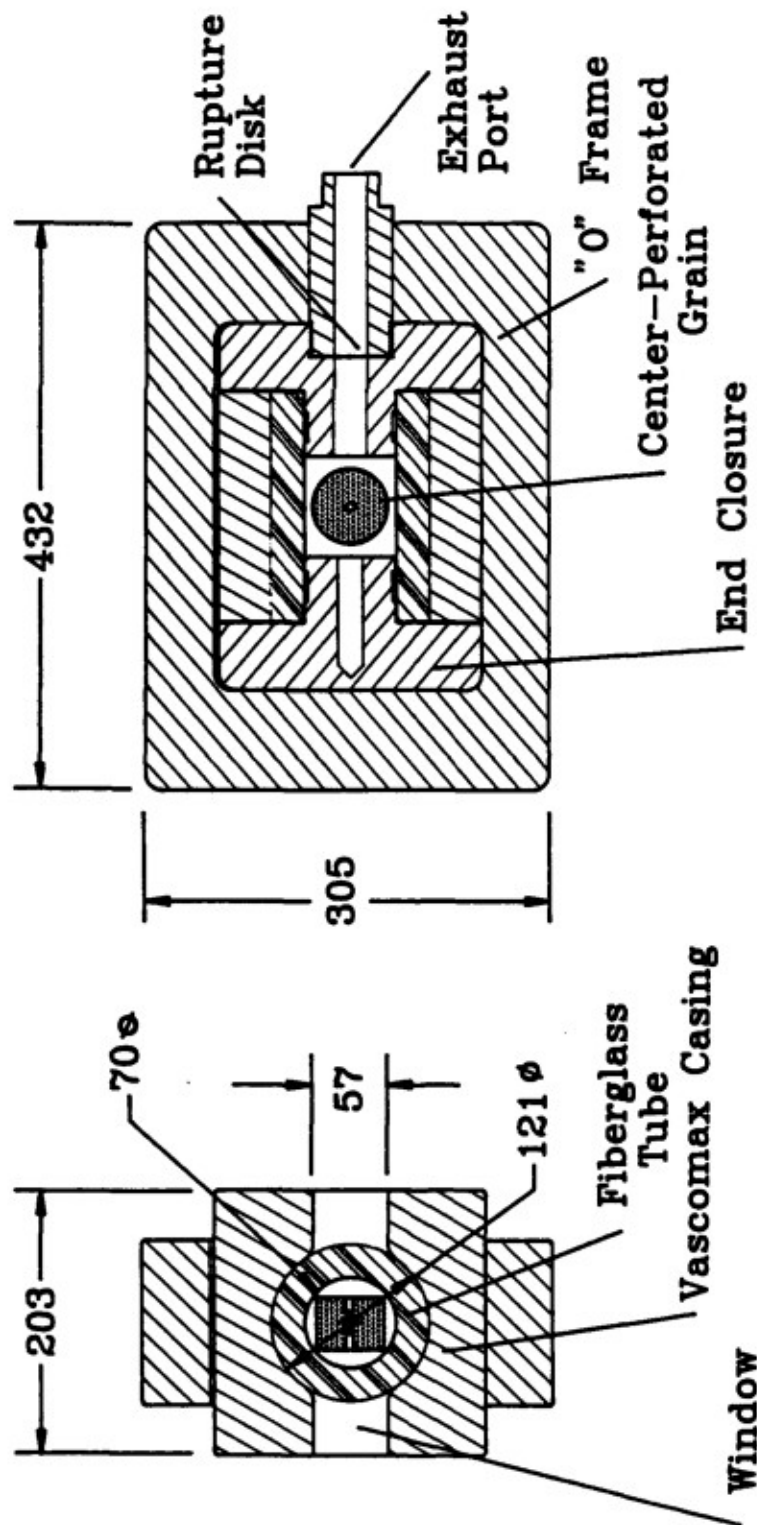


Figure 1.2 Experimental Setup for X-Ray Radiography of VHBR Propellant Combustion



NOTE:

All dimensions shown
are in millimeters.

Figure 1.3 High Pressure Double Windowed Chamber

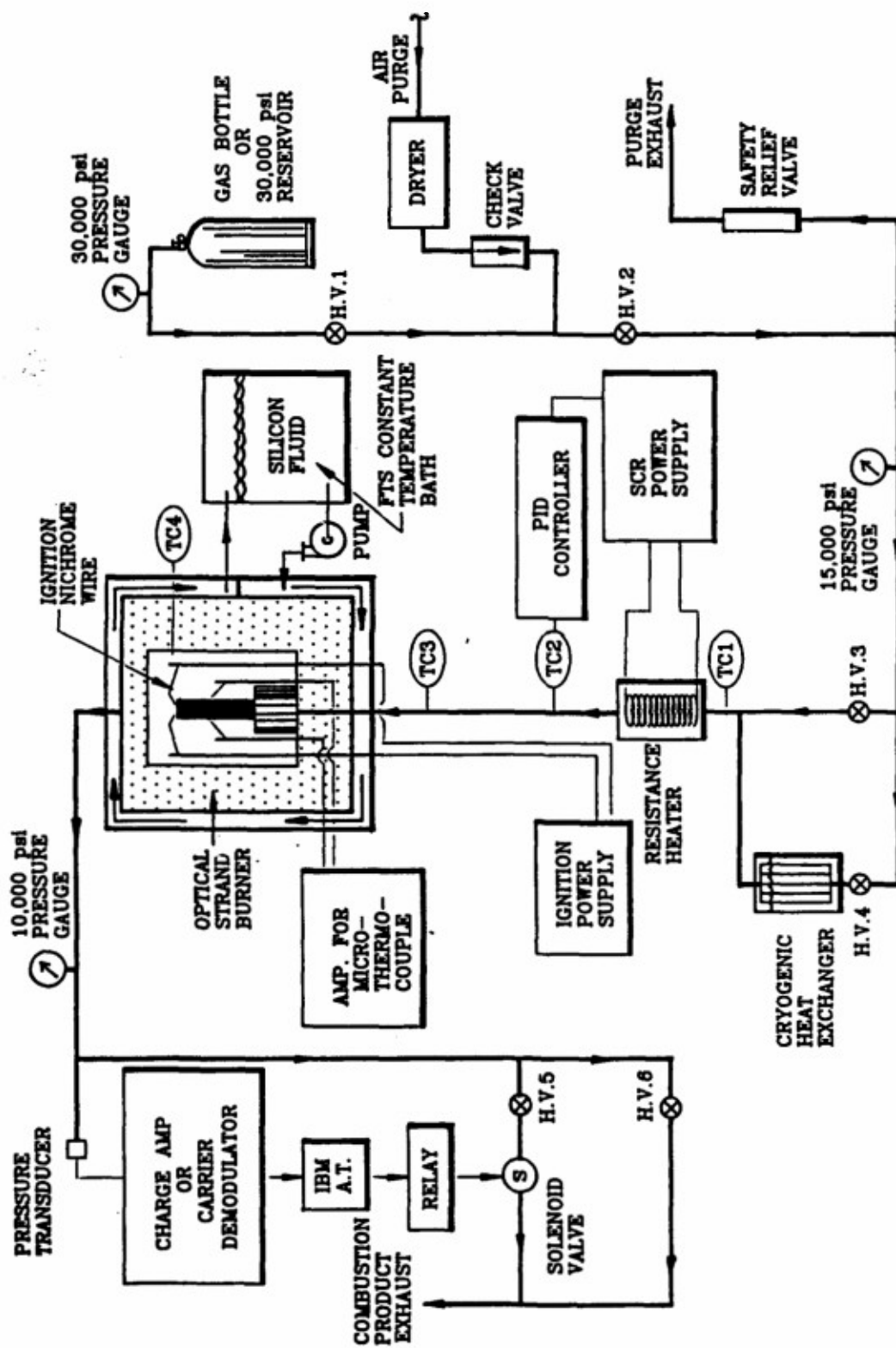


Figure 1.4 Pressure & Temperature Controlled Optical Strand Burner

cm (2.0 in.) in length. For each test, the external surface of the propellant sample was coated with a very thin layer of flame inhibitor (cellulose acetate); this provided a very effective means for preventing side burning, especially at higher pressures.

1.3 DISCUSSION OF RESULTS

Quantitative results obtained from this study include burning rate measurements from a real-time X-ray radiography system and a pressure and temperature controlled optical strand burner. In addition to these results, this study helped to answer some questions concerning the combustion mechanisms associated with very high burning rate behavior of solid propellants. Detailed results are provided in Appendices A, B, and C.

1.3.1 Results Obtained From Real-Time X-Ray Radiography Study

The medium-pressure and the high-pressure double-windowed test rigs were used in conjunction with the real-time X-ray radiography (RTR) system to observe the combustion phenomena of three formulations of VHBR propellants. These propellants contained 0, 2, and 4% boron hydride, the burning rate catalyst.

1.3.1.1 Results Obtained From the Medium-Pressure Test Rig

The grain configuration for these tests was an end-burning solid cylinder. X-ray images were typically recorded at 2000 or 4000 pictures per second. The maximum chamber pressure was 172 MPa (25,000 psi) with a test duration of approximately 100 ms.

The first series of tests conducted in this chamber used a propellant grain that was encased in a thin fiberglass casing. The X-ray images obtained from these tests clearly showed that the burning surface did not regress with a planar contour (see Figure 5, Appendix A). In later tests, the fiberglass casing was removed and a coating of cellulose acetate, a flame inhibitor, was applied to the circumferential and base areas. This resulted in a grain that do burn with a fairly planar contour (see Figure 6, Appendix A). Once a planar burning surface was obtained the linear burning rates were readily deduced. These burning rates are plotted as a function of pressure for all three formulations in Appendix A, Figures 8 and 9.

Observation of the X-ray videos revealed that all of the tests conducted in this chamber showed that the propellant grain remained as one piece, i. e., the grain showed no signs of break-up. This result was confirmed by analyzing individual X-ray images with the image processing system: the grain remained fairly cylindrical throughout the test (see Figure 7, Appendix A).

1.3.1.2 Results Obtained From the High-Pressure Double-Windowed Test Rig

Test involving all three formulations of VHBR propellant were performed in the high-pressure double-windowed chamber with a maximum pressure reaching 331 MPa (48,000 psi). Each propellant grain had a single perforation diameter of 0.63 cm (0.25 in.), outer diameter of 5.08 cm (2.00 in.), and a length of 3.38 cm (1.33 in.). All tests were conducted under similar conditions, i. e. same igniter pressure, sample geometry and mass. The video images were recorded at 500 pps with the high-speed video camera (Spin Physics 2000).

Figure 4 of Appendix C shows some of the results of a test involving the 0% boron hydride formulation. Over two hundred video images were obtained during this test which lasted over 400 ms. The four images in this figure clearly show the outward progression of the inner radius of the grain as the relatively high density propellant is replaced by low density gases. The pressure-time trace emphasizes how the progressive nature of a center-perforated grain create a tremendous increase in pressure after a long interval of relatively slow pressure rise.

For all three propellant formulations, the burning rates as a function of pressure were deduced. Figures 6, 7, and 8 of Appendix C contain plots of burning rate versus pressure for all three formulations.

The solid line in each of these plots represent data that was obtained from the medium-pressure test rig with an end-burning configuration.

1.3.2 Results Obtained From Temperature Sensitivity Measurements

Strand burning rates for the 0% boron hydride formulation were measured at three temperatures: -10, 20, and 70°C. These burning rates are presented in Figure 13 of Appendix C. Each point on the graph represents data obtained from a single test. A slope break is observed at 21 MPa. Below the slope break, the pressure exponents of the burning rates are quite close; however, above the slope break, the pressure exponent at 70°C is larger than those at the other two temperatures.

The temperature sensitivity for the 0% boron hydride formulation is plotted in Figure 14 of Appendix C. Discontinuities in the temperature sensitivity occur at the burning rate slope-break point of 21 MPa. As the initial temperature of the propellant increases, the sensitivity decreases.

1.4 SUMMARY AND CONCLUSIONS

1. From the X-ray images of the tests conducted in the medium-pressure test rig (end-burning grain), grain deconsolidation was not observed under transient test conditions up to 172 MPa (25,000 psi).
2. An increase of boron hydride concentration from 0 to 2% has a significant effect on the burning rate. However, a further increase in boron hydride from 2 to 4% does not change the magnitude by any significant amount. Slope breaks in log-log plots of burning rate versus pressure were noted for these VHBR propellants.
3. The measured pressure-time traces and recorded X-ray images for identical test conditions show a high degree of reproductibility. This implies a high potential of utilizing this family of VHBR propellants for gun interior ballistic purposes.
4. Interrupted burning tests of the 0% formulation revealed that dimples were generated in the burning surface; however, microscope images of the recovered samples indicated that very insignificant amounts of subsurface reaction occurred. This can be verified by the fact that the color of the subsurface zone is the same as in the virgin material.
5. In the high-pressure double-windowed (HPDW) tests, the X-ray images show that the propellant grains remain as consolidated charges without breaking into small fragments at pressures up to 331 MPa (48,000 psi).
6. The transient burning rates obtained in the HPDW test rig (center perforated grain) are reasonably close to the transient burning rates measured in the O-frame chamber with an end burning configuration.
7. A recovered grain which extinguished at 331 MPa (48,000 psi) showed a rough burning surface. The entire surface is covered with dimples which are visible to the naked eye. These dimples are approximately 0.5 mm in diameter by 0.5 mm deep. From SEM photographs, smaller, less populated dimples are evident; on the microscopic scale, the binder's surface is quite smooth.
8. For the 0% boron hydride formulation, the transient burning rates are approximately 22% lower than the strand burning rates.
9. The temperature sensitivity was measured as a function of pressure and initial temperature. The sensitivity increases as the temperature decreases.

1.5 REFERENCES

1. Juhasz, A. A., May, I. W., Aungst, W. P., Lynn, F. R., "Combustion Studies of Very High Burning Rate (VHBR) Propellants," Ballistic Research Laboratory Memorandum Report ARBRL-MR-03152, February 1982.
2. Salizzoni, R. M., Hsieh, W. H., Kuo, K. K., Juhasz, A. A., "Study of Combustion Behavior of Very High Burning Rate Propellants," *Proceedings of the 11th International Symposium on Ballistics*, May 1989, Vol. I, pp. 129-140.
3. Telydyne McCormick Selph, Technical Bulletin No. 74-7, 1974.
4. Helmy, A. M., "Criteria Analysis of VHBR Solid Propulsion System for In-Tube Burning Rocket Application," AIAA/SAE/ASME 19th Joint Propulsion Conference, AIAA-83-111, June 1983.
5. Salizzoni, R. M., Hsieh, W. H., Kuo, K. K., Peretz, A., "Some High-Pressure Combustion Characteristics of VHBR Propellants," *Proceedings of the 26th JANNAF Combustion Meeting*, October 1989, Vol. I, pp. 255-266.
6. McCarty, K. P., Isom, K. B., Jacox, J. L., "Nitramine Propellant Combustion," AIAA Paper No. 79-1132, AIAA/SAE/ASME 15th Joint Propulsion Conference, June 18-20, 1979, Las Vegas, Nevada.

CHAPTER 2

CONVECTIVE AND RADIATIVE IGNITION PROCESSES OF LOW VULNERABILITY AMMUNITION PROPELLANTS

2.1 INTRODUCTION

2.1.1 Background and Motivation

As is the unfortunate case with most combustible materials, the solid propellants employed in rocket and ballistic propulsion systems are extremely hazardous in nature. The military and industrial community has long recognized these dangers and placed significant emphasis on reducing the probability of costly system failures which can result in the loss of irreplaceable human lives and expensive material.¹⁻⁴ Part of this hazards reduction program involves the formulation of solid propellants which exhibit desirable "insensitive" munition behavior.^{2,5} These materials, typically used in large caliber ballistic rounds, are classified by the military as low vulnerability ammunition (LOVA) solid propellants. Many LOVA candidates now under consideration are based on cyclotrimethylenetrinitramine (RDX) and cyclotetramethylenetetra-nitramine (HMX). These nitramine-based propellants display a high thermal stability, a low sensitivity to ballistic vulnerability, low smoke output and high specific impulse or impetus.⁶ With the advent of LOVA propellant formulations, which are by design difficult to ignite, there is increased interest in understanding the ignition characteristics of composite solid propellant materials to both desirable and undesirable stimuli.

Due to the extreme temperatures, pressures, geometric complexities, and short time scales involved, the fundamental physical and chemical processes which characterize the ignition of solid propellants in ballistic applications have always been difficult to examine. For example, a typical large caliber ballistic round is shown in Figure 2.1. The igniter tube is located in the center of a main solid-propellant bed which is composed of either granular or stick-shaped propellant. The igniter tube usually contains several grains of pyrotechnic material which is easily ignited by either a mechanical or electrical primer system. The resulting combustion gases enter the main propellant bed through a series of holes and heat the grains or sticks via convection from hot gases, radiation from burning particles and hot gases, and conduction from hot impinging particles.⁷

The standard method of determining propellant formulation effectiveness in a gun system is to employ a simulator. A simulator is an instrumented version of a particular gun chamber which measures important ballistic performance information. These tests, through a systematic trial and error approach, provide an excellent method of determining the optimum igniter and charge loading density for a given ballistic system. Many such tests, for various caliber weapons, have been carried out with LOVA propellants.⁸⁻¹¹ However, simulator tests, by virtue of their complex geometries, are difficult to interpret in terms of the fundamental information which can be more easily obtained by using small-scale laboratory tests. This shortcoming was identified at a JANNAF workshop coordinated by Stiefel and Kuo.¹²

Small-scale tests, by incorporating simple geometries and quantifiable energetic stimuli, lend themselves to realistic model validation of chemical and physical processes which are important to the ignition process. These tests, however, are not without some drawbacks. Typically, the design of a test focuses on the energy input to the sample from a single, external source. Since the process inside a gun chamber involves a number of different heating mechanisms, several small-scale tests would be required to fully characterize the propellant material. This process is not only expensive and time-consuming, but most laboratories do not possess the necessary equipment to consider such a comprehensive analysis.

2.1.2 Problem Statement

The ignition process of solid propellant materials is affected by a large number of parameters. Included in this list of parameters is the mechanism or source of external energetic input to the sample which starts the ignition process. Many excellent research programs have been carried out to observe and understand the ignition response of solid propellant materials to a single, external stimulus. However, the ability to relate the results of these programs

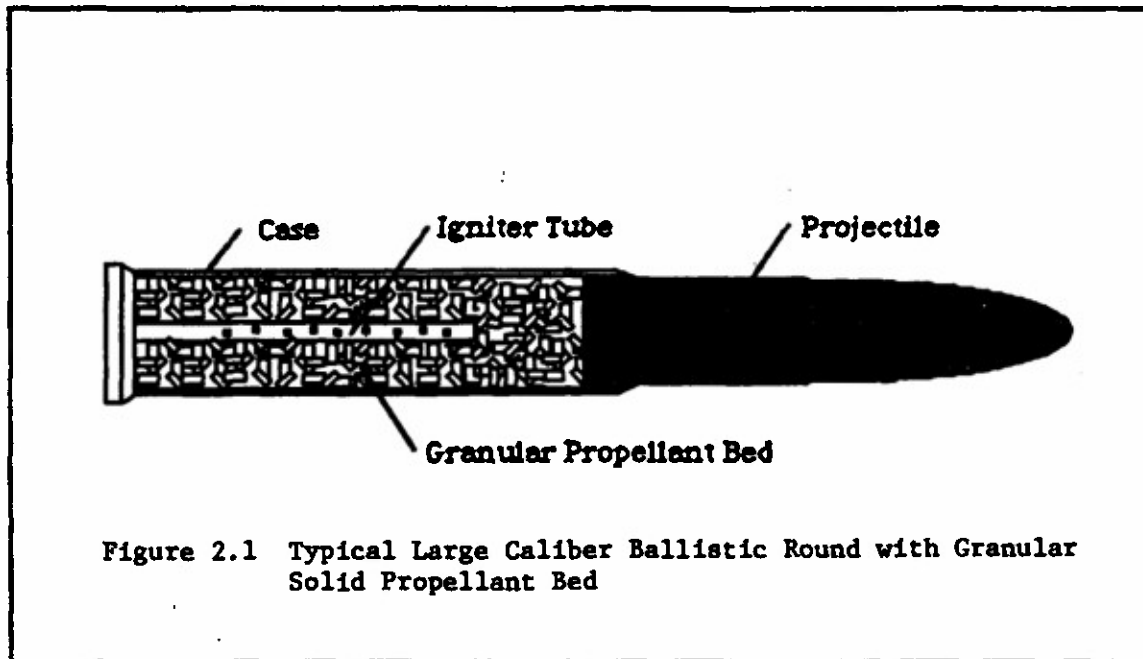


Figure 2.1 Typical Large Caliber Ballistic Round with Granular Solid Propellant Bed

to the propellant response when subjected to a different type of stimulus does not exist. A global ignition theory for solid propellant materials which includes the effects of different stimuli has not yet been discovered.

This program addressed part of this problem; the relationship between the ignition characteristics of XM-39, an RDX-based solid propellant, subjected to various thermal energetic stimuli. The thermal mechanisms are convective heating by a high temperature, high pressure gaseous flow and radiative heating from a CO₂ laser source. Both of these mechanisms are representative of what is found in the main propellant bed of a ballistic round during the ignition process.

2.1.3 Program Objectives

The intent of this program is to increase the effectiveness of the small-scale laboratory testing process and to better understand the ignition response of LOVA propellants to the thermal stimuli present within a gun chamber. This includes convective heating from a hot, gaseous flow and radiative heating from a CO₂ laser source. An experimental program has been carried out to study each of these processes independently using small-scale laboratory test methods. A theoretical and numerical analysis is used to examine the relationships between these two different thermal mechanisms.

The major objectives for the program are twofold: (1) to separately examine the ignition of RDX-based solid propellant grains in well controlled experiments and identify important physical mechanisms to the different ignition processes and (2) use theoretical and empirical analyses of the test configurations, which compensate for the different heat-transfer and fluid-mechanical aspects of the external thermal input while considering similar underlying chemical reactions, to compare and relate the results of the experimental studies. From the understanding obtained in this study, coupled with other relevant studies, the ability to predict solid propellant ignition under various conditions is enhanced.

The specific steps taken in the study are:

1. reconstruction of a shock tunnel facility.
2. examination of the convective ignition of XM-39 with a shock tunnel facility.
3. reconfiguration of the shock tunnel into a shock tube.
4. examination of the conductive ignition of XM-39 using a shock tube facility.
5. examination of the radiative ignition of XM-39 using a CO₂ laser test facility.

6. observation, using optical and scanning electron microscopy (SEM), of pretest and post-test sample surfaces from the ignition tests.
7. generation of an empirical relationship between the experimental data.
8. formulation of a simple one-dimensional theoretical model for the conductive and radiative test configurations based partially on experimental observations.
9. concurrent numerical solution of the one-dimensional radiative and conductive model using experimental ignition delay data for validation.

2.2 EXPERIMENTAL APPROACH

The experimental aspect of this project was made up of two separate test programs. The first of these tests was designed to examine the ignition of RDX-based XM-39 solid propellant grains when subjected to predominantly convective heating from a high temperature, high pressure flow field. This type of flow is representative of what is found in standard gun chambers during the practical ignition process. From the literature, it has already been shown that a shock tunnel facility provides an excellent means of generating the necessary flow conditions.¹³⁻¹⁹ Therefore, the shock tunnel facility used previously by Birk and Caveny^{13,14} and Kashiwagi et al.¹⁵⁻¹⁸ was obtained, reconstructed and used to generate the high temperature, high pressure gas field required for this portion of the project.

A second test was used to observe ignition of the same solid propellant when subjected to laser-generated radiative heating. An existing CO₂ laser facility, especially designed to study solid propellant ignition under high pressure conditions²⁰⁻²², was utilized for this part of the experimental study. These tests were designed to provide data for eventual theoretical model validation and to obtain insight into the important physical processes which occur during the ignition of nitramine-based solid propellants.

The two facilities are very briefly described in the following sections. Further descriptions of the convective ignition test equipment can be found in Appendices D through G. For more details on the radiative ignition test equipment see Appendix H and the cited references.

2.2.1 Convective Ignition Tests

2.2.1.1 HPCL Shock Tunnel Facility

The High Pressure Combustion Laboratory Shock Tunnel Facility is a total of 24.1 m (79 ft) long. The major components are the driver section (9.7 m/31.8 ft), driven section (8.5 m/27.9 ft) and the exhaust chamber (5.9 m/19.3 ft). The inside diameter of the tunnel is approximately 9.718 cm (3.826 in.). The driver section has a maximum rating of 12.4 MPa (1800 psia) and is charged with helium gas. The driven section can be vacuumed down to pressures as low as 1.38 kPa (0.2 psia) and the test gas can be composed of any combination of oxygen and nitrogen. The tunnel is operated remotely via a test console located just outside the test cell. Firing of the tunnel is accomplished through a double burst diaphragm technique in order to achieve consistent incident shock strengths.

The shock tunnel is used to create a reservoir of high temperature, high pressure gas which in turn induces a convective flow through the test section. Ideally this flow is of a steady temperature and pressure throughout the available test time. Under certain "tailored interface" conditions, the shock tube theoretically should provide the maximum useful test time. Experimental measurements found the maximum available test time occurred with an incident shock wave Mach number of 3.70 - 3.80 into air or nitrogen.

2.2.1.2 Convective Ignition Test Section

The test section is located at the end of the driven section and is characterized by a sudden cross-sectional area change from the 9.718 cm (3.826 in.) diameter round shock tunnel to a 2.858 cm (1.125 in.) square duct. A cut-out side view of the test section is shown in Figure 2 of Appendix D. Quartz windows located on the top and sides of the test section (side windows not shown in the figure) provide optical access. Perforated plates are located at both the upstream entrance and downstream exit. The downstream exit plate acts as a nozzle which chokes the flow and controls the velocity of gas through the test section. The upstream perforated plate was added to help damp out

initial pressure oscillations caused by the starting transient of the flow when the shock wave passes through the test section and to act as a flow straightener.

2.2.1.3 *Diagnostics for Convective Ignition Tests*

Diagnostics are highlight in Figure 3 of Appendix D. Three or four Kistler 601B1 pressure transducers located along the driven section of the tunnel detect the arrival of the shock wave at fixed locations and are used to measure the speed of the incident shock wave. Another Kistler 601B122 pressure transducer is located in the test section, 2.54 cm (1.0 in.) upstream of the sample, as can be seen in Figure 2 of Appendix D. To determine ignition delay, five RCA 1P28 photo-multiplier tubes with filters are used remotely via fiber optic tubes mounted on the top window of the test section. High speed visualization of the event is accomplished through the two side windows using a Kodak Spin Physics SP2000 high-speed video system with backlighting.

2.2.1.4 *Test Samples*

The propellant used for this study was XM-39 (Lot #A5-1184-113) which has a formulation of 76% RDX, 12% cellulose acetate butyrate (CAB), 7.6% acetyl triethyl citrate (ATEC), 4% nitrocellulose (NC), and 0.4% ethyl centralite (EC). The grain geometry was cylindrical with a nominal diameter of 7 mm (0.28 in.) and length trimmed to a constant 0.74 cm (0.29 in.). The graphite coating was removed prior to testing, and the surface was polished until it was visually smooth. The sample was mounted in the test section with the induced flow perpendicular to the length of the grain.

2.2.2 *Radiative Ignition Tests*

2.2.2.1 *CO₂ Laser Ignition Test Facility*

The CO₂ laser irradiation facility, shown schematically in Figure 3 of Appendix H, was constructed for a previous program and has been well-documented.^{20,21} A Coherent Super 48 high-powered CO₂ laser is used as the radiative source. This laser is capable of generating 800 watts in the continuous wave mode and 3500 watts in the pulsed mode. The beam is directed to the test chamber by a series of silicon mirrors and, for safety reasons, the path is completely enclosed by anodized guide tubes.

2.2.2.2 *High Pressure Test Chamber*

The high pressure test chamber was built in 1982²² as part of a program with the Naval Ordnance Station. The chamber is designed to be operated at internal pressures up to 5,000 psia. Two long, narrow plexiglass windows located on the "front" and "back" of the circular chamber provide optical access to allow for high speed filming of the ignition or flame spreading event. A gallium arsenide window, protected from combustion products by a potassium chloride window, is mounted on the top of the chamber to allow for passage of the CO₂ laser beam. The sample is mounted on a special section which is inserted into the bottom of the chamber.

2.2.2.3 *Diagnostics for Radiative CO₂ Laser Ignition Tests*

Ignition delay time was measured using a silicon photodiode positioned within the high pressure test chamber. Data from this diode is stored on a Nicolet digital oscilloscope which is triggered by the firing of the CO₂ laser. Two types of cameras were used to film the ignition event and determine the location of ignition. A conventional video camera was used to look at the color of the flame and to give reasonably good spatial resolution. A Spin Physics 2000 high speed video camera was used to obtain the necessary time resolution of the ignition and flame development.

2.2.2.4 *Test Samples*

The XM-39 solid propellant samples for the radiative ignition test had the same chemical formulation as the samples used in the convective ignition portion of this program. The samples were obtained in stick form, approximately 10.16 cm (4 in.) in length and 0.7 cm (.28 in.) in diameter, and were not perforated or graphite coated.

These sticks were cut by hand using a razor blade into short discs of about .7 cm (.28 in.). These discs were glued into place on the sample holder such that irradiation is upon the flat end of the disc-shape. The sample holder is inserted into the center of the test chamber.

2.3 EXPERIMENTAL RESULTS AND DISCUSSION

The results of the convective and radiative ignition tests are summarized in the sections below. Detailed presentation of these results has been made previously in numerous publications which are provided as Appendices D through H. Because there is a significant amount of radiative ignition data available in the literature for nitramine-based propellants, a very small number of tests were performed to provide ignition delay data for possible model validation. The availability of experimental data which could assist in characterizing the convective ignition of nitramine propellants is scarce, at best. Therefore, the convective ignition testing was much more comprehensive, involving significantly more diagnostic complexity.

2.3.1 Convective Ignition Test Results

2.3.1.1 Freestream Oxygen Dependency

For the tests performed in a nitrogen environment, no ignition or luminous flame was detected by either the high speed video or the photomultiplier tube detection system. When the test gas was changed to air, ignition of the XM-39 solid propellant grain was observed for many of the imposed test conditions. A definite freestream oxidizer dependency of the ignition delay time was observed in the convective ignition tests. This result substantiates previous observations by others. Birk and Caveny^{13,14} showed a similar result for HMX/PU propellant. In a 100% nitrogen environment, no ignition was observed for Reynolds numbers between 7,000 and 10,000. As oxidizer was added to the test gas, ignition in this Reynolds number range was observed and the ignition delay time decreased as the concentration of oxygen in the test gas increased. Additionally, Chang and Rocchio⁸ have also shown that oxidizer rich igniters can reduce long ignition delays in gun simulator studies.

2.3.1.2 Ignition and Flame-Spread Observation

Visual observation of the ignition location and subsequent flame-spreading on the propellant sample were considered very important. The observed phenomena was similar for all tests in which ignition was observed. Still pictures taken from the high speed video along with a detailed discussion can be found in Appendix D (Figure 7). Ignition was always observed in the region of boundary layer separation in a location just beyond 90° from the leading edge. Flame spread was across the downstream surface. There was minimal flame spreading, if any, in the upstream direction.

2.3.1.3 Ignition Delay Time

The measurement of ignition delay time was accomplished with photomultiplier tubes. The trace which first recorded a signal larger than three times the average noise value was used to determine the ignition delay value. The ignition delay times obtained in this fashion were compared to the observed video results for clarification. In many cases, a flash of light from the sample surface was observed on the video very early during the t_{ign} time (<3 ms). Because this coincides with the arrival of the shock wave and the transient start-up time, this phenomena was not easily observed on the more sensitive photomultiplier versus time trace. This phenomenon was also observed by Birk and Caveny^{13,14} in their study of nitrocellulose propellants. It can be explained using the following rationalization. When the incident shock wave arrives in the test section, the heating rates to the sample are very high. This has been substantiated by the heat flux data taken by Birk and Caveny.^{13,14} Gasification of the propellant material can take place and subsequent reactions observed. However, this 'transient' ignition was not always able to sustain burning for the entire test time because the heating rates decrease sharply with the onset of the quasi-steady flow through the test section. The sample, once quenched, would usually, but not always, reignite later during the steady-state convective heating period and sustain burning until the end of the test time. It is this second ignition point which has been labeled the ignition delay time (t_{ign}).

The conditions and ignition delay time results for the tests performed in air are given in Table I of Appendix G. A correlation similar to that performed by Keller et al.¹⁹ was found using the convective ignition delay time data for the XM-39 LOVA solid propellant. This analysis is completely described in Appendix G.

2.3.1.4 Microscopic Analysis of Propellant Surface Characteristics

Both optical and scanning electron microscopy (SEM) analyses were performed on recovered test samples. The results of this study are given in Appendix G in the form of a series of micro-photographs with accompanying descriptions. The micro-photographs indicate the formation of a liquid 'melt' layer similar to that described by numerous other researchers and a number of rice-like structures are visible across the surface. There are also a number of circular holes in the surface, especially in the region where ignition was observed.

2.3.2 Radiative Ignition Test Results

2.3.2.1 Test Conditions

Since a major goal of this program is the comparison of the radiative and convective ignition behavior for XM-39 LOVA solid propellant, the conditions for the two tests had to be as similar as possible. Therefore, the test gas used for all radiative ignition tests was air and the pressure of the gas in the test chamber was the same as those experienced in the test section of the shock tunnel facility (200-500 psia). The heating rates vary over the surface of the sample in the convective ignition test so a simple analysis based on stagnation heating of an inert sample was carried out to determine the heat flux rates to be used with the CO₂ laser facility in the radiative ignition tests. Heating rates were varied from 100 to 400 W/cm².

2.3.2.2 Observed Ignition and Flame-Spreading

Direct high-speed video of the ignition event was obtained and used to get an idea of the ignition location. The method used for all of these tests was to mark the location of the surface of the propellant using adjustable reticles on the viewing screen. The position at which light could first be observed was compared to the surface location. For all ignition tests, the location of the first luminous reaction was always very near the surface or at the surface.

2.3.2.3 Ignition Delay Time

The ignition delay time was measured using a silicon photodiode and checked using the high-speed video image. The data from this portion of the test program are shown in Table I of Appendix H. Included in this table is the pressure of the air in the test chamber, the incident heat flux from the CO₂ laser and the ignition delay time. The standard method for portraying ignition delay data for radiative ignition tests is a plot of the delay time versus incident heat flux on a log-log plot (see Figure 5 of Appendix H). The slope of the data collected for the XM-39 solid propellant when plotted using this method is approximately equal to -1.3. It can be theoretically shown for constant fully absorbed radiative heating of a semi-infinite, one-dimensional medium to a fixed temperature value, the slope of time to temperature versus heat flux is equal to -2.0. If the value of the slope is less than -2.0 (ie. -2.5) it would imply an additional heat input from a source, such as chemical reactivity, plays an important role in determining the ignition delay time.

Allowing for less than full absorption of the incident radiant flux due to surface reflectivity and beam attenuation due to interactions with gas phase species and particles, a slope of -1.3 can reasonably be interpreted as a dominant inert heating mechanism in the radiative ignition process. This does not mean that gas-phase reactivity is not important to the process. This only means that the time required to achieve ignition is dominated by the inert heat-up time and that once gasification is achieved, the chemical reaction time is very short.

2.3.2.4 Pressure Dependency

Radiative ignition tests were run over the entire range of pressures which were measured in the shock tunnel tests so that comparisons could be made (200 - 500 psia). Within the capabilities of the diagnostic equipment, no variation in the light emission time was observed in the pressure range studied.

2.4 COMPARATIVE ANALYSIS OF CONVECTIVE AND RADIATIVE PROCESSES

In this section, the physical and chemical processes which are important to the ignition of XM-39 composite solid propellant under either convective or radiative heating are discussed in detail. There is also a description of how the two processes may be more directly related.

2.4.1 General Description of the Convective Ignition Process

The convective ignition of nitramine composite propellant material involves many complex physical and chemical processes. Based on the observations made during the experimental portion of this study and inferred from other studies described in the literature, the following is a summary of the important mechanisms which lead to the ignition of these materials when exposed to convective thermal heating. Figure 7 in Appendix G has been composed to assist in the understanding. The picture represents the formation of boundary layer flow over the surface of a nitramine-based composite solid propellant grain in the geometry under study. The freestream gases are at a very high pressure and temperature while the propellant surface is initially at a uniform low temperature.

During the first part of the event, the flowing hot gases convectively heat the propellant sample without any resulting chemical reactions. This represents the inert heat-up time of the sample, which can be very significant in length. Because of the nature of the flow, the heating of this surface is not uniform in the flow direction and the problem must be considered as two-dimensional. As the temperature of the surface of the propellant rises, conduction heat transfer carries the energy to the interior of the solid material and the heat flux to the sample is reduced due to the lower thermal gradient between the surface and the gases. Due to the composite nature of the propellant, the conductivity of the material is not uniform and this heat flux could be very uneven. Also there are gas to surface and surface to chamber wall radiative heat transfer components which must be considered.

Eventually, somewhere on the propellant surface, the solid material begins to decompose, liquefy and/or evaporate. This most probably occurs near the leading edge where the heating rates to the solid material are the highest and the temperature increase is the most rapid. Many experimental studies have provided evidence of the formation of a liquid 'melt' layer. The composition of this liquid remains unknown but it could include melted propellant and decomposition products which result from a reaction that involves a solid to liquid phase change. Additionally, some of the solid material could decompose and evaporate directly into the gas phase. Finally, the liquid melt layer subjected to further heating will also either evaporate or decompose into the gaseous phase.

Up to this point, the majority of the heating is assumed to be convective flux from the freestream flow. Some exothermic reactions could occur in the solid and liquid phases but it is generally accepted that these reactions are probably not as significant to the ignition as the exothermicity of the gas-phase reaction processes. These gas-phase reactions display a delay time during which oxidizers from the propellant and freestream mix with fuels and further heating by the freestream occurs. Therefore the decomposition products generated at the leading edge of the sample will not react completely until much further downstream. The resulting chemical reactions at this downstream location generate a relatively large amount of energy. Some of this energy is lost to the test chamber walls and the freestream but a significant amount acts as a heat feedback mechanism to the sample surface which generates more gas-phase decomposition products. The heat feedback mechanism provides a means by which the propellant can 'feed' upon itself. Ignition results when the exothermic reactions in the gas-phase become the dominant source of heat flux to the propellant surface and the freestream heating is no longer required to maintain the reactivity of the propellant.

There are many complications to the above description which must be considered. First, because of the shear forces at the gas-liquid interface, the liquid surface will flow along the solid surface. The effects of this liquid layer are very dependent on the heating rates, flow conditions and thickness of the layer. Secondly, the liquid layer is actually a two-phase flow. Gaseous bubbles have been observed within this layer by various studies, including this one. The importance of this phenomena to the overall ignition process is not fully understood but it has been examined by Li et al. [23], who theoretically included the two-phase nature of the nitramine surface in a combustion model. They concluded that consideration of the gaseous phase in the condensed phase had a negligible effect on the final solution.

Due to the delay time associated with the mixing processes and the requirement that exothermic gas-phase reaction must occur in close proximity to the sample surface, an allowance must be made to increase the residence time of the decomposition products within the reaction zone. This is described in terms of a dimensionless Damkohler number, (Da):

$$Da = \frac{t_{\text{flow}}}{t_{\text{reaction}}} \quad (2.4.1)$$

If the Da is very small, the time during which the gaseous species are in the reaction zone is much less than the time needed for chemical reaction to occur. If this is the case, the gaseous species generated from the propellant surface are carried by the flow and dissipated downstream. Without heat-feedback from gas-phase reactions, ignition cannot occur. It is therefore desirable to increase the value of the Damkohler number. This is done by increasing the residence time and decreasing the reaction time. This can be accomplished by the formation of a recirculation region near the surface of the propellant. This type of flow raises the value of the Da by increasing the residence time, mixing rates and heat transfer effects of the gases near the surface (see Figure 7 in Appendix G). Ignition can locally occur near this recirculation region because the heat feedback to the surface generates gaseous decomposition products which provide the necessary oxidizer and fuel for the reaction zone. From this local ignition region, flamespread over the propellant sample occurs.

2.4.2 General Description of the Radiative Ignition Process

Many of the processes described above for the convective ignition process are also important to radiative ignition. There are several basic differences that must be accounted for, though. Figure 2.2 includes the mechanisms which are considered to be important. Initially, the surface of the solid propellant is heated inertly by incident radiative energy. Due to the radiative properties of the solid propellant surface, some of this incident energy is absorbed, some is reflected away from the surface, and some is transmitted into the condensed phase. Within the solid-phase, heating is due to conduction from the rise in temperature at the surface and in-depth absorption of the transmitted incident radiative energy. The absorption and reflective processes are very difficult to analyze but represent important differences between radiative, conductive and convective heating processes. As in the case of convective heating, at some point past the solid phase will decompose, vaporize, liquefy and/or melt.

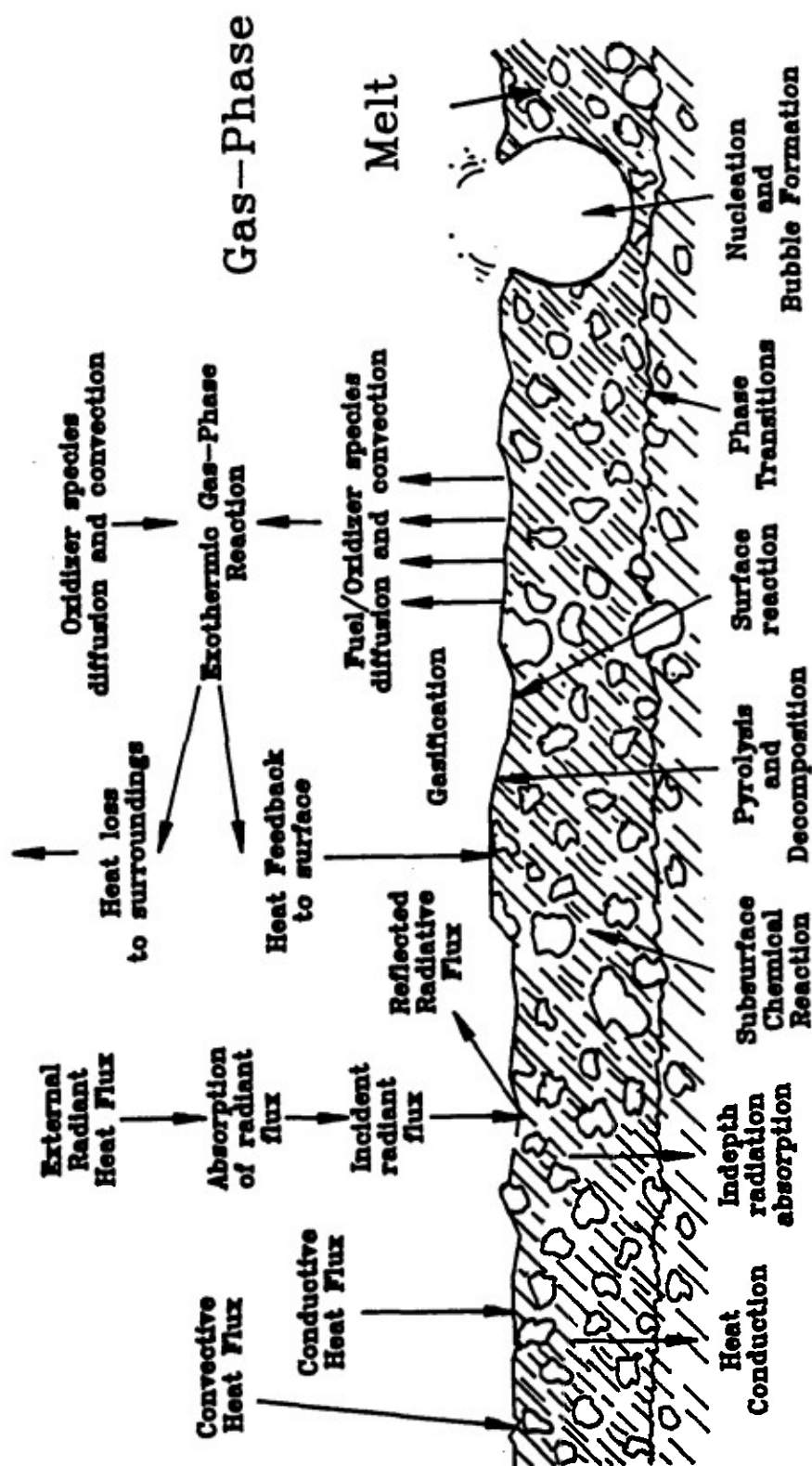
Usually the bulk of the decomposition processes will occur very near the surface of the propellant but surface reactions are possible. With nitramine propellants a thin liquid 'melt' layer is known to form on the surface of the propellant. It is assumed that the liquid layer is of similar composition to that observed under convective heating. As gases evolve from the surface, some of the external radiative energy is absorbed and reflected before it can reach the sample surface. This attenuates the heat flux to the sample surface but could the absorption process could enhance gas-phase reactivity. The gaseous species generated from the propellant mix due to diffusion and natural convective processes with each other and ambient gases. Exothermic chemical reactions in the gas-phase occur resulting in heat feedback to the sample surface. Up to this time the net flow of energy has been from the propellant surface to the surrounding environment. With the increase in exothermic reactivity in the gas-phase, this process is reversed and the propellant has achieved an ignition condition.

2.4.3 Comparative analysis of the Radiative and Convective Processes

There are major physical differences between the convective and radiative processes which must be considered and compensated for appropriately for the results to be properly related. An empirical study is described in Appendix H which would provide a general correlation of ignition delay time (time to first light emission) as a function of several external parameters.

2.5 THEORETICAL APPROACH

Although an empirical analysis, such as that described in Appendix H, would be useful in identifying how selective external parameters affect the ignition delay time of a solid propellant, it would not provide a quantifiable understanding of why these parameters affect the phenomena observed. To supplement this type of empirical analysis, it would be extremely helpful to include a reasonably strong theoretical study of the process.



Composite Solid Propellant

Figure 2.2 Important Chemical and Physical Processes Which Characterize Thermal Ignition

In the discussion below, a one-dimensional theoretical model of the ignition process for XM-39 solid propellant is proposed. This model can be used to study either the radiative or conductive test configurations through proper adjustments to the initial and boundary conditions. Originally, this program had intended to include a comprehensive model of the convective ignition configuration. However, based on the experimentally observed ignition phenomena of the convective process, it became clear that a numerical solution of the complex two-dimensional, recirculating flow with chemical reactivity in both the gas and condensed phases would require a significant amount of computational effort despite the inclusion of several questionable assumptions. This approach is not reasonable because the many assumptions and simplifications would seriously jeopardize the effectiveness of the convective ignition model to provide the necessary comparison to the radiative or conductive ignition results.

As is always the case with mathematical model development, simplifications and adjustments must be made. It must be kept in mind, the purpose of the study is not to generate a predictive model for the conductive and radiative ignition of XM-39 solid propellant, but to present a simplified model which, if validated concurrently by the ignition data of both tests, may provide some indication of commonality between the ignition response of XM-39 solid propellant when subjected to distinctly different thermal input mechanisms. The model shares the same ignition chemistry in the gas and condensed phases, while compensating for the proper physical configurations and mechanisms. In the following sections, the chemical model is presented, the governing mathematical equations are derived and possible solution methods are discussed.

2.5.1 Chemical Model

The ignition model is to be used only as a comparative tool, therefore it is not necessary to consider a complex chemical model. Appropriately applied to this problem is an approach similar to that of Price and Boggs [24]. Their model is ideal for use in the theoretical development for this program for three reasons: (1) it globally accounts for important chemical processes which are believed to be responsible for nitramine ignition, (2) it has been applied previously, with some success, to experimental data for an HMX/PU composite propellant and (3) its relative simplicity regarding the number and type of chemical reactions considered. The major chemical paths are shown in Figure 2.3. The model assumes there are two separate, competing pathways with only five species considered: XM-39, A, B, freestream oxidizer O_2 , and product P.

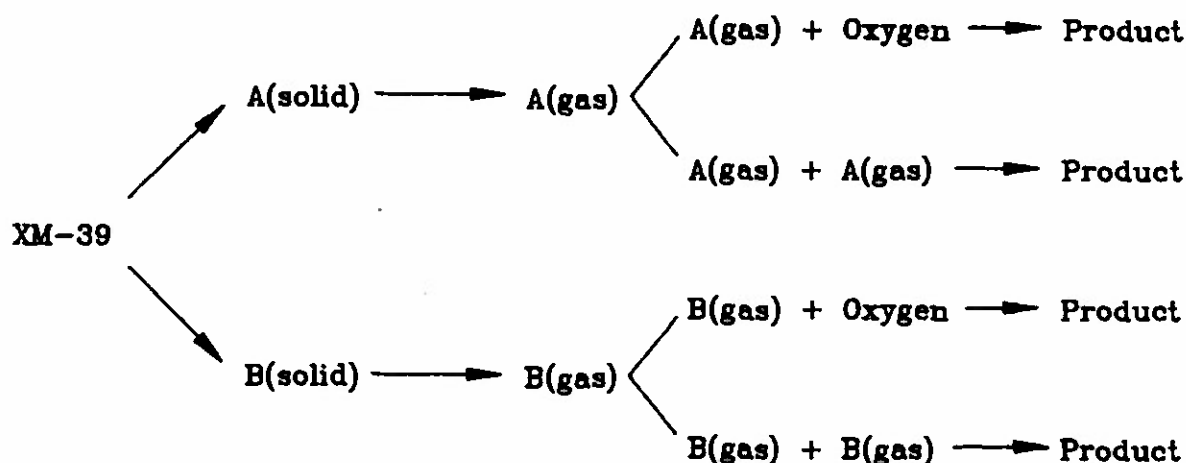


Figure 2.3 Reaction Pathways for the Chemical Model of Ignition

Within the condensed phase, freestream oxidizer is not considered. Path A is an endothermic process; path B is an exothermic process. At the surface of the propellant, both solid A and solid B vaporize to become gaseous A and gaseous B. Within the gas phase, species A can react with itself in a fashion similar to a monopropellant or with the freestream oxidizer. Species B can react in a likewise fashion; however, the two gas-phase species cannot react with each other. This type of model hopefully accounts for the major processes which occur during the ignition of XM-39 LOVA propellant while maintaining the simplicity of a globally lumped chemical reaction.

Because the chemical model is global, pre-determination of reaction rate constants and activation energies is very difficult. To appropriately model the complex ignition chemistry for nitramine-based materials would be a monumental task. The globally lumped model which has been proposed should be sufficient to provide an indication of whether the chemical nature of the ignition process is similar for the different methods of external energy input considered. An error minimization technique will be incorporated to help determine the appropriate values of activation energies and rate constants which can be used. Initial estimates can be obtained from the original model proposed by Price and Boggs.²⁴

2.5.2 Simplifying Assumptions and Discussion

The following is a list of assumptions used to simplify the ignition model:

- (1) solid and gas-phases are one-dimensional.
- (2) neglect composite nature of propellant and treat as homogeneous material.
- (3) gas pressure is constant (momentum equation unnecessary).
- (4) gases obey the perfect gas law.
- (5) indepth absorption of radiative energy is included.
- (6) material and thermal properties of the solid are constant.
- (7) neglect the effects of the liquid layer.
- (8) neglect diffusional and viscous stress terms in the gas-phase energy equation.
- (9) neglect the buoyancy terms in the gas-phase energy and species equations.
- (10) consider the gas-phase as a non-participating medium with respect to the incident energy flux.

The assumption of one dimensionality (1) is based on the geometry of the test situation. The effect of sample edges on the ignition process are ignored. This is a comparative analysis between the conductive and radiative ignition processes, therefore the effect of the composite nature on the variation of ignition between these two methods is not as important as the gas-phase processes (2). No external forces are applied to the ambient gas so the pressure remains relatively constant (3). It is common in the study of combustion to assume the perfect gas law holds (4). Indepth absorption can be considered by including a term based on an exponential factor (5). The opacity of the propellant material is unknown but many researchers consider this to be important to the ignition process. Further simplification is achieved through assumptions (6), (7), (8), (9), and (10) which are common to combustion modeling. If necessary, future considerations of this problem may expand the model to compensate for many of these effects.

2.5.3 Governing Equations

Provided below are the governing equations for the ignition model based on the assumptions listed above. The y-coordinate is normal to the sample surface with $y = 0$ at the gas/solid phase interface.

Solid-Phase Energy:

$$\frac{\partial T}{\partial t} + V_{\text{reg}} \frac{\partial T}{\partial y} = \alpha_s \frac{\partial^2 T}{\partial y^2} + \frac{(S_s)}{\rho_s c_s} \quad (2.5.1)$$

The regression rate of the solid surface is approximated by the following term which assumes the rate is a function of the surface temperature and the amount of reacted material:

$$V_{\text{reg}} = (Y_{A(s)} + Y_{B(s)}) A_s \exp \left[-\frac{E_s}{R_u T} \right]_{y=0} \quad (2.5.2)$$

The energy source term is given by the following expression which includes terms for chemical reactivity and indepth absorption of radiative energy:

$$S_g = \left\{ A_{A(s)} (1 - Y_{A(s)} - Y_{B(s)}) \exp \left[-\frac{E_{A(s)}}{R_u T} \right] \right\} \Delta H_{RA(s)} + \\ \left\{ A_{B(s)} (1 - Y_{A(s)} - Y_{B(s)}) \exp \left[-\frac{E_{B(s)}}{R_u T} \right] \right\} \Delta H_{RB(s)} + \beta \dot{q}_{\text{rad}} (1 - \rho_{\text{ref}}) \exp[\beta y] \quad (2.5.3)$$

Solid-Phase Species:

$$\frac{\partial Y_{A(s)}}{\partial t} + v_{\text{reg}} \frac{\partial Y_{A(s)}}{\partial y} = A_{A(s)} (1 - Y_{A(s)} - Y_{B(s)}) \exp \left[-\frac{E_{A(s)}}{R_u T} \right] \quad (2.5.4)$$

$$\frac{\partial Y_{B(s)}}{\partial t} + v_{\text{reg}} \frac{\partial Y_{B(s)}}{\partial y} = A_{B(s)} (1 - Y_{A(s)} - Y_{B(s)}) \exp \left[-\frac{E_{B(s)}}{R_u T} \right] \quad (2.5.5)$$

Gas-Phase Continuity:

$$\frac{\partial \rho_g}{\partial t} + \frac{\partial (\rho_g v_g)}{\partial y} = 0 \quad (2.5.6)$$

Equation of State for the Gas-Phase:

$$P = \rho_g R_u T \sum_i \frac{Y_i}{MW_i} \quad (2.5.7)$$

Gas-Phase Energy:

$$\rho_g \frac{\partial (c_{p,g} T)}{\partial t} + \rho_g v_g \frac{\partial (c_{p,g} T)}{\partial y} = \frac{\partial}{\partial y} \left(k_g \frac{\partial T}{\partial y} \right) + S_g \quad (2.5.8)$$

The source term for the gas-phase energy equation includes the effects of freestream oxidizer:

$$S_g = \left\{ A_{A(g)} Y_{A(g)}^2 \exp \left[-\frac{E_{A(g)}}{R_u T} \right] \right\} \Delta H_{RA(g)} + \left\{ A_{AO(g)} Y_{A(g)} Y_{O(g)} \exp \left[-\frac{E_{AO(g)}}{R_u T} \right] \right\} \Delta H_{RAO(g)} \\ + \left\{ A_{B(g)} Y_{B(g)}^2 \exp \left[-\frac{E_{B(g)}}{R_u T} \right] \right\} \Delta H_{RB(g)} + \left\{ A_{BO(g)} Y_{B(g)} Y_{O(g)} \exp \left[-\frac{E_{BO(g)}}{R_u T} \right] \right\} \Delta H_{RBO(g)} \quad (2.5.9)$$

Gas-Phase Species Conservation:

$$\rho_g \left(\frac{\partial Y_i}{\partial t} + v_g \frac{\partial Y_i}{\partial y} \right) = \frac{\partial}{\partial y} \left(\rho_g D_i \frac{\partial Y_i}{\partial y} \right) + S_i \quad (2.5.10)$$

where the source terms for the individual species considered are given by:

$$S_{A(g)} = - \left\{ A_{A(g)} Y_{A(g)}^2 \exp \left[-\frac{E_{A(g)}}{R_u T} \right] + A_{AO(g)} Y_{A(g)} Y_{O(g)} \exp \left[-\frac{E_{AO(g)}}{R_u T} \right] \right\} \\ S_{B(g)} = - \left\{ A_{B(g)} Y_{B(g)}^2 \exp \left[-\frac{E_{B(g)}}{R_u T} \right] + A_{BO(g)} Y_{B(g)} Y_{O(g)} \exp \left[-\frac{E_{BO(g)}}{R_u T} \right] \right\}$$

$$SO(g) = - \left(AAO(g) Y_A(g) Y_O(g) \exp \left[- \frac{E_{AO}(g)}{R_u T} \right] + ABO(g) Y_B(g) Y_O(g) \exp \left[- \frac{E_{BO}(g)}{R_u T} \right] \right) \quad (2.5.11)$$

to complete the problem, the species equation for the final product is given by:

$$Y_P = 1 - Y_A(g) - Y_B(g) - Y_O(g) \quad (2.5.12)$$

2.5.4 Initial and Boundary Conditions

The initial and boundary conditions are used to define the type of problem. By varying these conditions the model can be used to solve either a radiative or conductive ignition situation. The initial conditions ($t=0$) for the solid-phase ($y < 0$) are the same regardless of whether the problem is radiative or conductive in nature. These are given by:

$$T = T_i; Y_A(s) = 0; Y_B(s) = 0 \quad (2.5.13)$$

Within the gas phase ($y > 0$), the initial condition, T_0 , depends on the problem. If the problem is radiative, the value of T_0 is equal to T_i . A conductive problem relies on the high temperature of the gas-phase (T_0) to drive the ignition process:

$$T = T_0; Y_j(g) = Y_{j,i}; v_g = 0 \quad (2.5.14)$$

Boundary conditions at $y = -\infty$ assume the propellant material acts as a semi-infinite body over the course of the test period:

$$T = T_i; Y_A(s) = 0; Y_B(s) = 0 \quad (2.5.15)$$

at $y = +\infty$:

$$\frac{\partial T}{\partial x} = 0; \frac{\partial Y_j(g)}{\partial x} = 0; v_g = 0 \quad (2.5.16)$$

At $y = 0$ there is a coupling of the gas and solid phases through the following:

$$\begin{aligned} T_g &= T_s; \rho_g v_g = \rho_s v_{reg}; \\ |\rho_s v_{reg} Y_j|_{y=0-} &= |\rho_g v_g Y_j|_{y=0+} - \rho_g D_j \frac{\partial Y_j}{\partial y} - \dot{w}_j; \\ \left| k_s \frac{\partial T}{\partial y} \right|_{y=0-} - |\rho_s v_{reg} c_s T|_{y=0-} &= - \left| k_g \frac{\partial T}{\partial y} \right|_{y=0+} + |\rho_g v_g c_g T|_{y=0+} + \\ &\quad \rho_g T \sum_j c_{g,j} D_j \frac{\partial Y_j}{\partial y} + \dot{q}_{rad} \end{aligned} \quad (2.5.17)$$

where \dot{q}_{rad} is the laser heat flux input value which for conductive ignition problems should be set equal to zero

2.5 SUMMARY AND CONCLUSIONS

The following conclusions about the convective ignition of XM-39 LOVA propellant can be reached based on the results obtained and discussed above:

1. Convective ignition and flame spreading phenomena of XM-39 solid propellant have been successfully observed using the technique of Birk and Caveny [13,14]. Strong evidence of gas-phase ignition mechanism has

been experimentally observed. Sustained convective ignition occurs in the region near the boundary layer separation point.

2. The presence of freestream oxidizer is very important to the ignition process. In the absence of oxidizer in the test gas, no convective ignition was observed. Ignition was achieved in tests carried out in an air atmosphere.
3. Two possible sites of ignition have been identified: circumferential surface ignition and edge surface ignition. Separate correlations have been developed for these two types of ignition phenomena.
4. From observation, the sample surface can reach ignition due to incident and reflected shock wave heating during the transient start-up time of the test. The heating is very intense but very short in duration. However, if the thermal profile during this period is too thin to achieve self-sustained ignition, subsequent ignition could occur during the nearly steady-state operating time.
5. Microscopic analysis of recovered propellant samples shows the formation of a liquid layer. The composition of this liquid and its importance to the ignition process is still unknown and should be studied further.
6. After ignition the flame propagates from the shoulder region to the rear stagnation point. The sample acts as a flame holder; in the wake region the local flow velocity is reduced and the flame can sustain.

With respect to the radiative ignition of nitramine propellants:

1. Radiative ignition tests have been successfully carried out using a high pressure CO₂ laser ignition facility.
2. Ignition delay times for XM-39 solid propellant has been successfully correlated to the incident heat flux.
3. Little or no pressure dependency was observed for the radiative ignition of XM-39 in the range of pressures between 150 and 550 psig.

Due to the physical differences between the separate testing methods, proper comparison can only be carried out using a theoretical analysis coupled with the experimental program. Separate models for analyzing the convective and radiative ignition tests have been formulated. The chemical models employed by both the convective and radiative analyses are identical. Concurrent solution of these models using the experimental data obtained in this program for validation should provide a strong indication of the possible link between the mechanisms of ignition when the propellant material is subjected to different forms of thermal heating.

REFERENCES of CHAPTER 2

1. Boggs, T.L., Atwood, A.I., Graham, K.J., Lepie, A.H., Price, C.F., Richter, H.P. and Zurn, D.E. (1985), "Hazards of Solid Rocket Propellants," Invited Paper presented at the Fall Technical Meeting of the Eastern Section of the Combustion Institute, Philadelphia, PA, November 4-6.
2. Rocchio, J.J. (1981), "The Low Vulnerability Ammunition (LOVA) Program: A Progress Report," 1981 JANNAF Propulsion Systems Subcommittee Meeting, CPIA Publication 340.
3. Mellor, A.M. (1986), "Energetic Material Hazard Initiation Assessment," JANNAF Propulsion Systems Subcommittee Meeting, CPIA Publication 446, Vol. I, pp. 21-29.
4. Mellor, A.M. and Boggs, T.L. (1987), Technical Editors "Energetic Materials Hazard Initiation: DoD Assessment Team Final Report."
5. Rocchio, J.J. (1986), "The Low Vulnerability Solid Propellant," AIAA Preprint 86-1589.
6. Boggs, T.L. (1984), "The Thermal Behavior of Cyclotrimethylenetrinitramine (RDX) and Cyclotetramethylenetetranitramine (HMX)," AIAA Progress in Astronautics and Aeronautics: Fundamentals of Solid Propellant Combustion, Vol. 90, edited by K.K. Kuo and M. Summerfield, pp. 121-175.
7. Varney, A.M. (1988), "Primers and Igniters," AIAA Progress in Astronautics and Aeronautics: Gun Propulsion Technology, Vol. 109, edited by L. Stiefel, pp. 1-33.
8. Chang, L.M. and Rocchio, J.J. (1988), "Simulator Diagnostics of the Early Phase Ignition Phenomena in a 105-mm Tank Gun Chamber," Technical Report BRL-TR-2890, Ballistic Research Laboratory, Aberdeen Proving Ground, Md.
9. Stiefel, L. and Costello, J.C. (1988), "Ignition of 25mm Insensitive Propellant Charges: Studies of the Early Portion of the Pressure-Time Curve," 25th JANNAF Combustion Meeting, CPIA Publication 498.
10. Rodriguez, L.N. (1988), "Ignition/Temperature Coefficient Study for HELOVA Propellant," Report No. JHTR-1174, Naval Ordnance Station, Indian Head, Md.
11. Messina, N.A. Ingram, L.S. and Tricarico, S.A. (1988), "25mm Ballistic Simulator for XM919 Ignition System/Charge Design Studies," 25th JANNAF Combustion Subcommittee Meeting, CPIA Publication 498.
12. Stiefel, L. and Kuo, K. K. (1988), "Workshop Report: Ignition of Low Sensitivity Gun Propellant Charges," 25th JANNAF Combustion Meeting, CPIA Publication 498.
13. Birk, A. and Caveny, L.H. (1980), "Convective Ignition of Propellant Cylinders in a Developing Cross-Flow Field," MAE Report No. 1486, Department of Mechanical and Aerospace Engineering, Princeton University.
14. Birk, A. and Caveny, L.H. (1980), "Convective Ignition of Propellant Cylinders in a Developing Flowfield," AIAA Journal, Vol. 18, No. 11, pp. 1363-1370.
15. Kashiwagi, T., MacDonald, B.W., Isoda, H. and Summerfield, M. (1970), "Ignition of Solid Polymeric Fuels by Hot Oxidizing Gases," AOSR Scientific Report #70-2935 TR.
16. Kashiwagi, T., MacDonald, B.W., Isoda, H. and Summerfield, M. (1971), "Ignition of a Solid Polymeric Fuel in a Hot Oxidizing Stream," 13th Symposium (International) on Combustion, Combustion Institute, Pittsburgh, Pa., pp. 1073-1086.

17. Kashiwagi, T. and Summerfield, M. (1973), "Ignition and Flame Spreading Over a Solid Fuel: Non-Similar Theory for a Hot Oxidizing Boundary Layer," 14th Symposium (International) on Combustion, Combustion Institute, Pittsburgh, Pa., pp. 1235-1247.
18. Kashiwagi, T., Kotia, G.G. and Summerfield, M. (1975), "Experimental Study of Ignition and Subsequent Flame Spread in a Hot Oxidizing Gas Stream," Combustion and Flame, Vol. 24, No. 3-4, pp. 153-160.
19. Keller, J.A., Baer, A.D. and Ryan, N.W. (1966), "Ignition of Ammonium Perchlorate Composite Propellants by Convective Heating," AIAA Journal, Vol. 4, No. 8, pp.1358-1365.
20. Chen, D.M. (1988), "Pyrolysis, Ignition and Combustion of Solid Fuels for Ramjet Applications," Ph. D. Thesis, The Pennsylvania State University, Department of Materials Science and Engineering.
21. Kim, J.U. (1988), "Laser Ignition of Nitramine Composite Propellants," Ph. D. Thesis, The Pennsylvania State University, Department of Mechanical Engineering.
22. Kuo, K.K., Andiroglu, E. and Kamath, H. (1982), "Development and Design of a Laser Ignition Test Chamber," Final Report to the Ignition Devices Division, Naval Ordnance Station, Indian Head, Md.
23. Li, S.C., Williams, F.A. and Margolis, S.B. (1990), "Effects of Two-Phase Flow in a Model for Nitramine Deflagration," Combustion and Flame, Vol. 80, pp. 329-349.

CHAPTER 3

COMBUSTION AND SEGREGATION OF PROGRAMMED SPLITTING STICK PROPELLANTS

3.1 INTRODUCTION

3.1.1 Motivation and Objectives

For certain gun propulsion systems, stick propellants (SPs) have proven to be superior to conventional randomly packed granular propellants. Indeed, they give increased muzzle velocity due mainly to increased loading density, improved performance reproductibility, increase charge design flexibility and reduced pressure oscillations and overshoots.¹⁻¹⁰ These advantages have motivated a strong development of different types of SPs to enhance their qualities and reduce their defects. One of the qualities sought is progressivity. The simplest stick propellant, a long cylinder without perforations, is regressive because the burning surface decreases during the ballistic cycle. Single- and multi-perforated SPs are almost neutral or slightly progressive. A progressive charge could be employed to reduce the pressure peak in the early phase of the ballistic cycle allowing the achievement of a larger loading density, and hence a higher muzzle velocity, without exceeding certain specified maximum gun pressure. Therefore, progressivity is a very desirable property in SP charges.

To better understand the importance of progressivity, it is necessary to relate the pressure-travel curve of the ballistic cycle to the elastic strength of the gun,¹¹ as shown in Figure 3.1. After the shot start pressure is reached, pressure in the gun is determined by the competition between the gas generation rate due to the propellant burning and the rate at which new volumes is created by the displacement of the projectile. The pressure increases very rapidly at the beginning of the ballistic cycle of a conventional charge because the gas generation rate is relatively high and the velocity of the projectile is still low. Once the peak pressure is reached, the pressure decays very fast because the gas generation rate decreases due to the regressive property of conventional charges, and the projectile velocity increases. The projectile speed at the muzzle is roughly proportional to the area under the pressure-travel curve; therefore, in order to increase this speed, more propellant has to be burned. However, if a heavier charge is used, the pressure will exceed the gun strength. The only way to solve this problem without changing the gun is to maintain a low initial gas generation rate which increases as the ballistic cycle advances. This is the property called progressivity.

Several novel progressive charges have been proposed, such as erosive-augmented burning, pressure-supported perforation-augmented burning, perforation-augmented burning, consolidated propellant charges, monolithic charges, multiple granulations, multi-layered propellants, programmed ignition and Programmed Splitting Sticks (PSS).¹² PSS propellants, the topic of this research, were first proposed by A. W. Horst and F. W. Robbins in 1983;¹³ they later filed a patent in 1986.¹⁴ The objective of this propellant is to provide a theoretically unlimited progressivity using the propellant extrusion technology presently available. The basic idea is to extrude a stick propellant with a shape that will provide a discontinuous increase in the burning surface at a certain time in the ballistic cycle. In order to generate the increased burning surface, Horst and Robbins designed a grain that will split into several smaller parts in a programmed manner, i.e., at any predetermined time in the ballistic cycle. With this remarkable property, PSS could represent a significant advance in ballistic research.

PSS are non-perforated stick propellants with several radial slits along the full length of the grain, resembling a cut pie in cross section (see Figure 3.2). The grain is held together by a thin band around its periphery and the ends are sealed to avoid early ignition of the internal surface. Burning of the grain starts on the outer surface and, when the external band burns through, the grains splits into several wedge-shaped pieces. The splitting of the stick propellants substantially increases the burning surface, producing a highly progressive charge. Theoretically, PSSs can provide any degree of progressivity by changing the band thickness and the number of internal slits. The manufacture of PSSs is assumed to be relatively simple because the material employed is the same used in conventional propellants and the forming process is basically the same as the one presently used: extrusion in long strands. A technique for sealing the ends may represent the major challenge. In theory, PSSs offer many qualities and could be produced with small changes to present technology.

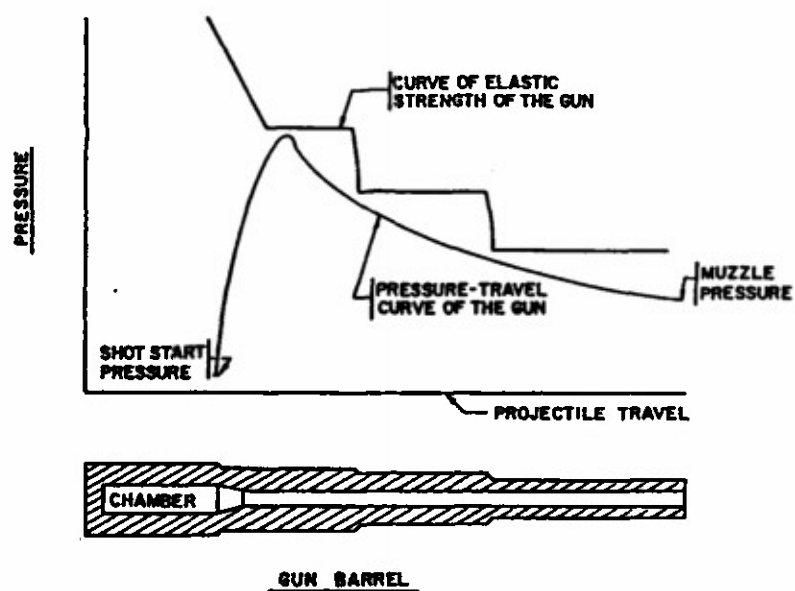


Figure 3.1 Pressure-travel Curve and Elastic Strength of the Gun

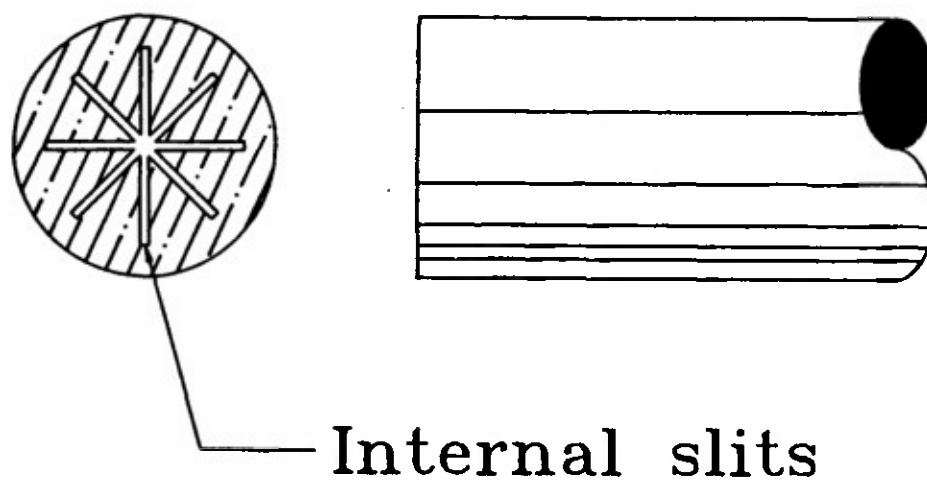


Figure 3.2 Programmed Splitting Stick Propellants

Combustion of PSS propellants, however, is not yet fully understood. Indeed, in the limited research reported, the actual behavior of PSS charges disagrees with what was theoretically expected.^{12,15,16} Nevertheless, PSS propellants do offer better performance than conventional charges; a 10% increase in the muzzle velocity of the projectile has been reported.¹⁶ The mismatch between the expected and actual results indicates that important mechanisms governing PSS propellant combustion have been ignored. In conclusion, it is necessary to know what those mechanisms are and to assess their effect in the propellant performance in order to design practical artillery charges.

The objectives of this research are (1) to study the dynamic splitting mechanisms involved in the combustion of PSS propellants and to develop a reliable end-seal technique; (2) to develop a predictive model for simulating the combustion process of PSS bundles; and (3) to compare the calculated results with experimental data obtained from simulated gun tests.

3.2 METHOD OF APPROACH

3.2.1 Experimental Approach

The experimental research of combustion and splitting of PSS propellants was divided into two parts: the study and visualization of combustion and splitting mechanisms, and the development of a good end sealing technique. A good end sealing technique was required because, according to the research work done previously,^{15,16} the suspected reason for the unexpected performance of PSS propellants has been the early failure of the end seal that causes the unprogrammed splitting of the grains. Consequently, this research focused at first on end-seal methods and experimental procedures to test the seal performance.

The first set of test firings were made in a small fiberglass chamber that permitted the visualization of combustion and splitting processes using real-time X-ray radiography. However, since the section of propellant sample that can be tested in this chamber is too thin, there was not enough contrast and it was not possible to see the splitting process with sufficient resolution. A second set of test firings was conducted in a simulated gun (SG) chamber with the main purpose of testing the performance of different end-seal materials and methods developed in this research. The mechanisms responsible for unprogrammed splitting processes were soon discovered during this second set of tests. The limitations of the SG chamber, however, made necessary an improved test chamber. These limitations are the impossibility to visualize the combustion and splitting processes and the relatively low maximum working pressure, around 140 MPa (20,000 psi), which is less than one half the peak pressure of a gun (over 345 MPa or 50,000 psi).

A test chamber, a high-pressure double-windowed (HPDW) chamber, was designed and built to improve on the limitations of the other two chambers. The HPDW chamber allows for testing of propellant samples of thicker sections.

Four kinds of tests were performed in the SG chamber: interrupted burning, slow venting, closed bomb and simulated gun. Most of the tests conducted in the SG chamber were of the interrupted burning type. In this kind of test, the burning process was interrupted at a pre-determined chamber pressure in order to recover the partially burned grains and study the splitting mechanisms involved. In slow venting tests, the SG chamber was vented through an orifice to partially simulate the increase volume created by the projectile motion in a gun barrel. A closed bomb test constitutes a rather standard and easy test to estimate the instant when the grains split. Finally, simulated gun tests are more difficult to perform, and test preparation has to be extremely careful since a projectile is loaded into the barrel. Tests performed in the HPDW chamber were of the closed bomb type.

Chapter 2 of Appendix I describes in detail the end sealing materials and methods developed, the three test chambers already mentioned and the instrumentation used. Additionally, a description of the data reduction processes employed is included.

3.2.2 Theoretical Approach

The physical model considered in this work divides the interior volume of the combustion chamber and barrel into six basic separate regions: (a) breech side gas region, (b) projectile side gas region, (c) interbundle gas region, (d) two intergranular gas regions, and (e) two solid propellant regions. These six regions are shown in Figure 3.3. The breech side gas region (BGR) consists of the ullage between the charge and the breech. BGR receives the combustion products of the primer and the igniter base pad charge; however, this region does not include condensed phase igniter products. The volume of the BGR increases with time because the igniter burns out and the solid propellant charge is displaced forward towards the projectile side. The projectile side gas region (PGR) includes the ullage between the propellant charge and the projectile. The volume of PGR decreases in the early stages of the ballistic cycle, as the charge moves forward and the projectile remains still, and increases later when the projectile accelerates in the barrel. The interbundle gas region (IBGR) includes the ullage between the two bundles of PSS. The intergranular (IGGR) gas regions include the volume between the grains. Condensed phase combustion products are neglected in this region since they are usually very small. Finally, the solid propellant regions include the propellant grains and assume that all the grains in a bundle move together inside the chamber and barrel.

A lumped parameter model is used for the BGR, IBGRs and PGR. This simplification is quite good at the beginning of the ballistic cycle because the volumes involved are relatively small. Once the projectile moves a sufficient distance along the barrel, the volume of these gas regions will be too large to have an accurate simulation with a lumped parameter model; at this stage, however, the pressure is relatively low and the inaccuracy will be of no great concern. These lumped parameter regions are used as the boundary conditions of the more involved model for the intergranular gas regions.

The intergranular gas regions are modeled by one-dimensional non-viscous equations, including mass, momentum, energy and five species conservation equations. All these equations have a source term due to the interaction with the solid propellant region and to species generation as a consequence of chemical reaction. The boundary conditions are given by the lumped parameter region in each end.

The solid propellant region is also modeled, in general, using one-dimensional equations. The grains are divided into families, corresponding to each propellant bundle, with common characteristics; a single grain of each family is modeled assuming that the rest of the grains behave in exactly the same way. The energy equation for the solid propellant is used only at the beginning of the combustion cycle to calculate the heat transfer toward the grain and the resulting surface temperature, in an attempt to predict ignition and flame spreading. Once the grain surface temperature reaches a threshold in a particular axial location, ignition is assumed and the empirical burning rate law is used. After ignition, the energy equation is no longer necessary and therefore is not solved. An important part of this model corresponds to the calculation of the new burning surface area created by grain splitting.

Detailed governing equations for various region, boundary and initial conditions, and numerical solution method are given in Chapter 3 of Appendix I.

3.3 DISCUSSION OF RESULTS

Detailed results obtained from this study are given in Chapter 4 of Appendix I. A summary of these results is given below. The most important conclusion of this research is that PSS grains can produce augmented burning surface area as expected, when used under the proper conditions. The main variables which affect the performance of PSS charges include the end-sealing technique, length of grains, propellant formulation, and design of the ignition system.

There are two modes for PSS grain fragmentation: normal splitting, the expected mode, and premature or abnormal fracture. Abnormal fracture of PSS grains is responsible for the undesirable performance of this propellant found by previous researchers. For the purpose of this research, normal splitting is defined as the fragmentation of PSS grains due to band breaking or band burning. Fragments generated by normal splitting are shaped as long slivers. On the other hand, abnormal fracture of PSS grains is defined as grain fragmentation due to generalized breaking of the propellant. Abnormal fracture generates small irregular fragments.

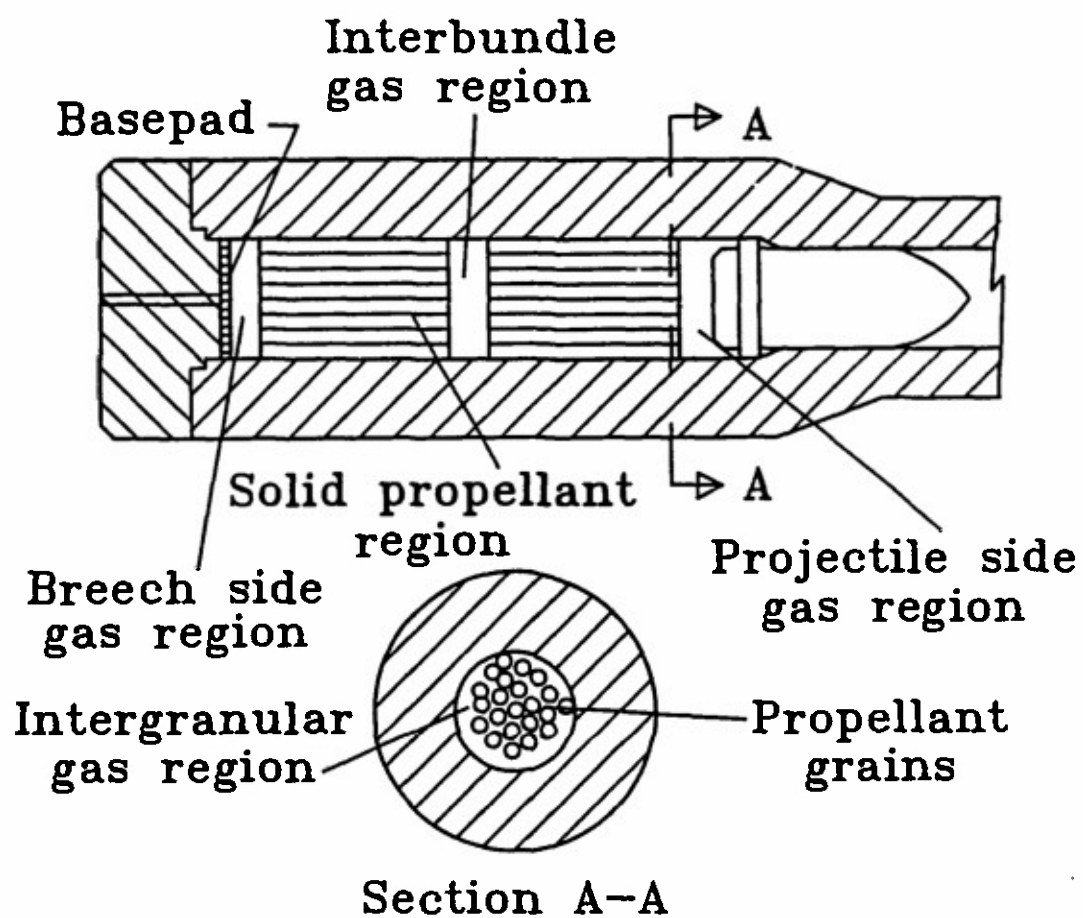


Figure 3.3 Different Regions Considered in the Model

Normal splitting PSS grains, considering the definition given above, may be produced by dynamic forces coupled to a reduced band thickness. Once the band thickness is small enough, the band itself may break due to external forces acting on the grain. However, sometimes the grain does not split after the band is completely burned; the slivers remain together held by the end seals. The actual instant at which splitting occurs depends on the magnitude of the forces and the strength and length of the grains. This fact, which agrees with the concept of effective band thickness,¹⁶ makes it difficult to predict the precise instant when splitting occurs. Additionally, splitting dependence on dynamic forces suggests that PSS grains may not split in a perfectly uniform way in a real gun environment if dynamic forces are not uniform in all the grains.

End-seal failure has been stated as the mechanism producing abnormal fracture of PSS grains by previous researchers. However, there are other mechanisms besides end-seal failure producing premature fragmentation of PSS grains. Examination of propellant recovered from interrupted burning tests indicates that seals made with the appropriate technique survive the high pressure and temperature environment in the combustion chamber. Notwithstanding, PSS grains can be prematurely fractured by dynamic forces generated by rapid combustion of the propellant, pressure waves and high pressurization rates. The mechanisms for abnormal fraction can, therefore, be classified into two groups: seal failure and action of external forces. Seal failure, and the subsequent ignition of the internal surface, over pressurizes the slits producing the premature fragmentation of the grain. External dynamic forces include impact of the grains against solid walls, axial compression produced by large pressure gradients along the chamber, and radial compression due to the difference between external and internal pressures.

A reliable end seal can be obtained, as mentioned before; however, the method developed in this research is too labor-intensive to be used on a large scale. In order to produce practical artillery charges with PSS propellants, a sealing technique adapted to mass production of PSS grains must be developed.

Abnormal fracture of PSS grains can be controlled by a careful design of the charge and the ignition system. Grain length has a strong effect on premature fracture. Shorter grains are stronger and provide a more predictable performance. Propellant mechanical properties can also significantly affect the charge sensitivity to dynamic forces. The ignition system determines the magnitude of dynamic forces in the early stages of the ballistic cycle, having a significant effect on premature fracture of PSS grains.

Flame spreading in the surface of the slits seems to be slower and less uniform than in the external surface of the grains. All the recovered grains with evidence of internal burning show portions of the internal surface without indication of burning. Additionally, in most cases of internal burning, burning surface area curves display little or no increase in the burning surface area, and show waves typical of the ignition transient during the whole event. This particular characteristic of the curves, no increase in the burning surface area and prolonged ignition transient waves, suggests that ignition of the surface of the slits was still progressing when the rupture disk went off. Delayed ignition of the internal surface is produced by the collapse of the internal void of the slits, preventing the easy flow of hot gases after the band burns through. Internal void collapse in the early stage of combustion is evident in the X-ray images obtained.

Results from the theoretical model and numerical code (PROSTICK) developed in this research explain the particular behavior observed in the tests conducted. The long ignition delay at the beginning of the ballistic cycle and the effect of the position of the charge in the chamber with respect to the igniter are justified by the model as a process of heat transfer enhanced by the velocity of the gases. The movement of the stick bundles in the chamber and the collision of the bundles against the projectile base and against each other is also demonstrated by this model.

The code IBHVG2 gives pressure traces quite different from the experimental results due to its inherent incapacity to simulate flame spreading and the ignition transient that, for this research, are important. The importance of flame spreading in this research is due to the low loading density used in the tests. When higher loading densities are used, as in real guns, the ignition transient is much shorter and flame spreading is more uniform; in that case, IBHVG2 seems to provide fairly accurate results.

3.4 SUMMARY AND CONCLUSIONS

1. The dynamic splitting mechanisms and combustion processes of programmed splitting stick propellants have been studied experimentally and theoretically. Results from this study indicate that the PSS grains can produce augmented burning surface area as expected.
2. The mechanisms responsible for abnormal fracture of PSS grains are end-seal failure and action of external dynamic forces.
3. From this work, it was proven that a reliable end seal can be achieved.
4. Abnormal fracture of PSS grains can be controlled by a careful charge design (shorter grain and better mechanical properties) and a proper ignition system (to reduce external dynamic forces).
5. Flame spreading in the surface of the slits is slower and less uniform than in the external surface of the grains. Internal void collapse in the early stage of combustion, which was observed from the recorded X-ray images, causes ignition delay of the internal surface.
6. A theoretical model and numerical code was developed to simulate the burning and splitting processes of PSS charges.
7. Comparison of numerical results and experimental data showed good agreement in terms of time histories of chamber pressure and projectile velocity.
8. Results from this theoretical work can be used to explain behaviors observed in the related experimental tests conducted. The long ignition delay at the beginning of the ballistic cycle and the effect of the charge position in the chamber with respect to the igniter are exhibited by the numerical results. The movement of the stick bundles in the chamber and the collision of the bundles against the projectile base and against each other is also demonstrated by this model.
9. The theoretical model and numerical code can contribute to the understanding of the processes involved in PSS propellant combustion and will help to design practical PSS propellant charges.

3.5 REFERENCES of CHAPTER 3

1. Robbins, F. W. and Horst, A. W., "Slotted Stick Propellant Study," Proceedings of the 20th JANNAF Combustion Meeting, CPIA Publ. 383, Vol. I, Oct. 1983, pp. 377-386.
2. Robbins, F. W. and Horst, A. W., "A Simple Theoretical Analysis and Experimental Investigation of Burning Processes for Stick Propellants," Proceedings of the 18th JANNAF Combustion Meeting, CPIA Publ. 347, Vol. II, 1981, pp. 25-34.
3. Minor, T. C., "Ignition Phenomena in Combustible-Cased Stick Propellant Charges," Proceedings of the 19th JANNAF Combustion Meeting, CPIA Publ. 366, Vol. I, 1982, pp. 555-567.
4. Horst, A. W., "A Comparison of Barrel-Heating Processes for Granular and Stick Propellant Charges," Memorandum Report ARBRL-MR-03193, U.S. Army Ballistic Research Laboratory, Aberdeen Proving Ground, MD, 1983.
5. Chiu, D., Grabovsky, A., and Downs, D., "Closed Vessel Combustion Studies of Stick Propellants," Proceedings of the 20th JANNAF Combustion Meeting, CPIA Publ. 383, Vol. I, 1983, pp. 393-402.
6. Minor, T., "Mitigation of Ignition-Induced, Two-Phase Flow Dynamics in Guns through the Use of Stick Propellants," Technical Report ARBRL-TR-02508, U.S. Army Ballistic Research Laboratory, Aberdeen Proving Ground, MD, 1983.
7. Robbins, F. W., Kudzal, J. A., McWilliams, J. A., and Gough, P. S., "Experimental Determination of Stick Charge Flow Resistance," Proceedings of the 17th JANNAF Combustion Meeting, CPIA Publ. 329, Vol. II, 1980, pp. 97-118.
8. Gough, P. S., "Continuum Modeling of Stick Charge Combustion," Proceedings of the 20th JANNAF Combustion Meeting, CPIA Publ. 383, Vol. I, 1983, pp. 351-363.
9. Gough, P. S., "Modeling of Rigidized Gun Propelling Charges," Contract Report ARBRL-CR-00518, U.S. Army Ballistic Research Laboratory, Aberdeen Proving Ground, MD, 1983.
10. Horst, A. W., Robbins, F. W., and Gough, P. S., "Multi-Dimensional, Multiphase Flow Analysis of Flamespreading in a Stick Propellant Charge," Proceedings of the 20th JANNAF Combustion Meeting, CPIA Publ. 383, Vol. I, 1983, pp. 365-386.
11. Krier, H. and Adams, M. J., "An Introduction to Gun Interior Ballistics and a Simplified Ballistics Code," in Interior Ballistics of Guns (H. Krier and M. Summerfield, eds.), AIAA Progress in Astronautics and Aeronautics, Vol. 66, 1979.
12. Robbins, F. W. and Horst, A. W., "High-Progressivity/Density (HPD) Propelling Charge Concepts; Progress of Programmed Splitting Stick Propellant," Memorandum Report BRL-MR-3547, U.S. Army Ballistic Research Laboratory, Aberdeen Proving Ground, MD, September 1986.
13. Robbins, F. W. and Horst, A. W., "Feasibility Study of Programmed Splitting-Stick Propellant Charge Concept," Third International Gun Propellant Symposium, October 1984, pp. 304-317.
14. Horst, A. W. and Robbins, F. W., "Programmed Splitting Solid Propellant Grain for Improved Ballistic Performance of Guns," U.S. Patent #4,581,998, April, 1986.
15. Robbins, F. W., Minor, T. C., and Horst, A. W., "Continued Studies of Programmed-Splitting Stick Propellant," Memorandum Report BRL-MR-3624, U.S. Army Ballistic Research Laboratory, Aberdeen Proving Ground, MD, 1987.
16. Kuo, K. K. and Robbins, F. W., "Workshop Report: Combustion Characteristics of Stick Propellants," 25th JANNAF Combustion Meeting, NASA Marshall Space Flight Center, Huntsville, AL, October 1988.

Appendix A

UNCLASSIFIED

STUDY OF COMBUSTION BEHAVIOR OF VERY HIGH BURNING RATE PROPELLANTS USING A REAL-TIME X-RAY RADIOGRAPHY SYSTEM

R. M. Salizzoni⁺, W. H. Hsieh⁺⁺, K. K. Kuo⁺⁺⁺
Department of Mechanical Engineering
The Pennsylvania State University
University Park, PA 16803

and

A. A. Juhasz^{*}
U.S. Army Ballistic Research Laboratory
Aberdeen Proving Ground, MD 21005

ABSTRACT

Some of the major parameters affecting the burning rate of a propellant are its formulation, the chamber pressure, the initial temperature of the propellant, and the flow condition in the vicinity of the burning surface. For a very high burning rate (VHBR) solid propellant, it is suspected that the confinement of the grain and the rate of pressurization could also significantly influence the burning rate. The primary objective of the present research is to study the burning mechanism of VHBR propellants by determining the effect of these parameters on the burning rate and the instantaneous burning surface profile. A second objective is to conduct a feasibility study for using real-time X-ray radiography to observe the combustion phenomena of VHBR propellant.

The real-time X-ray radiography system is used to determine the instantaneous burning surface profile of the VHBR grain at framing rates up to 4000 pps (system maximum rate= 12,000 pps). The cylindrical grain [2.86 cm (1.125 in) diameter by 2.54 cm (1.0 in) long] is end burned in a fiberglass or carbon-fiber composite tube [6.4 mm (0.25 in) thick] with transient chamber pressures up to 180 MPa (26,000 psi) and a test duration of approximately 100 ms. Linear burning rates up to 70 cm/s (28 in/s) at 140 MPa (20,000 psi) were observed with no evidence of any "unconventional" burning mechanism, i. e. volumetric burning or grain break-up.

INTRODUCTION

The term very high burning rate (VHBR) propellant refers to a solid propellant which has exhibited apparent burning rates between 1 and 500 m/s (3 and 1600 ft/s). VHBR is so named since conventional propellants burn up to 0.5 m/s (1.5 ft/s) and explosives above 2000 m/s (6500 ft/s). Some researchers like Fifer¹ and Kooker² prefer the term VHLR which stands for very high linear regression rates. In this paper, the terms VHLR and VHBR are synonymous. The burning rates for a VHBR propellant lie in the range between normal deflagration (subsonic combustion) and detonation (supersonic combustion). One of the possible explanations for this seemingly high burning rate is porous burning; the combustion does not occur only at the surface of the propellant (layer-by-layer burning) but actually penetrates the surface and burns inside of the propellant (volumetric burning)³.

The most prominent burning rate catalysts for a VHBR propellant are the salts of boron hydrides (particularly B_2H_6 and B_2H_4). VHBR propellants are composite propellants, and a typical chemical formulation would consist of a fuel, an oxidizer, and a binder. The fuel would be the boron hydride salt, while the oxidizer could be HMX, RDX, AN, TAGN, or KNO_3 (or a combination of these), and the binder could be CTPB, carbowax4000, GAP, NC/DNT/A4, epoxy, or PNC.

An application of a VHBR propellant was discussed by Helmy⁴ where he outlined the design criteria for VHBR solid propulsion system in an in-tube burning rocket. An objective of the in-tube propulsion system is to produce a maximum thrust in a minimal amount of time. Higher rocket velocities within the launcher provide greater range, accuracy, and effectiveness of a weapons system such as an anti-tank missile or anti-aircraft missile. A propellant with a very high burning rate is almost a necessity for such high-performance missile systems.

⁺ Graduate Assistant

⁺⁺ Research Associate

⁺⁺⁺ Distinguished Alumni Professor

^{*} Team Leader for IBD, BRL

This paper is approved for public release; distribution is unlimited.

UNCLASSIFIED

One of the first VHBR propellants marketed was manufactured by Teledyna McCormick Selph under the trademark of HIVEHITE (High Velocity Ignition Propagation Cord). One application of the HIVEHITE propellant was in high energy transfer cords which consisted of a core of HIVEHITE encased by a protective lead jacket and further restrained by successive layers of polycoat and fiberglass braid. With these cords, the ignition of the HIVEHITE could be initiated at one end and propagate through the cord at a nominal rate of 250 m/s (800 ft/s). The cords were completely sealed and contained all of the products of combustion. If a number of these cords were attached to a parachute harness, the parachutist could release his harness instantly in an emergency situation, such as landing in water on a windy day⁵.

Since the first applications of HIVEHITE in the early 1970's, interest in the combustion phenomena of VHBR propellants has increased steadily because of its potential use in interior ballistics as a monolithic or travelling charge. A simple and useful tool for studying combustion characteristics is the conventional closed bomb. From the measured P-t trace, the instantaneous quantity of combustion product gases and the mass of propellant consumed can be deduced. For this type of test, the burning rate determined is often called the apparent burning rate, since the propellant regression rate is not actually being measured through direct observation, and some assumptions, such as constant burning surface area, are often made.

In the early 1980's, a burning rate study for different formulations of VHBR propellants was conducted at the U. S. Army Ballistic Research Laboratory, using the closed bomb as a major diagnostic tool³. One of their objectives was to study the confinement effects of the grain on the propellant burning rate. The samples used in the study consisted of unconfined, bare cylinders, 12.7 mm (0.5 in) diameter by 50.8 mm (2.0 in) long, and cylinders of the same size grain that were encased in steel sleeves 1.57 mm (0.062 in) thick. They found that the apparent burning rates for the confined samples were often considerably higher than the unconfined samples. For one of the formulations tested, the burning rate increased from 2.3 m/s (7.5 ft/s) at 50 MPa (7250 psi) in the unconfined sample, to 247 m/s (810 ft/s) in the confined sample. A second observation worth noting here is that the burning rate data for the unconfined samples were considerably less reproducible when compared to the confined samples.

While deducing the closed bomb pressure-time data is arduous work at best, determining the actual combustion processes and being able to predict them, appears to be a much more formidable task. Kooker and Anderson² postulated a potential combustion mechanism that would account for the "unconventionally" high burning rates exhibited by VHBR propellants. They then developed a theoretical model consisting of numerous partial differential equations which were solved numerically.

The predominant combustion mechanism in Kooker and Anderson's model involves a stress-induced, grain surface break-up that ejects solid propellant fragments into the surrounding flame thereby creating a two-phase reacting flow. Their model also incorporates several different modes of combustion. At the onset of ignition, the VHBR propellant burns as a conventional propellant with a fundamental burning rate which is primarily a function of pressure and initial temperature. As the combustion progresses, pores begin to form in the burning surface allowing pressure in the pores to be higher than that in the flame zone above the surface. The higher pressure gas within the pores induce a stress in the surrounding propellant, while an axial stress caused by the chamber pressure intensifies the shearing effects. At a threshold shear stress, the burning surface begins to fracture and eject pieces of solid propellant into the flame creating a two-phase flow. At this point, the grain surface no longer regresses at the fundamental burning rate but regresses at a faster rate based upon the speed of grain deconsolidation. As the deconsolidation continues, the surface area of the burning propellant in the two-phase flow increases drastically causing rapid chamber pressurization which further increases the fundamental burning rate.

Kooker and Anderson compare the models predicted P-t trace² with data obtained from Juhasz, et al³. The model does predict the rapid pressurization, but the calculated rise was premature by approximately +8 ms when compared to an actual P-t trace obtained from a closed bomb experiment by Juhasz. Even though it seems that Kooker and Anderson's theoretical model can predict the very high burning rates that have been deduced from closed bomb test data, their proposed burning mechanism has not been confirmed with direct observation.

Other theories such as in-depth (porous or volumetric) burning have attempted to explain the apparent high burning rates of VHBR propellant. Questions concerning the effect of boron hydride concentration on the burning rate have been raised. In a workshop report entitled "Boron Hydrides in a Very High Burning Rate (VHBR) Applications"⁶, Juhasz discussed in detail many of the unresolved questions dealing with VHBR propellant and its formulation. He also discussed the recent developments in VHBR research and suggested a plan for future research to answer some of the questions.

METHOD OF APPROACH

MOTIVATION FOR A REAL-TIME X-RAY RADIOGRAPHY SYSTEM

One of the most common tests performed for the study of high-pressure combustion behavior of solid propellants is a closed bomb test. In a conventional closed bomb test, a sample of propellant is burned in a sturdy, metal enclosure with all of the combustion products remaining in the chamber. The pressure-time traces measured from the closed bomb test can be used to deduce the gas generation rate in the chamber. With the instantaneous burning surface area estimated through the use of a form function for the propellant grain geometry, the linear burning rate can be determined as a function of chamber pressure. Since the burning surface areas are not measured directly, there are non-negligible errors involved in the burning rate data reduction process; thus, the term "apparent" burning rate is often adopted.

Some closed bomb tests use a strong, optically transparent material (such as sapphire) for the construction of the combustion chamber. In these tests, the propellant can be observed during the test, but the view is sometimes obstructed by the flame or the buildup of combustion products inside the chamber. If a cylindrical chamber is used, the image may also be distorted due to the refraction of light.

A real-time X-ray radiography system can help eliminate some of the uncertainties associated with conventional high-pressure combustion tests by actually observing the grain's geometry as it is consumed instead of making assumptions about its shape. A schematic of the X-ray system used in this study is shown in Fig. 1. The X-rays are produced in the X-ray head, pass through the test rig and are intercepted by the image intensifier. The image intensifier transforms the X-ray image into a visible light image. The visible light image is then recorded on a high-speed video camera and later analyzed with the image processing equipment.

By burning a propellant grain in a chamber which is fairly transparent to X-rays, many instantaneous, 2-dimensional images of the regressing propellant sample can be generated during a test firing. Figure 2 shows a typical image as it would be viewed on the video monitor. In this figure, the primary components are labelled. Unlike X-ray film radiography, the real-time X-ray radiography system produces an image that portrays thicker and/or denser regions as being darker areas. During an actual test firing, the only noticeable change in the image results from the regression of the propellant; as the propellant burns, the zone occupied by propellant is replaced by relatively low-density gas phase causing the image to become lighter.

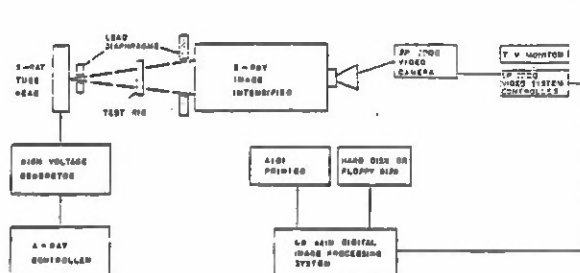


Fig. 1 Layout of the Real-Time X-Ray Radiography System

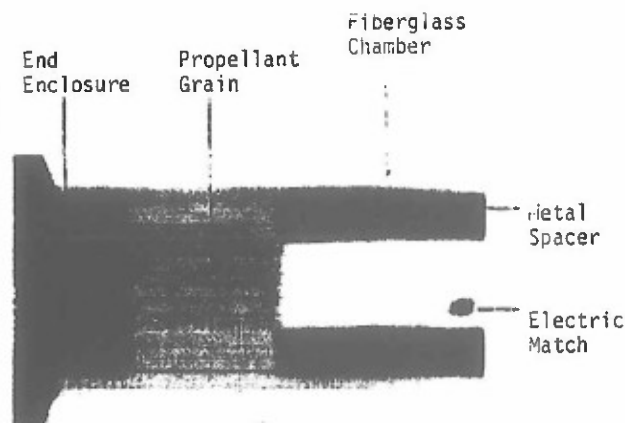


Fig. 2 Typical X-Ray Image Obtained from the X-Ray System

X-RAY SYSTEM COMPONENT DESCRIPTION

X-Ray Generating Equipment. A continuous stream of X-rays are produced by a Phillips MG321 constant-potential X-ray system, which consists of a high-voltage power supply, a controller that regulates the power supply, and an X-ray head which emits the X-rays. There are two X-ray heads that can be used with this system. The first head (MCN167) can emit X-rays up to 160 kV, and the second head (MCN321) up to 320 kV.

Image Intensifier. The image intensifier (Precise Optics, model PI2400 ATF) transforms the X-ray image of the test rig into a visible light image that can be recorded with any common camera. As the X-rays enter the image intensifier, they are partially absorbed by a cesium iodide screen [229 mm (9") diameter]. The cesium iodide, with a decay time constant of 650 ns, emits electrons which are then focused onto an output screen, which in turn, creates an image in visible light.

High-Speed Video Camera. The high-speed video camera (Kodak, Spin Physics SP2000) is an electronic video camera which records its image onto a special magnetic tape. It can record from 60 to 12,000 pictures per second (pps) at a framing rate of 60 to 2000 frames per second. There are five possible framing rates; 60, 200, 500, 1000, or 2000 frames per second. Each of these speeds allow the frame to be divided into 1, 2, 3, or 6 pictures. The SP2000 camera can also record the output of two different camera heads simultaneously, but the system has its own special camera head; therefore, an ordinary camera cannot be used.

Image Processing System. The digital image processing system (Quantex QX9210) has a 2.4 MB dual 8" floppy diskette drive and 50 MB hard disk for the storage of 150 images. This system is used to enhance and analyze the X-ray images recorded by the high-speed video camera.

Thermal Printer. The thermal printer (Advanced Imaging Devices, Inc., model CT1500) produces a high-resolution, black-and-white hard copy of any video image onto thermal paper. These pictures can then be transferred to an ordinary piece of paper or to a transparency.

TEST RIG DESIGN

A test rig has been designed and constructed for the VHBR propellant combustion study. A schematic of the current design is shown in Fig. 3, and a description of some of the major components is given in this section.

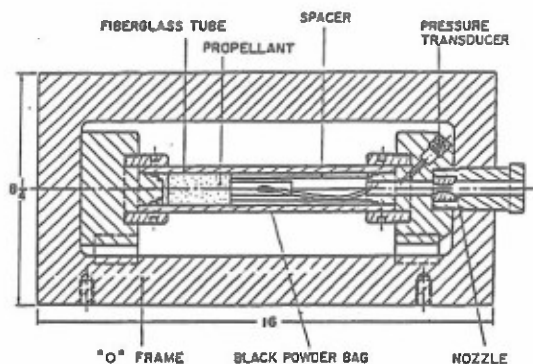


Fig. 3 Schematic of Test Rig for VHBR Propellant Combustion Tests

In a VHBR propellant combustion test, the sample [2.86 cm (1 1/8") diameter by 2.54 cm to 5.08 cm (1" to 2") long] is positioned inside of a fiberglass tube [4.13 cm (1 5/8") O.D., 2.86 cm (1 1/8") I.D., by 22.86 cm (9.0") long] and ignited from one end by an igniter assembly consisting of an Atlas M-100 electric match and a bag of black powder. A fiberglass tube, which is designed to be disposable, acts as a bursting diaphragm for the test. During a test, the chamber pressurizes to a maximum pressure between 100 MPa and 170 MPa (15,000 and 25,000 psi) at which time the tube ruptures and the chamber depressurizes rapidly.

The purpose of the end enclosures is to provide structural support for the fiberglass tube and the pressure seals. The pressure seal consists of a brass ring, an O-ring, and a wedge-shaped, brass back-up ring. Retainers are placed around the outside circumference of the fiberglass tube in the vicinity of the pressure seals to prevent the tube from expanding during the test.

A venting nozzle is sometimes inserted at the downstream end of the chamber to release a portion of the combustion product gases during the test, thereby, controlling the pressurization rate of the chamber. In other tests, a solid plug may be used to replace the venting nozzle for conducting constant-volume combustion tests. A tubular metal spacer with two cut-away windows is often inserted into the fiberglass tube between the downstream end enclosure and the propellant grain to prevent the grain from moving during the test. The chamber pressure is measured with a Kistler piezoelectric pressure transducer (model 607C4) capable of measuring up to 690 MPa (100,000 psi).

PROPELLANT SAMPLE PREPARATION

Three different formulations of VHBR propellants have been tested in this study and are identified by Aerojet (the manufacturer) formulation numbers, namely, 730, 732, and 734 with 0, 2.0, and 4.0 weight percentage boron hydride, respectively. Since these tests involve an end burning grain, a flame inhibitor had to be found that would prevent the hot combustion gases from igniting the base and circumferential areas of the grain. Based upon a suggestion given by K. White of BRL, cellulose acetate was used as the flame inhibitor. Cellulose acetate is a polymer which is a solid. When dissolved in acetone, a liquid mixture is created that can then be applied to the propellant surface; the cellulose acetate becomes solid again after the acetone evaporates.

In the sample preparation, a bare piece of cylindrical propellant with a diameter of 2.69 cm (1 1/16"), is coated with cellulose acetate on its circumference using a small paint brush until an outer diameter of 2.86 cm (1 1/8") is obtained. The final diameter corresponds to the inside diameter of the fiberglass tube. The base of the grain is also inhibited with the same thickness of cellulose acetate. To avoid the formation of large bubbles, the flame inhibitor is not applied in a single coat; instead, it is applied to the propellant surface in as many as 20 coats, alternating with a 15 minute drying period between coats.

GRAIN THICKNESS MEASUREMENT USING X-RAY RADIOGRAPHY

Since in-depth, porous burning is a possible burning mechanism of a VHBR propellant, one of the goals of the current study is to measure the thickness (or density) of the propellant grain during a test firing using the X-ray system. Since X-ray attenuation is a function of density, thickness, and composition of an object, X-ray radiography cannot precisely distinguish between the density and thickness of a grain. For this reason, it is easier to disprove in-depth, porous burning than to verify it. If the X-ray intensity of the condensed phase of the propellant does not change during a test firing, then it can be said that no change in density or thickness occurs. If, however, the X-ray intensity increases during a test firing, the cause could be side burning of the grain and/or a decrease in density. If side burning occurs at the top or the bottom regions of the X-ray image, it can be recognized easily (see Fig. 4a), but if the side burning occurs near the center of the image, it could not be distinguished from in-depth, porous burning (see Fig. 4b). If many tests show an increase in X-ray intensity with no evidence of side burning, it could be inferred with reasonable certainty that in-depth, porous burning was the cause.

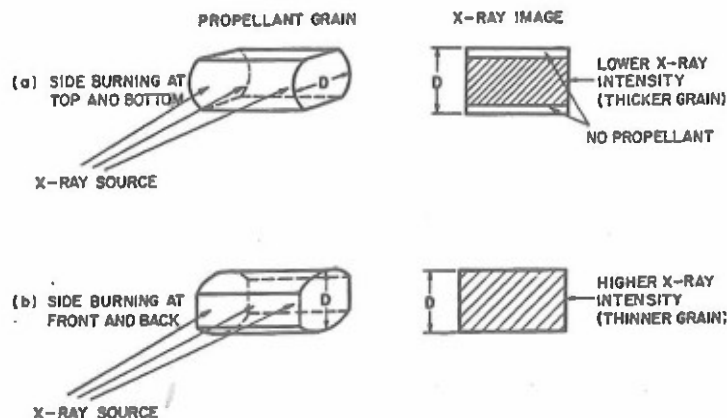


Fig. 4 Illustrative Schematic of Side Burning Phenomena

The general procedure for determining the thickness of a propellant grain using the real-time X-ray radiography system is quite simple, but the details are not so straight-forward. Only the general procedure will be explained here. During a test firing, the propellant grain is surrounded by a fiberglass tube. In order to obtain instantaneous thickness measurements of a test sample during a test firing, calibration images are recorded under the same conditions as the test firing, i. e. the same test rig location, X-ray head location, incoming X-ray intensity, image intensifier location, high-speed camera head position, camera lens aperture, and video recording speed. The only difference between the test firing images and the calibration images is the propellant sample; for the calibration images, the cylindrical propellant sample is replaced by propellant slabs of uniform thickness that are positioned outside of the test chamber in front of the empty fiberglass tube. Ten calibration images are recorded in this way, with the thickness of the propellant slabs ranging from 0 to 2.86 cm (0 to 1 1/8") incremented by 0.32 cm (1/8"). After a test firing, the video image of the sample during the test firing can be compared to the calibration images using the Quantex digital image processing system.

For obtaining propellant thickness distributions, it is necessary to determine the region of the X-ray test firing image where the thickness of the propellant grain is of a specified value with certain tolerance (e.g. 1.27 ± 0.16 cm). The tolerance of ± 0.16 cm is one-half of the uniform slab thickness increment of 0.32 cm which is used in generating the calibration images. Using the Quantex, the test image is compared to the calibration image of the specified thickness (1.27 cm). The image processor then determines which region(s) on the test firing image has the same intensity as the calibration image and highlights those regions on the test image by turning them white. These white regions (isophote regions) correspond to regions with a propellant thickness of the specified thickness (e.g. 1.27 ± 0.16 cm). Two pictures from the Quantex showing the results of this type of analysis are presented in the Results section of this paper.

RESULTS

In this study, the combustion behavior of three formulations of very high burning rate (VHBR) propellants were investigated and observed by using a real-time X-ray radiography system. The propellant formulations are assigned identification numbers: 730 for 0% boron hydride, 732 for 2% boron hydride, and 734 for 4% boron hydride (weight percentage). The results of this study are presented according to the following three major categories:

1. burning mechanisms of VHBR propellants determined qualitatively from the X-ray images.
2. burning mechanisms studied using propellant thickness measurements obtained from the X-ray radiography system.
3. the effect of boron hydride concentration on the combustion characteristics of VHBR propellant and a discussion on the reproducibility of the pressure-time traces.

BURNING MECHANISMS OF VHBR PROPELLANTS DETERMINED QUALITATIVELY FROM THE X-RAY IMAGES

The first formulation of propellant tested was the 732 which was cast into a thin fiberglass casing [0.079 cm (1/32") thick] whose diameter is 0.005 cm (0.002 in) smaller than the inside diameter of the fiberglass combustion chamber. Since the propellant was cast, a strong bond was created between the propellant and its casing. For some tests, the casing remained on the propellant (encased grain), and in other tests the casing was removed and the grain was inhibited with cellulose acetate on all surfaces except the front end (inhibited grain).

Figure 5 shows the results of a test firing of the 732 formulation with the casing being left intact (encased grain). Two hundred instantaneous, X-ray images were recorded during the test, but the four images shown in Fig. 5 are representative of the entire test. In this test, a brass nozzle with a throat diameter of 0.20 cm (0.079 in) was used to release combustion gases from the chamber throughout the test so that the pressurization rate of the chamber and test duration could be controlled. As the pictures indicate, the grain initially burns with a planar burning surface, but transforms into a conical burning surface as the test progresses. Seven tests using the 732 formulation were performed with the encased grain, and all of them showed this type of transformation from planar to conical burning. Two possible explanations for the presence of a conical burning surface are: 1) debonding of the propellant grain from the casing allowing the flame to propagate between the grain and casing and/or 2) heat transfer from the hot product gases through the casing, causing the circumference of the grain to become warmer (preheated) than the center resulting in a higher burning rate at the circumference. In these tests, even though the grain regresses conically, no evidence of any "unconventional" burning mechanisms was observed. Layer-by-layer burning is the predominate burning mechanism with no grain deconsolidation; a more quantitative method for substantiating these statements is discussed in the next section.

The pressure-time trace in Fig. 5 can be divided into three distinct regions. From 0 to 12 ms, the chamber was prepressurized by a bag of FFFg black powder (3.0 gm). From 12 to 82 ms, the pressurization is caused mainly by the burning of the VHBR propellant, and at 82 ms the fiberglass tube ruptured instantaneously causing the rapid depressurization of the chamber. The chamber pressure corresponding to each of the four X-ray images is marked on the P-t trace as A, B, C, and D.

The conical burning surface that is prevalent in the encased grain is much more difficult to analyze using X-ray radiography than a planar burning surface profile. It is preferable to have a planar burning surface profile illustrated by the following reasons:

1. With conical burning, the burning surface area is changing during the test, thus preventing an accurate determination of the burning surface area; with a planar burning surface, an assumption of constant burning surface area is reasonable.

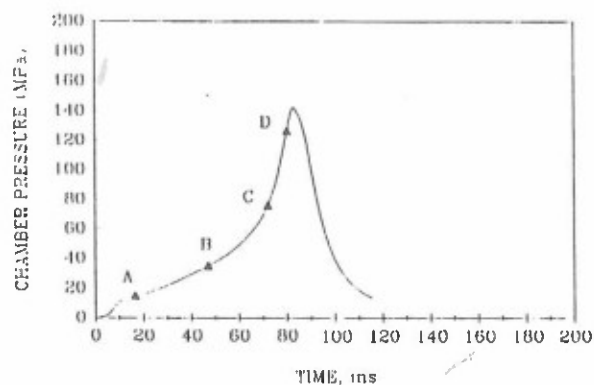
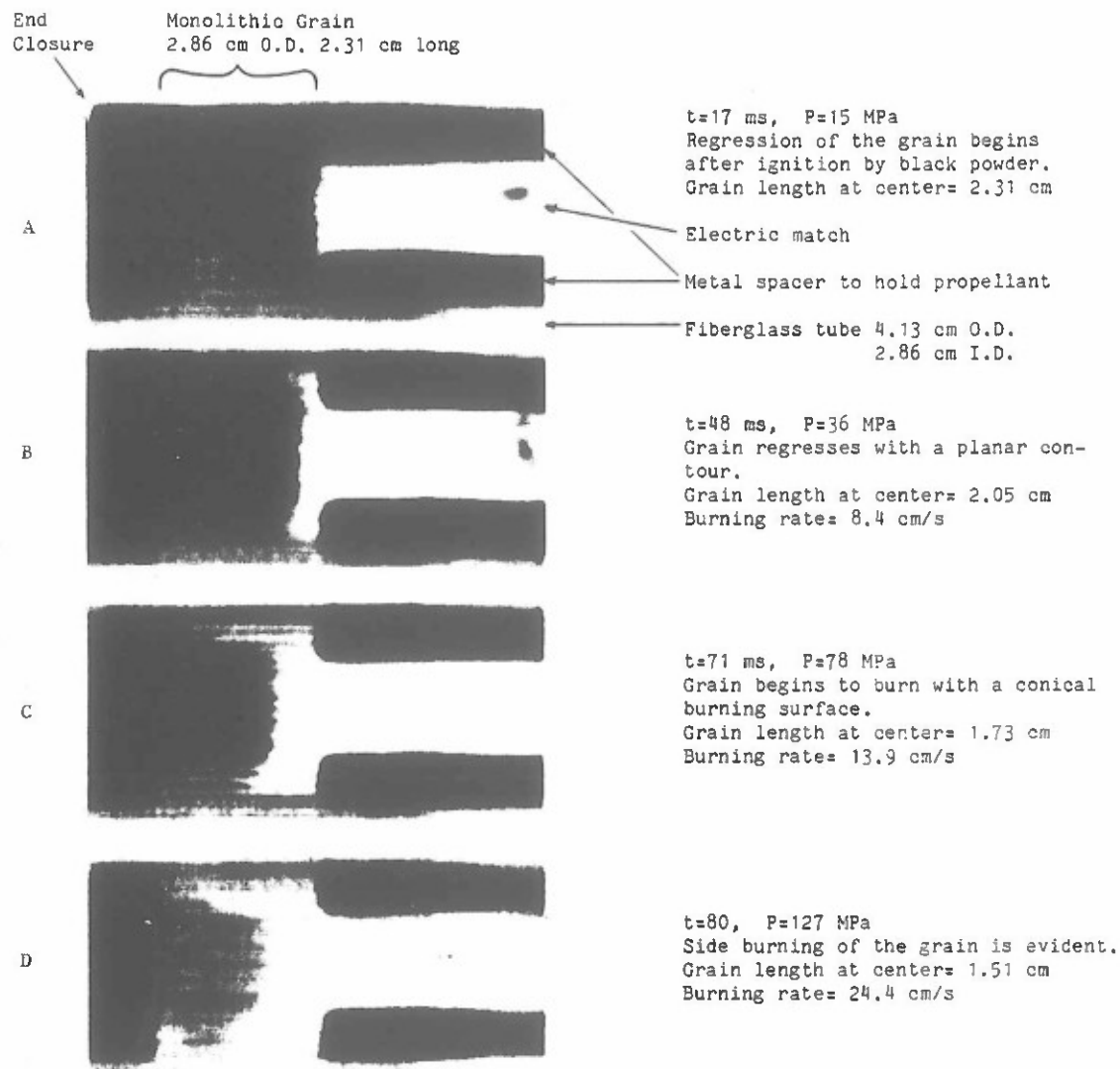


Figure 5 A Typical Set of Test Results for an Encased Propellant Grain

2. With a conical burning contour, it would be very difficult to distinguish from the X-ray image between a change in propellant density and a change in grain thickness. A planar burning surface would allow the separation of the thickness and density effects.
3. It is more difficult to obtain a linear burning rate from the X-ray image if the burning surface is conical.
4. There is a higher probability of reproducibility of test events if the burning surface remains planar.

Because of these complications associated with conical burning, considerable time and effort were devoted to the development of a procedure for the application of an effective flame inhibitor to the VHBR propellant grain surface for achieving a planar burning surface condition. The application of cellulose acetate as described in the Method of Approach section was found to be effective. The first test with the cellulose acetate was very promising, 60% of the grain regressed with a planar contour before the cellulose acetate was penetrated by the hot combustion gases. Eighteen tests were performed with the cellulose acetate flame inhibitor, each with a varying degree of success. However, for the last six tests involving all three propellant formulations, the propellant grain exhibited planar burning throughout the entire test. The results of one of these six tests are shown in Fig. 6.

In this test, formulation 734 was tested in a vented chamber with a brass nozzle which had a throat diameter of 0.19 cm (0.076 in). Comparing the X-ray images shown in Fig. 6 (inhibited grain) with those of Fig. 5 (encased grain), it can be seen that while a conical burning surface is predominant in the encased grain test, a planar burning surface is predominant in the inhibited grain test. Although the burning surface in Fig. 6 is not perfectly planar, the burning surface area is approximately constant throughout the test. The maximum pressure for this test was only 80 MPa (11,600 psi) because the brass nozzle was eroded from a diameter of 0.19 cm (0.076 in) to 0.27 cm (0.106 in); this erosion doubled the throat area and thereby slowed the pressurization of the chamber. Since the pressure was relatively low, the fiberglass tube did not rupture, and the chamber "slowly" depressurized as the combustion products flowed through the exit nozzle. The lead spot shown in images A through D was placed on the input screen of the image intensifier; this facilitates the installation and alignment of the test rig and X-ray radiography system in a highly reproducible manner.

In this test, the cellulose acetate worked quite well, but in some of the previous tests performed with the cellulose acetate, the flame penetrated the inhibitor causing the sides of the grain to burn. The diffusion of one or more propellant ingredients into the cellulose acetate could explain this variability; the longer the time between the application of the flame inhibitor and the test firing, the more flammable the inhibitor becomes. Based upon this observation, it appears that the tests should be performed within 36 hrs of the application of the cellulose acetate. The six most recent tests were performed within 36 hrs of the application of the inhibitor, and none of them showed any signs of the flame penetration into the inhibited layer of the propellant grain.

BURNING MECHANISMS STUDIED USING PROPELLANT THICKNESS MEASUREMENTS OBTAINED FROM THE REAL-TIME X-RAY RADIOGRAPHY SYSTEM

The procedure that is used to determine the thickness of the propellant grain was explained in the Method of Approach section. The objective of the thickness measurements is to determine which region(s) on an X-ray image of a propellant grain correspond to a specified thickness of propellant. To illustrate a typical result, the third X-ray image from Fig. 6 was analyzed, and the results are shown in Fig. 7. The four separated white regions in 7(b) indicate propellant thicknesses of 0.95, 1.59, 2.22, and 2.86 cm (3/8", 5/8", 7/8", and 9/8"). In an ascending order of thickness, the outermost ring represents the propellant thickness of 0.95 cm (3/8"), and the innermost region corresponds to a thickness of 2.86 cm (9/8"). To avoid over crowding the isophote lines, Fig. 7(c) shows three separate constant-thickness regions which are intermediate to those shown in Fig. 7(b). The ring structure of the constant-thickness regions implies no grain deconsolidation.

Under ideal conditions, the constant-thickness regions of a perfect cylindrical propellant grain should be a set of horizontal bands on the side view of the X-ray image. Due to the relatively short distance [approximately 100 cm (39 in)] from the X-ray source (focal point) of the X-ray tube head to the propellant sample and the finite size of the focal point [4 mm by 4 mm (0.16 in by 0.16 in)], there exists a geometric unsharpness effect which blurs an X-ray image. Therefore, the horizontal bands of the same thickness are connected to form ring structures.

Other possible reasons for the connection of the horizontal bands are non-planar burning of the propellant grain and/or porous burning near the regressing surface. The vertical white isophote

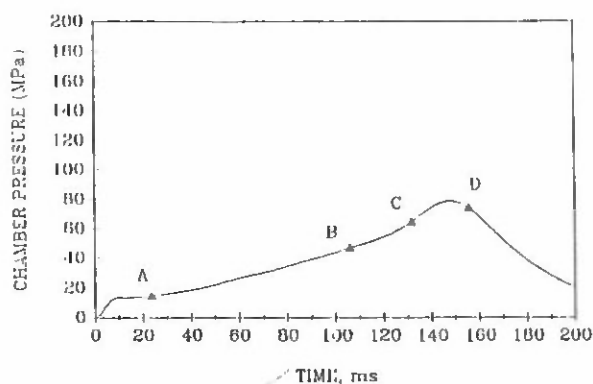
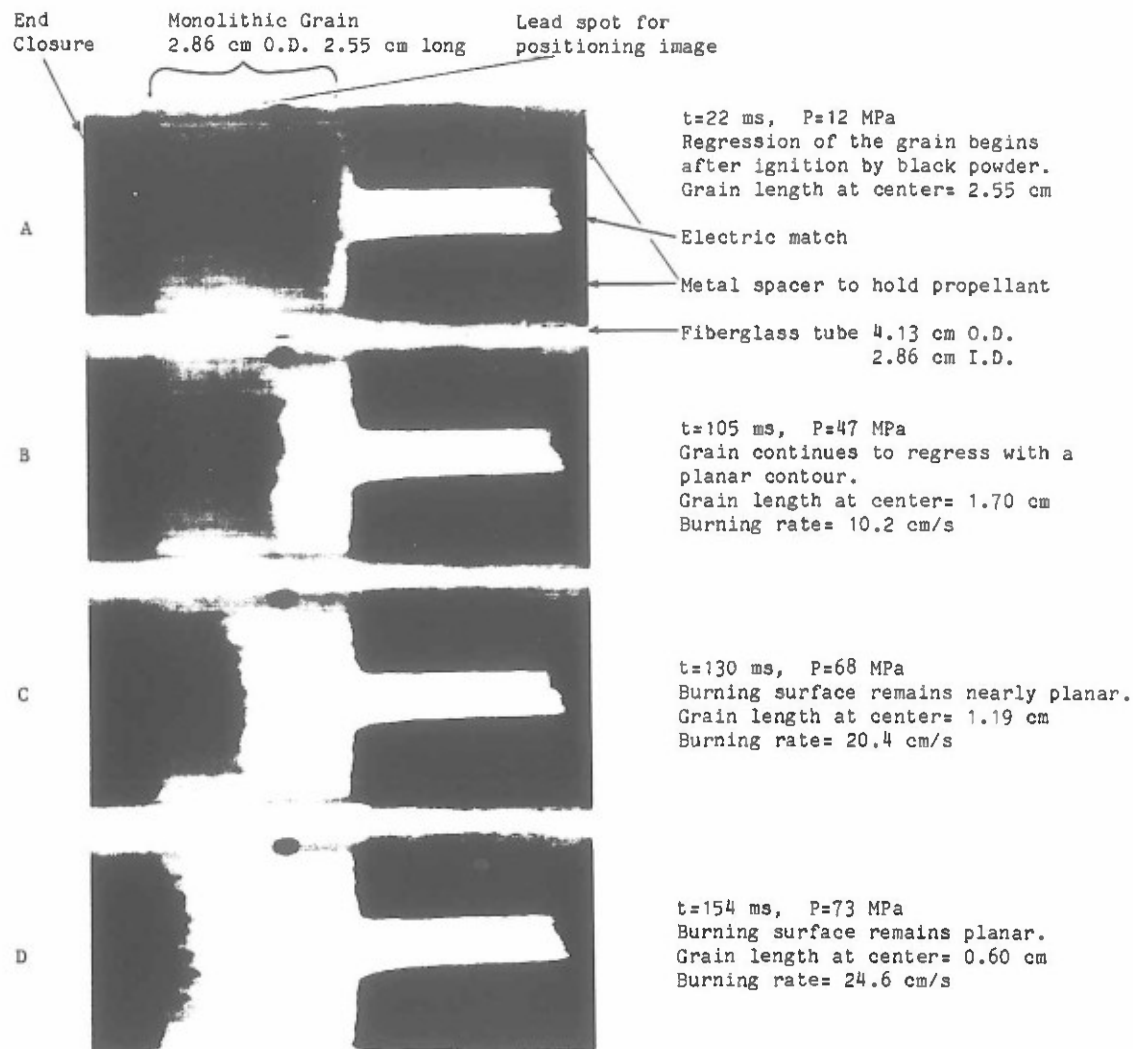


Figure 6 A Typical Set of Test Results for an Inhibited Propellant Grain

lines on the left end of the X-ray image (Fig. 7(b)) near the interface of the end enclosure and the propellant grain are caused mainly by any misalignment of the calibration images with the test image and intentional blurring of the image using the image analyzer.

Since the initial diameter of the grain was 2.86 cm (9/8"), the existence of the white isophote region in the center of Fig. 7(b) reveals that no circumferential or porous burning has occurred in that region any time before the instant the picture was recorded (130 ms after initial pressurization of the chamber). In general, a thicker white ring indicates that the gradient of thickness with respect to a particular direction is small, while a thinner white ring indicates a steeper gradient of thickness. Since portions of the burning surface have both large and small thickness gradients, it can be inferred that some regions on the burning surface developed indentations.

Even though porous burning may be responsible for some of the variations of spacing and band width, it can be estimated from these measurements that it does not penetrate below 3 mm (1/8") into the burning surface. Similar images were produced for the other formulations, and significant in-depth burning was not observed. These propellants burned in a layer-by-layer fashion.

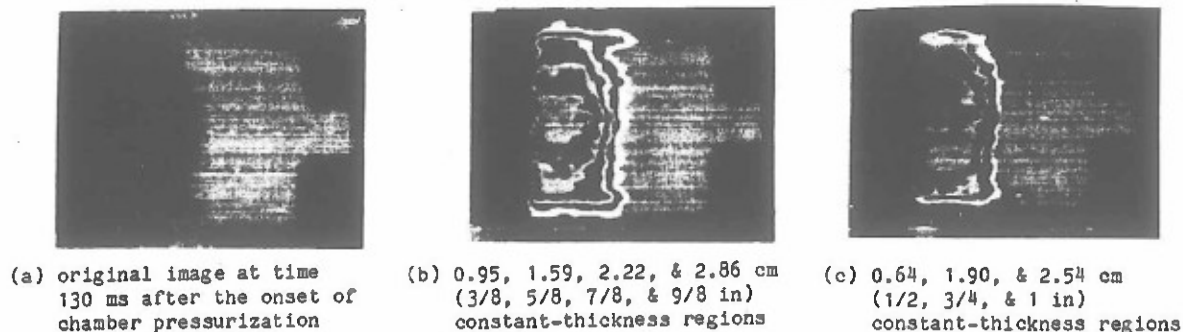


Fig. 7 Determination of Constant-Thickness Regions of a Burning VHBR Propellant Grain Using a Digital Image Processor

THE EFFECT OF BORON HYDRIDE CONCENTRATION ON THE COMBUSTION CHARACTERISTICS OF VHBR PROPPELLANT AND A DISCUSSION ON THE REPRODUCIBILITY OF THE PRESSURE-TIME TRACES

The burning rate and pressure data deduced from a typical test using VHBR propellant formulation 734 are given in Table I. The burning rate data were obtained by selecting 8 images from the test firing (video time corresponding to each image is given in column 1), measuring the length of the unburned grain using the image processor (columns 2 and 3), and then dividing the change in length by the change in time for 2 adjacent data points to obtain the burning rate (columns 4 and 5). The pressure (columns 7 and 8) is the average pressure between data points. More than one set of burning rate data can be obtained for each test firing simply by choosing a different set of images to be analyzed. Burning rate data were deduced for 11 test firings in this manner, and plots of the burning rates versus pressure (log-log plot) are shown in Figs. 8 and 9 for all three formulations tested. While the burning rates for the 732 (2% boron hydride) and the 734 (4% boron hydride) are comparable, the burning rates of the 730 (0% boron hydride) are considerably lower. This implies that the increase of boron hydride from 0 to 2% has a pronounced influence on the burning rate, but the increase from 2 to 4% does not significantly influence the magnitude of the burning rate. However, the addition of boron hydride from 2 to 4% does affect the burning rate exponent. Both the 730 and the 732 formulations reveal a noticeable change in burning rate exponent at 32 and 50 MPa (4600 psi and 7200 psi) respectively, but the 734 formulation has a less obvious change in burning rate exponent.

Table I Burning Rates Deduced from X-ray Images and Measured Chamber Pressure During a Typical Test Firing of 734 VHBR Propellant

TIME ON VIDEO IMAGE (sec)	LENGTH OF GRAIN		BURNING RATES		CHAMBER PRESSURE	
	(cm)	(in)	(cm/s)	(in/s)	(psi)	(MPa)
2.0565	2.55	1.00	0.0	0.0	1044	7.2
2.1000	2.29	0.90	6.0	2.4	3153	21.7
2.1205	2.03	0.80	12.7	5.0	4884	33.7
2.1390	1.70	0.67	17.8	7.0	6196	42.7
2.1515	1.46	0.58	19.2	7.6	7306	50.4
2.1645	1.19	0.47	20.8	8.2	8567	59.1
2.1790	0.86	0.34	22.8	9.0	10368	71.5
2.1885	0.60	0.24	27.4	10.8	11075	76.4

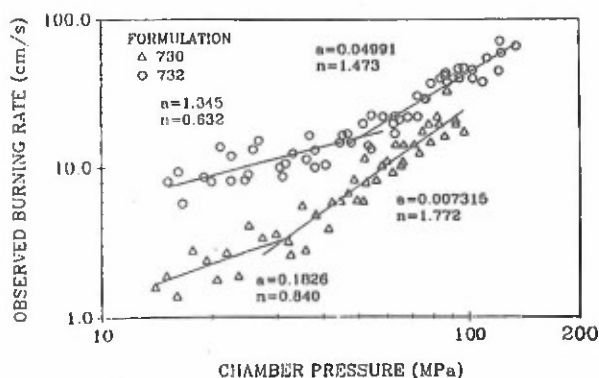


Fig. 8 Burning Rates vs. Pressure for VHBR Propellant Formulations 730 and 732

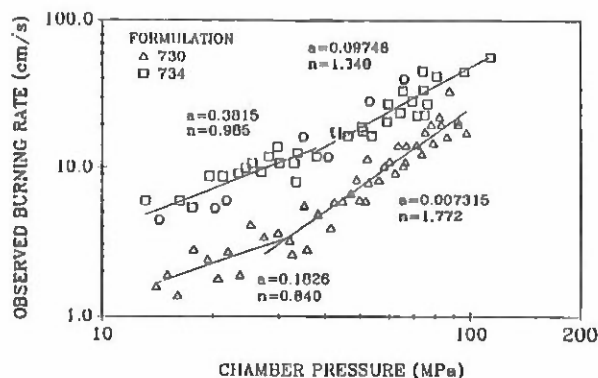


Fig. 9 Burning Rates vs. Pressure for VHBR Propellant Formulations 730 and 734

Since the burning rate of the 730 formulation (with no boron hydride) is lower than the other two formulations (with boron hydride), the rate of pressurization of the combustion chamber is also lower. In the tests involving the 730 formulation conducted with a vented chamber, the chamber depressurized after being pressurized to 13.8 MPa (2000 psi) by the combustion of a bag of black powder (igniter pressure). In similar tests with the 732 and the 734, the chamber pressure always increased after the attainment of the igniter pressure. The X-ray image indicated that the 730 had ignited, but it did not burn fast enough to compensate for the gases that were leaving the chamber through the exit nozzle. The igniter pressure for all of the tests has been approximately 15 MPa (2200 psi), and if the burning rates for each formulation at this pressure are compared (1.8 cm/s, 7.4 cm/s, and 5.5 cm/s for 730, 732, and 734 formulations, respectively) it is possible that the burning rate of the 730 formulation is not high enough to compensate for the combustion gases that are exiting through the venting nozzle. A simple conservation of mass calculation was performed for the vented chamber (assuming ideal gas) revealing that a burning rate of 2.5 cm/s (1.0 in/s) or greater was necessary to pressurize the chamber.

In the tests performed with the 730 formulation under constant-volume conditions (the brass nozzle was replaced by a solid plug), a sample of propellant residue was recovered. The recovered sample was highly porous (greater than 80% void fraction); the texture and color resembled steel wool. After analyzing the X-ray images from the test firings with the image analyzer, it was determined that the propellant grain had continued to burn after the fiberglass tube ruptured. This recovered propellant residue was very similar to the porous residue from the burning of the 730 formulation in ambient air. The 732 formulation was also burned in ambient air, however, no residue was recovered due to the vigorous burning phenomena.

An important characteristic of a gun propellant is its ability to reproduce the pressure-time history under identical test conditions. In order to test the reproducibility of the VHBR propellant, two pairs of constant-volume tests were performed: one pair with the 730 formulation (Fig. 10) and one pair with the 732 formulation (Fig. 11). The cellulose acetate flame inhibitor was used in all four of these tests. While there is some variation in the P-t traces for the 730 formulation, virtually no variation occurred in the 732 formulation. If the bottom curve in Fig. 10 is shifted to the left by 9 ms, very good agreement between the P-t traces is achieved (Fig. 12); a longer ignition delay time in the bottom curve of Fig. 10 could account for this effect. This may appear artificial, but the resulting plot (Fig. 12) shows that dP/dt (an indication of gas generation, and burning rate) is almost the same in both tests for the entire pressure range. Another point worth mentioning is the fact that the rupture pressure of the fiberglass tube is highly dependent upon the length of the test; the fiberglass tubes ruptured at approximately 110 MPa (16,000 psi) for the longer tests (Fig. 10) and approximately 150 MPa (21,700 psi) for the shorter tests (Fig. 11).

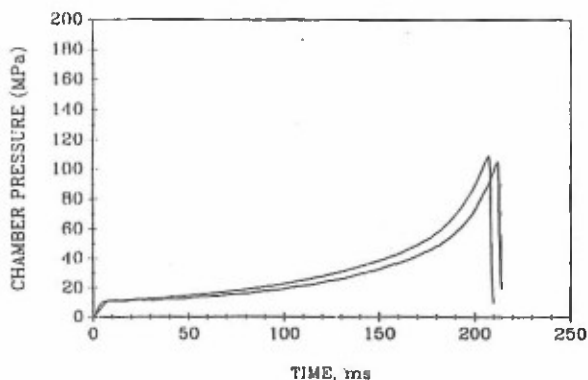


Fig. 10 Comparison of Two P-t Traces for Formulation 730 Under Identical Test Conditions

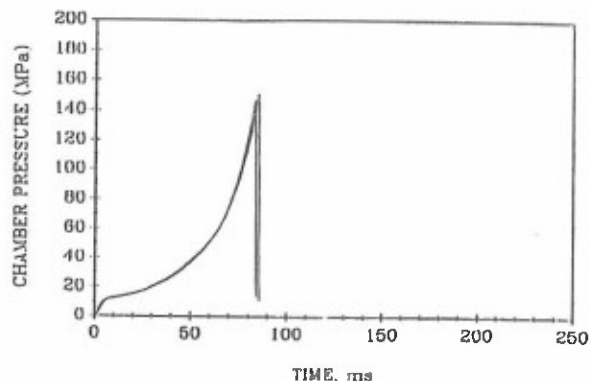


Fig. 11 Comparison of Two P-t Traces for Formulation 732 Under Identical Test Conditions

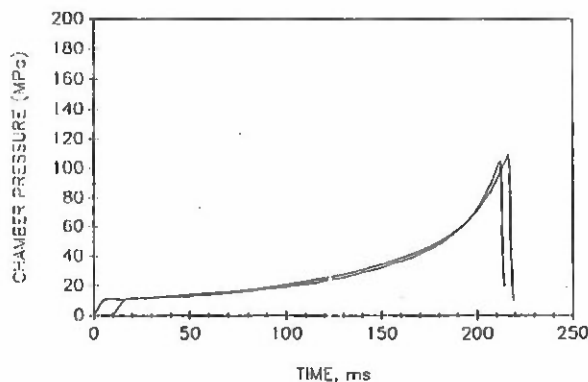


Fig. 12 Comparison of two P-t Traces for Formulation 730 after Adjusting the Initial Time for One Trace by 9 ms

CONCLUSIONS

1. The feasibility of using a real-time X-ray radiography system for observing the combustion phenomena of VHBR propellants has been demonstrated.
2. Three types of VHBR propellant with 0, 2, and 4% (weight percentage) boron hydride burning rate catalyst were tested: the results indicate that an increase of boron hydride concentration from 0 to 2% has a significant effect on the burning rate. However, a further increase in boron hydride from 2 to 4% does not change the magnitude of the burning rate by any significant amount. Slope breaks in log-log plots of burning rate versus pressure were noted for these propellants.
3. The X-ray images showed layer-by-layer burning mechanisms for all three propellant formulations. In this study, grain deconsolidation was not observed under the conditions tested.
4. The instantaneous grain geometry and thickness profiles of VHBR propellant samples were analyzed using isophote analysis of a digital image processor. Results indicate no volumetric burning was present in any of the tests conducted. Additional studies are required to determine whether the surface reaction layer exhibits porous burning or indentations.
5. The measured pressure-time traces and recorded X-ray images for identical, initial test conditions show a high degree of reproducibility. This implies the high potential of utilizing this family of VHBR propellants for gun interior ballistic purposes.

ACKNOWLEDGEMENTS

This work represents a part of the research results obtained under contract No. DAAL-D3-87-K-D064 sponsored by the Army Research Office, Research Triangle Park, NC, under the management of Dr. David M. Mann. The support and encouragement of technical monitors of BRL are also appreciated. The authors would like to thank Aerojet Propulsion Company for providing the propellant samples used in this study. The efforts of Mr. Robert Tompkins and Mr. Charles D. Bullock of BRL for the supply of fiberglass tubes and high-pressure seals are also acknowledged.

REFERENCES

1. R. A. Fifer, "Workshop Report: Combustion of Very High Burning Rate (VHBR) Propellants," 18th JANNAF Combustion Meeting, CPIA publication no. 347, Vol. II, October 1981.
2. D. E. Kocker and R. D. Anderson, "A Combustion Theory for Very High Regression-Rate Solid Propellant," AIAA/SAE/ASME 19th Joint Propulsion Conference, AIAA-83-1196, June 1983.
3. A. A. Juhasz, I. W. May, W. P. Aungst, F. R. Lynn, "Combustion Studies of Very High Burning Rate (VHBR) Propellants," Ballistic Research Laboratory Memorandum Report ARBRL-MR-03152, February 1982.
4. A. M. Helmy, "Criteria Analysis of VHBR Solid Propulsion System for In-Tube Burning Rocket Application," AIAA/SAE/ASME 19th Joint Propulsion Conference, AIAA-83-1111, June 1983.
5. Telydyne McCormick Selph, Technical Bulletin no. 74-7, 1974.
6. A. A. Juhasz, "Workshop Report - Boron Hydrides in Very High Burning Rate (VHBR) Applications," Ballistic Research Laboratory Technical Report BRL-TR-2854, October 1987.
7. editors R. A. Quinn and C. C. Sigl, "Radiography in Modern Industry," Eastman Kodak Company, 1980.

Appendix B

UNCLASSIFIED

SOME HIGH-PRESSURE COMBUSTION CHARACTERISTICS OF VHBR PROPELLANTS*

R. M. Salizzoni, W. H. Hsieh, A. Peretz, K. K. Kuo
 Department of Mechanical Engineering
 The Pennsylvania State University
 University Park, PA 16802

ABSTRACT

Very high burning rate (VHBR) propellants have high potential for achieving high mass generation rates and thrusts in extremely short time periods. Their burning characteristics have been studied under both quasi-steady and dynamic pressurization conditions using a strand burner, a real-time X-ray radiography system with a constant-volume bomb, and an interrupted burning test setup. Burning rates of VHBR propellants were found to depend strongly upon the boron hydride concentration, chamber pressurization rate, and operating conditions. Burning rate slope breaks of certain types of VHBR propellants were observed. Several recovered propellant samples showed very complex burning surface reaction zone structures. Some with a significant amount of dimples and craters below the surface level; others with both dimples and mushroom-shaped protrusions above the surface. The convection burning mechanism must be studied to describe these peculiar combustion phenomena.

INTRODUCTION

Previous work¹ of this study concentrated on using a real-time X-ray radiography system to observe the combustion processes of three very similar formulations of VHBR propellants. These three formulations contained 0, 2, and 4% of the boron hydride, $B_{10}H_{10}$, burning rate catalyst. Using the real-time X-ray system, instantaneous burning rates of the VHBR propellants were measured from a series of X-ray video images of the grain with chamber pressure reaching 172 MPa (25,000 psi) in 80 ms.

To familiarize the reader with the major findings of the previous work, some key results are summarized below.

1. An increase of boron hydride concentration from 0 to 2% has a significant effect on the burning rate. However, a further increase in boron hydride from 2 to 4% does not change the magnitude of the burning rate by any significant amount. Slope breaks in log-log plots of burning rate versus pressure were noted for these VHBR propellants.
2. From the X-ray images, grain deconsolidation was not observed under the conditions tested.
3. The measured pressure-time traces and recorded X-ray images for identical, initial test conditions show a high degree of reproducibility. This implies the high potential of utilizing this family of VHBR propellants for gun interior ballistic purposes.

As part of an ongoing effort to determine burning behaviors of VHBR solid propellants, this paper focuses on three primary objectives: 1) to measure the linear burning rates of VHBR propellants in an optical strand burner with quasi-steady pressures up to 38.4 MPa (5400 psi); 2) to study the burning surface geometry by interrupting the combustion process and recovering propellant samples through rapid depressurization; and 3) to observe the regression of propellant grains using a real-time X-ray radiography system as grains burn in a 50 cc constant volume chamber.

METHOD OF APPROACH

OPTICAL STRAND BURNER

A windowed strand burner with pressure control and nitrogen purge systems was used to obtain quasi-steady burning rates of VHBR propellants. Burning rate data were obtained in the following manner: 1) the propellant was placed vertically into the strand burner; 2) a 41 MPa (6000 psi) nitrogen bottle was used to pressurize the chamber and supplied purge gas to remove the combustion product gases; 3) an exhaust valve was adjusted until the chamber was pressurized to a desired steady-state pressure level; 4) a nichrome wire ignition system was employed to ignite the propellant sample; 5) recorded video images of a burning propellant are superimposed with a ruler; and 6) by determining the instantaneous length of the propellant strand as a function of time, the burning rate of the propellant was deduced.

*This work represents a part of the research results obtained under Contract No. DAAL-D3-87-K-DD64 sponsored by the Army Research Office, Research Triangle Park, NC, under the management of Dr. David M. Mann. The support and encouragement of Dr. Arpad A. Juhasz of DRL is also appreciated. The authors would like to thank Aerojet Propulsion Company and Veritay Technology, Inc. for providing the propellant samples used in this study. In particular, the authors would like to thank Mr. James T. Barnes and Mr. Edward D. Fisher of Veritay.

Approved for Public Release; Distribution is Unlimited.

UNCLASSIFIED

During a strand burner test, a Kistler piezoelectric pressure transducer was used to measure the p-t data, and the signal was digitized and recorded on a Nicolet 4094 digital oscilloscope. Because of the fast burning nature of the VHBR propellants, maintaining a constant pressure in the optical strand burner was impossible without changing the strand burner design. Thus, it was decided to let the chamber pressurize slightly during the test. In this study, the typical rise in pressure ranged from 1.4 to 2.8 MPa (200 to 400 psi). Therefore, the strand burner results reported here can only be regarded as quasi-steady burning rates.

X-RAY RADIOGRAPHY SYSTEM

The purpose of the real-time X-ray radiography system is to generate many instantaneous, 2-D images of a propellant grain as the grain burns in a high-pressure chamber. A schematic diagram of the X-ray system is shown in Fig. 1. The X-rays are produced in the X-ray head, pass through the test rig and are intercepted by the image intensifier. The image intensifier transforms the X-ray image into a visible-light image with a time constant less than 1 microsecond. This visible light image is then recorded with a high-speed video camera, and later analyzed with an image processing system. A detailed description of the X-ray system is given in Refs. 2 and 3.

TEST RIGS FOR X-RAY AND INTERRUPTED BURNING STUDIES

The test rig used in the X-ray system is shown in Fig. 2. The heart of the test rig is the composite tube which is made from either fiberglass or carbon-fiber. These tubes are not only capable of transmitting X-rays effectively, but can withstand pressures up to 172 MPa (25,000 psi). The pressure seals are located on the inside of the tube; for this reason, the inner diameter of the tube has a fixed value of 28.6 mm (1.125 in). However, the length and thickness of the composite tube are not restricted to one value. For instance, by varying the length from 22.9 to 11.4 cm (9" to 4.5"), the free volume ranges from 95 to 20 cc (5.8 in³ to 1.2 in³). In addition, a solid plug was used to block the exhaust port, facilitating a constant-volume test with 50 cc free volume. An electric match and 1.0 gm of Bullseye powder were used to prepressurize the chamber to 20 MPa (3000 psi) and ignite the propellant grain from its exposed end.

For the interrupted burning tests, the composite tube was replaced by a stainless steel tube [11.43 cm (4.5 in) long, with 1.74 cm (0.687 in) thickness]. The free volume for these tests was 23 cc (1.4 in³). To recover samples at three different pressures, the exhaust port [1.27 cm (0.50 in) diameter] was blocked by an aluminum bursting diaphragm with three different thicknesses. These burning diaphragms allowed the chamber to depressurize at nominal pressures of 13.8, 27.6, and 37.9 MPa (2000, 4000, and 5500 psi). An electric match and black powder (0.3 to 1.0 gm) were employed to prepressurize the chamber and to ignite the propellant grain.

PROPELLANT GRAIN PREPARATION

For the strand burner tests, the propellant samples were cut from a 400 gm block of propellant. The nominal length and diameter of the samples were 5 cm (2 in) and 0.6 cm (1/4 in), respectively. A nichrome wire was inserted through the diameter of the sample approximately 2 mm (0.08 in) from the top.

For the X-ray tests, a cylindrical propellant sample with a nominal diameter of 1.2 cm (0.5 in) and length of 2.54 cm (1.0 in) was coated with cellulose acetate on the circumferential area and base of the grain. After drying, this inhibited grain was then glued into a plexiglass holder with epoxy. The only exposed propellant surface was the end surface. To minimize X-ray attenuation, the plexiglass surrounding the sample was only 2.5 mm (0.1 in) thick. It is useful to note that the VHBR samples used in this series of X-ray tests are different from those reported in Ref. 1. This set of propellants was obtained from Veritay Technology Incorporated, and they are designated as TC-47A, TC-49A and TC-51. The formulations are given by Barnes et al.⁴ The TC-47A propellant has no boron hydride and can be regarded the baseline propellant. The TC-49A propellant has a 6% boron hydride replacement of RDX. The TC-51 propellant has a 3% boron hydride replacement of binder in the baseline propellant.

For the interrupted burning tests, the sample was coated with cellulose acetate and glued into a plexiglass holder in the same manner as those for X-ray tests. However, the samples had a different size with a diameter of 1.35 cm (0.53 in) and a length of 1.12 cm (0.44 in). The diameter was chosen to allow the same pressurization rate as the previous transient tests using the X-ray system. This ensured that the burning surface conditions were similar for both the previous X-ray tests and the extinguishment tests. The propellant samples used for the interrupted burning tests were also the same as the zero percent boron hydride propellant (730) tested in Ref. 1.

RESULTS AND DISCUSSION

STRAND BURNER RESULTS

Strand burning rate data for the 0% formulation (Aerojet 730) are plotted as a function of pressure in Fig. 3 along with the observed burning rate data deduced from transient tests utilizing the real-time X-ray radiography system. Each point on the strand burning rate plot is an average of several burning rates at a given pressure, while the X-ray points are individual burning rates. It was found that both sets of data follow the exponential burning rate law, $r_b = ap^n$. Burning rates obtained from the strand burner are consistently higher than those from the X-ray radiography, and while there are several differences between the two testing techniques which may contribute to this change in burning behavior, it is believed that the predominant difference is the rate of pressurization of the combustion chamber. The pressurization rate for transient burning in X-ray tests ranges from 100 to 1,100 MPa/s corresponding to chamber pressures of 14 and 56 MPa, respectively, as opposed to a low rate of 2 MPa/s for strand burner operating conditions. Slope breaks in the burning rate data are noticed for both testing techniques, and the burning rate exponents are quite similar in magnitude. An interesting observation is the fact that the slope breaks occur at the same burning rate, 3.2 cm/sec, while the corresponding pressures differ by a factor of 1.5.

Under certain pressure ranges, the strand burning rates of nitramine propellants could be higher than the dynamic burning rates of the same propellant as reported by Cohen and Strand.⁵ The burning surface structure of the propellant could also play an important role in the burning rate. Considering the evidence of the cratering structure of the propellant burning surface zone, to be discussed later, the surface zone corresponding to a given pressure has a specific thickness, surface area, and void fraction. For a highly transient pressurization, it takes time for the burning surface zone to adjust itself to a new structure. The cratering behavior is more pronounced at higher pressures for the VHBR propellants tested. Therefore, the burning surface zone structure variation could lag significantly behind the pressure changes, resulting in lower transient burning rates than steady-state condition. The theory of convective burning of a VHBR propellant deserves further study, since the cratering behavior is strongly coupled to the gas penetration and pyrolysis phenomena in the porous structure zone. This porous structure could also have a significant difference in surface temperature over the exposed surfaces.

Figure 4 contains three pictures of the 0% boron hydride formulation as it is burned at 3.4, 10.2, and 20.4 MPa with the length scale (in centimeters) shown in Fig. 4c, applicable to all three pictures. In all tests conducted, the luminous flame zone originated very close to the burning surface as the pictures indicate, but the height of the flame changes with pressure. At low pressure (3.4 MPa) the flame is long and faint, and as the pressure is increased the flame becomes shorter and more intense. Figure 4c is somewhat misleading because the actual video image indicates that there is not much of an extended luminous zone (less than 1 mm); most of the luminosity originates very near the burning surface which is slanted toward the camera. As the pressure is increased beyond the slope break point at $p = 20.4$ MPa, the luminous flame zone becomes taller and more intense which infers a change in the burning mechanism at the break point.

Some burning rate data have been obtained for the 4% boron hydride formulation (Aerojet 734), but most strands made from this propellant did not burn in a cigarette fashion; instead they burned very erratically with no particular burning surface geometry. Average burning rates were deduced and are in the order of 10 cm/sec at 10 MPa and 30 cm/sec at 40 MPa. In contrast, the burning rates for 0% boron hydride formulation at the same pressures are 1.5 and 10 cm/sec, respectively. This comparison shows the strong effect of the small percentage of boron hydride on the burning rate. It is interesting to note that at the end of all the tests with the 4% catalyst formulation, some highly porous residue was recovered, but no such residue was recovered for the 0% formulation. The chemical composition of this residue is under investigation.

INTERRUPTED BURNING TESTS

The purpose of these tests was to interrupt the combustion process at specified pressures so that the propellant sample can be recovered to observe the quenched burning surface zone. The burning rate data obtained from this study indicated that a slope break occurred in the exponential burning rate law (see Fig. 3, X-ray radiography data). Also, the strand burning rate data produced a slope break at the same burning rate. Since the strand burner pictures showed a change in flame characteristics at this burning-rate slope break point, one may suspect that the structure of burning surface zone may also change. The slope break in the transient tests occurred at 31.6 MPa (4580 psi) for Aerojet 730 formulation. For this reason, samples were extinguished at pressures above and below this break point.

Five samples of Aerojet 730 propellant were extinguished after rapid depressurization of the combustion chamber. One grain was recovered at 13.8 MPa (2000 psi), one at 27.6 MPa (4000 psi), two at 37.9 MPa (5500 psi), and one at 124 MPa (18,000 psi). A series of photographs were taken of the recovered samples with a telephoto lens and also with a microscope. Figures 5a, 5b, and 5c show respectively the samples recovered at 13.8 MPa (2000 psi), 37.9 MPa (5500 psi), and 124 MPa (18,000 psi).

The sample shown in Fig. 5c has a larger diameter than the rest; it has a diameter of 2.69 cm (1.06 in) and a length of 2.54 cm (1.00 in). It was burned in a 90 cc constant-volume chamber. The other recovered samples have a diameter of 1.35 cm (0.53 in) and a length of 1.12 cm (0.44 in); they were burned in a 23 cc constant-volume chamber. Figure 5c prominently shows a dimpled burning surface. Although Figs. 5a and 5b do not appear to have this type of dimpled surface, in reality they do, but the dimples are not as pronounced. Figure 5c also shows a very large and deep crater with a depth of 1.26 cm. An X-ray image was recorded for this test firing, and it revealed that this crater was formed 1 ms before the chamber depressurized. Figures 5a and 5b also show the existence of certain craters, but the craters are not as large.

The four smaller samples were cut through the diameter to reveal any subsurface burning phenomena. Figures 6a and 6b show the trimmed cross-sectional views of the recovered samples at 27.6 MPa (4000 psi) and 37.9 MPa (5500 psi), respectively. As indicated on these photographs, small craters were formed on the burning surface. These figures also reveal that the combustion seems to be progressing without much subsurface reaction. One could argue that the grain continued to burn slightly after depressurization; however, when this Aerojet 730 formulation burns at ambient pressure, a carbonaceous material is generated. These photographs show no evidence of such material.

X-RAY RADIOGRAPHY TESTS

As previously mentioned, Veritay Technology, Inc., supplied three formulations of Hycar-based VHBR propellants for the real-time X-ray tests. These three formulations are identified as TC-47A, TC-49A, and TC-51. The objective of this experiment was to observe the burning surface contour of the propellant grain as it burns in a 50 cc constant-volume test rig. The loading density for each test was approximately 0.1 gm/cc. Four X-ray tests were performed with the Veritay propellants. A summary of the p-t traces is shown in Fig. 7. Comparison of the p-t traces of Test 1 and Test 2 reveals that TC-49A burns considerably faster than TC-47A. A comparison of the p-t traces from Test 4 and Test 1 shows that the pressurization rate in Test 4 is significantly higher than that in Test 1. As a matter of fact, at 70 MPa (10,150 psi), the pressurization rate in Test 4 is 10 times higher than that in Test 1. This high pressurization rate is caused partially by the breakup of the propellant grain during Test 4. In this test, the real-time X-ray images of the TC-51 propellant sample showed that at 48 MPa (7,000 psi), the propellant grain began to break up into 3 large pieces. Two of these pieces moved downstream and burned very quickly. Neither the video image of Test 1 (with TC-47A) nor Test 2 (with TC-49A) indicated any evidence of grain breakup.

For Test 3 (with TC-51), the chamber was pressurized to 20.7 MPa (3,000 psi) and the propellant ignited; however, the chamber was unintentionally depressurized. Even though this depressurization was not rapid, the propellant extinguished. This recovered sample has an interesting burning surface structure. Figure 8 is a photograph of the recovered propellant sample in its plexiglass holder. The black spots are carbonaceous material protruding 0.5 to 2 mm (0.02 to 0.08 in) above the surface. Figures 9, 10, and 11 are magnified images of these protrusions. Figure 11 shows how the color changes from white at the base to black at the top. Many carbonaceous residues are in a mushroom form. The tall ones are black at the top and the short ones are brown at the top. The reason for darker colored tops is due to protrusion of the residue into the flame zone. Figure 12 reveals a pore at the center of the propellant burning surface. This particular pore has an approximate diameter of 0.12 mm and a depth of 0.20 mm. Many such pores exist on the surface, and they could be generated by: 1) initial porosity of the propellant; 2) self-generating porosity, due to convective burning; or 3) the ejection of RDX particles (0.15 mm diameter) from the surface of the propellant. The precise reason for porosity generation should be studied further. Figure 13 shows a cross-sectional view of the trimmed sample. The surface appears to be rough, even very near the unburned propellant. From all photographs discussed above, one can conclude that the burning surface zone of a VHBR propellant is non-planar and highly complex, with pores into the sample and/or residues protruding above the surface.

CONCLUSIONS

1. The strand burning rates of Aerojet VHBR propellants were consistently higher than the burning rates deduced from the X-ray radiography system for the 0% boron hydride formulation. However, a slope break in burning rate occurs at a burning rate of 3.2 cm/s (1.3 in/s) for both techniques of measurement. The burning rate exponents above and below the break point are quite similar for these two techniques. It is believed that the difference in pressurization rate and finite relaxation time of the burning surface reaction zone are the primary causes of this discrepancy.
2. The luminous flame of the Aerojet 0% boron hydride formulation revealed a change in structure at the slope break point. As the chamber pressure is increased up to the slope-break pressure, the flame becomes shorter, and at the slope-break, very little luminous flame is noticeable; most of the luminosity originates from very near the surface. At pressures above the slope-break point, the flame becomes taller and more intense.

3. Obtaining strand burning rate data for the Aerojet 4% boron hydride formulation was very difficult for three reasons: 1) the samples did not burn in a cigarette fashion; 2) a common video camera (30 fps) is too slow to observe the propellant burning at 30 cm/s; and 3) the flame is very bright, and the burning surface could not be seen easily.
4. Interrupted burning tests of the Aerojet 0% boron hydride formulation revealed that even though dimples were generated in the burning surface, very insignificant amounts of subsurface reaction occurred. This can be verified by the fact that the color of the subsurface zone is the same as the virgin material.
5. Formulation TC-51 of the Veritay propellant broke into three major pieces at approximately 48 MPa (7,000 psi). This resulted in a rapid pressurization of the chamber. Veritay's closed-bomb p-t data indicated a similar pressurization rate. Formulations TC-47A and TC-49A showed no signs of grain breakup.
6. One sample of the TC-51 formulation was recovered at a pressure less than 6.9 MPa (1,000 psi). The burning surface had many mushroom-shaped carbonaceous protrusions above the surface. The burning surface in general was very rough. For samples having a complex burning surface zone with a significant amount of porosity, the convective burning mechanism must be studied to understand their combustion behavior.

REFERENCES

1. Salizzoni, R. M., Hsieh, W. H., Kuo, K. K., and Juhasz, A. A., "Study of Combustion Behavior of Very High Burning Rate Propellants Using a Real-Time X-Ray Radiography System," Proceedings of the 25th JANNAF Combustion Meeting, October 1988, Vol. 2, pp. 303-315.
2. Hsieh, W. H., "Study of Strand and Erosive Burning of NOSOL-363 Stick Propellants," Ph.D. Thesis, The Pennsylvania State University, August 1987.
3. Hsieh, W. H., Char, J. M., Hsieh, K. C., and Kuo, K. K., "Modeling and Measurement of Erosive Burning of Stick Propellants," AIAA Paper No. 06-1451, AIAA/ASME/SAE/ASEE 22nd Joint Propulsion Conference, June 16-18, 1986, Huntsville, AL.
4. Oarnes, J. T., Fisher, E. O., Hollar, W., White, K., and Juhasz, A. A., "Characterization of the Combustion Behavior of Hycar-based VHBR Propellants," Proceedings of the 25th JANNAF Combustion Meeting, October 1988, Vol. 2, pp. 289-302.
5. Cohen, N. S. and Strand, L. D., "Analytical Model of High-Pressure Burning Rates in a Transient Environment," AIAA Journal, August 1980, Vol. 18, No. 8.

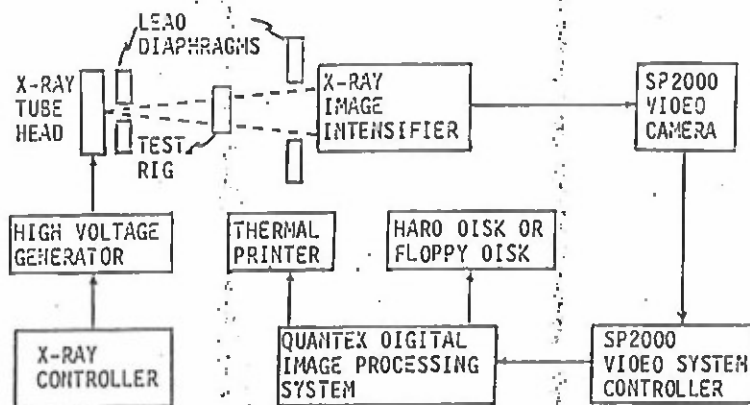


Fig. 1 Layout of the Real-Time X-Ray Radiography System.

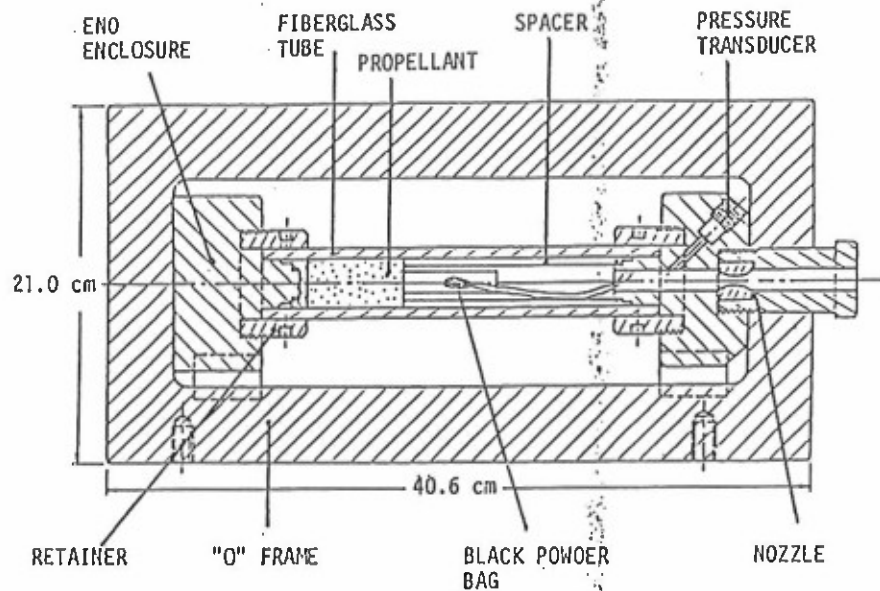


Fig. 2 Test Rig for X-Ray and Interrupted Burning Studies

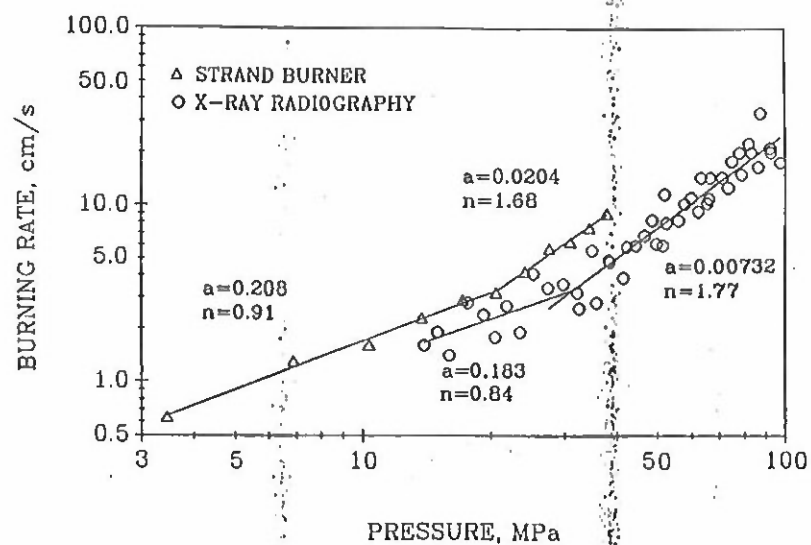


Fig. 3 Comparison of Burning Rate Data for the Strand Burner and X-Ray Test. Aerojet Formulation 730, 0% Boron Hydride.

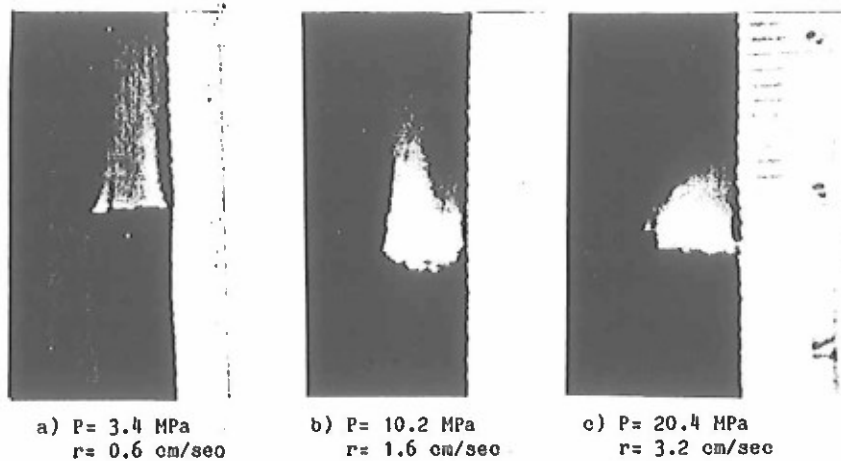
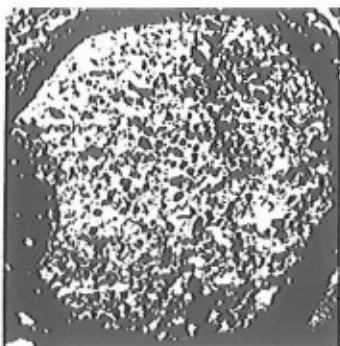
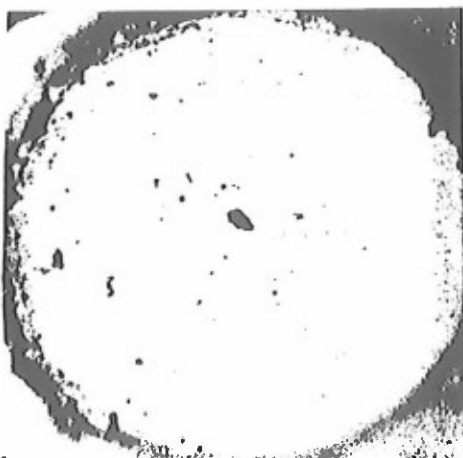


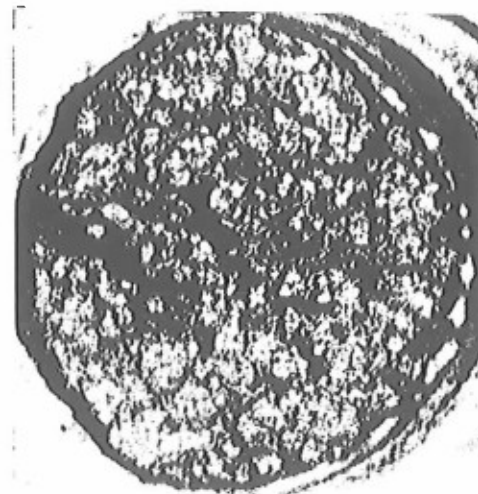
Fig. 4 Flame Structure for Strands of 0% Boron Hydride Propellant at Three Pressures



a) 13.8 MPa

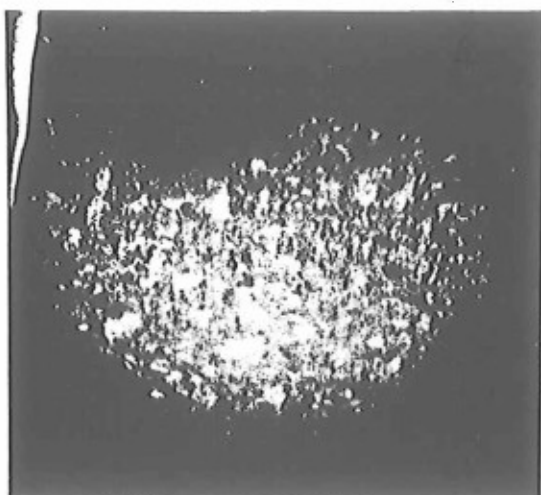


b) 37.9 MPa

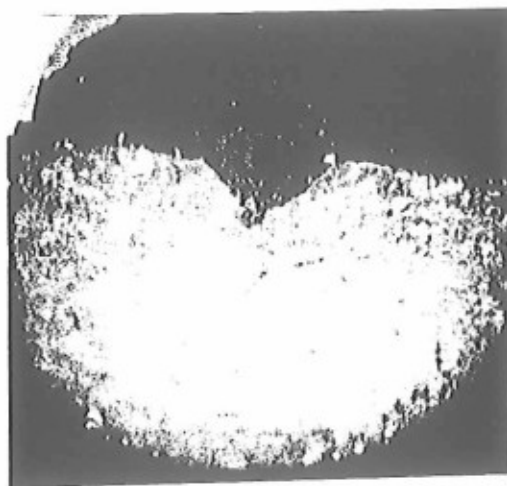


c) 124 MPa

Fig. 5 Recovered Samples of 0% Boron Hydride Propellant. Aerojet Formulation.



a) 27.6 MPa



b) 37.9 MPa

Fig. 6 Cross-Sectional Cut of 0% Boron Hydride Recovered Propellant Showing Craters Formed on the Burning Surface. Aerojet Formulation.

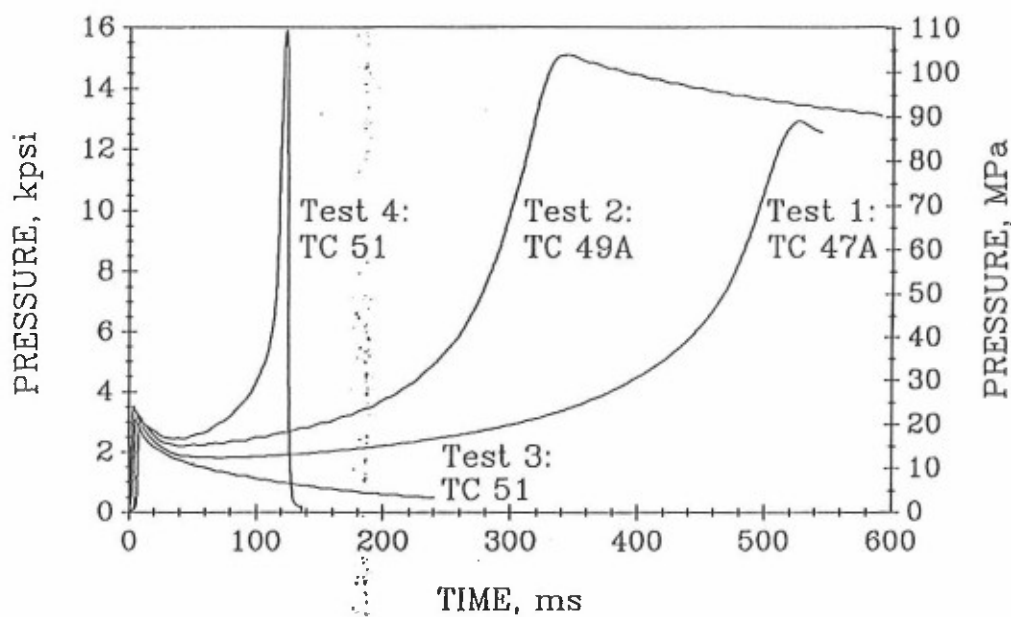


Fig. 7 Summary of P-t Traces for X-Ray Tests of Veritay Samples in a 50 cc Constant-Volume Chamber. Loading Density = 0.1 gm/cc.

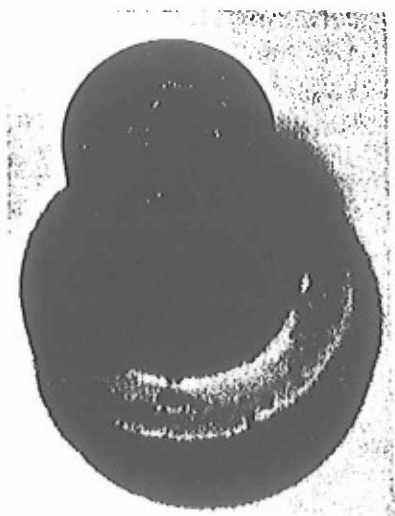


Fig. 8 Veritay TC-51 Recovered Sample in Plexiglass Holder.

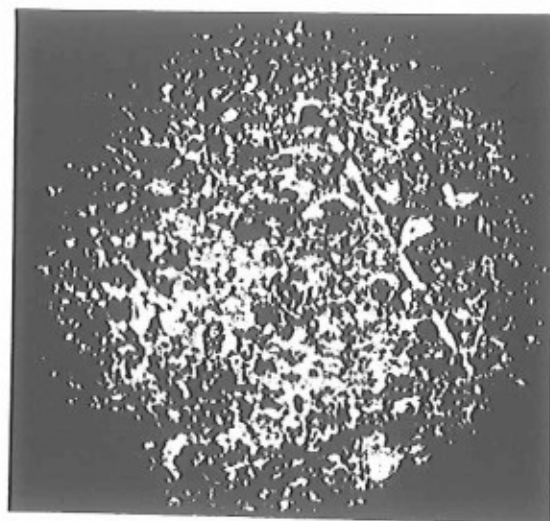


Fig. 9 Microscope Pictures of Carbonaceous Protrusions for Veritay TC-51 Recovered Sample.

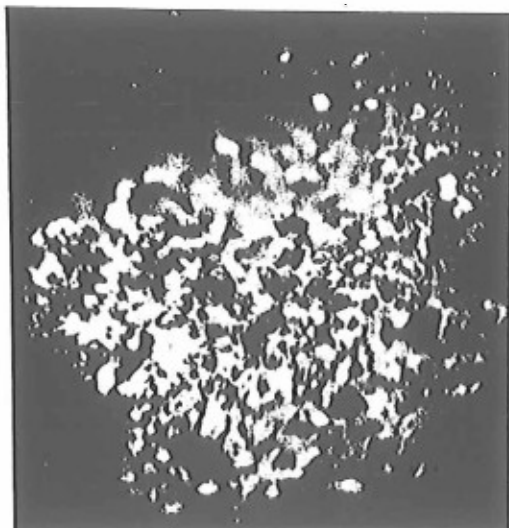


Fig. 10 Microscope Pictures of Carbonaceous Protrusions for Veritay TC-51 Recovered Sample.

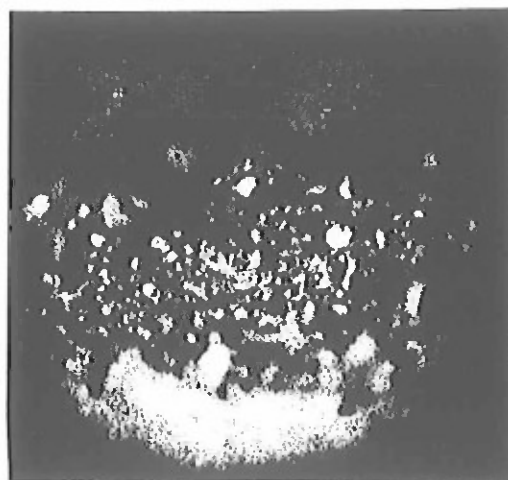


Fig. 11 Microscope Pictures of Carbonaceous Protrusions for Veritay TC-51 Recovered Sample.

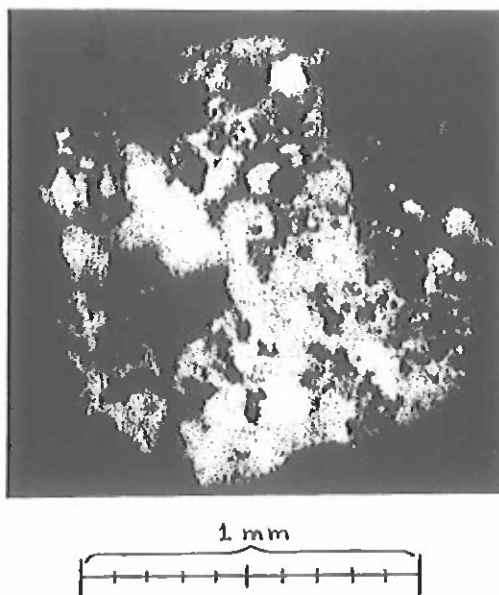


Fig. 12 Microscope Picture of Pore in the Recovered Sample of Veritay TC-51.

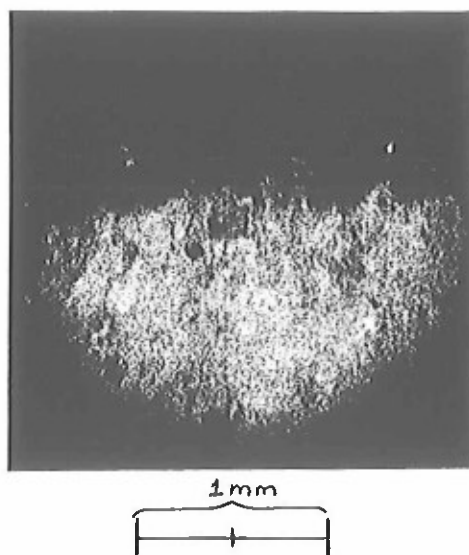


Fig. 13 Microscope Picture of Cross-Sectional Cut of Veritay TC-51 Recovered Sample.

Appendix C

UNCLASSIFIED

REGRESSION BEHAVIOR AND TEMPERATURE SENSITIVITY MEASUREMENTS OF
VERY HIGH BURNING RATE PROPELLANTS

R. M. Salizzoni, W. H. Hsieh, K. K. Kuo
Department of Mechanical Engineering
The Pennsylvania State University
University Park, PA 16803

ABSTRACT

The combustion behaviors of three formulations of very high burning rate (VHBR) propellants are being studied. These formulations contain 0, 2, and 4% boron hydride, $B_{10}H_{10}$, the burning rate catalyst. Two diagnostic tools were used in this study: a real-time X-ray radiography (RTR) system with a high-pressure double-windowed (HPDW) test rig and a pressure and temperature controlled optical strand burner (OSB). The RTR system is used to obtain instantaneous X-ray images of the solid propellant grain as it burns during a transient test at pressure up to 340 MPa (50,000 psi). The optical strand burner maintains a steady pressure up to 41.4 MPa (6,000 psi) and allows the initial temperature of the strand to be set from -40 C to +70 C (-40 F to +158 F).

For a typical RTR test using the HPDW test rig, the instantaneous, internal burning surface of a center-perforated grain was observed. The results show that the grain remained as a consolidated piece even at a high regression rate of 200 cm/s. From these images, instantaneous burning rates were deduced for all three formulations. These burning rates were compared with earlier results obtained by the authors from end-burning grains under similar transient conditions. These two sets of burning rates are in reasonable agreement.

The OSB was used to study the temperature sensitivity (σ_p) of VHBR propellants. Determining propellants' temperature sensitivities as functions of pressure and temperature is important in the study of transient burning phenomena. It was found that σ_p increases as initial temperature (T_i) decreases. As a result of a slope break in the burning rate, σ_p exhibits discontinuities as functions of pressure and T_i .

From a recovered sample which was extinguished at 331 MPa (48,000 psi), the burning surface was found to be non-smooth and covered with a melt layer containing many small indentations.

INTRODUCTION

The combustion behavior of three formulations of very high burning rate (VHBR) propellants was investigated. These formulations contain 0, 2, and 4% boron hydride, $B_{10}H_{10}$, the burning rate catalyst. This paper focuses on two primary objectives.

The first objective was to measure the burning rates of all three formulations using a real-time X-ray radiography (RTR) system. In these tests, a center-perforated grain of propellant was burned in a transient test with pressure levels reaching 330 MPa (48,000 psi). From the X-ray images obtained from these tests the inner radius of the grain was measured, and the burning rate was deduced. Burning rates for these propellants were reported previously^{1,2}, however, the maximum pressure was only 170 MPa (25,000 psi), and the grain was burning from the end instead of a center perforation. A comparison of these burning rates is given in the Results section.

The second objective was to determine the temperature sensitivity of the VHBR propellant. This was accomplished by using a temperature and pressure controlled optical strand burner (OSB). The temperature of the strand burner can be set from -40 C to +70 C (-40 F to +158 F), and the pressure can be maintained at levels up to 41 MPa (6000 psi). The 0% boron hydride formulation was tested at -10, 20, and 70 C and to the maximum pressure.

*This work has been funded by the U. S. Army Research Office under Contract No. DAAL03-87-K-0064. The support and encouragement of Dr. D. Mann of ARD and Mr. A. Horst, Mr. D. Kruczynski, and Dr. A. Juhasz of BRL are greatly appreciated. The authors would also like to thank Mr. L. Torreyson of Aerojet Solid Propulsion Company for supplying the VHBR propellant samples.

Approved for Public Release; Distribution is Unlimited

UNCLASSIFIED

To familiarize the reader with some of the major findings of the previous work, some key results from Refs. 1, 2, and 3 are summarized below.

1. An increase of boron hydride concentration from 0 to 2% has a significant effect on the burning rate. However, a further increase in boron hydride from 2 to 4% does not change the magnitude by any significant amount. Slope breaks in log-log plots of burning rate versus pressure were noted for these VHBR propellants.
2. From the X-ray images, grain deconsolidation was not observed under transient test conditions up to 172 MPa (25,000 psi).
3. The measured pressure-time traces and recorded X-ray images for identical test conditions show a high degree of reproducibility. This implies a high potential of utilizing this family of VHBR propellants for gun interior ballistic purposes.
4. The strand burning rates of the 0% boron hydride formulation were consistently higher than the burning rates obtained from the RTR system.
5. Interrupted burning tests of the 0% formulation revealed that dimples were generated in the burning surface; however, microscope images of the recovered samples indicated that very insignificant amounts of subsurface reaction occurred. This can be verified by the fact that the color of the subsurface zone is the same as the virgin material.

METHOD OF APPROACH

Real-Time X-Ray Radiography Study Using a High-Pressure Double-Windowed Test Rig

The purpose of the real-time X-ray radiography system is to generate many instantaneous images of the propellant grain as it burns in a high-pressure chamber. A schematic diagram of the X-ray system is shown in Fig. 1. The X-rays are produced in the X-ray head, pass through the test rig and are intercepted by the image intensifier. The image intensifier then transforms the X-ray image into a visible-light image with a time constant of less than 1 microsecond. This visible-light image is then recorded with a high-speed video camera and later analyzed with the image processing system. A detailed description of the X-ray system is given in Ref. 4.

Figure 2 shows a diagram of the high-pressure double-windowed (HPDW) test rig used in conjunction with the X-ray system. This chamber was designed for a maximum pressure of 414 MPa (60,000 psi). The free volume of the chamber is 320 cc. Five major components comprise this design: 1) the O-shaped frame, 2) two end closures, 3) a fiberglass tube, 4) a Vascomax steel casing which surrounds the fiberglass tube, and 5) a steel sample holder ring which is attached to the left-hand-side end closure. The rupture diaphragm is often replaced with a venting nozzle (not shown in Fig. 2); the venting nozzle helps to prolong the test event so that a large portion of the grain burns before the end of the test. The test always ends with the rupture of the fiberglass tube which causes a rapid depressurization of the chamber.

The heart of the chamber is the filament-wound fiberglass tube. Because of its relatively low X-ray attenuation and high strength, fiberglass is well suited for this particular application. The tube has an inner diameter of 6.99 cm (2.75 in.) and an outer diameter of 12.06 cm (4.75 in.). It can accommodate a cylindrical grain which has a diameter of 5.08 cm (2.0 in.) and a length of 5.08 cm (2.0 in.).

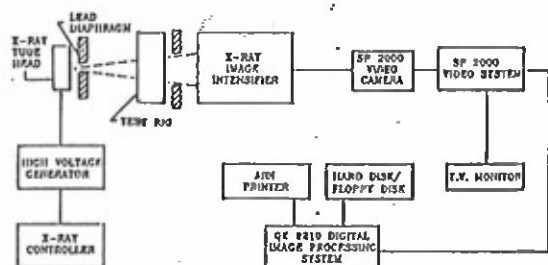


Fig. 1 Layout of the Real-time X-Ray Radiography System

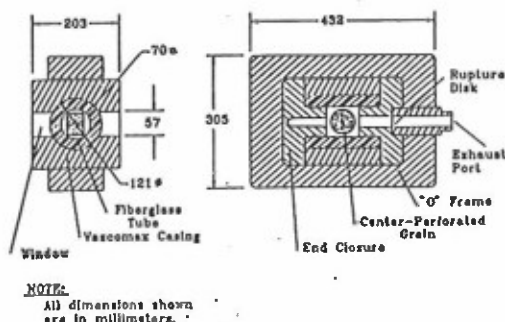


Fig. 2 High-Pressure Double-Windowed Test Rig

The grain is housed in a stainless steel sample holder which holds the axis of the grain parallel to the X-ray. The sample holder covers the entire circumference of the grain and leaves the ends completely open. A center-perforated grain is prepared by coating the outer circumferential and end surfaces with a coating of 1.1 mm (0.045 in.) thick flame inhibitor (cellulose acetate) and then gluing the grain into the holder with epoxy. In a typical test, the grain has a length of 3.38 cm (1.33 in.) and a perforation diameter of 0.63 cm (0.25 in.). It has a mass of 110 gm which creates a loading density of 0.34 gm/cc.

The chamber pressure is measured with two Kistler pressure transducers which are located in each end closure. The video images and the pressure-time traces are correlated by using a synchronization signal; when the ignition switch is activated, the Nicolet digital oscilloscope is triggered and a strobe light fires a single pulse in front of the video camera.

Pressure and Temperature Controlled Optical Strand Burner

The design conditions of the strand burner are as follows: the temperature range is -40 C to +70 C (-40 F to 158 F), and the pressure level range is vacuum to 41.4 MPa (6000 psi). A schematic diagram of the strand burner layout is shown in Fig. 3. In this design, both the strand burner chamber and the purge gas are maintained at the desired temperature. The temperature of the chamber is controlled by a recirculating constant-temperature bath of silicon fluid (Dow Corning 200, 1 or 5 centistoke). The time required for the strand burner to heat up from 20 to 70 C is 3 hours.

The temperature of the purge gas is regulated by a PID (proportional, integral, derivative) controller which can hold the temperature to within 0.3 C (0.5 F) of the set point. The PID controller senses the temperature of the gas leaving the heater and sends a control signal to the heater's power supply. The SCR (silicon control rectifier) power supply restricts the power to the heater by removing a percentage of the 60 Hz cycles in the 110 V line voltage. The resistance heater has a power output of 2000 W. Ideally, one could use this control loop as a flow meter: given the inlet and outlet temperature of the gas and the power to the heater, the mass flow rate could be deduced. Unfortunately, for a short duration tests, the thermal inertia of the system does not allow for an accurate determination of the mass flow rate.

For test temperatures below ambient a heat exchanger was required to cool the purge gas. After careful consideration of the design requirements, it was determined that a cryogenic heat exchanger was the best solution to the problem. It offers the following benefits: 1) boiling liquid nitrogen has a tremendous heat transfer coefficient, 2) high pressure tubing could be used for its construction, 3) it could be made to be relatively compact so that it could sit close to the strand burner, and 4) there are no moving parts to break down. Two hand valves were used to control the temperature of the gas entering the resistance heater. Typically the inlet to the heater is 15 C less than the set point. The heater is then used to accurately control the purge gas temperature.

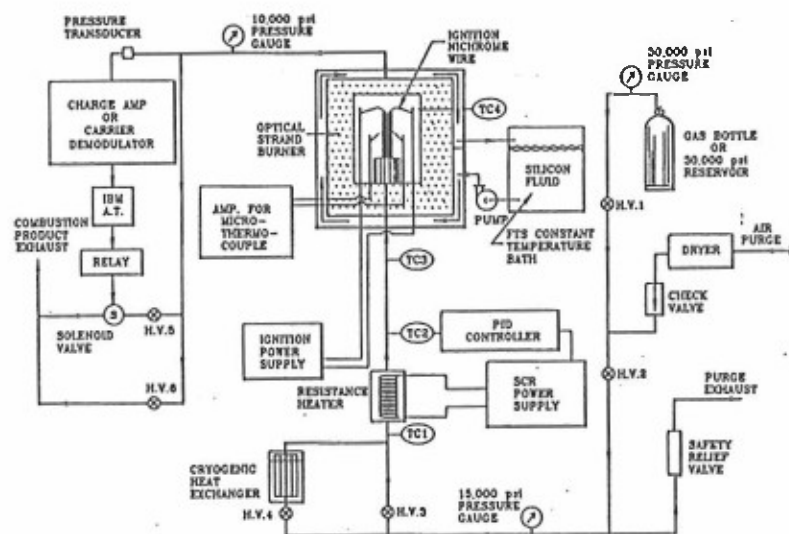


Fig. 3 Layout of the Pressure and Temperature Controlled Optical Strand Burner

After the strand is installed in the strand burner, air is used to purge the chamber. The purpose of this air flow is to enhance the heat transfer to the strand end to keep the temperature of the inlet line at the proper level. The air used in the preconditioning period usually contains a large amount of water vapor. If one wishes to conduct low temperature tests, the air must be dried before it enters the cryogenic heat exchanger; for this reason, a desiccant dryer, which contains 6.8 kg (15 lbs) of desiccant, is installed in the inlet line. This dryer can operate for approximately 30 hrs before the desiccant needs to be dried.

During the test, nitrogen gas is used to pressurize and purge the chamber. The nitrogen gas comes from two, 207 MPa (30,000 psi) reservoirs, which are pressurized by an ultra-high pressure hydraulic compressor. The nitrogen gas is supplied to the inlet of the compressor by a 17.2 MPa (2500 psi) compressed gas cylinder. The water vapor concentration in the cylinders is below 15 ppm; therefore, no condensation problem arises when this gas passes through the cryogenic heat exchanger.

The size of the propellant strand was 6.3 mm (0.25 in.) in diameter by 5.08 cm (2.0 in.) in length. For each test, the external surface of the propellant sample was coated with a very thin layer of flame inhibitor (cellulose acetate); this provided a very effective means for preventing side burning, especially at higher pressures. Some tests were performed without the flame inhibitor at lower pressures to determine if it changed the burning rate. No change in the burning rate was observed.

For temperature sensitivity tests, the propellant strand was allowed to be heated/cooled in the strand burner for at least 20 minutes before the test was conducted. A simple heat transfer calculation with a heat-transfer coefficient of $20 \text{ W/m}^2/\text{K}$ indicated that this would heat/cool the grain to within 0.5 C (0.9 F) of the set point.

A video camera records the images at 30 fps. To facilitate in the reduction of the burning rates, a ruler is superimposed on the propellant image by placing a semitransparent mirror between the strand burner and the camera.

RESULTS

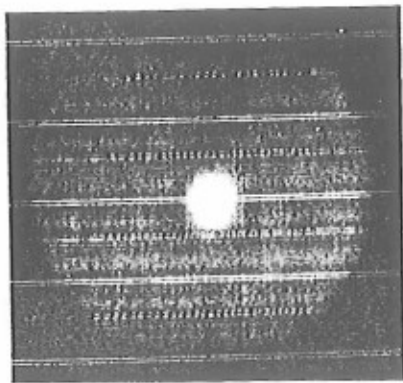
X-Ray Radiography Results

Tests involving all three formulations of VHBR propellant were performed in the high-pressure double-windowed chamber with a maximum pressure reaching 331 MPa (48,000 psi). Each test was conducted under similar conditions, i.e. same igniter pressure, sample geometry and mass. In these tests, both a venting nozzle and a rupture diaphragm were installed at the exit of the chamber. The rupture diaphragm was located downstream of the nozzle and burst at approximately 28 MPa (4000 psi); without the diaphragm the chamber may have depressurized before the ignition of the VHBR propellant. The video images were recorded at 500 fps with the high-speed video camera (Spin Physics 2000).

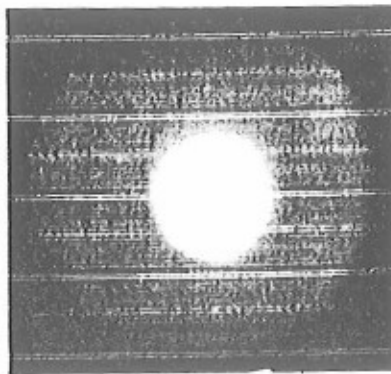
Figure 4 shows some of the results of a test involving the 0% boron hydride formulation. Over two hundred video images were obtained during this test which lasted over 400 ms. The four images in Fig. 4 clearly show the outward progression of the inner radius of the grain as the relatively high density propellant is replaced by low density gases. The pressure-time trace emphasizes how the progressive nature of a center-perforated grain can create a tremendous increase in pressure after a long interval of relatively slow pressure rise. A small decrease in pressurization rate is noticed at 335 ms; this is caused by the bursting of the rupture diaphragm at 26 MPa (3800 psi). In this test, a 1.59 mm (1/16 in.) venting nozzle was installed. Due to the strong nozzle restriction of the product gases leaving the HPDW test chamber, the drop in pressurization rate at 335 ms is almost unnoticeable.

The results depicted in Fig. 4 are typical of all the tests conducted in the HPDW chamber; that is they all have the same general characteristics. The characteristics of the video images of all tests can be summarized as follows.

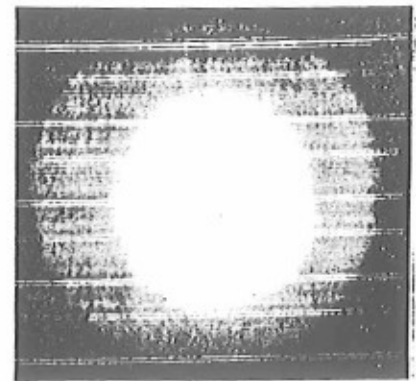
1. The inner burning surface regresses outward with a fairly circular contour. Using a digital image processor, the radius of the center cavity can be measured, and the burning rate can be deduced.
2. The propellant grain does not deconsolidate into fragments as it burns. This observation is consistent with previously reported results from an end-burning test configuration.
3. The flame inhibitor on the outer circumferential and end surfaces prevented those areas from burning. If the ends were to burn, the entire area corresponding to the grain would become lighter; this was not observed in any of the tests. However, in one of the tests, the flame inhibitor around the outer circumference did fail 6 ms before the end of the test.



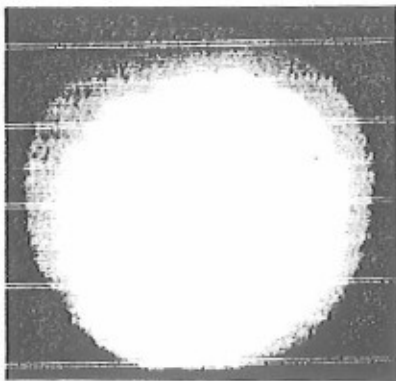
a) $t = 0$ ms
 $P = 0$ MPa
 Radius = 0.318 cm
 $r_b = 0.0$ cm/s



b) $t = 364$ ms
 $P = 31.2$ MPa
 Radius = 0.827 cm
 $r_b = 3.9$ cm/s



c) $t = 428$ ms
 $P = 90.0$ MPa
 Radius = 1.33 cm
 $r_b = 21$ cm/s



d) $t = 442$ ms
 $P = 333$ MPa
 Radius = 1.938 cm
 $r_b = 85$ cm/s

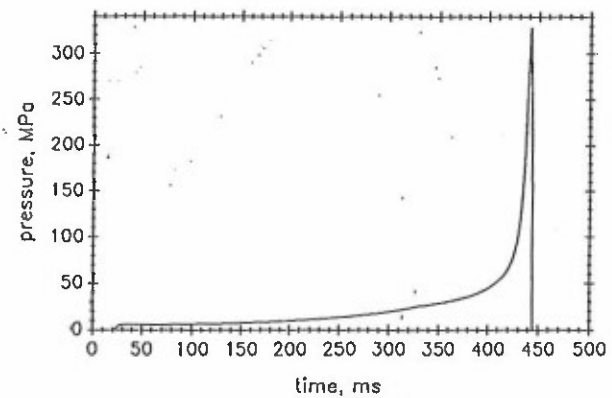


Fig. 4 Results of a Real-Time X-Ray Radiography Test using the High-Pressure Double-Windowed Test Rig. OX Boron Hydride Formulation.

Two p-t traces for the 2 and 4% boron hydride formulations are presented in Fig. 5. This comparison shows that the 4% sample burns slightly faster than the 2% sample and therefore generate p-t traces with a shorter time to reach the peak pressure.

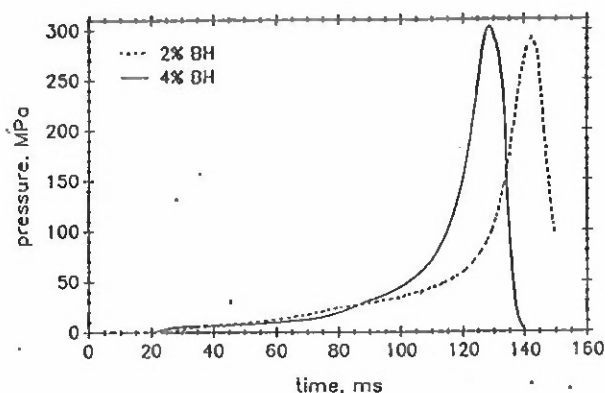


Fig. 5 Pressure-Time Traces for the 2 and 4% Boron Hydride Formulations

For all three propellant formulations, the burning rates as a function of pressure were deduced. The general procedure for this analysis is given below.

1. Using the image processor, the area of the center cavity is obtained for approximately 20 of the X-ray images at different times.
2. From the area, the radius was calculated using the assumption that the area is a perfect circle.
3. Since the time was known for each radius, the radius versus time data was curve fitted with a series of piecewise parabolas. For each data point, a parabola was fitted through five points (two above and two below) using a least-squares fit. The burning rate at this point was calculated from the derivative of the parabola. From the parabola, additional burning rate data were generated in the interval starting at the midpoint preceding the point in question and ending at the midpoint after it. This procedure continues until the burning rate data for the entire test period is deduced.
4. The pressure-time data was then used to generate a plot of burning rate versus pressure.

Figures 6, 7, and 8 contain plots of burning rate versus pressure for all three formulations. The solid line in each of these plots represent data which was reported in Ref. 1 and was obtained using X-ray radiography with a smaller "O"-frame chamber with an end-burning configuration. Each solid line represents the least squares fit of data obtained from four tests. However, the dashed line in these plots represents the center-perforation test data obtained from one test. Only one test was performed for each formulation due to the very limited number of fiberglass tubes available.

The new burning rate data for the 0% boron hydride formulation matches fairly well to the end-burning data. The new burning rate data for the 4% formulation appears to have the same slope as the end-burning data at pressures above 30 MPa, but a discrepancy occurs at pressures below 20 MPa. This discrepancy will be studied further as more HPDW tests are conducted.

Perhaps the most interesting burning rate plot is the plot for the 2% formulation. The center-perforated data has a definite slope break at 28 MPa while the end-burning data has a slope break at 60 MPa. The remarkable feature is the fact that the slopes above and below the respective break points look identical. Also, the burning rates above 60 MPa are identical even though these two sets of tests were conducted using two different batches of propellant.

One possible explanation for this shifting of burning rate data at lower pressures is a transient burning effect. Figures 9, 10, and 11 are plots comparing the rate of pressurization for the end-burning and the center-perforation tests. For the 2% formulation, between 15 and 23 MPa where the burning rates show a noticeable discrepancy, the values of dP/dt are very close. The pressurization rate does not seem to be causing this shifting of burning rate.

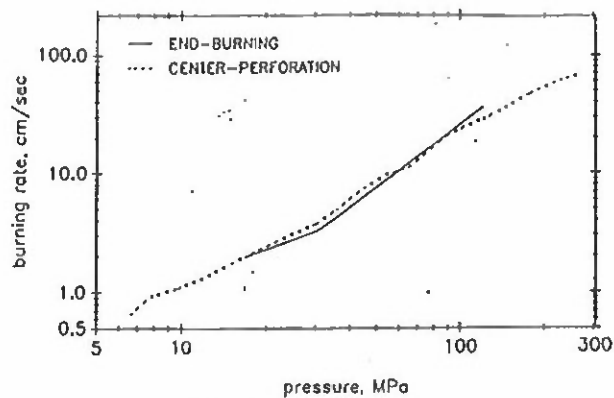


Fig. 6 Burning Rate versus Pressure from RTR System, 0% Boron Hydride Formulation

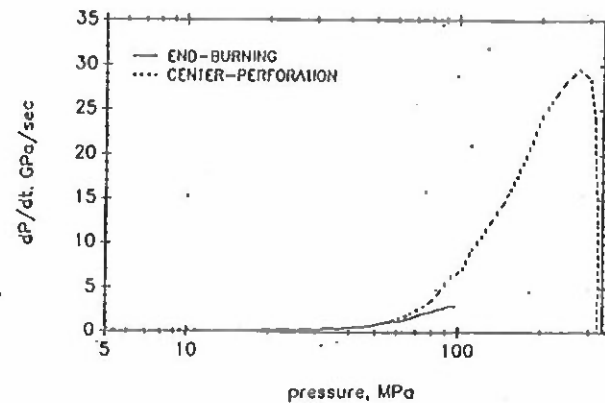


Fig. 9 Rate of Pressurization of Transient Burning Tests, 0% Boron Hydride

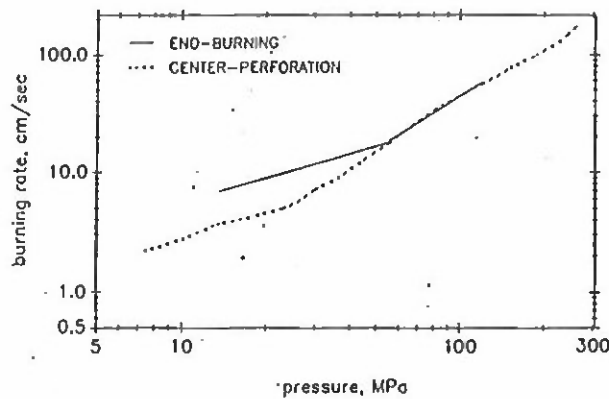


Fig. 7 Burning Rate versus Pressure from RTR System, 2% Boron Hydride Formulation

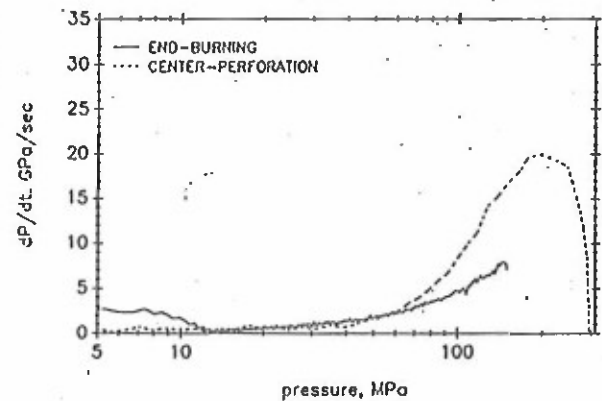


Fig. 10 Rate of Pressurization of Transient Burning Tests, 2% Boron Hydride

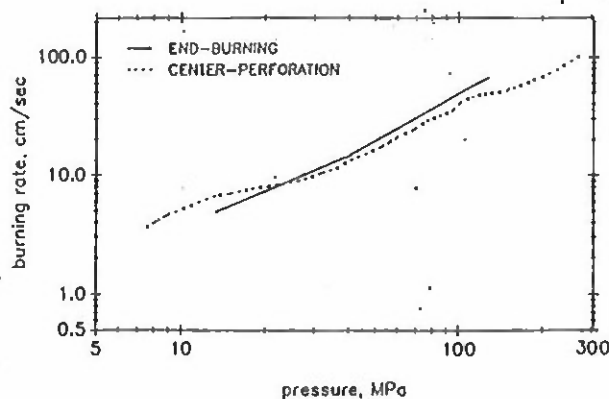


Fig. 8 Burning Rate versus Pressure from RTR System, 4% Boron Hydride Formulation

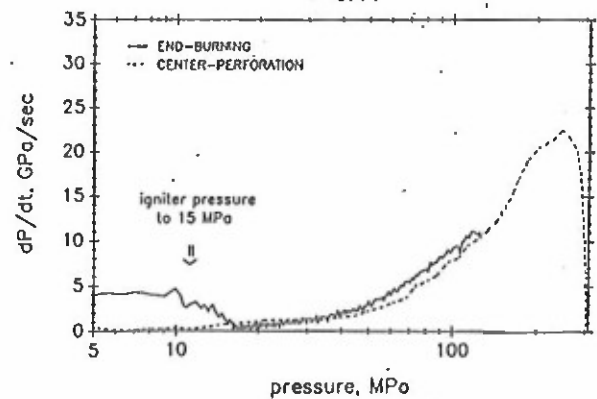


Fig. 11 Rate of Pressurization of Transient Burning Tests, 4% Boron Hydride

A slight change in propellant formulation could also explain the difference in the burning rate. The 0% formulation that was used for the end-burning tests was manufactured 3 1/2 years ago. The batch that was used for the most recent tests was made this year. Also, a different particle size distribution of the ingredients in these two batches of propellant could contribute to this burning rate shift phenomenon.

A recovered grain of the 0% boron hydride formulation which extinguished at 331 MPa (48,000 psi) shows a non-smooth burning surface. The entire surface is covered with dimples which are visible to the naked eye. These dimples are approximately 0.5 mm (0.020 in.) in diameter by 0.5 mm (0.020 in.) deep. These large dimples are created by the burning of the nitramine particles. Optical microscope images reveal partially burned nitramine particles at the bottom of some of these dimples. The surface of these nitramine particles is fairly smooth around the outer edge, but is rough towards the center. Figure 12 contains two SEM photographs of the recovered sample. This figure shows several interesting phenomena.

1. The smooth region in the center of 12 a) is the propellant's binder. In general it can be described as being smooth with many small, circular holes (20 microns).
2. The large object (200 by 200 microns) on the right side of Fig. 12 a) in the center is a partially burned nitramine particle. Only a portion of this particle can be seen, but its surface characteristics are still apparent; the outer edge is much smoother than the inner portion. The inner region has a somewhat crusty appearance.

Temperature Sensitivity Measurements of the 0% Boron Hydride Formulation

Strand burning rates for the 0% boron hydride formulation were measured at three temperatures: -10, 20, and 70 C. These burning rates are presented in Fig. 13. Each point on the graph represents data obtained from a single test. A slope break is observed at 21 MPa. Below the slope break, the pressure exponents of the burning rates are quite close. However, above the slope break, the pressure exponent at 70 C is larger than those at the other two temperatures. From this data, the temperature sensitivity of the propellant was determined in the following manner.

1. For a given pressure, the burning rates for all three temperatures were calculated from the Saint-Robert's burning rate law given in Table I.
2. A parabola was fitted exactly through these three data points. This produced an equation for the burning rate as a function of initial propellant strand temperature.

$$r_b = a + bT_i + cT_i^2 \quad (1)$$

where a, b, and c are functions of pressure.

3. The temperature sensitivity is defined as

$$\sigma_p = (\partial(\ln r_b) / \partial T_i)_p \quad (2)$$

For each pressure level, both the derivative and the burning rate were obtained at five values of initial temperature, and the temperature sensitivity was deduced.

The temperature sensitivity for the 0% boron hydride formulation is plotted in Fig. 14. Discontinuities in the temperature sensitivity occur at the burning rate slope-break point of 21 MPa. As the initial temperature of the propellant increases, the sensitivity decreases.

Using the parabola fitted burning rate in Eqn. (1), the burning rates at other initial temperatures (such as 5 and 45 C) can be plotted as a function of pressure as shown in Fig. 15.

Comparison of the Strand Burning Rates and the Transient Burning Rates for the 0% Boron Hydride Formulation

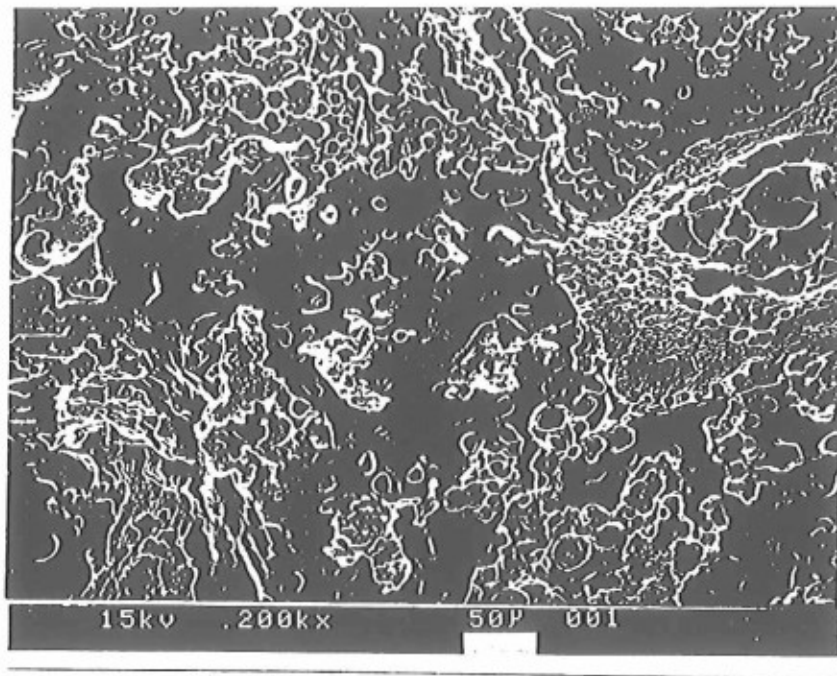
Figure 16 shows a comparison of strand burner burning rate data with the transient burning rate data. It is found that at a given pressure the strand burning rates are approximately 22% higher than those of the transient burning rates. This disproves the commonly accepted idea that transient burning rates under positive pressure excursion are higher than strand burning rates. The actual physical reason for a higher strand burning rate is not fully understood and should be further investigated.

SUMMARY AND CONCLUSIONS

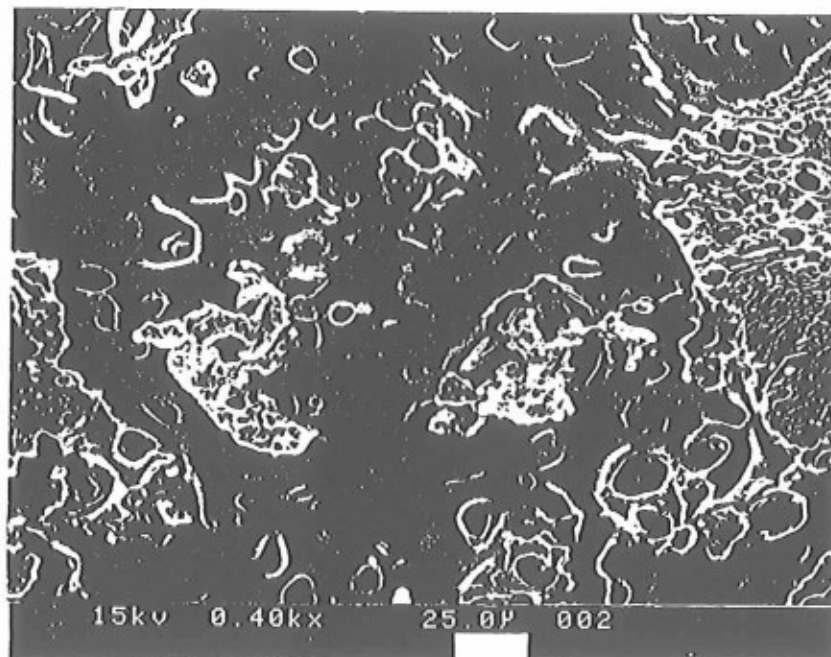
1. The burning rates of VHBR propellants have been measured in two different test rigs.
 - a) Steady state burning rates were measured using an optical strand burner with a broad range of pressure and initial temperature.
 - b) Transient burning rates were measured using a real-time X-ray radiography (RTR) system with a high-pressure double-windowed (HPDW) test rig for pressures up to 331 MPa (48,000 psi).
2. In the HPDW tests, the X-ray images show that the propellant grains remain as consolidated charges without breaking into small fragments.
3. The transient burning rates obtained in the HPDW test rig are reasonably close to the transient burning rates measured in the O-frame chamber with an end burning configuration.
4. A recovered grain which extinguished at 331 MPa (48,000 psi) showed a non-smooth burning surface. The entire surface is covered with dimples which are visible to the naked eye. These dimples are approximately 0.5 mm in diameter by 0.5 mm deep. From SEM photographs, smaller, less populated dimples are evident; on the microacopic scale, the binder's surface is quite smooth.
5. The transient burning rates are approximately 22% lower than the strand burning rates.
6. The temperature sensitivity was measured as a function of pressure and initial temperature. The sensitivity increases as the temperature decreases.

REFERENCES

1. Salizzoni, R. M., Hsieh, W. H., Kuo, K. K., Juhasz, A. A., "Study of Combustion Behavior of Very High Burning Rate Propellants," Proceedings of the 11th International Symposium on Ballistics, May 1989, Vol. I, pp. 129-140.
2. Salizzoni, R. M., Hsieh, W. H., Kuo, K. K., Juhasz, A. A., "Study of Combustion Behavior of Very High Burning Rate Propellants," Proceedings of the 25th JANNAF Combustion Meeting, October 1988, Vol. II, pp. 303-315.
3. Salizzoni, R. M., Hsieh, W. H., Kuo, K. K., Peretz, A., "Some High-Pressure Combustion Characteristics of VHBR Propellants," Proceedings of the 26th JANNAF Combustion Meeting, October 1989, Vol. I, pp. 255-266.
4. Hsieh, W. H., Char, J. M., Zanotti, C., Kuo, K. K., "Erosive and Strand Burning of Stick Propellants, Part I: Measurements of Burning Rates and Thermal-Wave Structures," Journal of Propulsion and Power, Volume 6, Number 4, July-August 1990, pp. 392-399.
5. McCarty, K. P., Isom, K. B., Jacox, J. L., "Nitramine Propellant Combustion," AIAA Paper No. 79-1132, AIAA/SAE/ASME 15th Joint Propulsion Conference, June 18-20, 1979, Las Vegas, Nevada.



a) 200 X Magnification



b) 400 X Magnification

Fig. 12 SEM Photographs of a Recovered Sample of the 0% Boron Hydride Formulation

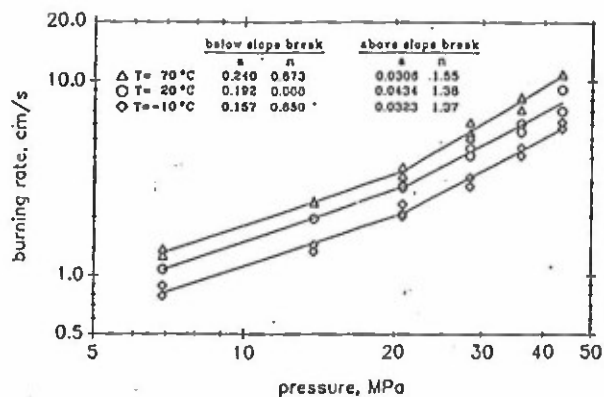


Table 1 Burning Rate Law for 0% Boron Hydride VHBR Propellant

$$r_b [\text{cm/s}] = a (P[\text{MPa}])^n$$

	below slope break		above slope break	
	a	n	a	n
T= 70 °C	0.240	0.873	0.0308	1.55
T= 20 °C	0.192	0.888	0.0434	1.38
T= -10 °C	0.157	0.850	0.0323	1.37

Fig. 13 Strand Burning Rates of the 0% Boron Hydride Formulation

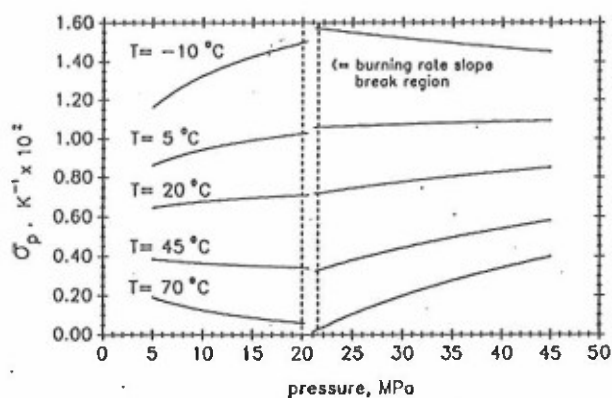


Fig. 14 Temperature Sensitivity of the 0% Boron Hydride Formulation

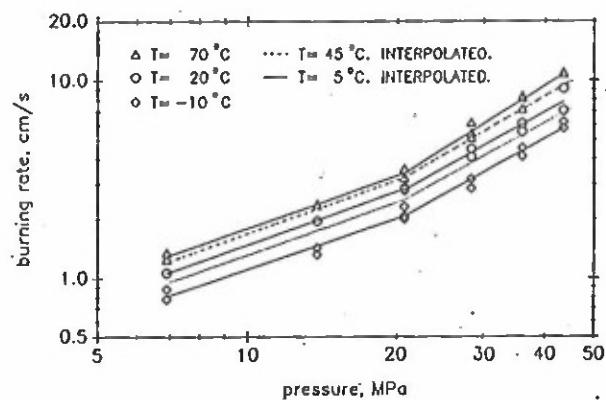


Fig. 15 Interpolated Burning Rates for T= 5 and 45 °C

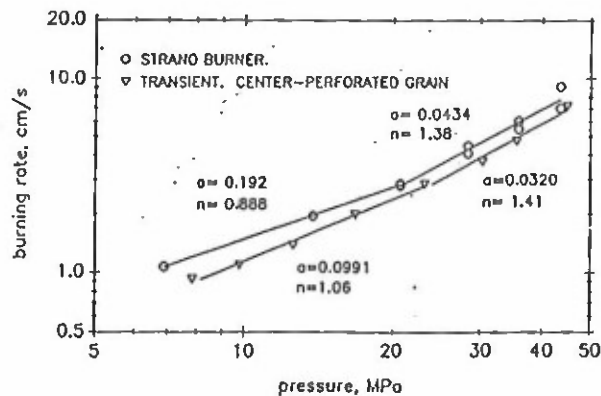


Fig. 16 Strand Burning Rates versus Transient Burning Rates. 0% Boron Hydride

Appendix D

CPIA PUBLICATION 529

VOLUME I

OCTOBER 1989

Reproduction is not authorized except
by specific permission from CPIA.

26th JANNAF COMBUSTION MEETING

VOLUME I

Jet Propulsion Laboratory
Pasadena, California
23-27 October 1989

CHEMICAL PROPULSION INFORMATION AGENCY

Operating under contract N00039-89-C-0001

THE JOHNS HOPKINS UNIVERSITY • APPLIED PHYSICS LABORATORY • LAUREL, MD.

Approved for public release; distribution is unlimited.

CONVECTIVE IGNITION OF LOVA PROPELLANTS SUBJECTED
TO CROSSFLOW HEATING CONDITIONS*

Staven Ritchie,[#] Wen Hsin Hsieh,^{\$} Kenneth K. Kuo[†]
Department of Mechanical Engineering
The Pennsylvania State University
University Park, Pa 16802

ABSTRACT

Convective ignition tests of XM39 low vulnerability ammunition (LOVA) propellants were carried out under crossflow test conditions using a shock tunnel facility. This type of test is better related to practical ignition in standard gun systems than other more common tests such as laser-induced radiative ignition. Ignition delay, defined as the time from initial test section pressure rise to the emission of light from the sample with sustained combustion, was determined using high-speed video and photomultiplier tube detection systems. For tests conducted in this study, ignition was always detected in the region of the separation point of the boundary layer. The flame would spread from the separation point over the downstream surface of the propellant. In some instances of higher test section pressure, the flame would also spread forward on the surface toward the stagnation point of the cylinder. It is theorized that the pyrolysis products from the shoulder regions and the stagnation point, where heating rates are highest, are carried by the flow and further reacted in the recirculation zone formed at the separation point. The subsequent gas-phase ignition then spreads over the sample surface. A correlation between a nondimensionalized ignition delay time and Nusselt number was obtained.

INTRODUCTION

Of recent interest in the gun community is the formulation of so-called 'insensitive' munitions which would be resistant to ignition from all but the desired stimulus. Of particular interest are formulations based on the nitramine RDX and HMX. These materials not only display a high thermal stability and a low sensitivity to ballistic vulnerability but also have ideal features of low smoke output and high specific impulse (rockets) or impetus (guns). However, these low vulnerability ammunition (LOVA) propellants are not without disadvantages. The most apparent problem associated with the practical use of a propellant is related to one of their desirable characteristics; by nature they are difficult to ignite. Therefore, the ignition characteristics of these propellants must be well understood if safe, reliable igniters are to be designed for gun systems employing these LOVA based munitions.

The ignition phenomenon of solid propellants involves complex physical and chemical processes. The event is initiated by the application of some external stimulus such as convective heat transfer from hot gases, radiative heat flux, impact, friction, etc. and ends with the self-sustained burning of the material. The physical and chemical interactions which occur during this period characterize the 'ignition' transient phenomenon and are function of both the material and the type of stimulus applied. Part of the difficulty in studying ignition behavior lies in the interpretation of the definition. The beginning of the ignition event, the initial application of some external stimulus, is easily determined, but the completion of the ignition processes, the onset of self-sustained combustion, is not as easily identified. For example, 'ignition' to the practical gun system designer is represented by a successful

*This work was performed under Contract Number DAAL03-87-K-0064 under the sponsorship of the Army Research Office, Research Triangle Park, North Carolina. The program manager is Dr. David Mann. His support of this research is greatly appreciated. Thanks also go to Dr. Joseph Rocchio for providing the propellant samples.

[#]Graduate Assistant, Ph.D. Candidate

^{\$}Assistant Professor

[†]Distinguished Alumni Professor

Approved for public release, distribution is unlimited.

triggering and resultant firing of the gun system (ie. the end result justifies the ignition of the propellant material used). However 'ignition' in an experimental setting, where laboratory constraints might not permit self-sustained burning of the material, may be represented by emission of light from a sample or the measurement of pyrolysis gases generated from the reacting sample. In the case of a theoretical model, 'ignition' would probably be based on some type of runaway temperature criteria.

In addition to the above interpretive problems, the mechanism of ignition is different for the different stimuli applied and thus comparison of data from various experiments is very difficult. It would be extremely useful if a set of experiments could be performed using a single propellant type in various ignition experiments which employ the same ignition threshold criteria. This would provide a clearer understanding of the subsequent results and, at the very least, useful quantitative comparisons between different ignition tests employing different mechanisms could be made.

Much information is already known about the combustion of nitramine propellants. The literature survey by Boggs¹ provides a very good overview of what has been done regarding the thermal decomposition of both RDX and HMX. Of particular interest, is the description of ignition studies with HMX in which the radiative ignition behavior of the nitramine is found to be more similar to double-base propellants than that of AP composite propellants. The study, first presented by Boggs et. al.², describes how HMX pellets display significant pre-ignition behavior after reaching a gasification threshold for a given laser induced heat flux input. The pellets, even after reaching the gasification threshold, were not able to sustain burning until another 'go/nogo' threshold had been reached. This is unlike AP-based propellants which ignite almost immediately after gasification is achieved. It was concluded in this study that the ignition of the nitramine propellant was occurring in the gas phase. Another study by Kim et al.^{3,4} examined laser induced pyrolysis and ignition processes of RDX based composite propellants using a high-powered CO₂ laser, similar to the work done on HMX by Boggs et. al. Based on fine wire thermocouple measurements, Kim found five separate reaction zones above the propellant surface during the ignition transient (1) a primary reaction zone, (2) a first preparation zone, (3) a secondary reaction zone, (4) a second preparation zone and (5) a final luminous flame zone. Again the importance of gas phase reactions on the ignition of the propellants via radiative heat flux has been substantiated.

Kubota⁵ examined the flame structure of both RDX- and AP-based composite propellants and described his findings. The RDX-based propellant exhibited a steady state flame structure similar to double-base propellants in which a visible standoff distance between the luminous flame and the propellant surface could be seen. It has been shown that the RDX composite, although displaying a physical structure similar to the AP-based propellant, has a combustion wave structure which is more similar to that of double-base homogeneous propellants. Although this work involved the visualization of steady flame structure, it further supports the above findings of Boggs et. al. and Kim et. al. in which the gas phase reactions are important to the combustion of nitramine propellants.

A recent JANNAF workshop, coordinated by Stiefel and Kuo⁶, was held to determine the status and shortcomings of nitramine propellant ignition research. A good portion of the workshop dealt with ignition of nitramine propellants in gun simulator studies. For example, Stiefel⁷ and Messinz⁸ discussed the work done with 25mm gun system simulators, Rodriguez⁹ examined the relationship between ignition system characteristics, the temperature coefficient, and round-to-round reproducibility using a 30 mm test fixture, other tests of this nature were described others⁶. These tests, although very valuable when determining the ideal charge/igniter design for a particular gun system, do not place as great an emphasis on understanding the basic fundamental physical and chemical processes which govern nitramine propellant ignition. With a better understanding of these processes, the above tests would become even more useful due to the data base which they provide.

Identified at the workshop was a lack of fundamental convective ignition information. Since this ignition mechanism is so important to the gun community, this was felt to be a major shortcoming. Convective ignition tests have been carried out successfully in the past by both Kashiwagi¹⁰ and Birk¹¹ using a shock tunnel facility. Kashiwagi studied ignition of solid fuels due to convective heating via hot shock tube generated gases. The geometry of the sample was a flat plate. Birk carried out a study of cylindrical nitrocellulose propellants which were ignited via convective crossflow heating by hot gases created by the same shock tunnel facility that Kashiwagi

used. Birk was able to visually determine, for nitrocellulose propellants, that ignition of the sample occurred either at the front stagnation point, the separation point of the boundary layer, or the rear stagnation (downstream wake) region depending on the imposed convective conditions, the percentage of oxidizer in the test gas, and the propellant formulation used. In addition, the ignition delay (defined as arrival of the pressure wave to the time of first light emission) could be measured and the effects of pressure variation, temperature, flow velocity and free stream oxidizer content on this delay time could be examined. The test method used by Birk was very effective and provided useful information regarding the ignition and flame spreading phenomenon for the nitrocellulose propellants studied.

This paper describes the convective ignition portion of an ongoing study of RDX-based XM-39 LOVA propellant carried out using the same shock tunnel facility as Birk and Kashiwagi with modifications to the test section only. The overall goal of the continuing study is to achieve a better understanding of convective ignition processes and examine possible relationships between the convective and more commonly examined radiative ignition behavior of this propellant. Although the CO₂ laser radiative test, as mentioned earlier when discussing the work of Kim et. al., provides greater control over heat flux input and is more commonly used due to its relative simplicity, the convective ignition test is more closely related to the actual ignition process used in practical gun systems where propellant ignition is obtained via hot gases from the igniter. The objectives of this project are to (1) visually examine the convective ignition phenomenon and subsequent flame spreading of RDX-based XM-39 propellant using high speed photography, (2) measure ignition delay (based on light emission from the sample) and examine possible correlations to convective flow parameters (Reynolds Number, Prandtl Number, Nusselt Number and Mach Number).

METHOD OF APPROACH

SHOCK TUNNEL FACILITY

The convective ignition experiments are carried out using a modified version of the shock tunnel used in previous studies by Kashiwagi and Birk as discussed above. The shock tunnel facility, shown schematically in Fig. 1, is a total of 24.1 m (79 ft) long. The driver section length is 9.7 m (31.8 ft) and the driven section length is 8.5 m (27.9 ft). The last 5.9 m (19.3 ft) section of the tunnel makes up the exhaust chamber for the induced flow. The inside diameter of the tunnel is approximately 9.718 cm (3.826 in.). The driver section has a maximum rating of 12.4 MPa (1800 psia) and is charged with helium gas. The driven section can be brought to pressures as low as 1.38 kPa (0.2 psia) and the test gas can be composed of any combination of oxygen and nitrogen. Firing of the tunnel is accomplished through a double burst diaphragm technique. The burst diaphragms are composed of soft aluminum sheets and are ruptured against a knife edge to minimize the amount of debris that ends up in the tunnel.

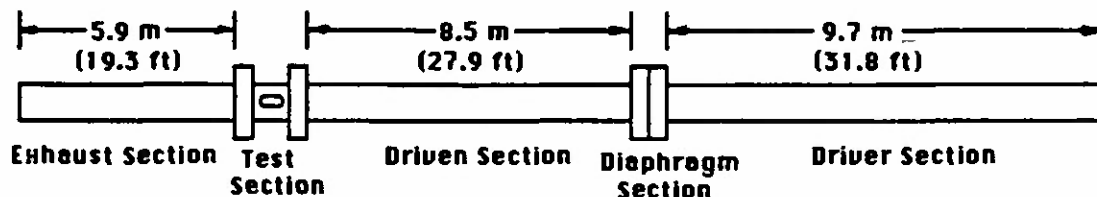


Figure 1. Schematic diagram of shock tunnel facility

The test section is located at the end of the driven section and is characterized by a sudden cross-sectional area change from the 9.718 cm (3.826 in.) diameter round shock tunnel to a 2.858 cm (1.125 in.) square duct. A cut-out side view of the test section is shown in Fig. 2. Quartz windows located on the top and sides of the test section (side windows not shown in the figure) provide optical access. Perforated plates are located at both the upstream entrance and downstream exit. The downstream exit plate acts as a nozzle which chokes the flow and controls the velocity of gas through the test section. The upstream perforated plate was not used by either Kashiwagi or Birk in their studies. It was added to help damp out initial pressure oscillations caused by the starting transient of the flow when the shock wave passes through the test section. Without the plate, the pressure in the test section would display extreme oscillations in the first three milliseconds of the test time. Addition of the plate lessens the magnitude and duration of these oscillations.

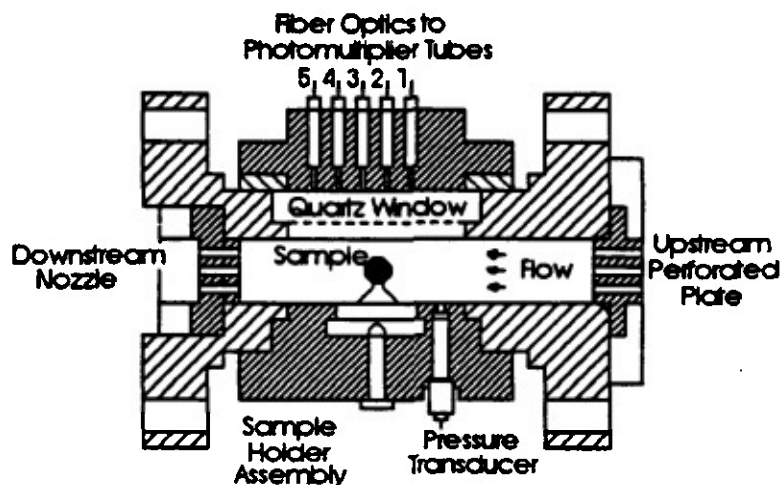


Figure 2. Cut-out side view of test section for convective ignition studies

The shock tunnel is used to create a reservoir of high temperature, high pressure gas which in turn induces a flow through the test section. The incident shock wave generated in the tunnel propagates down the driven section to the test section. Since the diameter of the tunnel is much larger than the opening to the test section, most of the shock wave is reflected off the flat end wall. The doubly shocked gas in the driven section of the tunnel is now at a very uniform high pressure and temperature. The high pressure induces flow through the test section and across the sample. Ideally this flow is of a steady temperature and pressure throughout the available test time. The major limitation of the shock tunnel is the time in which the flow is at these high temperatures and pressures. Under certain conditions, the shock tube facility provides a maximum of ~17 ms of useful test time. This time can be shortened if the conditions of the tunnel are not in the 'tailored' operating regime¹². Tailoring of the shock tunnel conditions is commonly used in shock tube studies and deals with minimizing the interaction of the reflected shock wave with the contact surface (the interface between the driver and driven gases). If the internal energies of the driver and driven gases are equal across the contact surface, the reflected shock will pass through the contact surface without creating any additional disturbances other than a Mach wave. If they are not equal, the interaction results in either an expansion wave or shock wave which is reflected back toward the test section. The arrival of this disturbance created by the interaction at the contact surface prematurely ends the test time. For the shock tunnel used in this study, tailored conditions were obtained when the incident shock wave had a Mach number between 3.60 and 3.90.

Prior to ignition testing, the uniformity of the flow passing through the test section and across the sample had to be examined. This was especially necessary because the addition of the upstream perforated plate would create a turbulent wake region upstream of the sample position which would have to dissipate prior to reaching the position in the test section where the sample was mounted. A set of high speed schlieren tests were carried out to visualize the flow approaching the sample. The results of these tests proved the flow approaching the sample was uniform.

Through control of the areas open to the flow on both the upstream perforated plate and downstream nozzle, the initial driver gas to driven gas pressure ratio and the initial pressure in the driven section, the shock tunnel is capable of producing a wide range of test conditions: pressures of 1.03 to 4.14 MPa (150 to 600 psia), temperatures of 950 to 1500 K (1710 to 2670 R), and velocities of 40 to 250 m/s (131 to 820 ft/s). As described earlier, the above conditions have, in certain cases, very short available test times depending on the deviation from the tailored regime.

Diagnostics for ignitions tests are highlighted in Fig. 3. Three Kistler 601B1 pressure transducers located along the driven section of the tunnel detect the arrival of the shock wave at fixed locations and are used to measure the speed of the incident shock wave. Another Kistler 601B122 pressure transducer is located in the test section, 1.91 cm (0.75 in.) upstream of the sample, as can be seen in Fig. 2. This

transducer provides test section pressure information. To determine ignition delay, five RCA 1P28 photomultiplier tubes with filters to prevent saturation are used remotely via fiber optic tubes which are mounted on the top window of the test section (see Fig. 2). High speed visualization of the event is accomplished through the two side windows. Usually a Kodak Spin Physics SP2000 high-speed video system is used with backlighting of the sample, but tests have been run under more complicated shadowgraph and schlieren conditions using the SP2000 video system. In addition, a Redlake Hycam high speed 16 mm movie camera with a higher frame rate has been used for a very limited number of tests.

Separate tests are carried out to measure gas temperature and flow velocity. To determine gas temperature, the sample holder is removed and one of the side ports is used to mount an S-type thermocouple in the center of the test section. The thermocouple was made of 25 μ m (0.001 in.) diameter wire; butt-welded at the ends to obtain as small a bead as possible. Theoretically, the direct thermocouple reading provides a temperature value between the total temperature and the static temperature of the flow. Corrections to this direct reading in order to compensate for any discrepancy were not deemed necessary for the low speed tests (40-55 m/s) where the difference between static and stagnation temperature values would be very small. The velocity of the flow was determined using two approximate methods. First, a pitot tube set-up incorporating a Validyne 215-51 diaphragm pressure transducer was used, but the response time was not fast enough to provide anything but a good estimate of the flow velocity within ± 5 m/s. However, during the course of the test firings an alternative measurement method was discovered. If the driven section of the shock tunnel is not thoroughly cleaned between test firings, reacting aluminum (or some other material) particles are carried through the test section throughout the duration of the test. Under the assumption of no slip velocity between the gas and the particle (fully entrained conditions), measurement of the streakline lengths captured on the high-speed video as the particles passed through the test section provides another approximate value of flow velocity. Comparison of the values obtained using both methods showed very good agreement (within ± 5 m/s).

TEST SAMPLE

The propellant used for this study was XM-39 (Lot #A5-1184-113) which has a formulation of 76% RDX, 12% CAB, 7.6% ATEC, 4% NC, and 0.4% EC. The grain geometry was cylindrical with a nominal diameter of 7 mm (0.28 in.) and length of 8.6 mm (0.34 in.). Unfortunately the samples were received in a less than ideal condition. The size (length and diameter) varied from grain to grain, the size of an individual sample was not uniform (not a perfect cylinder) and the surface was pitted and graphite coated. In order to try and maintain uniformity in the tests, each sample had to be carefully prepared. This was done by hand to minimize any possible damage to the sample which machining might cause. The length was trimmed to a constant 0.74 cm (0.29 in.), the graphite coating was removed, and the surface was polished until it was visually smooth.

The sample was then mounted in the test section so the induced flow was perpendicular to the length of the grain. This relatively simple grain/flow geometry was used in order to gain a more fundamental understanding of the underlying ignition mechanisms of the propellant. Mounting of the sample in the test section was accomplished by drilling a hole down the center of the cylindrical sample. A stainless steel rod is inserted through this hole and attached to end holders. The difference between the size of the test section (2.86 cm/1.125 in.) and the length of the sample (0.74 cm/0.29 in.) was occupied by inert teflon spacers on either side so the flow would 'see' essentially one long cylinder stretching across the entire test section. This was done to remove any possible end effects from the test.

TEST CONDITIONS

The shock tunnel has a maximum test time of about 17 msec under tailored conditions. From the literature it is well known that XM-39 displays long ignition delay times. Concern over whether the propellant would ignite within the available test regime dictated the conditions chosen for this study. The tests were performed in the region of the tailored interface conditions, incident shock wave Mach number between 3.60 and 3.90, which would provide the maximum testing time. Some tests were run at higher and lower incident Mach numbers because the sample would ignite prior to the premature ending of the test. The open area of both the upstream perforated plate and downstream nozzle were fixed so the velocity of the test gases was usually between 50 and 56 m/s (164.0 ft/s and 183.7 ft/s). At these lower velocities the propellant would have a better chance of achieving ignition within the available test time. The tests were carried out using air as the test gas which is indicative of practical ignition scenarios. The actual test conditions are listed in Table I of the Results section.

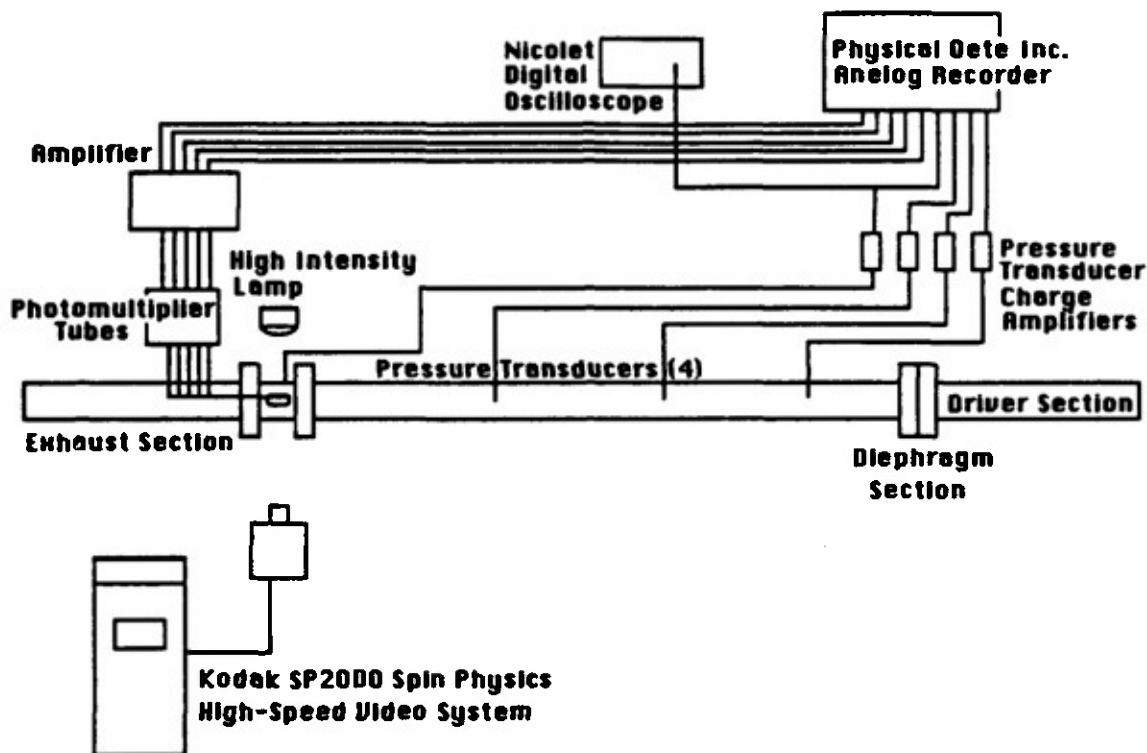


Figure 3. Schematic diagram of convective ignition diagnostics

RESULTS AND DISCUSSION

CALIBRATION TESTS

To obtain the gas-phase temperature of the convective stream within the test section, a set of calibration tests were carried out. For this set of tests, the Mach number of the incident shock wave, the test section pressure, and the gas-phase temperature were measured and correlated. Using this correlation, the temperature could be calculated if the incident shock wave Mach number and test section pressure are known. Transport properties such as thermal diffusivity and viscosity of the test gas were determined using these calculated temperatures.¹³ In addition, the gas-phase density was deduced using this temperature value and the measured test section pressure.

A typical temperature trace is shown in Fig. 4. The response time of the thermocouple was not fast enough to provide detailed information about the starting period of the flow, but it is assumed the plateau on the trace towards the end of the test time corresponded to the average gas temperature in the test section.

IGNITION TESTS

A total of sixteen ignition tests have been conducted at the conditions shown in Table I. This table lists the measured test section pressure and incident shock wave Mach number, the corresponding temperature value obtained via the correlation to calibration data, and the values of Reynolds number, Prandtl number, test section flow Mach number and Nusselt number. In addition, there are two listings for delay times associated with ignition, the time to light emission (t_{LE}) and the ignition delay time (t_{ID}).

The first delay time listed is the time until first light emission (t_{LE}). In most cases, emission of light from the sample was observed on the high-speed video record of the transient startup time. During this startup time, the shock wave arrives at the test section end heating rates are highest. However, this 'transient' ignition was not always able to sustain burning for the entire test time because the heating rates would decrease with the onset of the quasi-steady flow through the test section. The sample

once quenched would usually, but not always, reignite later during the steady state convective heating period and sustain burning until the end of the test time. It is this second ignition point which has been labeled the ignition delay time (t_{io}). The ignition delay was determined through analysis of both the photomultiplier output (100,000 data points per second) and the high speed video pictures (6,000 pictures per second).

TABLE I: Summary of test conditions and results

Test No.	Incident Mach No.	Pressure MPa (psia)	Test Section Parameters			Prandtl Number	Nusselt Number	Mach Number	t_{LE} msec	t_{io} msec
			Temperature °K (°R)	Reynolds Number						
051	3.808	1.89 (274)	1377 (2479)	35190		0.707	142.6	0.074	2.83	7.33
052	3.758	1.92 (278)	1319 (2374)	38755		0.716	150.8	0.076	3.17	5.50
053	3.869	1.81 (262)	1447 (2605)	31402		0.695	133.6	0.073	--	7.27
055	3.850	1.75 (254)	1425 (2565)	31259		0.699	133.2	0.074	--	9.41
056	3.915	1.72 (249)	1498 (2696)	28216		0.685	125.6	0.072	1.00	2.45
058	3.872	1.74 (252)	1450 (2610)	30086		0.694	130.3	0.073	1.17	1.50
059	3.971	2.65 (384)	1563 (2813)	39959		0.687	153.5	0.071	1.33	3.17
060	3.789	2.58 (374)	1355 (2439)	50472		0.710	175.7	0.076	--	2.82
061	3.780	2.57 (373)	1345 (2421)	51008		0.712	176.8	0.076	1.67	3.17
062	3.641	2.21 (320)	1234 (2221)	49761		0.725	174.2	0.077	--	5.64
063	3.934	2.37 (344)	1520 (2736)	37180		0.686	147.2	0.070	0.83	5.17
064	3.700	2.22 (322)	1252 (2254)	45989		0.723	166.5	0.073	2.83	3.64
065	3.898	1.99 (289)	1480 (2664)	31529		0.689	133.9	0.069	2.83	8.59
066	3.407	2.21 (320)	1173 (2111)	37330		0.728	147.6	0.055	--	11.46
067	3.602	1.72 (250)	1164 (2095)	41944		0.726	157.9	0.079	1.67	14.55
068	3.580	1.89 (274)	1172 (2110)	44619		0.728	163.6	0.077	1.33	5.33

The results of Test 067 have been chosen as a 'typical' example case in which to discuss the ignition phenomenon. It should be understood that this does not mean all the tests displayed identical results, but for this series of low speed tests the variation in the phenomenon observed was not extreme from case to case.

The pressure transducer output versus time for Test 067 is presented in Fig. 5. As can be seen, the trace can be divided into two sections. The 'transient starting time' is characterized by a sharp pressure rise followed by large oscillations caused by reflections of the incident shock wave within the test section. These large oscillations damp out in less than three milliseconds before the 'steady state' test time period begins. The static pressure during the steady state test time is not constant during the test but increases from a minimum value of 1.55 MPa (225 psia) to a maximum value of 1.90 MPa (275 psia). This corresponds to about a 20% increase in pressure over the duration of the test. This, unfortunately, is unavoidable as an average pressure value is used in all calculations and in the presentation of the results. Although this is undesirable, the pressure value during the majority of the test can be considered quasi-steady with tolerable pressure variation.

The output of the five RCA 1P28 photomultiplier tubes are shown in Fig. 6. The large initial deflection in the traces (the output of PMT 5 saturated the data acquisition system) corresponds to the arrival of the incident shock wave in the test section (time = 0). The photomultiplier can recover from this flashing in less than 2 ms. The large spike appearing soon after recovery (PMT 3) corresponds to a very bright flash from the top of the sample which can be seen very clearly in the video pictures (see Fig. 7) and is listed in Table I as t_{io} . The next deflection of the photomultiplier signal (particularly on PMT 2 and PMT 3 which are focused on the sample) is due to the onset of sustained ignition of the sample at 14.65 ms (t_{io}). The rarefaction wave arrives at the test section after ~17.60 ms (see Fig. 5) and the intensity of light from the burning sample drops and rises but the sample does not fully extinguish until 22.35 ms after the first detection of pressure rise in the test section.

Still photographs obtained from the high-speed video for Test 067 are shown in Fig. 7. Backlighting of the sample was used and the convective stream is moving from right to left. To provide some initial perspective, Fig. 7a is a pretest picture of the sample in the test section. The arrival of the shock wave is so bright that the video system saturates and is therefore not shown but this would correspond to time $t=0$. Figure 7b was taken to show the bright flash at the top of the test sample which corresponds to the large spike on the photomultiplier trace (PMT 3). This flash of light from the sample could only be seen in a single frame from the video. Thereafter the sample appears as seen in Fig. 7c until the ignition point at time $t = 14.67$ ms

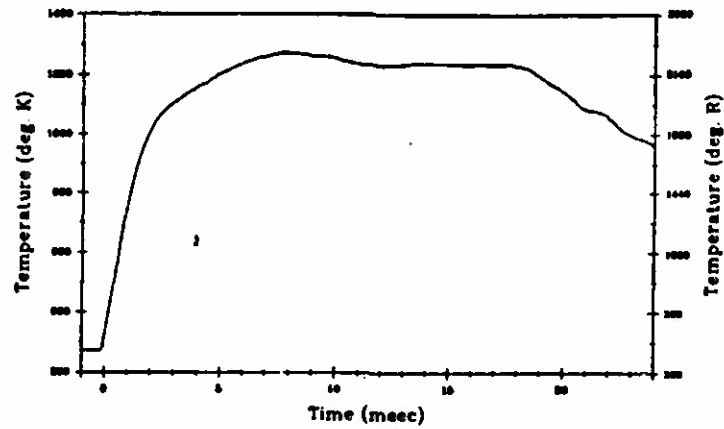


Figure 4. Typical test section gas phase temperature versus time trace

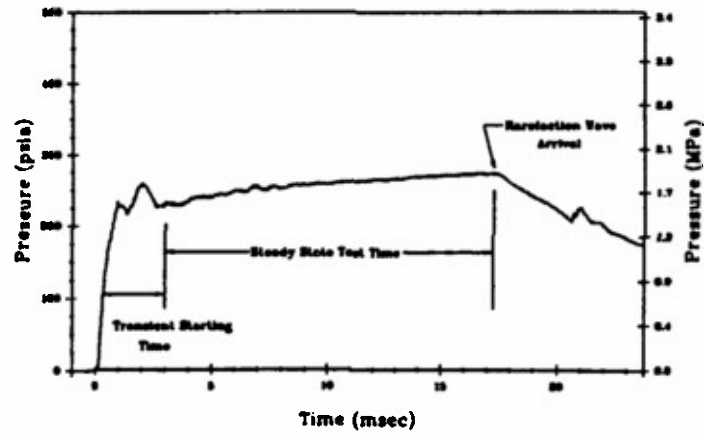


Figure 5. Typical test section pressure versus time trace (Test 067)

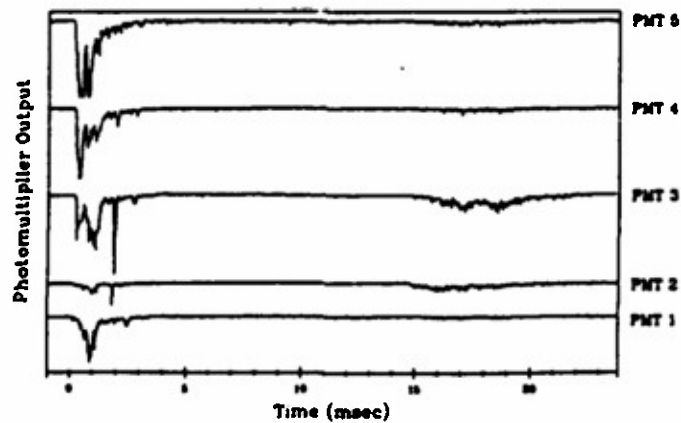


Figure 6. Typical photomultiplier output versus time trace (Test 067)



a. $t = 0-$ msec,
pretest image



h. $t = 15.83$ msec



o. $t = 17.00$ msec



b. $t = 1.67$ msec



i. $t = 16.00$ msec



p. $t = 17.17$ msec



c. $t = 14.33$ msec



j. $t = 16.17$ msec



q. $t = 18.33$ msec



d. $t = 14.67$ msec



k. $t = 16.33$ msec



r. $t = 18.50$ msec



e. $t = 14.83$ msec



l. $t = 16.50$ msec



s. $t = 18.67$ msec



f. $t = 15.00$ msec



m. $t = 16.67$ msec



t. $t = 19.50$ msec



g. $t = 15.17$ msec



n. $t = 16.83$ msec



u. $t = 19.67$ msec

Figure 7. Still photographs obtained from high-speed videotape of typical shock tunnel convective ignition test (Test 067).

(Fig. 7d) on the top of the sample only. In Fig. 7f, corresponding to $t = 15.00$ ms, burning can also be seen from the lower part of the sample. Subsequent frames show the increasing light emission from the waka region of the sample until eventually the burning spreads over the entire downstream surface (Figs. 7l and 7m). The final picture shown, Fig. 7t, corresponds closely to the arrival of the rarefaction wave when the burning is briefly interrupted as the pressure drops. The sample does continue to burn for several more milliseconds, but this is not of interest at this point other than to show resiliency of the flame which provides proof that actual ignition of the sample has occurred.

In some tests, such as 068, the burning became so intense it spread forward from the separation point of the boundary layer toward the stagnation point of the sample. The major difference between the two tests can be seen in Table I. The pressure in the test section for test 068 was much greater than for test 067. This lowered the ignition delay time considerably and affected the flame spread phenomenon after ignition had occurred. It should remain clear however, that the ignition of the sample, as it has been defined for this program, still occurred in the area of the separation point of the boundary layer.

One goal of this project is to examine possible correlations between the ignition delay time and the nondimensional parameters involved in the convective ignition process. Any general correlation will have to account for a large number of variables (e.g. Re_p , Pr , M_T , Y_{O_2} , propellant formulation, sample surface characteristics, etc.). For the data presented here, however, only a very simple correlation between the ignition delay time and the Nusselt number (see Fig. 8) is possible because of the limited range of test conditions imposed (see Table I). The ignition delay time, t_{ID} , was nondimensionalized using the characteristic flow residence time (diameter of the sample/velocity of the external flow in the test section). Since the velocity in the test section did not vary considerably this reference time was almost constant. The average Nusselt number was calculated using the formula given by Whitaker¹⁴:

$$Nu_p = (0.40Re_p^{0.5} + 0.06Re_p^{0.67})Pr^{0.4} \quad (1)$$

This plot is provided to show the potential for correlations of a more complex nature. As stated before, the data presented here represents a small range of test conditions. The velocity in the test section was held almost constant, all tests were carried out in air, and the formulation of the propellant was not varied. Therefore, the only variables changed by any significant amount were the test section pressure and temperature. The variation of these two variables is accounted for in the calculation of the Nusselt number. Further testing at different flow velocities and test gas oxidizer concentrations are planned to further generalize any future correlations. Presently, the ignition delay data are correlated with Nusselt number in the following formula:

$$t_{ID}/t_{res} = 179.71 - 0.87490Nu_p \quad (2)$$

This equation provides an adequate trend for the data with reasonable accuracy.

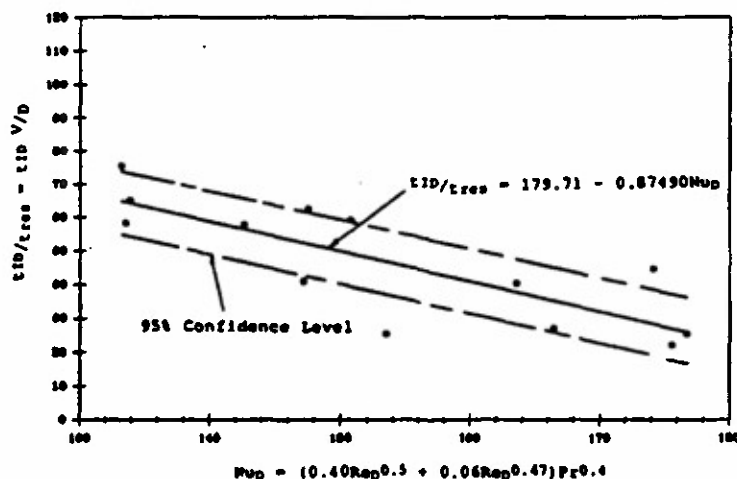


Figure 8. Nondimensionalized ignition delay time versus calculated Nusselt number

CONCLUSIONS

The following conclusions about the convective ignition of XM-39 propellant can be reached based on the results obtained and discussed above:

1. Convective ignition and flame spreading phenomenon of XM-39 solid propellant has been successfully observed using a shock tunnel facility.
2. From observation, the sample surface can reach momentary ignition due to incident and reflected shock wave heating during the transient startup time of the test. This heating is very intense but very short in duration and leads to light emission from the sample. However, the thermal profile during this period is too thin to sustain ignition after the heat input is reduced.
3. Sustained convective ignition usually occurs in the region near the separation point of the boundary layer. Probable gas-phase ignition mechanism - the high heating rates at the stagnation point and shoulder region of the sample create pyrolysis products which are carried by the flow into the recirculation zones formed by the boundary layer separation. Further heating at these points lead to ignition in the gas-phase.
4. During the test, the flame propagates towards the downstream stagnation point of the propellant sample. The sample is acting as a flame holder - in the wake region the local flow velocity is reduced and the flame can sustain.
5. In most tests, the luminous flame remained on the downstream side of the sample in the recirculating wake. However, as the test chamber pressure was increased, the luminous flame propagated upstream toward the front stagnation point of the sample. This is believed to be an effect of the higher heating rates to the front of the sample caused by the higher pressures.
6. A simple ignition delay to Nusselt number correlation provides an indication of the effect of the external flow parameters on the ignition of the LOVA propellant sample.

FUTURE WORK

Continuing tests will be carried out to improve upon the results obtained thus far.

- Freestream velocity measurements in the test section will be validated using Laser Doppler Velocimetry.
- More gas-phase temperature tests with a faster responding thermocouple will be conducted to better improve temperature/pressure/incident shock wave Mach number correlation.
- Further ignition testing at different flow velocities and using test gases with varying concentrations of oxygen will be carried out to expand on the range of data available for the development of more general correlations.

- 1 Boggs, T. L., "Thermal Behavior of RDX and HMX," AIAA Progress in Astronautics and Aeronautics: Fundamentals of Solid Propellant Combustion, edited by K. K. Kuo and M. Summerfield, Vol. 90, pp. 121-175.
- 2 Boggs, T. L., Price, C. F., Atwood, A. I., Zurn, D. E., and Oerr, R. L., "The Role of Gas Phase Reactions in Deflagration-to-Detonation Transition," 7th Symposium on Detonation, Vol. 1, June 1981, pp. 85-93.
- 3 Kim, J. U., Torikai, T., and Kuo, K. K., "Ignition Dynamics of Nitramine Composite Propellants under CO₂ Laser Heating," AIAA Paper No. 87-0564, presented at the AIAA 25th Aerospace Sciences Meeting, Reno, Nevada, 12-15 January 1987.
- 4 Fetherolf, B. L., Kim, J. U., Litzinger, T. A., and Kuo, K. K., "CO₂ Laser-Induced Pyrolysis and Ignition Processes of Nitramine Composite Propellants," Poster Paper No. P228 of the 22nd Symposium (International) on Combustion, Seattle, Wash., 14-19 Aug. 1988, p. 325.
- 5 Kubota, N., "Survey of Rocket Propellants and Their Combustion Characteristics," AIAA Progress in Astronautics and Aeronautics: Fundamentals of Solid Propellant Combustion, edited by K. K. Kuo and M. Summerfield, Vol. 90, pp. 1-52.
- 6 Stiefel, L. and Kuo, K. K., "Workshop Report: Ignition of Low Sensitivity Gun Propellant Charges," 25th JANNAF Combustion Meeting, Huntsville, Ala., 25 Oct. 1988.
- 7 Stiefel, L. and Costello, J. C., "Ignition of 25mm Insensitive Propellant Charges: Studies of the Early Portion of the Pressure-Time Curve," 25th JANNAF Combustion Meeting, Huntsville, Alabama, 24-25 October 1988.
- 8 Messine, N. A., Ingram, L. S., and Tricarico, S. A., "25mm Ballistic Simulator for XM919 Ignition System/Charge Design Studies," 25th JANNAF Combustion Meeting, Huntsville, Alabama, 24-25 October 1988.
- 9 Rodriguez, L., "Ignition/Temperature Coefficient Study for NELOVA Propellant," Naval Ordnance Station, Indian Head, Report No. INTR 1174, 27 May 1988.

- 10 Kashiwagi, T., MacDonald, B. W., Isoda, H. and Summerfield, M., "Ignition of Solid Polymeric Fuels by Hot Oxidizing Gases," AMS Report No. 947, October 1970.
- 11 Birk, A. and Caveny, L. H., "Convective Ignition of Propellant Cylinders in a Developing Cross-Flow Field," MAE Report No. 1466, Department of Mechanical and Aerospace Engineering, Princeton University, September 1980.
- 12 Wittlieff, C. E., Wilson, M. R., and Hertzberg, A., "The Tailored -Interface Hypersonic Shock Tunnel," Journal of Aerospace Sciences, Vol. 26, No. 4, April 1959, pp. 219-228.
- 13 Vasserman, A. A., Kazavchinskii, Y. Z. and Rabinovich, V. A., Thermophysical Properties of Air and Air Components, edited by A.M. Zhuravlev, Israel Program for Scientific Translations, Jerusalem, 1971.
- 14 Whitaker, S., "Forced Convection Heat Transfer Correlations for Flow in Pipes, Past Flat Plates, Single Cylinders, Single Spheres, and for Flow in Packed Beds and Tube Bundles," A.I.Ch.E. Journal, Vol. 18 (1972), pp 361-371.

Appendix E



AIAA 90-2194
Convective Ignition Phenomena of
LOVA Propellants

S.J. Ritchie, W.H. Hsieh and K.K. Kuo
The Pennsylvania State University
University Park, PA

AIAA/SAE/ASME/ASEE
26th Joint Propulsion Conference
July 16-18, 1990 / Orlando, FL

CONVECTIVE IGNITION PHENOMENA OF LOVA PROPELLANTS*

S.J. Ritchie,[#] W. H. Hsieh,^{\$} K. K. Kuo[†]
Department of Mechanical Engineering
The Pennsylvania State University
University Park, Pa 16802

Abstract

Crossflow convective ignition tests of RDX-based LOVA perforated stick solid propellant are carried out in air and nitrogen using a shock tunnel facility. Test conditions are in the range of pressure: 1.38 MPa - 2.77 MPa, temperature: 1100 K - 1500 K and flow velocity: 60 m/s - 70 m/s. Ignition, achieved only in the presence of ambient oxidizer, is always observed at or very near the surface of the sample in the region of the boundary layer separation point. Ignition delay time, determined using a photomultiplier tube detection system, is correlated to dimensionless convective flow parameters. Post-test microcopic analysis of samples show the formation of a liquid layer on the surface which grows in thickness near the separation point. A complex three-phase ignition process is postulated upon to assist with modeling considerations.

Introduction

Of recent interest in the gun and rocket community is the formulation of so-called 'insensitive' munitions which would be resistant to accidental ignition from all energy levels below the desired stimulus. Of particular interest are formulations based on the nitramines RDX and HMX. These materials not only display a high thermal stability and a low sensitivity to ballistic vulnerability but also have ideal features of low smoke output and high specific impulse (rockets) or impetus (guns). However, these low vulnerability ammunition (LOVA) propellants are not without disadvantages. The most apparent problem associated with the practical use of LOVA propellants is the difficulty in achieving consistent ignition when it is desired. Therefore, the ignition characteristics of these propellants must be well understood if safe, reliable igniters are to be designed for propulsion systems which use these types of propellants.

The ignition of solid propellants involves complex physical and chemical processes. The event is initiated by the application of some external stimulus such as convective heat transfer from hot gases, radiative heat flux, impact, friction, etc. and ends with the self-sustained burning of the material. The physical and chemical interactions which occur during this period

characterize the 'ignition' transient phenomena. These interactions and the time scales associated with them depend upon the nature of the material, the type of stimulus applied and the level of energy input. Part of the difficulty in studying ignition behavior lies in the interpretation of the definition. The beginning of the ignition event, the initial application of some external stimulus, is easily determined, but the completion of the ignition processes, the onset of self-sustained combustion, is not as easily identified. For example, 'ignition' in a laboratory setting may be represented by emission of light from a sample or the measurement of pyrolysis gases generated from a reacting sample. In the case of a theoretical model, 'ignition' is sometimes based on some type of runaway temperature criteria.^{1,2,3}

In addition to the above interpretive problems, the mechanism of ignition changes when different stimuli are applied and thus comparison of data from various experiments is very difficult. It would be extremely useful if a set of experiments could be performed using a single propellant type in various ignition experiments which employ the same ignition criteria. This would provide a clearer understanding of the subsequent results and, at the very least, useful quantitative comparisons between different ignition tests employing different mechanisms could be made.

Much information is already known about the ignition and combustion of nitramine propellants. The literature survey by Boggs⁴ provides a very good overview of what has been done regarding the thermal decomposition of both RDX and HMX. Of particular interest, is the description of ignition studies with HMX in which the radiative ignition behavior of the nitramine is found to be more similar to double-base propellants than that of AP composite propellants. The study, first presented by Boggs et al.⁵, describes how HMX pellets display significant pre-ignition behavior after reaching a gasification threshold for a given laser induced heat flux input. The pellets, even after reaching the gasification threshold, were not able to sustain burning until another 'go/no go' threshold had been reached. This is unlike AP-based propellants which ignite almost immediately after gasification is achieved. It was concluded in their study that

*This work was performed under the sponsorship of the Army Research Office, Research Triangle Park, North Carolina, Contract Number DAAL03-87-K-0064. The support and encouragement of Dr. D.H. Mann is highly appreciated.

[#]Ph.D. Candidate, Student Member of AIAA

^{\$}Assistant Professor, Member of AIAA

[†]Distinguished Professor, Associate Fellow of AIAA

ignition of nitramine propellants was occurring in the gas phase. Another study by Kuo and coworkers^{6,7} examined laser induced pyrolysis and ignition processes of RDX-based composite propellants using a high-powered CO₂ laser. Based on fine wire thermocouple measurements, Kuo and coworkers^{6,7} found five separate reaction zones above the propellant surface during the ignition transient (1) a primary reaction zone, (2) a first preparation zone, (3) a secondary reaction zone, (4) a second preparation zone and (5) a final luminous flame zone. Again the importance of gas-phase reactions on the ignition of the propellants via radiative heat flux has been substantiated.

Kubota⁸ examined the flame structure of both RDX- and AP-based composite propellants and described his findings. The RDX-based propellant exhibited a steady-state flame structure similar to double-base propellants in which a visible standoff distance between the luminous flame and the propellant surface could be seen. The RDX composite, although displaying a physical structure similar to the AP-based propellant, has a combustion wave structure which is more similar to that of double-base homogeneous propellants. Although this work involved the visualization of steady flame structure, it further supports the above findings of Boggs et al.⁵ and Kuo and coworkers^{6,7} in which gas-phase reactions are important to the combustion of nitramine propellants.

A recent JANNAF workshop, coordinated by Stiefel and Kuo⁹, was held to determine the status and technological gaps of nitramine propellant ignition research. A large portion of the workshop dealt with ignition of nitramine propellants in gun simulator studies. For example, Stiefel and Costello¹⁰ and Messina et al.¹¹ discussed work done with 25mm gun system simulators and Rodriguez¹² examined the relationship between ignition system characteristics, the temperature coefficient, and round-to-round reproducibility using high energy LOVA propellants in a 30 mm test fixture. These tests, although very valuable when determining the ideal charge/igniter design for a particular gun system, do not place as great an emphasis on understanding the basic fundamental physical and chemical processes which govern nitramine propellant ignition. Identified at this workshop was a lack of fundamental convective ignition information. Since this ignition mechanism is important to the gun community, this was felt to be a major technological gap.

Convective ignition tests have been carried out successfully in the past by both Kashiwagi et al.¹³ and Birk and Caveny¹⁴ using a shock tunnel facility. Kashiwagi et al.¹³ studied ignition of solid fuels due to convective heating via hot shock tube generated gases. The geometry of the sample was a flat plate. Birk and Caveny¹⁴ carried

out a study of cylindrical nitrocellulose propellants which were ignited via convective crossflow heating by hot gases created by the same shock tunnel facility that Kashiwagi et al.¹³ used. Birk and Caveny¹⁴ were able to visually determine, for nitrocellulose propellants, ignition of the sample occurred either at the front stagnation point, the separation point of the boundary layer, or the rear stagnation (downstream wake) region depending on the imposed convective conditions, the oxidizer percentage in the test gas, and the propellant formulation used. In addition, the ignition delay (defined as arrival of the pressure wave to the time of first light emission) could be measured and the effects of pressure, temperature, flow velocity and free stream oxidizer content on the this delay time could be examined. The test method used by Birk and Caveny¹⁴ was very effective and provided useful information regarding the ignition and flame spreading phenomenon for the nitrocellulose propellants studied.

This paper describes the convective ignition portion of an ongoing study of RDX-based XM-39 LOVA propellant carried out using the same shock tunnel facility as Birk and Caveny¹⁴ and Kashiwagi et al.¹³ The ultimate goal of the ongoing study is to achieve a better understanding of convective ignition processes and examine possible relationships between the convective and more commonly examined radiative ignition behavior of this propellant. Although the CO₂ laser radiative test, as mentioned earlier when discussing the work of Kuo and coworkers^{6,7}, provides greater control over heat flux input and is more commonly used due to its relative simplicity, the convective ignition test is more closely related to the actual ignition process used in practical gun systems where propellant ignition is obtained via hot gases from the igniter. The objectives of this project are to (1) visually examine the convective ignition phenomenon and subsequent flame spreading of RDX-based XM-39 propellant using high speed photography, (2) measure ignition delay (based on light emission from the sample) and examine possible correlations to convective flow parameters and (3) microscopically examine recovered propellant samples to determine the effects of burning on sample surfaces.

Method of Approach

Shock Tunnel Facility

The convective ignition experiments are carried out using a modified version of the shock tunnel used in previous studies by Kashiwagi et al.¹³ and Birk and Caveny¹⁴ as discussed above. The shock tunnel facility, shown schematically in Fig. 1, is a total of 24.1 m long. The driver section length is 9.7 m, the driven section length is 8.5 m and the exhaust section length is 5.9 m. The inside diameter of the tunnel is approximately 9.7 cm. The driver section has a maximum rating of 12.4 MPa and is

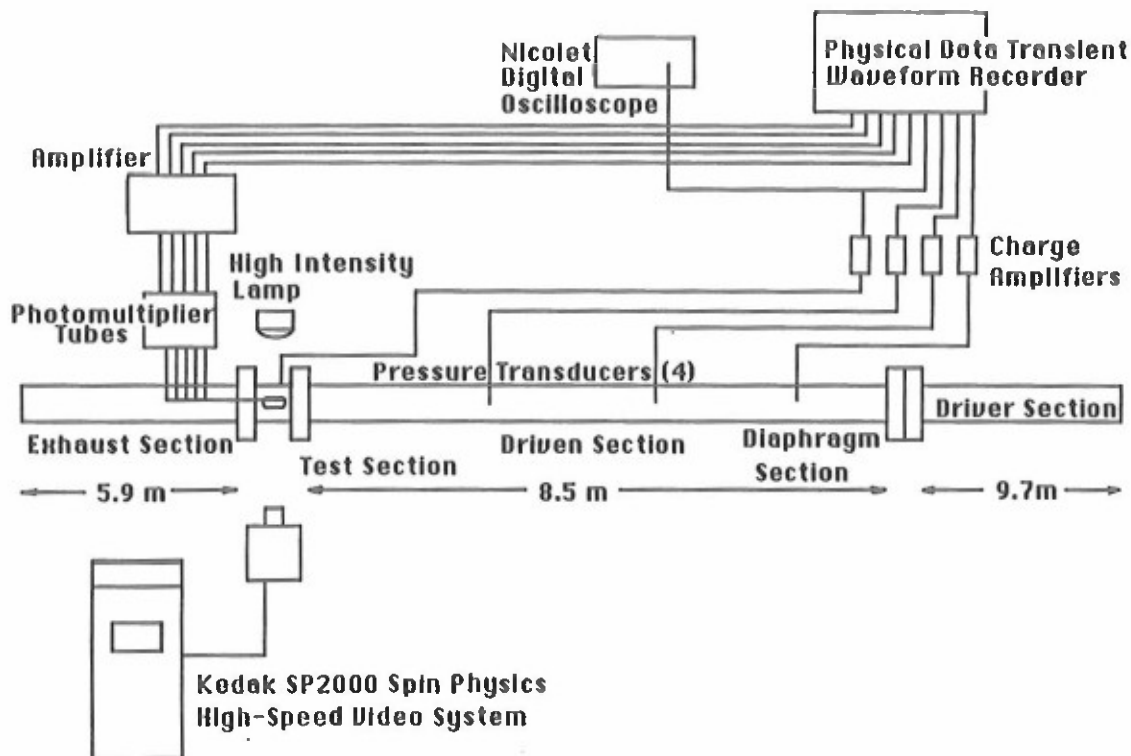


Figure 1: Schematic diagram of shock tunnel facility and diagnostics

charged with helium gas. The driven section can be brought to pressures as low as 1.38 kPa and the test gas can be composed of any combination of oxygen and nitrogen. Firing of the tunnel is accomplished through a double burst diaphragm technique. The burst diaphragms are composed of soft aluminum sheets and are ruptured against a knife edge to minimize debris in the tunnel.

The test section is located at the end of the driven section and is characterized by a sudden cross-sectional area change from the 9.7 cm diameter round shock tunnel to a 2.86 cm square duct. A cross-sectional side view of the test section is shown in Fig. 2. Quartz windows located on the top and sides of the test section (side windows not shown in the figure) provide optical access. Perforated plates are located at both the upstream entrance and downstream exit. The downstream exit plate acts as a nozzle which chokes the flow and controls the velocity of gas through the test section. The upstream perforated plate is used to help damp out initial pressure oscillations caused by the starting transient of the flow when the shock wave passes through the test section and to protect the sample from burst diaphragm debris. Prior to ignition testing, the uniformity of the flow passing through the test section and across the sample was visually examined using high speed schlieren photography. LDV measurements further validated the uniformity of the flow in the test section.

The shock tunnel is used to create a

reservoir of high temperature, high pressure gas which in turn induces a flow through the test section. The incident shock wave generated in the tunnel propagates down the driven section to the test section. Since the diameter of the tunnel is much larger than the opening to the test section, most of the shock wave is reflected off the flat end wall and the perforated plate. Upon reflection, the doubly shocked gas in the driven section of the tunnel reaches a very uniform high pressure and temperature. The high pressure induces flow through the test section and across the sample. Ideally this flow is of steady temperature and pressure throughout the available test time. The major limitation of the shock tunnel is the time duration of the flow at these high temperatures and pressures. Under certain operating conditions, the shock tunnel facility provides a maximum of ~17 ms of useful test time. This time can be shortened if the conditions of the tunnel are not in the 'tailored' operating regime¹⁵. Tailoring of the shock tunnel conditions is commonly used in shock tube studies and deals with minimizing the interaction of the reflected shock wave with the contact surface (the interface between the driver and driven gases). If the internal energies of the driver and driven gases are equal across the contact surface, the reflected shock will pass through the contact surface without creating any additional disturbances other than a Mach wave. If they are not equal, the interaction results in either an expansion wave or shock wave which is reflected back

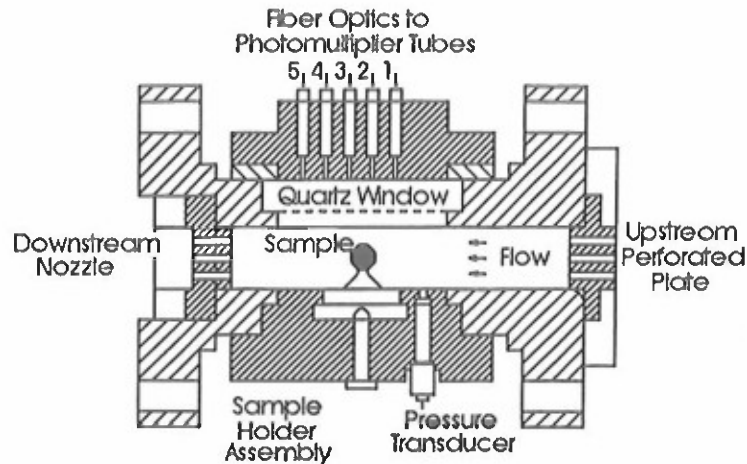


Figure 2: Cross-sectional side view of test section

toward the test section. The arrival of this disturbance created by the interaction at the contact surface prematurely ends the test time. For the shock tunnel used in this study, tailored conditions were obtained when the incident shock wave had a Mach number of ~ 3.72 .

Through control of the areas open to the flow on both the upstream perforated plate and downstream nozzle, the initial driver gas to driven gas pressure ratio and the initial pressure in the driven section, the shock tunnel is capable of producing a wide range of test conditions: pressures of 1.03 to 4.14 MPa, temperatures of 950 to 1500 K, and velocities of 60 to 250 m/s. As described earlier, the above conditions have, in certain cases, very short available test times depending on the deviation from the tailored regime.

Diagnostics for ignition tests are highlighted in Fig. 1. Three Kistler 601B1 pressure transducers located along the driven section of the tunnel detect the arrival of the shock wave at fixed locations and are used to measure the speed of the incident shock wave. Another Kistler 601B122 pressure transducer is located in the test section, 1.91 cm (0.75 in.) upstream of the sample, as can be seen in Fig. 2. This transducer provides test section pressure information. To determine ignition delay, five RCA 1P28 photomultiplier tubes are used remotely via fiber optic tubes which are mounted on the top window of the test section (see Fig. 2). Filters are used to reduce the observed range of wavelengths to the near ultraviolet centered around 3700 Å. High-speed visualization of the event is accomplished through the two side windows. Usually a Kodak Spin Physics SP2000 high-speed video system is used with backlighting of the sample, but tests have been run under more complicated shadowgraph and schlieren conditions with the SP2000 video system. In addition, a Redlake Hycam high-speed 16 mm movie camera with a higher frame rate has been used for a very limited number of tests.

Separate tests are carried out to measure gas temperature and flow velocity. To determine gas temperature, one of the side ports is used to mount a shielded K-type total-temperature thermocouple probe in the center of the test section. The velocity of the flow was determined using an LDV system.

Test Sample

The propellant used for this study was XM-39 (Lot #A5-1184-113) which contains a significant amount of RDX. The grain geometry is cylindrical in shape with a nominal diameter of 7 mm and length of 7.5 mm. There are sample variations; the size (length and diameter) varied from grain to grain, the shape of individual samples was not highly uniform (not a perfect cylinder) and the surface was pitted and graphite coated. In order to try and maintain uniformity in the tests, each sample was carefully prepared. This was done in such a way as to minimize any damage to the grain surface. The length was trimmed to a constant 7.4 mm, the graphite coating was removed, and the surface was polished until it was visually smooth.

The sample was mounted in the test section so the induced flow was perpendicular to the length of the grain. This relatively simple grain/flow geometry is used to gain a more fundamental understanding of the underlying ignition mechanisms of the propellant. Mounting of the sample in the test section was accomplished by drilling a hole along the center axis of the cylindrical sample. A stainless steel rod is inserted through this hole and attached to end holders. The difference between the width of the test section, 2.86 cm, and the length of the sample, 0.74 cm, was occupied by inert spacers on either side so the flow would 'see' essentially one long cylinder stretching across the entire test section. This was done to remove any possible end effects from the test.

Results

Calibration Tests

To obtain the gas-phase temperature and velocity of the convective stream within the test section, two sets of calibration tests were carried out. For the first set of tests, the Mach number of the incident shock wave, test section pressure and gas-phase temperature were measured and correlated. In the second set of tests, the gas velocity was measured and correlated to the incident shock wave Mach number and test section pressure. Using these correlations, the temperature and velocity of the flow in the test section can be deduced with reasonable accuracy if the incident shock wave Mach number and test section pressure are known. Transport properties and gas density were determined using deduced gas temperature and measured pressure values.

Ignition Tests

Two series of tests have been carried out with the XM-39 propellant. The first set of tests was done using nitrogen as the test gas. There was no ignition detected for any of these tests by either the video or by the photomultiplier tubes. The second set of tests was carried out using air as the test gas. The conditions for these tests are given in Table I. This table lists the incident shock wave Mach number, measured test section pressure, temperature and Mach number, Reynolds number, Prandtl number, and Nusselt number. The ignition delay time (t_{ID}) and dimensionless ignition delay (t^*_{ID}) defined as $t_{ID}/(D/V)$ are also listed. The nondimensionalization is accomplished using a residence time based on the diameter of the sample and the velocity of the flow. The Nusselt number 16 is calculated using the following formula for flow over a cylinder:

$$Nu = .027 Re^{.805} Pr^{.333} \quad (1).$$

In many cases, emission of light from the sample was observed on the high-speed video record of the transient start-up time. During this start-up time, the shock wave arrives at the test section and heating rates are highest. However, this 'transient' ignition was not always able to sustain burning for the entire test time because the heating rates would decrease with the onset of the quasi-steady flow through the test section. The sample, once quenched, would usually, but not always, reignite later during the steady-state convective heating period and sustain burning until the end of the test time. It is this second ignition point which has been labeled the ignition delay time (t_{ID}). The ignition delay was determined through analysis of both the photomultiplier output (100,000 data points per second) and the high-speed video pictures (6,000 pictures per second).

The ignition sequence was very similar for all of the tests in which ignition was observed. To better illustrate the observed

phenomena, the data and film obtained from Test Nos. 155 and 157 is described in detail below.

The pressure transducer output versus time for Test 155 is presented in Fig. 3. The trace can be divided into two sections. The 'transient starting time' begins with the arrival of the incident shock wave. Interaction of the incident wave with the sample and nozzles leads to pressure oscillations and turbulent flow conditions around the sample. Heat flux to the propellant can be over twice as large as that seen during the 'steady-state' period. The 'steady-state test time' begins after about three or four milliseconds. The test section pressure during this time does not oscillate but does increase from a minimum value of 1.45 MPa to a maximum value of 2.00 MPa. This corresponds to a 27% increase in pressure over the duration of the test. This, unfortunately, is unavoidable so an average pressure value is used in all calculations and in the presentation of the results. Although undesirable, the pressure value during the majority of the test can be considered quasi-steady with tolerable pressure variation.

The output of the RCA 1P28 photomultiplier tube which first registered ignition is shown in Fig. 4. The large initial deflection in the traces corresponds to the arrival of the incident shock wave in the test section (time = 0). The deflection of the photomultiplier signal due to the onset of sustained ignition of the sample is seen at 10.835 ms (t_{ID}). The rarefaction wave arrives at the test section after ~17.82 ms (see Fig. 3). The intensity of light from the burning sample is altered slightly at this time but the sample does not fully extinguish until 19.650 ms after the first detection of pressure rise in the test section.

Still photographs obtained from the high-speed video for Test 155 are shown in Fig. 5. Backlighting of the sample was used and the convective stream is moving from right to left. To provide some initial perspective, Fig. 5a is a pretest picture of the sample in the test section. The arrival of the shock wave is so bright that the video system saturates and is therefore not shown but this would correspond to time $t=0$. Thereafter the sample appears as seen in Fig. 5a until visible light can be seen on the top surface at time, $t = 11.167$ ms (Fig. 5b). Any light generated on the bottom of the sample would be hidden by the sample supports. The more sensitive photomultiplier tube detected ignition much earlier at 10.835 ms. In Fig. 5c, corresponding to $t = 11.500$ ms, the reaction has propagated downstream and grown in intensity and can now be seen on the lower half of the sample. Subsequent frames show increasing light emission from the wake region of the sample until eventually the burning spreads over the entire downstream surface at time $t = 13.334$ ms (Figs. 5d to 5o). Once the reaction has covered the

TABLE I: Summary of Test Conditions and Results for XM-39 Solid Propellant in Air

Test No	Shock Mach No.	Test Section		Reynolds Number	Prandtl Number	Nusselt Number	Mach Number	t _{ID} (ms)	t* _{ID}
		Pressure (MPa)	Temperature (K)						
050	3.88	4.16	1420	75942	0.699	203.4	0.070	0.00	0.00
051	3.81	1.87	1387	51285	0.705	148.7	0.101	7.33	76.8
052	3.76	1.93	1363	50654	0.709	147.5	0.095	5.50	53.6
053	3.87	1.90	1415	50538	0.700	147.2	0.101	7.27	78.9
055	3.85	1.90	1406	47723	0.702	140.1	0.095	9.41	93.5
058	3.87	3.02	1415	64032	0.700	177.4	0.082	1.50	13.2
059	3.97	2.77	1462	59386	0.692	166.3	0.084	3.17	28.0
060	3.79	2.70	1377	62976	0.707	175.6	0.086	2.82	25.0
061	3.78	2.70	1373	63293	0.707	176.3	0.086	3.17	27.7
062	3.64	2.30	1307	58462	0.718	166.2	0.086	5.64	50.0
063	3.93	2.50	1443	55985	0.695	158.8	0.087	5.17	48.0
064	3.70	2.29	1335	56720	0.713	161.9	0.088	3.64	32.6
065	3.80	2.07	1429	48720	0.698	142.2	0.090	8.59	83.7
067	3.60	1.77	1268	49072	0.720	144.5	0.096	14.55	138.7
068	3.58	2.63	1279	66190	0.721	184.0	0.086	5.33	45.6
147	3.98	1.77	1467	40783	0.691	122.8	0.091	8.28	81.2
148	3.37	2.23	1181	64846	0.728	181.6	0.090	16.15	138.0
150	3.96	2.05	1457	46622	0.693	136.9	0.089	6.63	62.0
152	3.78	1.99	1373	48711	0.707	142.8	0.090	14.38	131.9
153	3.60	2.04	1288	53013	0.720	153.8	0.091	14.65	135.6
154	3.42	2.08	1204	60649	0.728	172.0	0.093	16.01	141.7
155	3.90	1.79	1429	41930	0.698	126.0	0.092	10.84	107.3
156	3.75	2.06	1356	51267	0.710	126.8	0.092	10.07	96.8
157	3.91	1.76	1421	42282	0.697	149.0	0.090	7.47	69.2

downstream region of the sample it burns in essentially a steady-state fashion (Fig. 5p) until the end of the test time. The sample does continue to react for several milliseconds after the pressure drop at 17.82 ms caused by the arrival of the rarefaction wave as shown in Fig. 3. This is of interest since it shows the attainment of self-sustained ignition.

In order to better analyze the phenomena seen in Test 155, closeup video was taken of Tests 156 and 157. The still photographs from Test 157 are shown in Fig. 6. Of particular interest is the region of the initial location of the emitted light and the subsequent spreading of the reaction. Fig. 6a shows first visible light in a region 95° to 100° from the leading edge of the cylinder. In Fig. 6b the reaction propagates forward nearly reaching the top of the sample (90° from the leading edge) while it grows in intensity. In subsequent frames the reaction zone moves forward and recedes in an oscillatory fashion (Figs. 6c to 6f). The reaction settles into a steady-state position near the top of the sample (Figs. 6g and 6h). In Fig. 6i the reaction can be seen propagating towards the rear surface of the sample. Following this the reaction dies out and the test ends. Because of the change in optical path to the camera, more light is apparently required by the closeup pictures and therefore the intensity of the reaction as seen in Fig. 5 is not as apparent. For test 156, which was run at higher pressure, the luminous region of the flame propagated further past the top of the sample toward the front stagnation point and the steady-state position of the

flame was at the 90° point.

Microscopic analysis of propellant following the tests was carried out to examine what effect the burning (or lack of burning) had on the sample surface. Under 50X magnification, it was quite evident that a liquid or 'melt' layer had formed on the sample surface (Fig. 7). At the front stagnation point, the surface is slightly pitted and many small particles from the shock tunnel burst diaphragm become imbedded in the 'melt' layer (pos. 1). Between 30° and 45° from the leading edge, small wave formations appear on the surface (Fig. 7a). These wave formations have very small length scales which grow as one travels toward the location 90° from the leading edge (Fig. 7b). Just beyond the 90° point, there is a large agglomeration of liquid on the surface (Fig. 7c). The position of this liquid formation coincides very well with the location of first reaction as seen on the video. A second agglomeration which is slightly smaller than the one at ~95° can be seen at ~105° from the leading edge (pos. 5). The back surface and rear stagnation point of the sample is fairly smooth and free of particles (pos. 6 and 7). The only easily distinguishable difference between the burned and unburned samples is the coloring. Burned samples exhibit a darker shade of yellow/white (particularly on the downstream side of the sample and at the agglomeration points) while the unburned samples are more close to the original white. Unfortunately this cannot be seen in the photographs because of the lighting used.

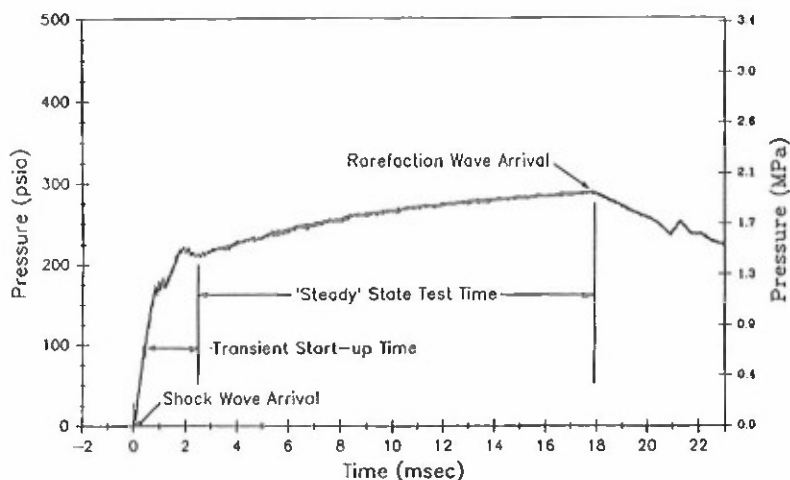


Figure 3: Typical test section pressure versus time trace (Test 155)

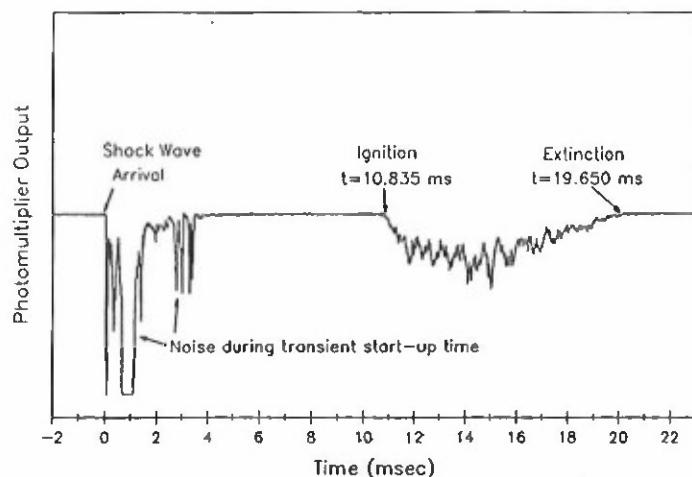


Figure 4: Typical photomultiplier output versus time trace (Test 155)

Discussion

A goal of this project is to examine possible correlations between the ignition delay time and nondimensional parameters involved in the convective ignition process. Previously, a correlation based on an average Nusselt number was attempted.¹⁷ Presented here is an improved correlation of dimensionless ignition delay (t_{ID}^*) as a function of a dimensionless heat transfer rate (Q^*) with the influence of free-stream temperature. Q^* is defined as:

$$Q^* = Nu \frac{(T_{\infty} - 480 K)}{298 K} \quad (2).$$

The value of 480 K was chosen as a surface temperature because it is close to the melting or liquefaction temperature for RDX quoted in much of the literature.⁴ The correlation is shown plotted in Fig 8.

For the data taken at relatively high values of Q^* , ignition took place during the 'transient start-up time' or followed this time very closely. The equation of the correlation for these data points is:

$$t_{ID}^* = 263.0 - 0.440 Q^* \quad (3).$$

As the value of Q^* is reduced, ignition would occur much later during the test. The equation for the best fit of this data is:

$$t_{ID}^* = 799.6 - 1.611 Q^* \quad (4).$$

The dashed line on the plot represents the 95% confidence ranges for convective ignition. As was expected, and further validated by the slope break in the correlation, the ignition characteristics of the propellant during the start-up of the test are significantly different from those observed during the steady-state or quasi-steady test time.

During the start-up time, heat flux to the sample is very large because of incident shock wave interactions, flow reversals and turbulent flow conditions around the sample. Because of these complexities, interpretation of data obtained during this highly transient period is very difficult. Fortunately, this period of time is very brief and the thermal profile in the sample is quite thin. When the high heat flux period ends, the thermal profile can adjust quickly to the new ambient heating conditions. For self-sustained ignition to occur, the heat feedback from the reaction zones must be able to maintain the the

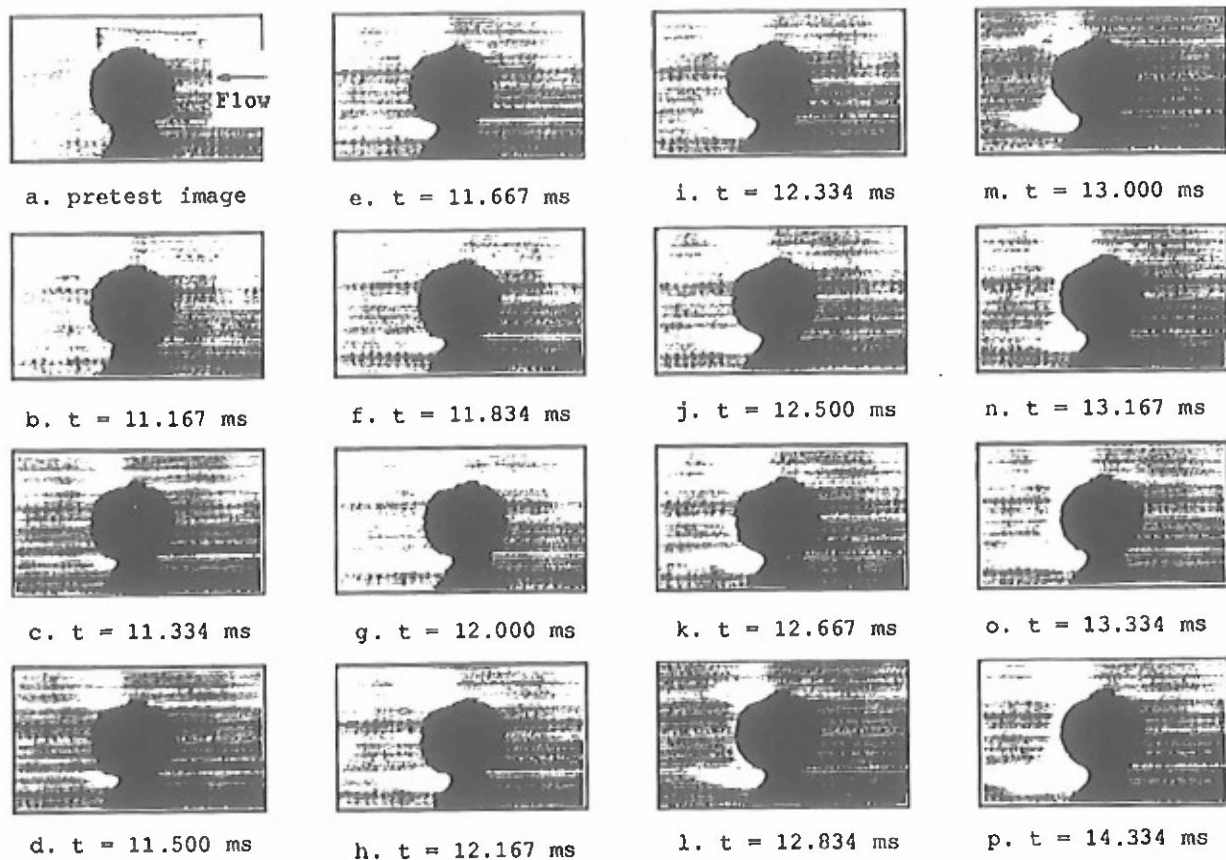


Figure 5: Photographs of shock tunnel convective ignition Test 155

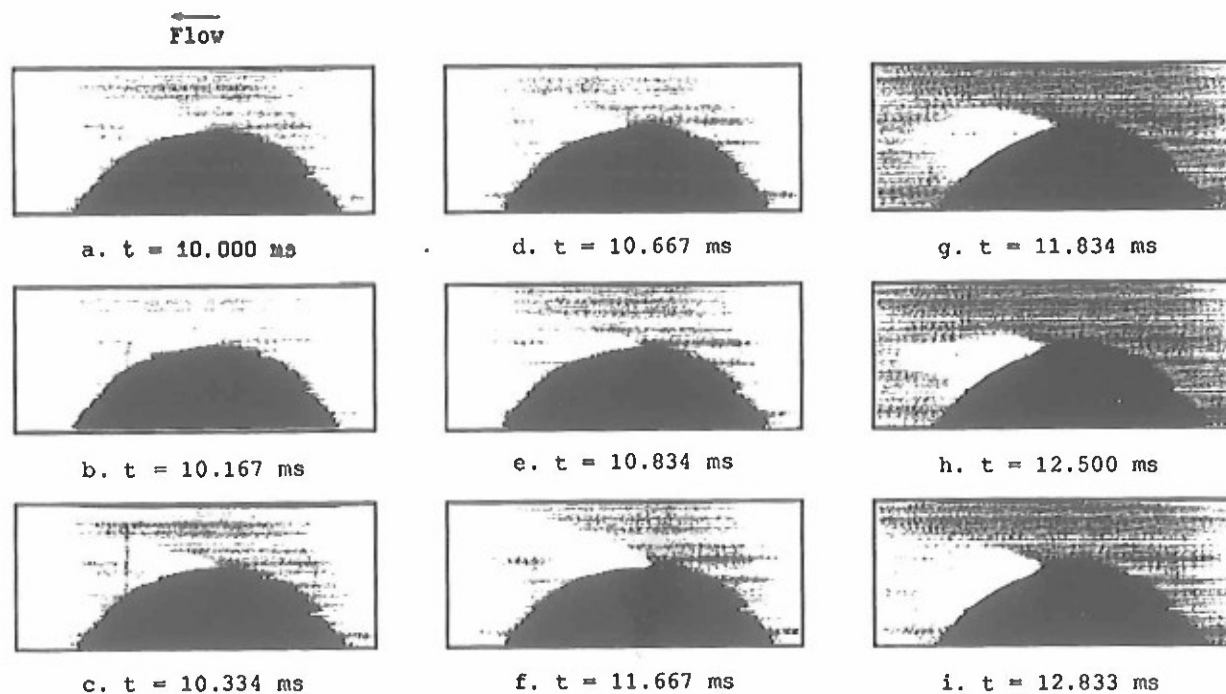
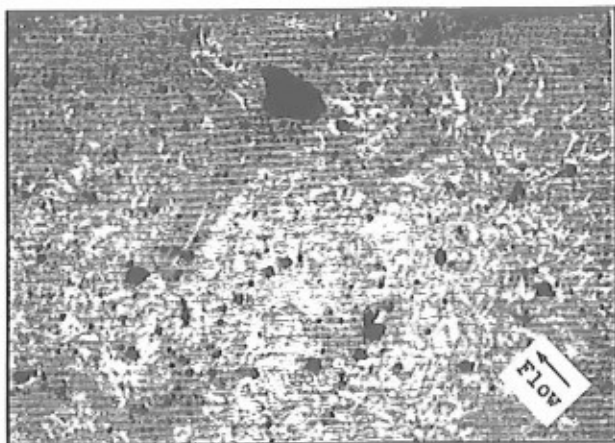


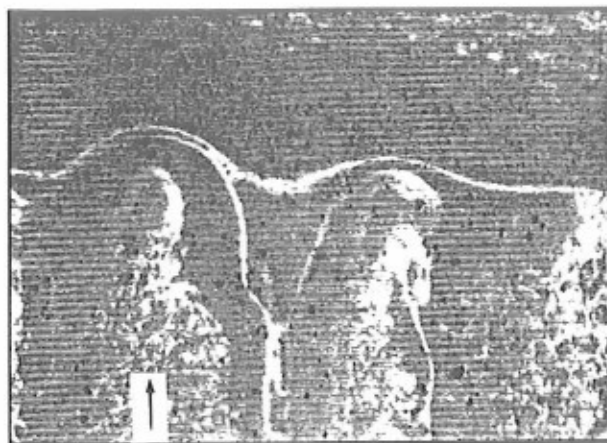
Figure 6: Photographs of shock tunnel convective ignition Test 157



a. Wave patterns on sample surface (pos. 2)



b. Wave patterns on sample surface (pos. 3)



c. Agglomeration of liquid (pos. 4)

50 μ m

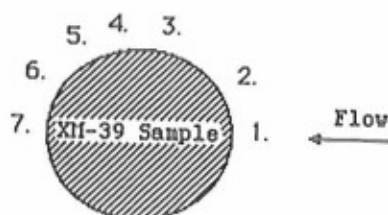


Figure 7: Microscopic photographs of sample surface (Test No. 147)

thermal energy input into the sample when the external heat source is lowered.

Once the steady-state test period has begun, the flow approaching the sample is laminar and the heat flux is much lower than in the initial transient period. The existence of uniform free-stream conditions which can be determined, provide a means of properly analyzing the data. From the correlation presented in Fig. 8, it is very obvious which samples were ignited by the high heating rates during the transient start-up time (Eqn. 3) and which were ignited by the uniform conditions of the nearly steady-state portion of the test (Eqn. 4).

The mechanism by which nitramine propellants ignite when subjected to crossflow heating conditions is very complex. There are three phases involved and the nature of each is not well understood. The liquid layer observed on the propellant surface could simply be melted ingredients of solid propellant or it could be a source of reacting material which is important to the ignition process. From

the literature this 'melting' has been observed many times but the actual composition of it is still open to argument. Discussed in the following paragraphs are several important characteristics which have been observed and are important to the ignition process.

The geometry of the sample allows examination of different flow regimes. Each of these regimes, numbered in Fig. 7, will be discussed separately. Position 1 corresponds to the stagnation point on the sample. At this point heating to the solid surface is relatively high compared to the remainder of the sample. Liquefaction and generation of gaseous pyrolysis products probably occurs in this region. Both the liquid and gases generated are carried into region 2 which includes laminar boundary layer development and the beginning of the transition region. Gas-phase reactions and possibly liquid-phase reactions could occur with heat feedback which generates more reactions within the two-film boundary layer and causing more liquefaction of the solid sample. Possibly important to this process is the amount of freestream oxidizer which

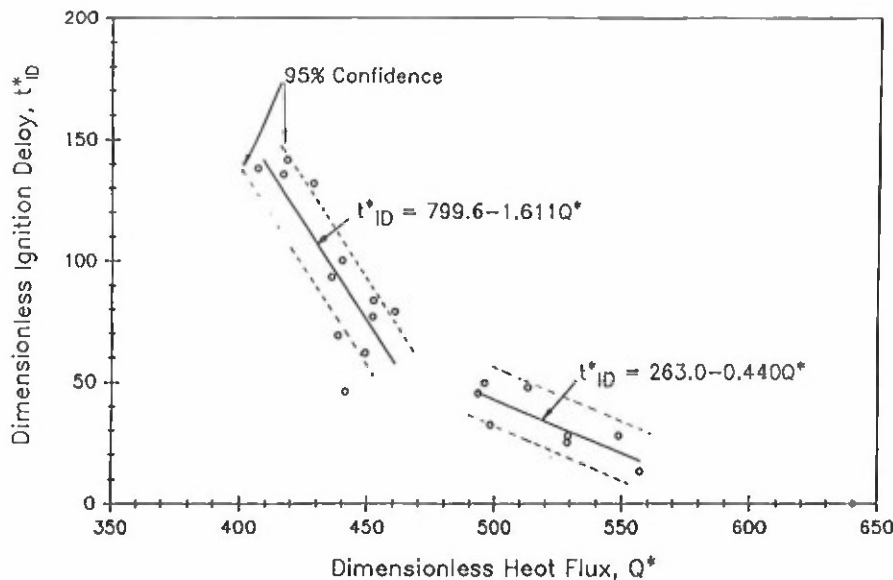


Figure 8: Correlation of Dimensionless Ignition Delay with Dimensionless Heat Flux

is entrained in the gaseous boundary layer.

Boundary layer transition to turbulence begins around position 3; the transition could be facilitated by the accumulation of liquid in the melt layer. Wave patterns on the recovered sample indicate the flow of liquid toward position 4. At position 4, the gaseous boundary layer separates. Upon separation, a small recirculation zone is formed in both the liquid and gaseous boundary layers. Experimental evidence suggests the flow of material from the front of the sample and reverse flow from the rear of the sample (position 5) increase the liquid layer thickness near the small recirculation zone. This growth of both boundary layers leads to the agglomeration of the liquid layer seen in Fig. 7c. The recirculation zones have high residence times and enough mixing of freestream oxidizer and pyrolysis products to generate ignition. It is believed that reactions between gaseous pyrolysis products generated at the front and rear surfaces of the sample react with freestream oxidizer in the gaseous recirculation zone. Heat feedback to the liquid and solid layers generates further pyrolysis gases which subsequently react until thermal runaway occurs and the sample ignites. The exact nature of the liquid layer and its role in the ignition process is unknown but it should not be ignored in the comprehensive understanding of the problem.

On the rear surface of the sample, positions 6 and 7, large recirculation zones create a stagnation point and laminar boundary layer which generate pyrolysis products and supply additional reactant species to the reaction zone. The interaction of the large recirculation zone with the small one is at position 5. Near this position another agglomeration of liquid is formed. The gaseous products generated along the rear surface contribute

to the ignition and combustion processes. As perceived from this study, the overall physical and chemical processes involved in convective ignition of a cylindrical XM-39 solid propellant grain is depicted in Fig. 9.

Conclusions

The following conclusions about the convective ignition of XM-39 propellant can be reached based on the results obtained and discussed above:

1. Convective ignition and flame spreading phenomena of XM-39 solid propellant has been successfully observed using a shock tunnel facility.
2. From observation, the sample surface can reach ignition due to incident and reflected shock wave heating during the transient start-up time of the test. The heating is very intense but very short in duration. However, if the thermal profile during this period is too thin to achieve self-sustained ignition, subsequent ignition could occur during the nearly steady-state operating time.
3. Microscopic analysis of recovered propellant samples shows the formation of a liquid layer. The composition of this liquid and its importance to the ignition process is still unknown and should be studied further.
4. Sustained convective ignition occurs in the region near the separation point of the boundary layer. Gas phase reactions in the ignition process of XM-39 propellant are important. Without freestream oxygen no ignition was observed.
5. During the test in which ignition was observed, the flame propagates from the shoulder region to the rear stagnation point. The sample acts as a flame holder; in the wake region the local

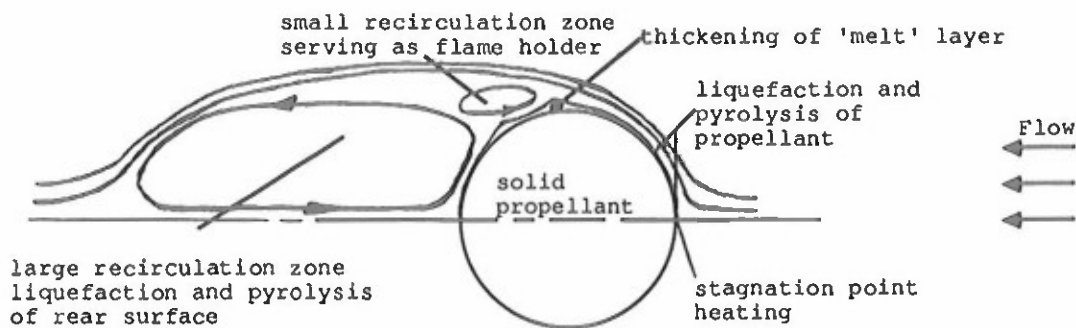


Figure 9: Major Physical and Chemical Processes Involved in Convective Ignition of a Cylindrical Solid Propellant Grain

flow velocity is reduced and the flame can sustain.

6. The luminous flame mostly remained on the downstream side of the sample in the recirculating wake. However, as the test chamber pressure was increased, the luminous flame could propagate upstream toward shoulder region of the sample. This is believed to be an effect of the higher heating rates to the front of the sample caused by the higher pressures.
7. A correlation between the dimensionless ignition delay time and a dimensionless heat transfer rate has been found.

1 Price, E.W., Bradley, H.H. Jr., Dehority, G.L., and Ibricic, M.M., "Theory of Ignition of Solid Propellants," *AIAA Journal*, Vol. 4, No. 7, July 1966, pp. 1153-1181.

2 Hermance, C.E., (1984) "Solid Propellant Ignition Theories and Experiments," *AIAA Progress in Astronautics and Aeronautics: Fundamentals of Solid Propellant Combustion*, edited by K. K. Kuo and M. Summerfield, Vol. 90, pp.239 - 304.

3 Kulkarni, A.K., Kumar, M., and Kuo, K.K., "Review of Solid Propellant Ignition Studies," *AIAA Paper* 80-120, June 1980; *AIAA Journal*, Vol. 20, No. 2, Feb. 1982, p. 243.

4 Boggs, T.L., "Thermal Behavior of RDX and HMX," *AIAA Progress in Astronautics and Aeronautics: Fundamentals of Solid Propellant Combustion*, edited by K. K. Kuo and M. Summerfield, Vol. 90, 1984, pp.121-175.

5 Boggs, T. L., Price, C. F., Atwood, a. I., Zurn, D. E., and Derr, R. L., "The Role of Gas Phase Reactions in Deflagration-to-Detonation Transition," *7th Symposium on Detonation*, Vol 1, June 1981, pp. 85-93.

6 Kim, J. U., Torikai, T., and Kuo, K. K., "Ignition Dynamics of Nitramine Composite Propellants under CO₂ Laser Heating," *AIAA Paper*

No. 87-0564, presented at the *AIAA 25th Aerospace Sciences Meeting*, Reno, Nevada, 12-15 January 1987.

7 Fetherolf, B. L., Kim, J. U., Litzinger, T. A., and Kuo, K. K., "CO₂ Laser-Induced Pyrolysis and Ignition Processes of Nitramine Composite Propellants," Poster Paper No. P228 of the *22nd Symposium (International) on Combustion*, Seattle, Washington, 14-19 August 1988, p. 325.

8 Kubota, N., "Survey of Rocket Propellants and Their Combustion Characteristics," *AIAA Progress in Astronautics and Aeronautics: Fundamentals of Solid Propellant Combustion*, edited by K. K. Kuo and M. Summerfield, Vol. 90, pp.1-52.

9 Stiefel, L. and Kuo, K. K., "Workshop Report: Ignition of Low Sensitivity Gun Propellant Charges," *25th JANNAF Combustion Meeting*, Huntsville, Alabama, 25 October 1988.

10 Stiefel, L. and Costello, J. C., "Ignition of 25mm Insensitive Propellant Charges: Studies of the Early Portion of the Pressure-Time Curve," *25th JANNAF Combustion Meeting*, Huntsville, Alabama, 24-25 October 1988.

11 Messina, N. A., Ingram, L. S., and Tricarico, S. A., "25mm Ballistic Simulator for XM919 Ignition System/Charge Design Studies," *25th JANNAF Combustion Meeting*, Huntsville, Alabama, 24-25 October 1988.

12 Rodriguez, L., "Ignition/Temperature Coefficient Study for HELOVA Propellant," Naval Ordnance Station, Indian Head, Report No. IHTR 1174, 27 May 1988.

13 Kashiwagi, T., MacDonald, B. W., Isoda, H. and Summerfield, M., "Ignition of Solid Polymeric Fuels by Hot Oxidizing Gases," *AMS Report No. 947*, October 1970.

14 Birk, A. and Caveny, L. H., "Convective Ignition of Propellant Cylinders in a Developing Cross-Flow Field," *MAE Report No. 1486*, Department of Mechanical and Aerospace Engineering, Princeton University, September 1980.

15 Wittliff, C. E., Wilson, M. R., and Hertzberg, A., "The Tailored-Interface Hypersonic Shock Tunnel," Journal of Aerospace Sciences, Vol. 26, No. 4, April 1959, pp. 219-228.

16 Knudsen, J.D. and Katz, D.L., Fluid Dynamics and Heat Transfer, McGraw-Hill, New York, 1958.

17 Ritchie, S.J., Hsieh, W.H. and Kuo, K.K., "Convective Ignition of LOVA Propellants Subjected to Crossflow Heating Conditions," 26th JANNAF Combustion Meeting, J.P.L., Pasadena, Calif., 23-27 October 1989.

Appendix F

UNCLASSIFIED

CONVECTIVE IGNITION OF LOVA PROPELLANTS*

S.J. Ritchie†, W.H. Hsieh§, and K.K. Kuot
Department of Mechanical Engineering
The Pennsylvania State University
University Park, PA 16802

ABSTRACT

Crossflow convective ignition tests of ROX-based LOVA solid propellant were carried out in air and nitrogen using a shock tunnel facility. Test conditions were in the range of pressure: 1.38 - 3.45 MPa (200 - 500 psia), temperature: 1100 - 1500 K (1980 - 2700°R) and flow velocity: 60 - 150 m/s (197 - 492 ft/s). Under these conditions, ignition was observed at or very near the sample surface in the region just beyond the gaseous boundary layer separation point only when oxidizer was present in the freestream flow. Ignition delay time, determined using a multi-channel photomultiplier tube detection system, was correlated to a dimensionless convective heat flux calculated using the flow conditions over the test sample. Post-test microscopic analysis of samples indicated the formation of an apparent liquid layer on the sample surface which grows in thickness near the flow separation location. The existence of numerous near-circular, crater-like holes was detected using scanning electron microscopy. The rims of these holes exhibit surface reactions and phase changes. The physical interactions between the flow and the test sample are discussed in detail to provide insight into the complex ignition process. Overall, the ignition mechanism is believed to be gas-phase in nature rather than a surface reaction mechanism.

INTRODUCTION

Of interest, in recent years, are solid propellant formulations based on nitramine ingredients such as ROX and HMX. These materials display high thermal stability and low sensitivity to ballistic vulnerability making them ideal candidates for low vulnerability ammunition (LOVA) propellants. Related to the LOVA characteristic of nitramine-based propellants, is the problem of achieving consistent ignition when it is desired. An understanding of the complex physicochemical processes which characterize the ignition transient is necessary if safe, reliable igniters are to be designed for propulsion systems which use these propellant types.

The purpose of this paper is to present the experimental results of an ignition study on ROX-based LOVA solid propellants when subjected to convective heating by a uniform high temperature, high pressure gas stream. The test geometry is a solid propellant cylinder subjected to perpendicular crossflow. Although laser radiative tests provide greater control over heat flux input and other parameters such as ambient pressure, the convective ignition test is more closely related to the actual ignition process used in many gun systems where propellant ignition is obtained via hot gases from the igniter. It is hoped the fundamental information gathered from this study of the complex ignition processes in a relatively simple flow field can be later used to better understand and predict the ignition response of ROX-based propellant in more practical combustion or propulsion scenarios. Background information on nitramine propellant ignition and combustion applicable to this program can be found in earlier papers by Ritchie et al.^{1,2}

The experimental objectives are to (1) visually examine the convective ignition phenomenon and subsequent flame spreading of RDX-based XM-39 propellant using high-speed video photography, (2) measure ignition delay (based on light emission from the sample) and examine possible correlations to convective flow parameters and (3) microscopically examine recovered propellant samples to determine the heating and burning effects on sample surfaces. The goal of this paper is to use the above observations and data to identify important

*This work was performed under Contract Number DAAL03-87-K-0064 under the sponsorship of the Army Research Office, Research Triangle Park, North Carolina. The program manager is Or. David Mann. His support of this research is greatly appreciated.

†Ph. O. Candidate

§Assistant Professor

‡Distinguished Professor

Approved for public release, distribution is unlimited.

UNCLASSIFIED

processes involved in the ignition of XM-39 LOVA propellant. This insight will provide guidelines for eventual theoretical model development.

METHOD OF APPROACH

SHOCK TUNNEL/CONVECTIVE IGNITION TEST FACILITY

A more detailed discussion of the shock tunnel facility can be found in Ritchie et al.^{1,2}, Birk³, Kashiwagi⁴. Very briefly, the shock tunnel is used to create a reservoir of high-temperature, high-pressure gas which, in turn, induces a flow through the test section and across the sample. The test section, a cross-section side view is shown in Fig. 1, is a 2.86 cm x 2.86 cm (1.125 in. x 1.125 in.) square duct. Quartz windows located on the top and sides of the test section (side windows not shown in the figure) provide optical access. Perforated plates are located at both the upstream entrance and downstream exit. The downstream exit plate acts as a nozzle which chokes the flow and controls the gas velocity through the test section. The upstream perforated plate is used to damp out initial pressure oscillations caused by the interaction of the incident shock wave with the sample and to protect the test sample from large pieces of burst diaphragm debris.

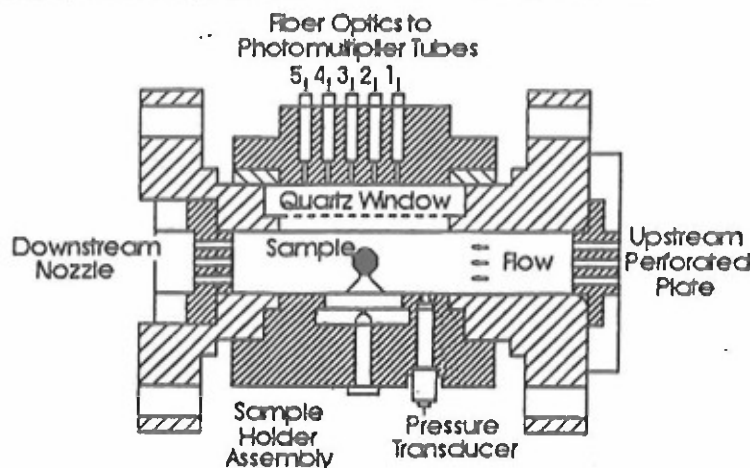


Figure 1: Cross-sectional side view of test section

Through control of the areas open to the flow on both the upstream perforated plate and downstream nozzle, the initial driver gas to driven gas pressure ratio and the initial pressure in the driven section, the shock tunnel is capable of producing a wide range of test conditions: pressures of 1.03 - 4.14 MPa (150 - 600 psia), temperatures of 950 - 1500 K (1710 - 2700 °R), and velocities of 60 - 250 m/s (197 - 820 ft/s). These values were measured in separate calibration tests using an LDV system and a shielded thermocouple. The major limitation of the shock tunnel facility is the test time available. The maximum time available is ~18 ms but for most flow conditions the ignition delay time is much shorter.

Diagnostics for ignition tests include: pressure transducers along the shock tunnel driven section to detect the shock wave arrival at fixed locations from which the incident shock wave speed is deduced, a pressure transducer located in the test section upstream of the sample (see Fig. 1), and five filtered RCA 1P28 photomultiplier tubes which measure light intensity in the near ultraviolet centered around 0.3700 μm are used remotely via fiber optic tubes (see Fig. 1) to measure ignition delay. High-speed visualization is accomplished through side windows using a high-speed Kodak Spin Physics SP2000 video system with backlighting of the sample.

TEST SAMPLE

The propellant used for this study was XM-39 (Lot #A5-1184-113) which contains a significant amount of RDX. The grain geometry is cylindrical in shape with a nominal diameter of 0.7 cm (.275 in.) and length of 0.74 cm (.291 in.). The condition of the samples was not uniform for all tests: the diameter was not constant from grain to grain, the shape of individual samples was never a perfect cylinder and the surface was pitted and graphite

coated. In order to try and maintain more uniformity in the tests, each propellant grain was trimmed to a constant length of 0.74 cm (.291 in.), the graphite coating was removed, and the surface was polished until it was visually smooth.

The sample was mounted in the test section with the induced flow perpendicular to the length of the grain. Mounting was accomplished by drilling a hole along the center axis of the cylindrical sample. A stainless steel rod is inserted through this hole and attached to end holders. The difference between the test section width, 2.86 cm (1.125 in.), and the sample length is occupied by inert spacers on both sides so the flow would 'see' essentially one long cylinder stretching across the entire test section. This was done to try and minimize end burning effects from the test.

RESULTS

Two sets of tests have been carried out with XM-39 LOVA propellant. The first used nitrogen as the test gas in the low velocity range of the shock tunnel, ~65 m/s (213 ft/s). No ignition or luminous flame was detected for these tests by either the video or the photomultiplier tubes. The second set was carried out in the same velocity range using air as the test gas. The conditions for the second set of tests is given in Table I. This table lists the incident shock wave Mach number, measured test section pressure, temperature, Mach number, Reynolds number, Prandtl number, Nusselt number, ignition delay time (t_{ID}) and dimensionless ignition delay (t^*_{ID}). t^*_{ID} is defined as $t_{ID}/(D/V)$; it represents the ratio of ignition delay time to the flow residence time based on the sample diameter and the approach velocity. The Nusselt number⁵ is calculated using the following formula for flow over a cylinder:

$$Nu = .027 Re_D^{.805} Pr^{.331} \quad (1).$$

In many cases, light emission from the sample was detected very early (< 3 ms) during the shock tunnel transient start-up time. During this start-up time, the shock wave arrives at the test section and heating rates are highest. However, this 'transient' ignition was not always able to sustain burning for the entire test time because the heating rates decrease sharply with the onset of the quasi-steady flow through the test section. The sample, once quenched, would usually, but not always, reignite later during the steady-state convective heating period and sustain burning until the end of the test time. It is this second ignition point which has been labeled the ignition delay time (t_{ID}). The ignition delay was determined through analysis of both the photomultiplier tube output (100,000 data points per second) and the high-speed video pictures (6,000 pictures per second).

The sequence of events was very similar for all tests in which ignition was observed. These observations have been well documented previously^{1,2} so only a brief description is given here. Figure 2 contains pressure vs. time (Fig. 2a) and photomultiplier tube output vs. time (Fig. 2b) plots as well as photographs taken from the high speed video showing the location where first visible light is observed (Fig. 2c).

The pressure-time trace can be divided into two sections. The 'transient starting time' begins with the incident shock wave arrival. Interaction of the incident wave with the sample and nozzles leads to pressure oscillations and turbulent flow conditions around the sample. In the subsequent 'quasi-steady test time', the pressure does not oscillate but slowly increases from a minimum value of 1.45 MPa (210 psia) to a maximum value of 2.00 MPa (290 psia). This corresponds to a 27% increase in pressure over the test duration. This variation, unfortunately, is unavoidable so an average pressure value is used in all calculations and in the presentation of results. Although undesirable, the pressure value during the majority of the test can be considered quasi-steady with tolerable variations.

The large initial deflection in the photomultiplier trace corresponds to the incident shock wave arrival in the test section (time = 0). The deflection in the photomultiplier signal due to the onset of sustained ignition is seen at 10.835 ms (t_{ID}). The rarefaction wave arrives at the test section after ~17.82 ms. The light intensity from the burning is altered slightly at this time but the sample does not completely extinguish until 19.650 ms after the first pressure rise in the test section.

TABLE I: Summary of Test Conditions and Results for XM-39 Solid Propellant in Air

Data Set Two

Test No	Shock Mach No.	Test Section Pressure		Temperature		Reynolds Number	Prandtl Number	Nusselt Number	Mach Number	tID (ms)	t*ID (-)
		MPa	(psia)	(K)	(R)						
050	3.88	3.79	(550)	1420	(2556)	71441	0.699	193.5	0.071	0.00	0.00
051	3.81	1.72	(250)	1385	(2493)	43376	0.705	129.9	0.094	7.33	76.8
053	3.87	1.72	(250)	1415	(2547)	41506	0.700	125.1	0.094	7.27	78.9
055	3.85	1.59	(230)	1405	(2529)	40004	0.702	121.6	0.096	9.41	93.5
056	3.92	1.64	(238)	1440	(2592)	39698	0.696	120.4	0.095	None	--
058	3.87	2.78	(403)	1415	(2547)	59061	0.700	166.2	0.082	1.50	13.2
059	3.97	2.56	(371)	1460	(2628)	54877	0.692	153.7	0.084	3.17	28.0
060	3.79	2.49	(361)	1375	(2475)	58122	0.707	164.6	0.086	2.82	25.0
061	3.78	2.49	(361)	1375	(2475)	59058	0.707	166.8	0.086	3.17	27.7
062	3.64	2.34	(340)	1305	(2349)	59667	0.718	168.9	0.088	5.64	50.0
063	3.93	2.32	(337)	1445	(2601)	51066	0.695	147.5	0.087	5.17	48.0
064	3.70	2.34	(340)	1335	(2403)	58309	0.713	165.4	0.089	3.64	32.6
065	3.90	2.03	(294)	1430	(2574)	45987	0.698	135.7	0.090	8.59	83.7
066	3.41	2.32	(337)	1200	(2160)	65898	0.728	184.0	0.091	11.46	100.6
067	3.60	1.79	(260)	1270	(2286)	48929	0.720	144.1	0.094	14.55	138.7
068	3.58	2.65	(385)	1280	(2304)	65775	0.721	183.1	0.085	5.33	45.6
145	3.80	1.03	(150)	1340	(2412)	29905	0.712	96.6	0.103	None	--
146	3.75	1.86	(270)	1360	(2448)	48305	0.710	142.0	0.093	None	--
147	3.98	1.86	(270)	1465	(2637)	42716	0.691	127.5	0.091	6.28	54.4
148	3.37	2.41	(349)	1180	(2124)	69814	0.728	192.7	0.090	13.59	115.9
149	4.02	1.31	(190)	1435	(2583)	33664	0.697	105.6	0.099	None	--
150	3.96	2.13	(309)	1455	(2619)	48587	0.693	141.6	0.089	4.91	46.0
151	3.86	2.13	(309)	1410	(2538)	50089	0.701	145.6	0.089	3.87	35.9
153	3.60	2.13	(309)	1290	(2322)	55726	0.720	160.0	0.091	13.04	121.9
154	3.42	2.13	(309)	1205	(2169)	62743	0.728	176.9	0.093	15.40	137.8
156	3.91	1.86	(270)	1430	(2574)	45019	0.697	133.4	0.092	8.61	83.0
157	3.75	2.13	(309)	1355	(2439)	53424	0.710	154.0	0.090	7.30	67.6
158	3.93	2.41	(349)	1445	(2601)	53525	0.695	153.2	0.086	3.06	28.1
159	3.81	2.41	(349)	1385	(2493)	55952	0.705	159.5	0.087	5.30	48.1
160	3.75	2.41	(349)	1360	(2448)	57511	0.710	163.4	0.087	6.83	60.3
161	3.60	2.41	(349)	1290	(2322)	61592	0.720	173.5	0.088	12.07	105.0
162	3.40	2.41	(349)	1195	(2151)	67442	0.728	187.5	0.090	15.52	134.3
163	3.79	1.86	(270)	1375	(2475)	46963	0.707	138.7	0.093	10.55	100.6
164	3.58	1.86	(270)	1280	(2304)	51827	0.721	151.1	0.095	15.61	147.1
165	4.22	1.59	(230)	1565	(2817)	35472	0.685	131.9	0.095	7.41	75.2
166	3.74	1.59	(230)	1355	(2439)	40808	0.710	127.6	0.096	12.66	124.2

Shown in the high speed images are, the propellant sample at three different times: (1) prior to the test ($t=0$), (2) after a luminous region is first observed at a location approximately $+90^\circ$ from the leading edge ($t=11.334$ ms), and (3) after flame spreading has covered the downstream surface ($t=13.334$ ms). The convective stream is moving from right to left in all pictures.

Photographs from an optical microscopic study (magnification = 50X) of a recovered propellant sample are shown in Fig. 3. A detailed description of each photograph is given due to the limited resolution of the reproduction. At the front stagnation point, position A, the surface is slightly pitted and many small particles from the shock tunnel burst diaphragm are imbedded in the surface layer. Between 30° and 45° from the leading edge at location B, small wave formations appear on the surface indicating the formation of a liquid 'melt' layer. The wave formations could be created by bubble formation and the complex flow structure on the propellant surface or it could be due to the existence of some freestream turbulence generated by the upstream perforated plate. These wave formations grow in size between 45° and 90° from the leading edge at location C. Just beyond the 90° point at region D, there is a large liquid agglomeration on the surface. The position of this liquid formation coincides very closely to the first reaction location as seen on the video. Although it is not easily discernible in the photographs, there are many bubbles entrained within this agglomeration. A second agglomeration which is slightly smaller than the one at $\sim 95^\circ$ can be seen at $\sim 105^\circ$ from the leading edge in region E. The back surface (region F) and

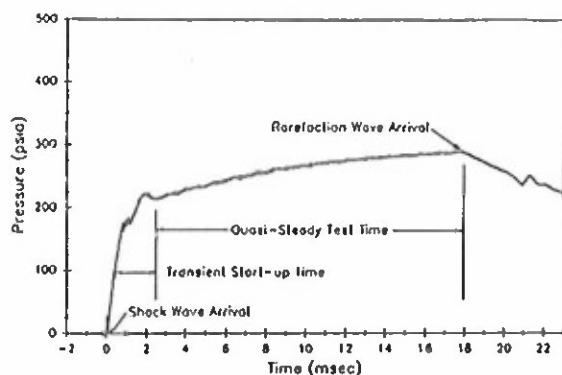


Figure 2a: Typical test section pressure versus time trace (Test 155).

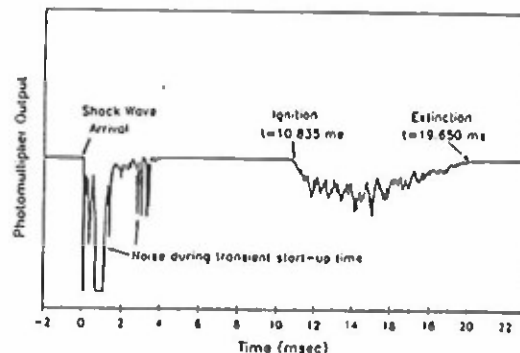


Figure 2b: Typical test section photomultiplier tube output versus time trace (Test 155).

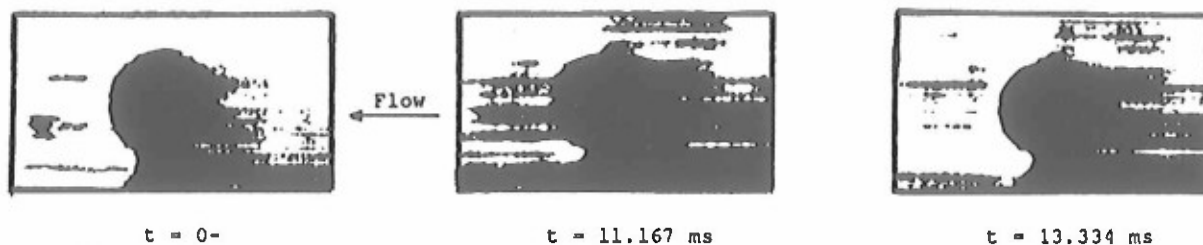


Figure 2c: High-speed video images from a typical convective ignition test firing (Test 155)

rear stagnation point (region G) are similar to the front surface only free of particles and shock tunnel debris. The only easily distinguishable difference between the burned and unburned samples is the coloring. Burned samples exhibit a darker shade of yellow/white (particularly on the downstream side and at the agglomeration points) while the unburned samples more closely resemble the original white coloring of the propellant. Unfortunately this is only distinguishable under actual viewing conditions and is not clearly visible in the photographic representation.

A scanning electron microscope (SEM) was used to examine the sample surface under even higher magnification. These photographs are shown in Fig. 4. The first two pictures show a pretest propellant surface (Fig. 4a and 4b). The surface, although it had been polished, is actually quite rough when examined under very high magnification (1600X). The next series of photographs are of a sample which has ignited under convective heating conditions. The letter associated with each photograph corresponds to the general area highlighted in Fig. 3. Note: the area covered by the photograph does not correspond to the area of the square box on the top view of the sample in Fig. 3 and the magnification used for each photograph is not the same. The magnification was chosen to highlight particular structures on the sample surface.

Figure 4c shows the front stagnation region A. The surface in this region, and over the entire propellant surface, is very rough with many rice-like structures which have an approximate diameter of $4\text{ }\mu\text{m}$. Scattered randomly about this region are small circular holes, often appearing in small groups. Further along the sample, in region B, the surface appears similar to the stagnation region (see Fig 4d). However, the surface structures are less independent and appear to have agglomerated into larger clumps. There are still holes in the surface but these do not appear as frequently as in the front stagnation zone.

Each photograph covers
a .50 mm x .50 mm area
(~.020 in. x .020 in.)

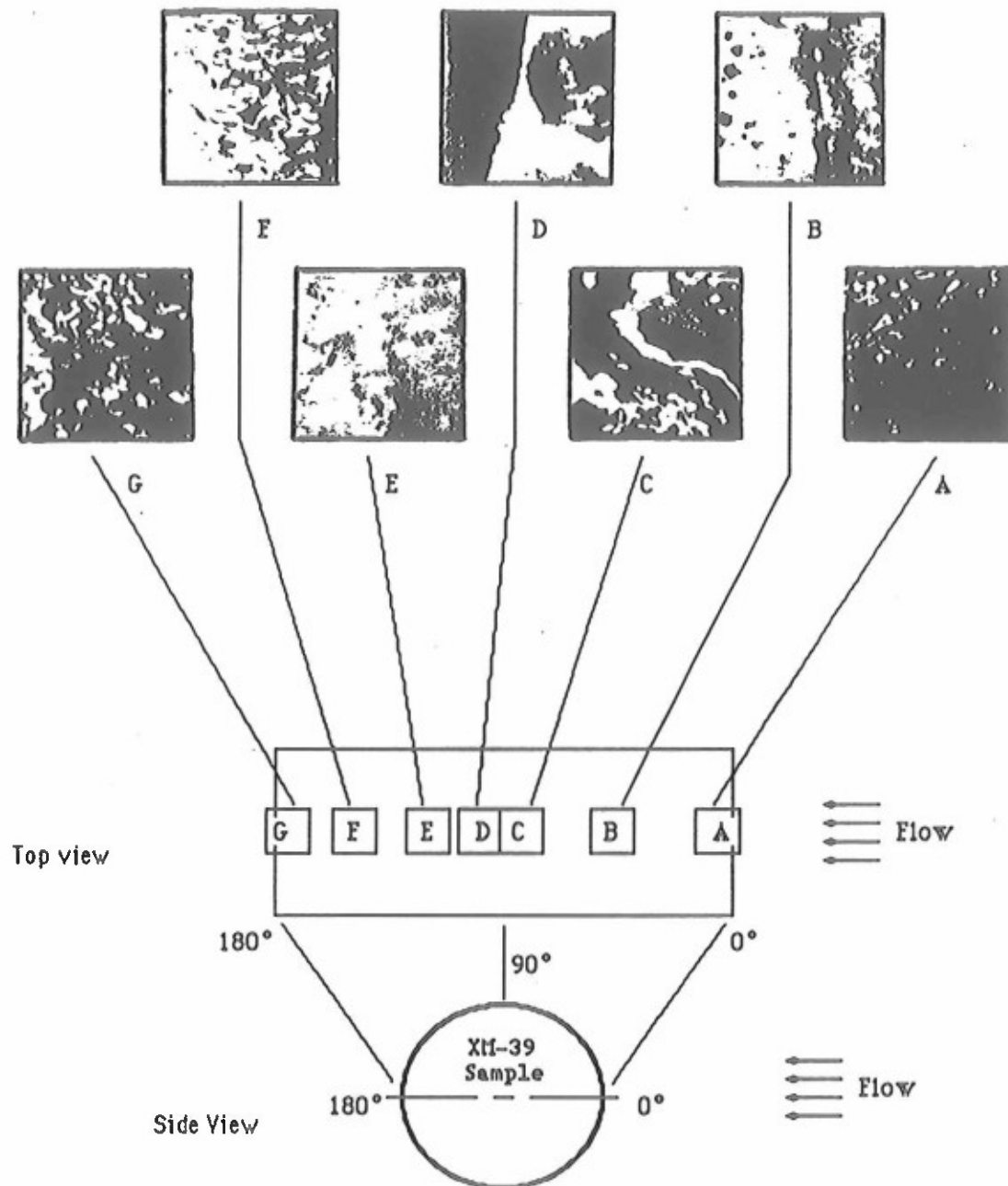


Figure 3: Photographs of magnified post-test propellant surface (mag.=50X)

At position D, where the large agglomeration forms on the sample surface, Fig. 4e clearly shows a change in the surface structure. At the ridge of the agglomeration the individual rice-like shapes have become very closely grouped and have apparently 'melted' together. Again there are circular holes located in close proximity to the ridge region but not in large quantities. Just downstream from the agglomeration region, near E, there is a very densely packed, large number of circular holes (see Fig. 4f). Some of these holes display a whitish edge indicating a change in the physical nature of the material probably due to phase changes and chemical reactions. The structure of these crater-like holes was examined under even greater magnification (1600X) and is shown in Fig. 5. Further along the sample in region F and at the rear stagnation point G, the surface has the same description as the leading edge locations, A and B.

DISCUSSION

IGNITION DELAY CORRELATION

One of the major objectives was to find a correlation between the ignition delay time for XM-39 LOVA propellant and the freestream flow parameters: pressure, temperature and velocity. If the chemistry is relatively fast, the ignition delay should depend almost entirely on the heat-up for the solid material and a correlation based on the heat flux into an inert cylinder should provide reasonable results. This analysis is very similar to that used in presenting data from radiative ignition tests. The average nondimensional heat flux term (Q^*) was calculated using the following formula:

$$Q^* = Nu \left[\frac{(T_s - 480 \text{ K})}{T_m} \right] \left[\frac{(T_s + 480 \text{ K})}{2(T_m)} \right]^{1/2} \quad (2)$$

The first term is the average Nusselt number calculated using Eq. (1). The second term compensates for the temperature difference between the propellant surface and the freestream flow. The third term accounts for changes in the conductivity of air at the film temperature. The value of 480 K was chosen as a surface temperature because it is close to the melting or liquefaction temperature for RDX quoted in the literature⁶. In the correlation development, the reference temperature was taken to be 273 K. The dimensionless ignition delay time for data set two is plotted against the dimensionless heat flux in Fig. 6. If the all data points are considered together, there is a significant amount of scatter in the results. This scatter is significantly reduced if the tests which display clear evidence of propellant end-surface burning (in the gaps between the sample and the inert spacers) are separated from the tests which did not. Evidence of end-surface burning is easily found during the post-test microscopic analysis of the sample surface. Based upon the above distinction, there are two families of data shown in the same plot (Fig. 6). Correlation equations for these two families of data are given below:

Surface ignition, $t^*_D = 494.7 - 21.24 Q^*$

End/Gap ignition, $t^*_D = 472.5 - 21.94 Q^*$

At a given heat flux, the end or gap ignition process has a shorter ignition delay time than the surface ignition process. This is reasonable because hot gases from the convective stream cause the edge regions of the propellant to reach ignition conditions sooner than the surface region. This type of edge enhanced ignition has been studied previously by Vorsteveld and Hermance⁷. When the end surfaces of the propellant grain are in close contact with the spacers, the edge effect is eliminated resulting in a longer ignition delay time.

When the possibility of end- or edge-ignition is accounted for, the resulting data correlate very well. The small amount of data scatter could be due to one or more of the following reasons: (1) the surface and shape of the test samples were not as consistent as would have been desired. Imperfections created during the manufacturing process and during the removal of the graphite coating could lead to variations in the measured results; (2) the correlations make no allowance for changes in the sample surface condition such as the presence of circular holes and the rice-like structures; (3) the high heating rates to the propellant during interaction with the incident shock wave are not considered; and (4) there

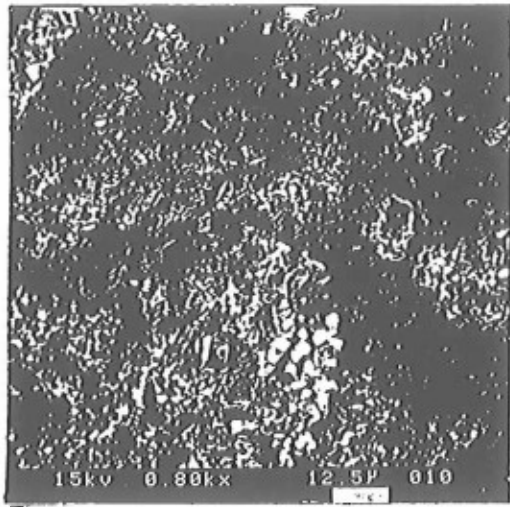


Figure 4a: Unburned XM-39 LOVA propellant - graphite coating removed, surface polished. (magnification = 800X)

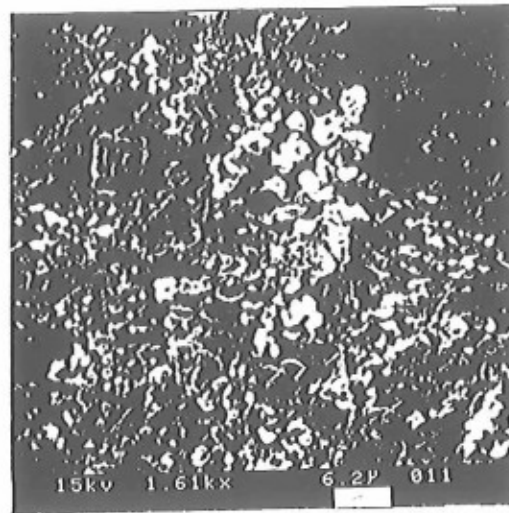


Figure 4b: Unburned XM-39 LOVA propellant - graphite coating removed, surface polished. (magnification = 1600X)

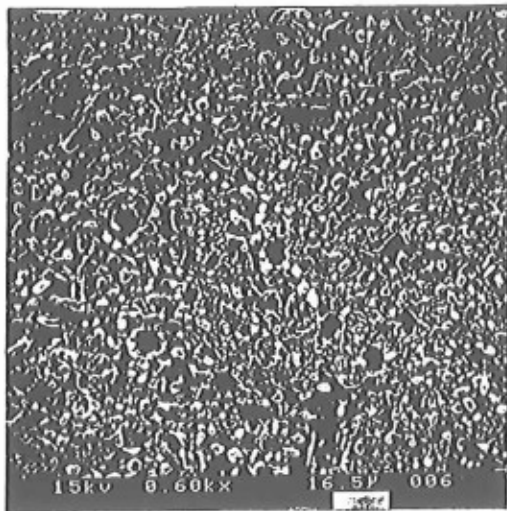


Figure 4c: Burned XM-39 LOVA propellant - Upstream stagnation region A. (magnification = 600X)

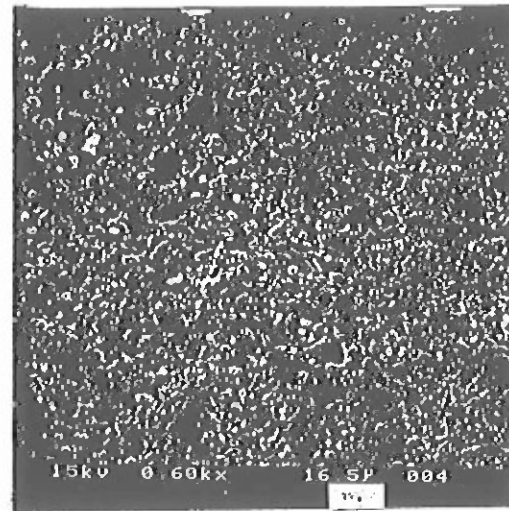


Figure 4d: Burned XM-39 LOVA propellant - Upstream surface B. (magnification = 600X)

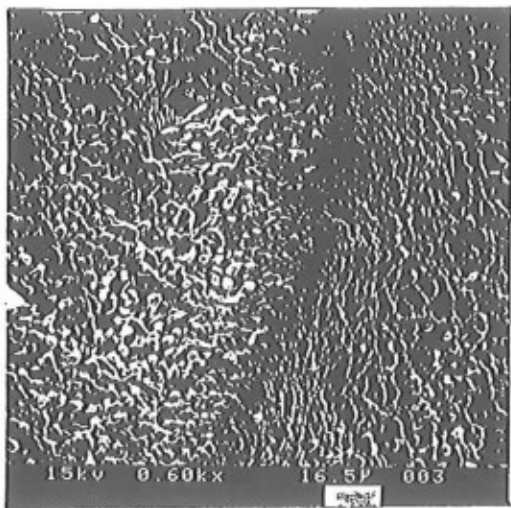


Figure 4e: Burned XM-39 LOVA propellant - liquid agglomeration at location D. (magnification = 600X)

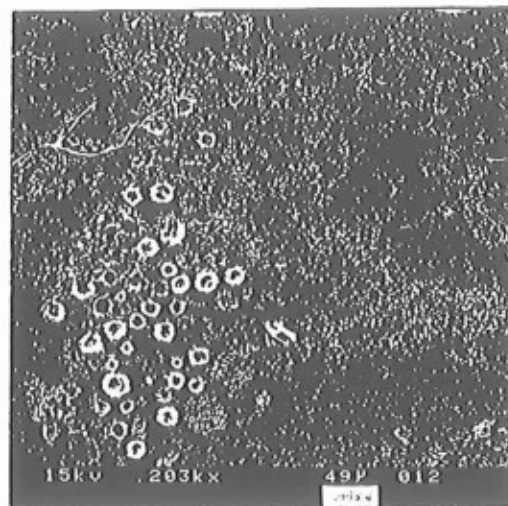


Figure 4f: Burned XM-39 LOVA propellant - Crater-like structures near region E. (magnification = 200X)

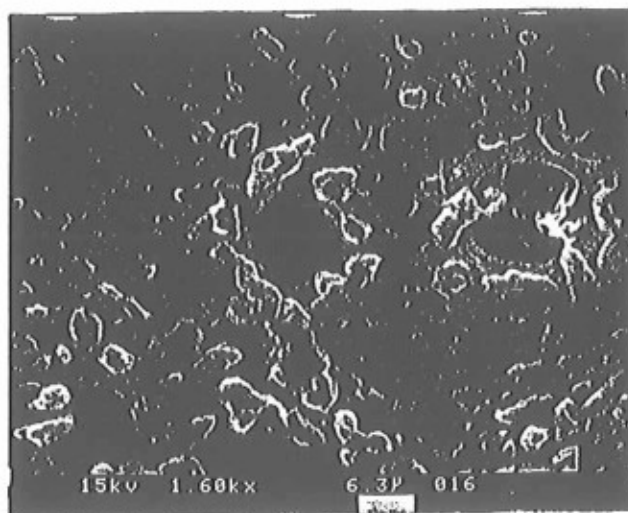


Figure 5: Circular, crater-like holes located at position E. (magnification = 1600X)

is no consideration given to possible heat feedback from exothermic chemical reactions in the gas, solid or liquid phases.

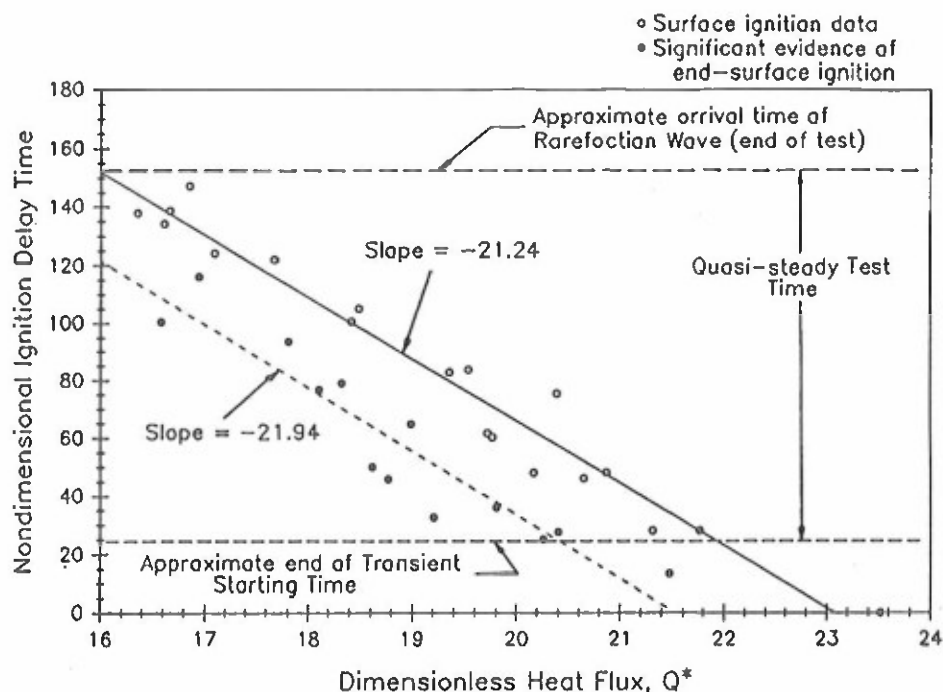


Figure 6: Dimensionless ignition delay time versus dimensionless heat flux

PHYSICAL AND CHEMICAL CHARACTERISTICS OF CONVECTIVE IGNITION

The convective ignition of XM-39 LOVA propellant involves many complex physical and chemical processes. Based on the observations made during this study, the following summary describes in detail many of these processes which lead to ignition under the conditions imposed by the shock tunnel convective ignition test.

Due to the nature of the shock tunnel test apparatus, a transient flow settling or start-up time exists which lasts ~3 ms. During this start-up time, heat flux to the sample is very large because of incident shock wave interactions, flow reversals and turbulent flow conditions around the sample. The complexity of the flow makes interpretation of data obtained during this period very difficult. However, the importance of this period should not be neglected. The propellant surface temperature rises very rapidly during these first few milliseconds and liquefaction, decomposition and vaporization of solid material can occur prior to the start of the quasi-steady flow test time. It is assumed, due to the brevity of the settling time, the thermal profile in the sample is quite thin. For self-sustained ignition to occur during this time, heat feedback from the reaction zones must maintain the thermal energy input into the sample when the external heat source is reduced. If ignition can not be supported when the high heat flux period ends, the thermal profile should adjust quickly to the new ambient heating conditions.

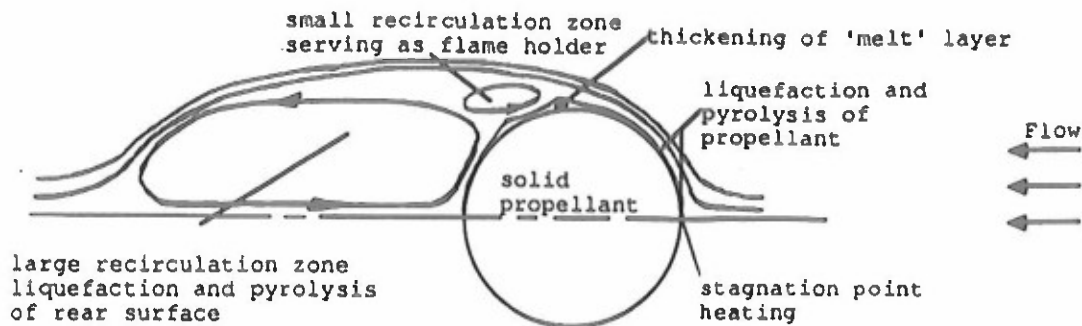


Figure 7: Major physical and chemical processes involved in convective ignition of a cylindrical solid propellant grain

By the time the flow in the test section has settled into a quasi-steady state, many physical processes have already occurred. These include liquid 'melt' layer formation and some solid propellant decomposition or evaporation into the gas phase. The conditions which exist and lead to the eventual ignition during the steady flow time are discussed relative to the regimes shown in Fig. 7.

At the leading edge, stagnation flow conditions exist. This region is characterized by very high heat flux into the solid material from the external flow and local pressure values are at a maximum. The high heating rates lead to liquefaction, decomposition and vaporization of the solid material which form liquid and gaseous boundary layers on the sample surface. Small circular holes have been observed on the upstream surface. These holes can be attributed to possible foreign particle impingement, dewetting of propellant crystals from the surface region, and fast pyrolysis of local active sites.

Within the gaseous boundary layer formed along the upstream circumferential surface, oxidizer from the freestream mixes and reacts with pyrolysis products from the propellant. The heat generated along with continued heating from the freestream can sustain continued pyrolysis, vaporization and liquefaction of the solid surface. At the gas-liquid interface, vaporized and decomposed propellant is added to the gaseous boundary layer as the heating continues from both the external convective stream and heat feedback from chemical reactions which could occur in both the gaseous and condensed phases. The 'liquid' boundary layer is highly non-uniform. Gaseous bubbles are formed within the liquid layer and at the solid-liquid interface as the propellant vaporizes and decomposes. These bubbles are carried within the liquid 'melt' layer until eventually they reach the gas-liquid interface. These bubbles could be the reason for the flow structures described previously (see Fig. 3). At the liquid-solid interface the propellant, as it is heated, undergoes liquefaction, vaporization and decomposition. In addition, the liquid layer appears to form around solid structures which resemble rice kernels when observed with a SEM.

Gaseous boundary layer separation occurs around 80° to 85° from the leading edge. Just beyond this separation point, flow reversals in the gas phase increase mixing. Since the liquid layer is driven by the shear force of the gaseous flow, the flow reversal in the gaseous layer leads to a flow reversal in the liquid layer thus increasing the mixing and the heat transfer to the solid propellant surface. Processes which were occurring in the boundary layer continue but the heat flux from the convective stream and the local pressure at the sample surface are now at their minimum values. Eventually recirculation zones are formed in both the gaseous flow and the predominantly liquid boundary layer which grows significantly in size forming the agglomeration seen in Figs. 3 and 4e. Ignition occurs within this flow region due to the long residence time and increased mixing of the pyrolysis products, vaporized propellant, and freestream oxidizer in the gaseous phase. The gas-phase reactions locally increase the heating rates into the liquid and subsequently the solid phase and thus achieve self-sustained combustion. In this region a large number of the crater-like holes

are observed on the propellant surface. It is postulated that these represent the location of very active crystals of RDX which gasify and react.

On the downstream surface of the sample the large recirculation zones formed in the wake create a rear stagnation point and subsequently a boundary layer flow. These areas develop much as the forward areas do and supply additional reactant species to the reaction zone located just beyond the boundary layer separation point. At a point near 110° from the leading edge the boundary layer formed on the rear surface interacts with the separation region. Near this position another agglomeration of liquid is formed as the boundary layer thickens. The gaseous products generated along the rear surface contribute to the ignition and combustion processes.

SUMMARY AND CONCLUSIONS

The following conclusions about the convective ignition of XM-39 LOVA propellant can be reached based on the results obtained and discussed above:

1. Convective ignition and flame spreading phenomena of XM-39 solid propellant has been successfully observed using a shock tunnel facility. Strong evidence of gas-phase ignition mechanism has been experimentally observed. Sustained convective ignition occurs in the region near the boundary layer separation point.
2. Two possible sites of ignition have been identified: circumferential surface ignition and edge surface ignition. Two separate correlations have been developed for these two types of ignition phenomena.
3. From observation, the sample surface can reach ignition due to incident and reflected shock wave heating during the transient start-up time of the test. The heating is very intense but very short in duration. However, if the thermal profile during this period is too thin to achieve self-sustained ignition, subsequent ignition could occur during the nearly steady-state operating time.
4. Microscopic analysis of recovered propellant samples shows the formation of a liquid layer. The composition of this liquid and its importance to the ignition process is still unknown and should be studied further.
5. After ignition the flame propagates from the shoulder region to the rear stagnation point. The sample acts as a flame holder; in the wake region the local flow velocity is reduced and the flame can sustain.

1 Ritchie, S.J., Hsieh, W.H., and Kuo, K.K., "Convective Ignition of LOVA Propellants Subjected to Crossflow Heating Conditions," 26th JANNAF Combustion Meeting, 23-27 October 1989 Pasadena, CA, CPIA Publication 529, Vol. I, pp. 1-12.

2 Ritchie, S.J., Hsieh, W.H., and Kuo, K.K., "Convective Ignition Phenomena of LOVA Propellants," AIAA Paper 90-2194, AIAA/SAE/ASME/ASEE 26th Joint Propulsion Conference, Orlando, FL, 16-18 July 1990.

3 Birk, A. and Caveny, L.H., "Convective Ignition of Propellant Cylinders in a Developing Cross-Flow Field," MAE Report No. 1486, Department of Mechanical and Aerospace Engineering, Princeton University, September 1980.

4 Kasiwagi, T., MacDonald, B.W., Isoda, H. and Summerfield, M., "Ignition of Solid Polymeric Fuels by Hot Oxidizing Gases," AMS Report No. 947, October 1970.

5 Knudsen, J.D. and Katz, D.L., Fluid Dynamics and Heat Transfer, McGraw-Hill, New York, 1958.

6 Boggs, T.L., "Thermal Behavior of RDX and HMX," AIAA Progress in Astronautics and Aeronautics: Fundamentals of Solid Propellant Combustion, edited by K.K. Kuo and M. Summerfield, Vol 90, 1984, pp. 121-175.

7 Vorsteveld, L.G. and Hermance, C.E., "Effect of Geometry on Ignition of a Reactive Solid: Square Corner," AIAA Journal, Vol. 25, No. 4, April 1987, pp. 592-597.

Appendix G

An Experimental Ignition Study of RDX-Based Solid Propellant Grains Subjected to Crossflow Convective Heating

Steven J. Ritchie[#], Wen-Hsin Hsieh[§], and Kenneth K. Kuo[†]
The Pennsylvania State University, University Park, PA 16802

Abstract

Crossflow convective ignition tests of RDX-based XM-39 LOVA solid propellant grains were carried out in air and nitrogen using a shock tunnel facility. Test conditions were in the range of pressure: 1.38 - 3.45 MPa (200 - 500 psia), temperature: 1100 - 1500 K (1980 - 2700°R) and flow velocity: 60 - 70 m/s (197 - 230 ft/s). In the tests carried out in air, ignition was observed at or very near the sample surface in the region just beyond the gaseous boundary layer separation point. No ignition was observed for the tests carried out in nitrogen. Ignition delay time was correlated to a dimensionless convective heat flux calculated from flow parameters. Post-test microscopic analysis of samples indicated the formation of an apparent liquid layer on the exposed surface which grows in thickness in the vicinity of the flow separation location. The existence of numerous near-circular, crater-like holes was detected using scanning electron microscopy. The rims of these holes exhibit evidence of surface reactions and phase changes. The physical interactions between the flow and test sample are discussed to provide insight into the complex ignition process. The ignition mechanism is believed to be gas-phase in nature rather than a surface reaction mechanism.

Introduction

Of recent interest to the propulsion community are solid propellant formulations based on nitramine ingredients such as cyclotrimethylenetri-nitramine (RDX) and cyclotetramethylenetetranitramine (HMX). These materials display high thermal stability and low sensitivity to ballistic vulnerability making them ideal candidates for low vulnerability ammunition (LOVA) propellants. Related to the LOVA characteristic of nitramine-based propellants, is the problem of achieving consistent ignition when it is desired. Understanding the complex physicochemical processes which characterize the ignition transient is necessary if safe, reliable igniters are to be designed for propulsion systems employing these propellant types.

[#]Ph. D. Candidate, Dept. of Mechanical Engineering

[§]Assistant Professor, Dept. of Mechanical Engineering

[†]Distinguished Professor, Dept. of Mechanical Engineering

There is available, in the literature, a limited amount of information on the ignition of nitramines subjected to a radiative thermal input^{1,2,3}. The benefit of the radiative ignition test is the control over heat flux input independent of other parameters such as environmental pressure. The radiative heat source is usually a CO₂ laser or an arc-image furnace. The major disadvantage of this test is the lack of hot gas adjacent to the propellant surface. Cohen and Decker⁴ used a shock tube to study the ignition of HMX and RDX in shock heated nitrogen gas. This accounted for the presence of a hot gas at the propellant surface but it was predominantly a conductive heating mechanism. Typical large caliber gun systems, which would employ LOVA solid propellants, achieve ignition via convective heating from a hot gaseous stream generated by an igniter. This particular shortcoming has been addressed in this study by employing a test method which simulates the convective heating process.

Several programs have studied convective heating and ignition of solid propellants. The work done by Kashiwagi et al.⁵ and Birk and Caveny^{6,7} is of particular importance. Kashiwagi et al.⁵ used a shock tunnel facility to generate a high pressure, high temperature gas flow over a solid fuel sample. The geometry of the sample was a flat plate. The purpose of the study was to examine the effect of freestream oxidizer concentration on the ignition delay time and ignition location of a convectively heated solid fuel. This type of experiment allowed Kashiwagi et al.⁵ to make definitive statements regarding the gas phase ignition behavior of the solid fuels in question.

Birk and Caveny^{6,7} used the same shock tunnel facility as Kashiwagi et al.⁵ to study the convective ignition and flame-spreading phenomena of individual solid propellant grains. Some minor modifications to the test section were made, but the essential nature of the test was the same. The shock tunnel was used to generate a high temperature, high pressure gas stream over a solid propellant sample under flow conditions similar to those expected in large caliber gun chambers. The sample geometry was a 0.7 cm (.275 in.) diameter cylindrical propellant grain mounted perpendicular to the gas stream. The published results were primarily for single-base, double-base, and triple-base nitrocellulose propellants with some very limited data for an HMX/PU composite propellant. Ignition delay time and ignition location on the sample were measured using photomultiplier tubes optically focused on specific locations of the sample via fiber optic tubing. The entire ignition event was monitored visually using high speed cameras and a schlieren lighting system. Following the tests, recovered samples were analyzed

microscopically for any important surface features which would assist in understanding the decomposition mechanisms. In addition to testing the propellant samples, calibration was accomplished using an instrumented cylinder which included a miniature pressure transducer and several thin film heat flux gages. With this instrumented cylinder, Birk and Caveny^{6,7} were able to examine the starting transient of the shock tunnel generated flow and the effect it had on heat transfer to the sample. This set-up provided an excellent opportunity to study the ignition and flame-spread phenomena of nitrocellulose propellants and to a limited degree an HMX/PU composite propellant.

Presented here are the results of an experimental ignition study on an RDX-based LOVA solid propellant using the same shock tunnel facility and technique as Birk and Caveny^{6,7}. The results of Birk and Caveny^{6,7} provide excellent background and insight into the interpretation of these more recent measurements. It is hoped the fundamental information gathered from this study of complex ignition processes in a relatively simple flow field can be used to better understand and predict the ignition response of RDX-based propellant in more practical combustion or propulsion scenarios.

The experimental objectives are to (1) visually examine the convective ignition phenomenon and subsequent flame spreading of RDX-based XM-39 propellant using high-speed video photography, (2) measure ignition delay (based on light emission from the sample) and examine possible correlations to convective flow parameters and (3) microscopically examine recovered propellant samples to determine the heating and burning effects on sample surfaces. The goal of this paper is to use the above observations and data to identify important processes involved in the ignition of XM-39 LOVA propellant. This will provide guidelines for eventual theoretical model development.

Method of Approach

Shock Tunnel Test Facility

The shock tunnel facility is identical to that used in other programs described above. A detailed discussion of the facility can be found in Kashiwagi et al.⁵, Birk and Caveny^{6,7} and Ritchie et al.^{8,9}. Briefly, the shock tunnel is used to create a reservoir of high-temperature, high-pressure gas which, in turn, induces a flow through the test section and across the sample. The test section, a cross-sectional side view is shown in Fig. 1, is a 2.86 cm x 2.86 cm (1.125 in. x 1.125 in.) square duct. Quartz windows, located on the top and sides (side windows not shown), provide

optical access. A perforated plate located at the downstream exit acts as a nozzle which chokes the flow and controls the gas velocity. One major modification to the set-up used by Birk and Caveny^{6,7} was the addition of a perforated plate to the upstream entrance of the test section. This was added to damp out initial pressure oscillations caused by the interaction of the incident shock wave with the sample and to protect the sample from damage by large pieces of burst diaphragm debris which are carried by the shock tunnel flow into the test region following the ignition event.

In lieu of heat flux and pressure calibration tests, as were performed by Birk and Caveny^{6,7}, the velocity, temperature and pressure of the gaseous flow through the test section were measured in calibration runs. These parameters were deemed more important as boundary conditions for eventual theoretical analysis than heat flux measurements. It was felt, on at least a qualitative basis, the heat flux data of Birk and Caveny^{6,7} could be used to analyze the ignition results obtained in the present study with regard to the starting transient of the shock tunnel test and the heating trends on various parts of the sample.

Pressure was measured at the test section wall with a Kistler 601B101 piezoelectric pressure transducer (see Fig. 1). The velocity was measured using a TSI Laser Doppler Velocimetry system and correlated to test section pressure and incident shock wave Mach number. The temperature measurements were carried out using a Paul Beckman Company 300 Series K-Type Micro-miniature Thermocouple. This commercially available thermocouple probe provides fast response time (~3 ms) and accuracies of 0.25%. The measured temperature data agreed very closely to expected values calculated using one-dimensional shock tube/tunnel theory. The temperature-time traces were evaluated by looking for a constant temperature plateau during the expected 17-20 ms test time following the shock wave arrival. The average temperature of this plateau was determined and correlated to the incident shock wave Mach number and the test section pressure value. In all ignition tests, the incident wave Mach number and pressure are measured and the temperature and velocity evaluated from the calibration curves.

Through control of the areas open to the flow on both the upstream perforated plate and downstream nozzle, the initial driver gas to driven gas pressure ratio, and the initial pressure in the driven section, the shock tunnel is capable of producing a wide range of test conditions: pressures of 1.03 - 4.14 MPa (150 - 600 psia), temperatures of 950 - 1500 K (1710 - 2700 °R), and velocities of 60 - 250 m/s (197 - 820 ft/s). The major limitation of the shock tunnel facility is the maximum

available test time of 17 - 20 ms, but for most flow conditions the ignition delay time is much shorter than this.

Diagnostics for ignition tests include: pressure transducers along the shock tunnel driven section to detect the shock wave arrival at fixed locations from which the incident shock wave speed is deduced, a pressure transducer located in the test section upstream of the sample (see Fig. 1), and five filtered RCA 1P28 photomultiplier tubes which measure light intensity in the near ultraviolet centered around 0.3700 μm used remotely via fiber optic tubes to measure ignition delay. Because preliminary tests of XM-39 showed significant flame spread into the downstream wake region, the fiber optic tubes were configured linearly, as shown in Fig. 1, to cover the entire span of the test section. High-speed visualization is accomplished through side windows using a high-speed Kodak Spin Physics SP2000 video system with backlighting of the sample.

Test Sample

The propellant used for this study was XM-39 (Lot #A5-1184-113): 76% RDX, 12% CAB, 7.6% ATEC, 4% NC, and 0.4% EC. The grain geometry is cylindrical in shape with a nominal diameter of 0.7 cm (.275 in.) and length of 0.74 cm (.291 in.). The condition of the samples was not uniform: the diameter was not constant from grain to grain, the shape of individual samples was never a perfect cylinder and the surface was pitted and graphite coated. In order maintain more uniformity in the tests, each propellant grain was trimmed to a constant length of 0.74 cm (.291 in.), the graphite coating was removed, and the surface was polished until it was visually smooth.

The sample was mounted in the test section with the induced flow perpendicular to the length of the grain. Mounting was accomplished by drilling a hole along the center axis of the cylindrical sample. A stainless steel rod is inserted through this hole and attached to end holders. The difference between the test section width, 2.86 cm (1.125 in.), and the sample length is occupied by inert spacers so the flow would 'see' essentially one long cylinder stretching across the entire test section. This was done to minimize end burning effects.

Discussion of Results

Tests were carried out within a limited flow regime for the shock tunnel facility. The flow velocity was fixed at approximately 65 m/s (213 ft/s) using a perforated-plate nozzle downstream as was done by Kashiwagi et al.⁵ The pressure

and temperature of the convective stream were altered by varying the initial values of pressure in the shock tunnel and the incident shock speed until an ignition 'envelope' was obtained. Reynolds numbers for this study ranged between 30,000 and 50,000. Two sets of tests were carried out in this fashion with XM-39 LOVA propellant. One set used nitrogen as the test gas; the other used air.

For the tests performed in a nitrogen environment, no ignition or luminous flame was detected by either the high speed video or the photomultiplier tube detection system. This result substantiates previous observations by others. Birk and Caveny^{6,7} showed a similar result for HMX/PU propellant. In a 100% nitrogen environment, no ignition was observed for Reynolds numbers between 7,000 and 10,000. As oxidizer was added to the test gas, ignition in this Reynolds number range was observed and the ignition delay time decreased as the concentration of oxygen in the test gas increased. Additionally, Chang and Rocchio¹⁰ have also shown that oxidizer rich igniters can reduce long ignition delays in gun simulator studies.

When tested in air, ignition of the XM-39 propellant grain was observed for many of the imposed test conditions. The results of a typical test (No. 155) are summarized here. Figure 2 contains pressure vs. time (Fig. 2a) and photomultiplier tube output vs. time (Fig. 2b) plots. Still photographs taken from the high speed video showing the observed location of first visible light are provided in Fig. 3.

The pressure-time trace can be divided into two sections. The 'transient starting time' begins with the incident shock wave arrival. Interaction of the incident wave with the sample and nozzles leads to pressure oscillations and turbulent flow conditions around the sample. In the subsequent 'quasi-steady test time', the pressure does not oscillate but slowly increases from a minimum value of 1.45 MPa (210 psia) to a maximum value of 2.00 MPa (290 psia). This corresponds to a 27% increase in pressure over the test duration. This variation, unfortunately, is unavoidable so an average pressure value is used in all calculations and in the presentation of results. Although undesirable, the pressure value during the majority of the test can be considered quasi-steady with tolerable variations.

The large initial deflection in the photomultiplier trace corresponds to the incident shock wave arrival in the test section (time = 0). The deflection in the photomultiplier signal due to the onset of sustained ignition is seen at 10.835 ms (t_{ip}). The rarefaction wave arrives at the test section after ~17.82 ms. The light intensity from the burning is altered slightly at this time but the sample does not

completely extinguish until 19.650 ms after the first pressure rise in the test section.

Still photographs obtained from the high-speed video for Test 155 are shown in Fig. 3. Backlighting was used and the convective stream is moving from right to left. To provide some initial perspective, Fig. 3a is a pretest picture of the sample in the test section. The arrival of the shock wave is so bright that the video system saturates and is therefore not shown but this would correspond to time $t=0$. Thereafter the sample appears as seen in Fig. 3a until visible light can be seen on the top surface at time, $t = 11.167$ ms (Fig. 3b). Any light generated on the bottom of the sample would be hidden by the sample supports. The more sensitive photomultiplier tube detected ignition much earlier at 10.835 ms. In Fig. 3d, corresponding to $t = 11.500$ ms, the reaction has propagated downstream and grown in intensity and can now be seen on the lower half of the sample. Subsequent frames show increasing light emission from the wake region of the sample until eventually the burning spreads over the entire downstream surface at time $t = 13.334$ ms (Figs. 3e to 3o). Once the reaction has covered the downstream region of the sample it burns in essentially a steady-state fashion (Fig. 3p) until the end of the test time. The sample does continue to react for several milli-seconds after the pressure drop at 17.82 ms caused by the arrival of the rarefaction wave as shown in Fig. 2a. The described events for ignition and flame spreading of XM-39 RDX-based composite propellant are very similar to the observations of Birk and Caveny^{6,7} for nitrocellulose-based propellants. It is obvious that many of the important physical processes involved in the convective ignition of these different types of propellants are the same.

In many cases, light emission from the sample was detected very early (< 3 ms) during the shock tunnel transient start-up time. This phenomenon was also observed by Birk and Caveny^{6,7} in their study of nitrocellulose propellants. When the incident shock wave arrives in the test section the heating rates to the sample are very high. This has been substantiated by the heat flux data taken by Birk and Caveny.^{6,7} Gasification of the propellant material can take place and subsequent reactions observed. However in both the tests done for this program and those done previously by Birk and Caveny^{6,7}, this 'transient' ignition was not always able to sustain burning for the entire test time because the heating rates decrease sharply with the onset of the quasi-steady flow through the test section. The sample, once quenched, would usually, but not always, reignite later during the steady-state convective heating period and sustain burning until the end of the

test time. It is this second ignition point which has been labeled the ignition delay time (t_{ID}). The ignition delay was determined through analysis of both the photomultiplier tube output (100,000 pts/sec.) and the high-speed video pictures (6,000 pict/sec.).

The conditions for the second set of tests are given in Table I. This table lists the test section pressure, temperature, Mach number, Reynolds number, Prandtl number, Nusselt number, ignition delay time (t_{ID}) and dimensionless ignition delay (t^*_{ID}). t^*_{ID} is defined as $t_{ID}/(D/V)$; it represents the ratio of ignition delay time to the flow residence time based on the sample diameter and the approach velocity. The average Nusselt number¹¹ is calculated using the following formula for flow over a cylinder:

$$\overline{Nu} = .027 Re_D^{.805} Pr^{.333} \quad (1).$$

Birk and Caveny^{6,7} used Reynolds number as the independent parameter in presentation of their results. The average Nusselt number, as calculated using the above equation, is more closely associated with heat transfer to the sample. The heat flux data taken by Birk and Caveny show the variation in heat transfer rates as a function of angular location from the leading edge. By using an average value, it is assumed the heat transfer rates over the surface vary accordingly. Therefore an increase in the average Nusselt number is representative of an increase in the local Nusselt numbers at the various surface locations.

Photographs from an optical microscopic study (magnification = 50X) of a recovered propellant sample are shown in Fig. 4. A detailed description of each photograph is given due to the limited resolution of the reproduction. At the front stagnation point, position A, the surface is slightly pitted and many small particles from the shock tunnel burst diaphragm are imbedded in the surface layer. Between 30° and 45° from the leading edge at location B, small wave formations appear on the surface indicating the formation of a liquid 'melt' layer. The wave formations could be created by bubble formation and the complex flow structure on the propellant surface or it could be due to the existence of some freestream turbulence generated by the upstream perforated plate. These wave formations grow in size between 45° and 90° from the leading edge at location C. Just beyond the 90° point at region D, there is a large liquid agglomeration on the surface. The position of this liquid formation coincides very closely to the first reaction location as seen on the video. Although it is not easily discernible in the

photographs, there are many bubbles entrained within this agglomeration. A second agglomeration which is slightly smaller than the one at $\sim 95^\circ$ can be seen at $\sim 105^\circ$ from the leading edge in region E. The back surface (region F) and rear stagnation point (region G) are similar to the front surface only free of particles and shock tunnel debris. The only easily distinguishable difference between the burned and unburned samples is the coloring. Burned samples exhibit a darker shade of yellow/white (particularly on the downstream side and at the agglomeration points) while the unburned samples more closely resemble the original white coloring of the propellant. Unfortunately this is only distinguishable under actual viewing conditions and is not clearly visible in the photographic representation.

A scanning electron microscope (SEM) was used to examine the sample surface under even higher magnification. These photographs are shown in Fig. 5 and correspond to Test 148. The first two pictures show a pretest propellant surface (Fig. 5a and 5b). The surface, although it had been polished, is actually quite rough when examined under very high magnification (1600X). The next series of photographs are of a sample which has ignited under convective heating conditions. The letter associated with each photograph corresponds to the general area highlighted in Fig. 4. Note: the area covered by the photograph does not correspond to the area of the square box on the top view of the sample in Fig. 4 and the magnification used for each photograph is not the same. The magnification was chosen to highlight particular structures on the sample surface.

Figure 5e shows the front stagnation region A. The surface in this region, and over the entire propellant surface, is very rough with many rice-like structures which have an approximate diameter of $4\text{ }\mu\text{m}$. Scattered randomly about this region are small circular holes, often appearing in small groups. Further along the sample, in region B, the surface appears similar to the stagnation region (see Fig 5d). However, the surface structures are less independent and appear to have agglomerated into larger clumps. There are still holes in the surface but these do not appear as frequently as in the front stagnation zone.

At position D, where the large agglomeration forms on the sample surface, Fig. 5e clearly shows a change in the surface structure. At the ridge of the agglomeration the individual rice-like shapes have become very closely grouped and have apparently 'melted' together. Again there are circular holes located in close proximity to the ridge region but not in large quantities. Just downstream

from the agglomeration region, near E, there is a very densely packed, large number of circular holes (see Fig. 5f). Some of these holes display a whitish edge indicating a change in the physical nature of the material probably due to phase changes and chemical reactions. The structure of these crater-like holes was examined under even greater magnification (1600X) and is shown in Fig. 5g. Further along the sample in region F and at the rear stagnation point G the surface has the same description as the leading edge locations, A and B.

Birk and Caveny⁶ also carried out a SEM analysis of recovered sample surfaces. The micro-photographs are very similar to those presented here. The nitrocellulose-based propellants had a large number of the crater-like holes over their entire surface, including the upstream edge of the sample. The HMX/PU propellant showed significant signs of the formation of a liquid 'melt' layer and numerous craters as observed in this program for XM-39. Unfortunately, for many of the pictures, the flow conditions and the angular location on the sample are not provided. This makes comparison to the present results for XM-39 very subjective.

Ignition Delay Correlation

One objective was to find a correlation between the ignition delay time for XM-39 LOVA propellant and the freestream flow parameters: pressure, temperature and velocity. If the chemistry is relatively fast, the ignition delay should depend almost entirely on the heat-up for the solid material and a correlation based on the heat flux into an inert cylinder should provide reasonable results. This analysis is very similar to that used in presenting data from radiative ignition tests. The average nondimensional heat flux term (Q^*) was calculated using the following formula:

$$Q^* = \overline{Nu} \left[\frac{(T_s - 480 \text{ K})}{T_{ref}} \right] \left[\frac{(T_\infty + 480 \text{ K})}{2(T_{ref})} \right]^{1/2} \quad (2).$$

The first term is the average Nusselt number calculated using Eq. (1). The second term compensates for the temperature difference between the propellant surface and the freestream flow. The third term accounts for changes in the conductivity of air at the film temperature. Obviously, the temperature of the propellant surface will be dependent on time and the angular location from the

leading edge. To simplify the analysis, a constant temperature for the surface of the propellant was chosen. The value of 480 K was used because it is close to the melting or liquefaction temperature for RDX quoted in the literature. This simplification assumes that a constant 'average' heat flux is applied to the XM-39 propellant based solely on the freestream flow parameters. In the correlation development, the reference temperature was taken to be 273 K. The dimensionless ignition delay time for data set two is plotted against the dimensionless heat flux in Fig. 6. If all data points are considered together, there is a significant amount of scatter in the results. This scatter is significantly reduced if the tests which display clear evidence of propellant end-surface burning (in the gaps between the sample and the inert spacers) are separated from the tests which did not. Evidence of end-surface burning is easily found during the post-test microscopic analysis of the sample surface. Based upon the above distinction, there are two families of data shown in the same plot (Fig. 6). Correlation equations for these two families of data are given below:

$$\text{Surface ignition,} \quad t_{ID}^* = 519 - 0.539 Q^*$$

$$\text{End/Gap ignition,} \quad t_{ID}^* = 471 - 0.517 Q^*$$

At a given heat flux, the end or gap ignition process has a shorter ignition delay time than the surface ignition process. This is reasonable because hot gases from the convective stream cause the edge regions of the propellant to reach ignition conditions sooner than the surface region. This type of edge enhanced ignition has been studied previously by Vorsteveld and Hermance¹². When the end surfaces of the propellant grain are in close contact with the spacers, the edge effect is eliminated resulting in a longer ignition delay time.

When the possibility of end- or edge-ignition is accounted for, the resulting data correlate very well. The small amount of data scatter could be due to one or more of the following reasons: (1) the surface and shape of the test samples were not as consistent as would have been desired. Imperfections created during the manufacturing process and during the removal of the graphite coating could lead to variations in the measured results; (2) the correlations make no allowance for changes in the sample surface condition such as the presence of circular holes and the rice-like structures; (3) the high heating rates to the propellant during interaction with the incident shock wave and the variation in surface

temperatures are not considered; and (4) there is no consideration given to possible heat feedback from exothermic chemical reactions in the gas, solid or liquid phases.

Physical and Chemical Characteristics of the Convective Ignition Test

The convective ignition of XM-39 LOVA propellant involves many complex physical and chemical processes. Based on the observations made during this study, the following summary describes in detail many of these processes which lead to ignition under the conditions imposed by the shock tunnel convective ignition test.

Due to the nature of the shock tunnel test apparatus, a transient flow settling or start-up time exists which lasts ~3 ms. During this start-up time, heat flux to the sample is very large because of incident shock wave interactions, flow reversals and turbulent flow conditions around the sample. The complexity of the flow makes interpretation of data obtained during this period very difficult. However, the importance of this period should not be neglected. The propellant surface temperature rises very rapidly during these first few milliseconds and liquefaction, decomposition and vaporization of solid material can occur prior to the start of the quasi-steady flow test time. It is assumed, due to the brevity of the settling time, the thermal profile in the sample is quite thin. For self-sustained ignition to occur during this time, heat feedback from the reaction zones must maintain the thermal energy input into the sample when the external heat source is reduced. If ignition can not be supported when the high heat flux period ends, the thermal profile should adjust quickly to the new ambient heating conditions.

By the time the flow in the test section has settled into a quasi-steady state, many physical processes have already occurred. These include liquid 'melt' layer formation and some solid propellant decomposition or evaporation into the gas phase. The conditions which exist and lead to the eventual ignition during the steady flow time are discussed relative to the regimes shown in Fig. 7.

At the leading edge, stagnation flow conditions exist. This region is characterized by very high heat flux into the solid material from the external flow and local pressure values are at a maximum. The high heating rates lead to liquefaction, decomposition and vaporization of the solid material which form liquid and gaseous boundary layers on the sample surface. Small circular holes have been observed on the upstream surface. These holes can be attributed to

possible foreign particle impingement, dewetting of propellant crystals from the surface region, and fast pyrolysis of local active sites.

Within the gaseous boundary layer formed along the upstream circumferential surface, oxidizer from the freestream mixes and reacts with pyrolysis products from the propellant. The heat generated, along with continued heating from the freestream, can sustain continued pyrolysis, vaporization and liquefaction of the solid surface. At the gas-liquid interface, vaporized and decomposed propellant is added to the gaseous boundary layer as the heating continues from both the external convective stream and heat feedback from chemical reactions which could occur in both the gaseous and condensed phases. The 'liquid' boundary layer is highly non-uniform. Gaseous bubbles are formed within the liquid layer and at the solid-liquid interface as the propellant vaporizes and decomposes. These bubbles are carried within the liquid 'melt' layer until eventually they reach the gas-liquid interface. These bubbles could be the reason for the flow structures described previously (see Fig. 4). At the liquid-solid interface the propellant, as it is heated, undergoes liquefaction, vaporization and decomposition. In addition, the liquid layer appears to form around solid structures which resemble rice kernels when observed with a SEM.

Gaseous boundary layer separation occurs around 80° to 85° from the leading edge. Just beyond this separation point, flow reversals in the gas phase increase mixing. Since the liquid layer is driven by the shear force of the gaseous flow, the flow reversal in the gaseous layer leads to a flow reversal in the liquid layer thus increasing the mixing and the heat transfer to the solid propellant surface. Processes which were occurring in the boundary layer continue but the heat flux from the convective stream and the local pressure at the sample surface are now at their minimum values. Eventually recirculation zones are formed in both the gaseous flow and the predominantly liquid boundary layer which grows significantly in size forming the agglomeration seen in Figs. 4 and 5e. Ignition occurs within this flow region due to the long residence time and increased mixing of the pyrolysis products, vaporized propellant, and freestream oxidizer in the gaseous phase. The gas-phase reactions locally increase heat-transfer to the liquid and subsequently the solid phase and thus achieve self-sustained combustion. In this region a large number of the crater-like holes are observed on the propellant surface. It is postulated that these represent the location of very active crystals of RDX which gasify and react.

Birk and Caveny^{6,7} proposed that a gas phase Damkohler number defined as the ratio of the residence time in the mixing zone to the reaction time was an important dimensionless parameter which could assist in characterizing the observed ignition phenomena. If the Damkohler number is much greater than one, the reaction is much faster than the flow time and the reactants are consumed almost immediately within the vicinity of initial gasification. The location of initial gasification would be at the front and rear surface stagnation points, where the solid surface heating rates are greatest. The results from this program can be interpreted in this manner, the Damkohler number must not be very large and therefore the reactants need greater residence time as is associated with the recirculation region just beyond the separation point.

On the downstream surface of the sample the large recirculation zones formed in the wake create a rear stagnation point and subsequently a boundary layer flow. These areas develop much as the forward areas do and supply additional reactant species to the reaction zone located just beyond the boundary layer separation point. At a point near 110° from the leading edge the boundary layer formed on the rear surface interacts with the separation region. Near this position another agglomeration of liquid is formed as the boundary layer thickens. The gaseous products generated along the rear surface contribute to the ignition and combustion processes.

Conclusions

The following conclusions about the convective ignition of XM-39 LOVA propellant can be reached based on the results obtained and discussed above:

1. Convective ignition and flame spreading phenomena of XM-39 solid propellant have been successfully observed using the technique of Birk and Caveny.^{6,7} Strong evidence of gas-phase ignition mechanism has been experimentally observed. Sustained convective ignition occurs in the region near the boundary layer separation point.
2. The presence of freestream oxidizer is very important to the ignition process. In the absence of oxidizer in the test gas, no convective ignition was observed. Ignition was achieved in tests with air as the test gas.
3. Two possible sites of ignition have been identified: circumferential surface ignition and edge surface ignition. Separate correlations have been developed for these two types of ignition phenomena.

Test No.	Pressure MPa (psia)	Temperature (K) (R)	Reynolds No.	Prandtl No.	Nusselt No.	Mach No.	t _{ID} (ms)	t* _{ID} (-)
050	3.79 (550)	1420 (2556)	71441	0.699	193.5	0.071	0.00	0.00
051	1.72 (250)	1385 (2493)	43376	0.705	129.9	0.094	7.33	76.8
053	1.72 (250)	1415 (2547)	41506	0.700	125.1	0.094	7.27	78.9
055	1.59 (230)	1405 (2529)	40004	0.702	121.6	0.096	9.41	93.5
056	1.64 (238)	1440 (2592)	39698	0.696	120.4	0.095	None	--
058	2.78 (403)	1415 (2547)	59061	0.700	166.2	0.082	1.50	13.2
059	2.56 (371)	1460 (2628)	54877	0.692	153.7	0.084	3.17	28.0
060	2.49 (361)	1375 (2475)	58122	0.707	164.6	0.086	2.82	25.0
061	2.49 (361)	1375 (2475)	59058	0.707	166.8	0.086	3.17	27.7
062	2.34 (340)	1305 (2349)	59667	0.718	168.9	0.088	5.64	50.0
063	2.32 (337)	1445 (2601)	51066	0.695	147.5	0.087	5.17	48.0
064	2.34 (340)	1335 (2403)	58309	0.713	165.4	0.089	3.64	32.6
065	2.03 (294)	1430 (2574)	45987	0.698	135.7	0.090	8.59	83.7
066	2.32 (337)	1200 (2160)	65898	0.728	184.0	0.091	11.46	100.6
067	1.79 (260)	1270 (2286)	48929	0.720	144.1	0.094	14.55	138.7
068	2.65 (385)	1280 (2304)	65775	0.721	183.1	0.085	5.33	45.6
145	1.03 (150)	1340 (2412)	29905	0.712	96.6	0.103	None	--
146	1.86 (270)	1360 (2448)	48305	0.710	142.0	0.093	None	--
147	1.86 (270)	1465 (2637)	42716	0.691	127.5	0.091	6.28	54.4
148	2.41 (349)	1180 (2124)	69814	0.728	192.7	0.090	13.59	115.9
149	1.31 (190)	1435 (2583)	33664	0.697	105.6	0.099	None	--
150	2.13 (309)	1455 (2619)	48587	0.693	141.6	0.089	4.91	46.0
151	2.13 (309)	1410 (2538)	50089	0.701	145.6	0.089	3.87	35.9
153	2.13 (309)	1290 (2322)	55726	0.720	160.0	0.091	13.04	121.9
154	2.13 (309)	1205 (2169)	62743	0.728	176.9	0.093	15.40	137.8
155	1.79 (260)	1429 (2572)	41930	0.698	126.0	0.092	10.84	107.3
156	1.86 (270)	1430 (2574)	45019	0.697	133.4	0.092	8.61	83.0
157	2.13 (309)	1355 (2439)	53424	0.710	154.0	0.090	7.30	67.6
158	2.41 (349)	1445 (2601)	53525	0.695	153.2	0.086	3.06	28.1
159	2.41 (349)	1385 (2493)	55952	0.705	159.5	0.087	5.30	48.1
160	2.41 (349)	1360 (2448)	57511	0.710	163.4	0.087	6.83	60.3
161	2.41 (349)	1290 (2322)	61592	0.720	173.5	0.088	12.07	105.0
162	2.41 (349)	1195 (2151)	67442	0.728	187.5	0.090	15.52	134.3
163	1.86 (270)	1375 (2475)	46963	0.707	138.7	0.093	10.55	100.6
164	1.86 (270)	1280 (2304)	51827	0.721	151.1	0.095	15.61	147.1
165	1.59 (230)	1565 (2817)	35472	0.685	131.9	0.095	7.41	75.2
166	1.59 (230)	1355 (2439)	40808	0.710	127.6	0.096	12.66	124.2

Test No.	Pressure MPa (psia)	Temperature (K) (R)	Reynolds No.	Prandtl No.	Nusselt No.	Mach No.	t _{ID} (ms)	t* _{ID} (-)
050	3.79 (550)	1420 (2556)	71441	0.699	193.5	0.071	0.00	0.00
051	1.72 (250)	1385 (2493)	43376	0.705	129.9	0.094	7.33	76.8
053	1.72 (250)	1415 (2547)	41506	0.700	125.1	0.094	7.27	78.9
055	1.59 (230)	1405 (2529)	40004	0.702	121.6	0.096	9.41	93.5
056	1.64 (238)	1440 (2592)	39698	0.696	120.4	0.095	None	--
058	2.78 (403)	1415 (2547)	59061	0.700	166.2	0.082	1.50	13.2
059	2.56 (371)	1460 (2628)	54877	0.692	153.7	0.084	3.17	28.0
060	2.49 (361)	1375 (2475)	58122	0.707	164.6	0.086	2.82	25.0
061	2.49 (361)	1375 (2475)	59058	0.707	166.8	0.086	3.17	27.7
062	2.34 (340)	1305 (2349)	59667	0.718	168.9	0.088	5.64	50.0
063	2.32 (337)	1445 (2601)	51066	0.695	147.5	0.087	5.17	48.0
064	2.34 (340)	1335 (2403)	58309	0.713	165.4	0.089	3.64	32.6
065	2.03 (294)	1430 (2574)	45987	0.698	135.7	0.090	8.59	83.7
066	2.32 (337)	1200 (2160)	65898	0.728	184.0	0.091	11.46	100.6
067	1.79 (260)	1270 (2286)	48929	0.720	144.1	0.094	14.55	138.7
068	2.65 (385)	1280 (2304)	65775	0.721	183.1	0.085	5.33	45.6
145	1.03 (150)	1340 (2412)	29905	0.712	96.6	0.103	None	--
146	1.86 (270)	1360 (2448)	48305	0.710	142.0	0.093	None	--
147	1.86 (270)	1465 (2637)	42716	0.691	127.5	0.091	6.28	54.4
148	2.41 (349)	1180 (2124)	69814	0.728	192.7	0.090	13.59	115.9
149	1.31 (190)	1435 (2583)	33664	0.697	105.6	0.099	None	--
150	2.13 (309)	1455 (2619)	48587	0.693	141.6	0.089	4.91	46.0
151	2.13 (309)	1410 (2538)	50089	0.701	145.6	0.089	3.87	35.9
153	2.13 (309)	1290 (2322)	55726	0.720	160.0	0.091	13.04	121.9
154	2.13 (309)	1205 (2169)	62743	0.728	176.9	0.093	15.40	137.8
155	1.79 (260)	1429 (2572)	41930	0.698	126.0	0.092	10.84	107.3
156	1.86 (270)	1430 (2574)	45019	0.697	133.4	0.092	8.61	83.0
157	2.13 (309)	1355 (2439)	53424	0.710	154.0	0.090	7.30	67.6
158	2.41 (349)	1445 (2601)	53525	0.695	153.2	0.086	3.06	28.1
159	2.41 (349)	1385 (2493)	55952	0.705	159.5	0.087	5.30	48.1
160	2.41 (349)	1360 (2448)	57511	0.710	163.4	0.087	6.83	60.3
161	2.41 (349)	1290 (2322)	61592	0.720	173.5	0.088	12.07	105.0
162	2.41 (349)	1195 (2151)	67442	0.728	187.5	0.090	15.52	134.3
163	1.86 (270)	1375 (2475)	46963	0.707	138.7	0.093	10.55	100.6
164	1.86 (270)	1280 (2304)	51827	0.721	151.1	0.095	15.61	147.1
165	1.59 (230)	1565 (2817)	35472	0.685	131.9	0.095	7.41	75.2
166	1.59 (230)	1355 (2439)	40808	0.710	127.6	0.096	12.66	124.2

Table 1 Summary of Test Conditions and Results for XM-39 Solid Propellant in Air

- Fig. 1** Cross-sectional side view of convective ignition test section.
- Fig. 2 a)** Test section pressure vs. time trace (Test No. 155)
- Fig. 2 b)** Test section photomultiplier output vs. time trace (Test No. 155).
- Fig. 3** High-speed video images of convective ignition test events (Test No. 155).
- Fig. 4** Magnified (50X) post-test XM-39 solid propellant surface (Test No. 148).
- Fig. 5 a)** Pretest XM-39 Solid Propellant - graphite coating removed and surface polished (Test No. 148, mag. = 800X).
- Fig. 5 b)** Pretest XM-39 Solid Propellant - graphite coating removed and surface polished (Test No. 148, mag. = 1600X).
- Fig. 5 c)** Post-test XM-39 Solid Propellant - Upstream stagnation region A (Test No. 148, mag. = 600X).
- Fig. 5 d)** Post-test XM-39 Solid Propellant - Upstream surface region B (Test No. 148, mag. = 600X).
- Fig. 5 e)** Post-test XM-39 Solid Propellant - Liquid agglomeration at location D (Test No. 148, mag. = 600X).
- Fig. 5 f)** Post-test XM-39 Solid Propellant - Crater-like structures near region E (Test No. 148, mag. = 200X).
- Fig. 5 g)** Circular, crater-like holes located at position E (Test No. 148, mag. = 1600X).
- Fig. 6** Plot of Dimensionless ignition delay time vs. dimensionless heat flux, Q^* .
- Fig. 7** Major physical and chemical processes involved in the convective ignition of a cylindrical solid propellant grain

4. From observation, the sample surface can reach ignition due to incident and reflected shock wave heating during the transient start-up time of the test. The heating is very intense but very short in duration. However, if the thermal profile during this period is too thin to achieve self-sustained ignition, subsequent ignition could occur during the nearly steady-state operating time.
5. Microscopic analysis of recovered propellant samples shows the formation of a liquid layer. The composition of this liquid and its importance to the ignition process is still unknown and should be studied further.
6. After ignition the flame propagates from the shoulder region to the rear stagnation point. The sample acts as a flame holder; in the wake region the local flow velocity is reduced and the flame can sustain.

Acknowledgements

This work was performed under Contract Number DAAL03-87-K-0064 under the sponsorship of the Army Research Office, Research Triangle Park, North Carolina. The program manager is Dr. David Mann. His support of this research is greatly appreciated.

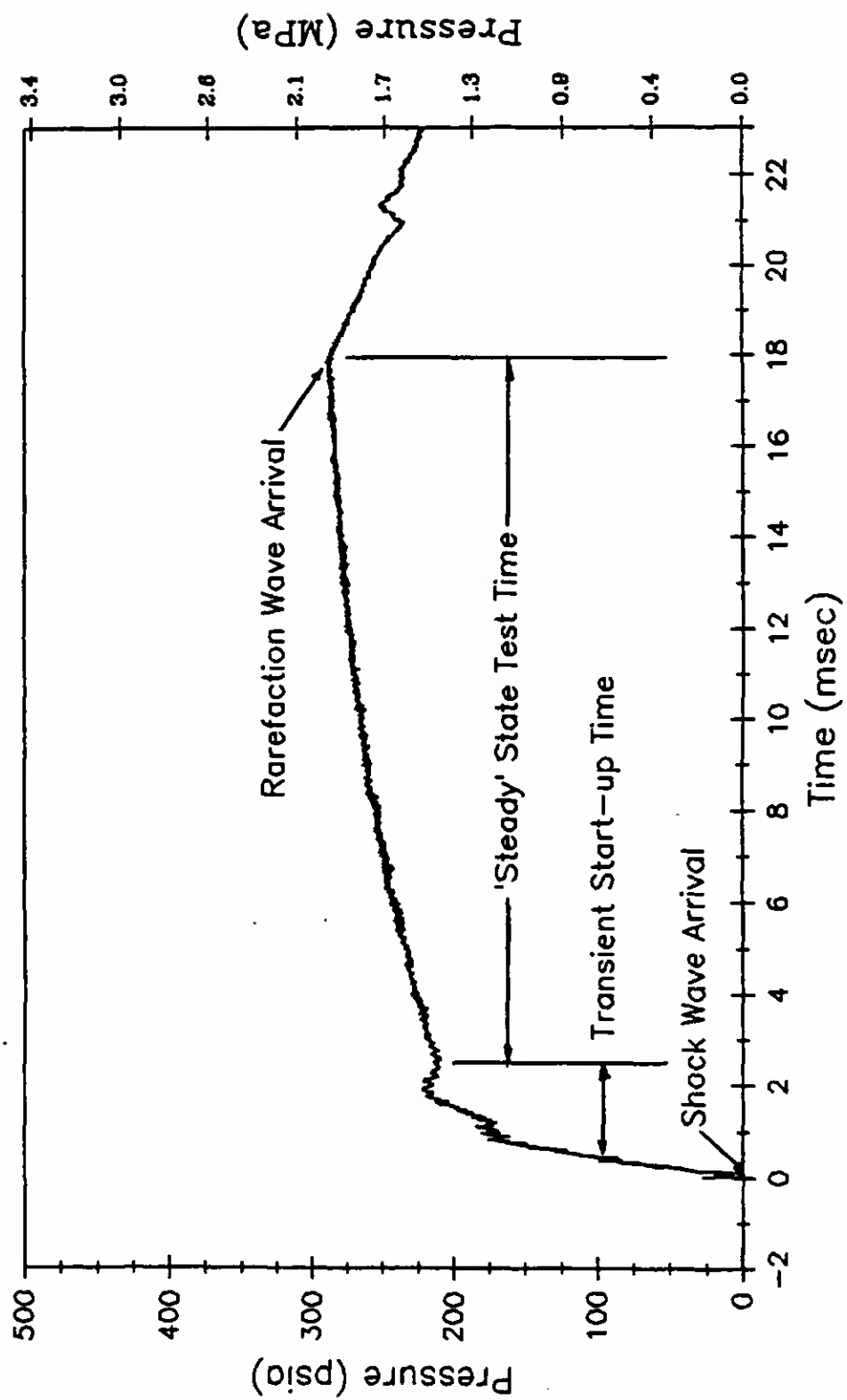
References

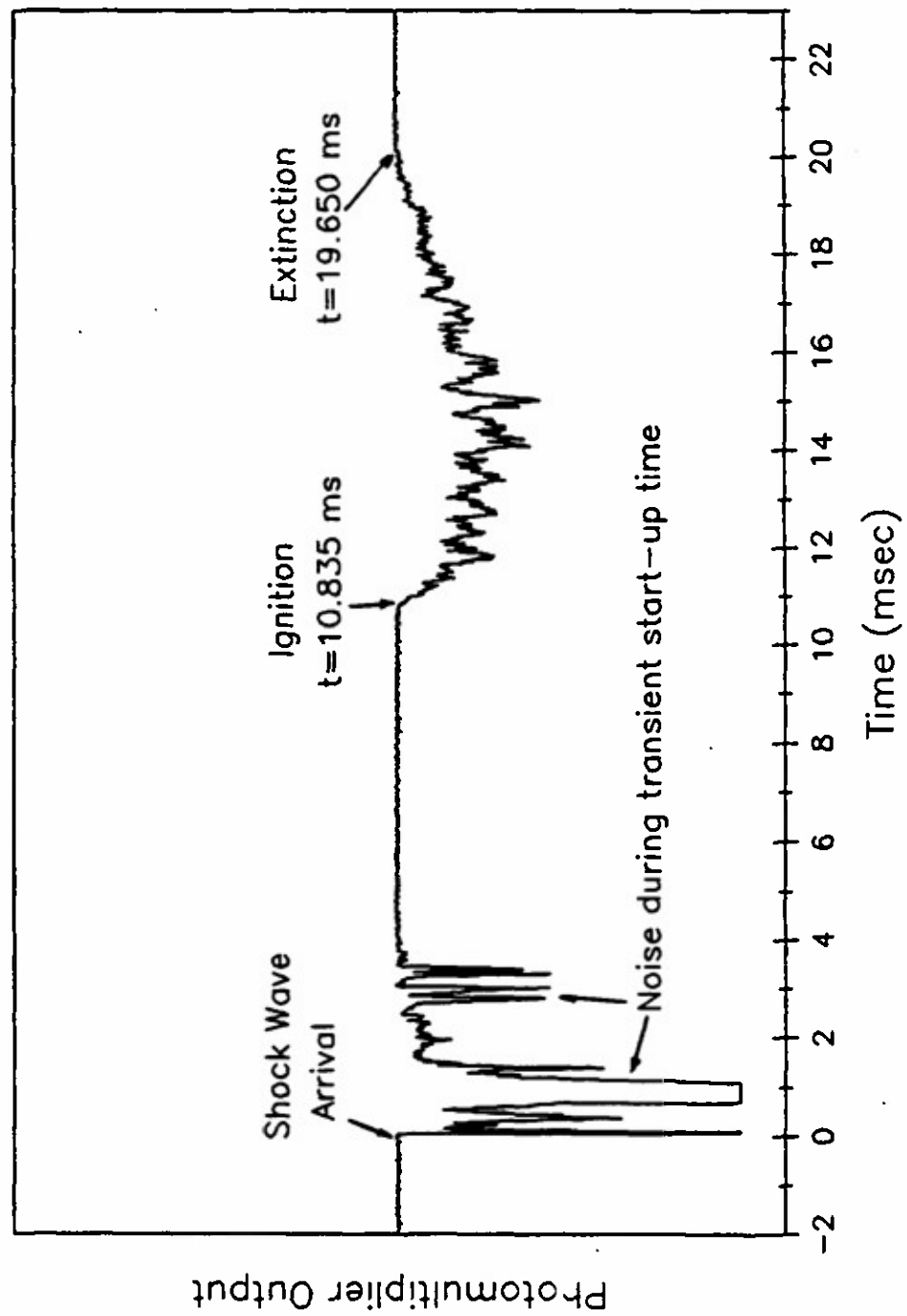
- 1 Boggs, T.L., "Thermal Behavior of RDX and HMX," AIAA Progress in Astronautics and Aeronautics: Fundamentals of Solid Propellant Combustion, edited by K.K. Kuo and M. Summerfield, Vol 90, 1984, pp. 121-175.
- 2 Kim, J. U., Torikai, T., and Kuo, K. K., "Ignition Dynamics of Nitramine Composite Propellants under CO₂ Laser Heating," AIAA Paper No. 87-0564, presented at the AIAA 25th Aerospace Sciences Meeting, Reno, Nevada, 12-15 January 1987.
- 3 Boggs, T. L., Price, C. F., Atwood, a. I., Zurn, D. E., and Derr, R. L., "The Role of Gas Phase Reactions in Deflagration-to-Detonation Transition," 7th Symposium on Detonation, Vol 1, June 1981, pp. 85-93.
- 4 Cohen, A. and Decker, L. J., "Shock Tube Ignition of Nitrocellulose and Nitramines," 16th JANNAF Combustion Meeting, CPIA Pub. 308, Vol. 1, Dec. 1979, pp.541-546.
- 5 Kashiwagi, T., MacDonald, B. W., Isoda, H. and Summerfield, M., "Ignition of Solid Polymeric Fuels by Hot Oxidizing Gases," AMS Report No. 947, October 1970.

- 6 Birk, A. and Caveny, L. H., "Convective Ignition of Propellant Cylinders in a Developing Cross-Flow Field," MAE Report No. 1486, Department of Mechanical and Aerospace Engineering, Princeton University, September 1980.
- 7 Birk, A. and Caveny, L.H., "Convective Ignition of Propellant Cylinders in a Developing Flowfield," AIAA Journal, Vol. 18, No. 11, Nov. 1980, pp. 1363-1370.
- 8 Ritchie, S.J., Hsieh, W.H., and Kuo, K.K., "Convective Ignition of LOVA Propellants Subjected to Crossflow Heating Conditions," 26th JANNAF Combustion Meeting, 23-27 October 1989 Pasadena, CA, CPIA Publication 529, Vol. 1, pp. 1-12.
- 9 Ritchie, S.J., Hsieh, W.H., and Kuo, K.K., "Convective Ignition Phenomena of LOVA Propellants," AIAA Paper 90-2194, AIAA/SAE/ASME/ASEE 26th Joint Propulsion Conference, Orlando, FL, 16-18 July 1990.
- 10 Chang, L.M. and Rocchio, J.J., "Simulator Diagnostics of the Early Phase Ignition Phenomena in a 105-mm Tank Gun Chamber," Technical Report BRL-TR-2890, March 1988.
- 11 Knudsen, J.D. and Katz, D.L., Fluid Dynamics and Heat Transfer, McGraw-Hill, New York, 1958.
- 12 Vorsteveld, L.G. and Hermance, C.E., "Effect of Geometry on Ignition of a Reactive Solid: Square Corner," AIAA Journal, Vol. 25, No. 4, April 1987, pp. 592-597.

Table 1 Summary of Test Conditions and Results for XM-39 Solid Propellant in Air

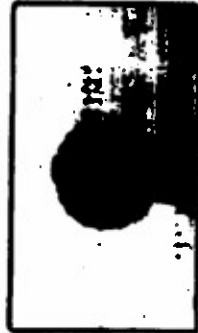
- Fig. 1** Cross-sectional side view of convective ignition test section.
- Fig. 2 a)** Test section pressure vs. time trace (Test No. 155)
- Fig. 2 b)** Test section photomultiplier output vs. time trace (Test No. 155).
- Fig. 3** High-speed video images of convective ignition test events (Test No. 155).
- Fig. 4** Magnified (50X) post-test XM-39 solid propellant surface (Test No. 148).
- Fig. 5 a)** Pretest XM-39 Solid Propellant - graphite coating removed and surface polished (Test No. 148, mag. = 800X).
- Fig. 5 b)** Pretest XM-39 Solid Propellant - graphite coating removed and surface polished (Test No. 148, mag. = 1600X).
- Fig. 5 c)** Post-test XM-39 Solid Propellant - Upstream stagnation region A (Test No. 148, mag. = 600X).
- Fig. 5 d)** Post-test XM-39 Solid Propellant - Upstream surface region B (Test No. 148, mag. = 600X).
- Fig. 5 e)** Post-test XM-39 Solid Propellant - Liquid agglomeration at location D (Test No. 148, mag. = 600X).
- Fig. 5 f)** Post-test XM-39 Solid Propellant - Crater-like structures near region E (Test No. 148, mag. = 200X).
- Fig. 5 g)** Circular, crater-like holes located at position E (Test No. 148, mag. = 1600X).
- Fig. 6** Plot of Dimensionless ignition delay time vs. dimensionless heat flux, Q^* .
- Fig. 7** Major physical and chemical processes involved in the convective ignition of a cylindrical solid propellant grain







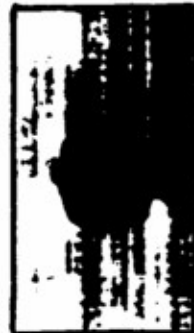
a. pretest image



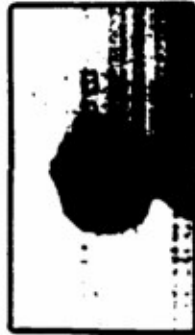
b. $t = 11.167$ ms



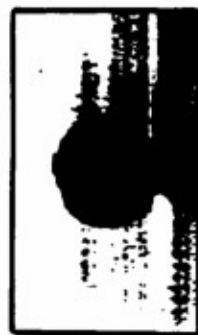
c. $t = 11.334$ ms



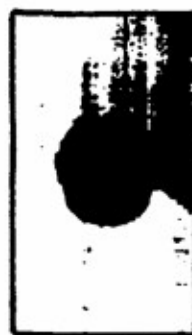
d. $t = 11.500$ ms



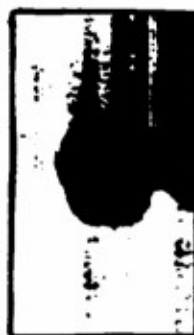
e. $t = 11.667$ ms



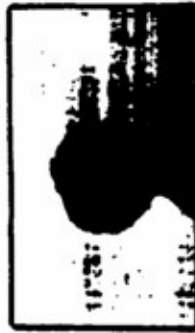
f. $t = 11.834$ ms



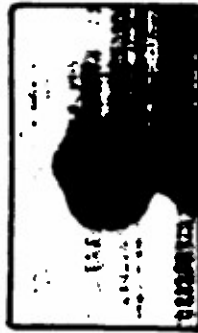
g. $t = 12.000$ ms



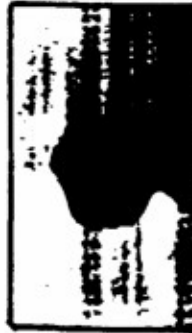
h. $t = 12.167$ ms



i. $t = 12.334$ ms



j. $t = 12.500$ ms



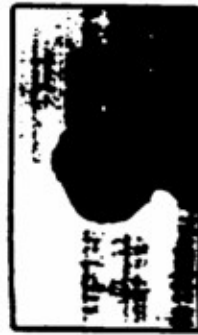
k. $t = 12.667$ ms



l. $t = 12.834$ ms



m. $t = 13.000$ ms



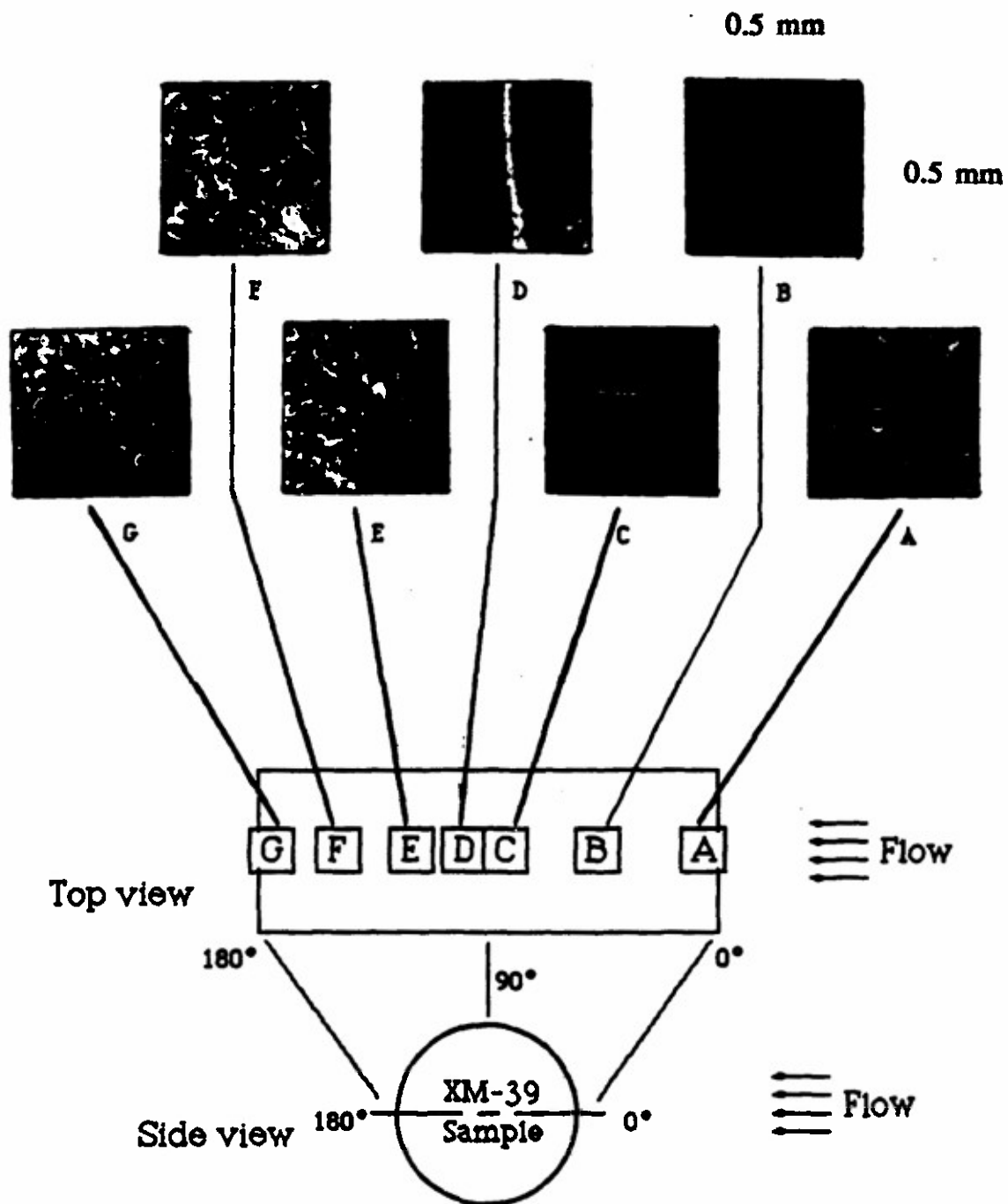
n. $t = 13.167$ ms



o. $t = 13.334$ ms

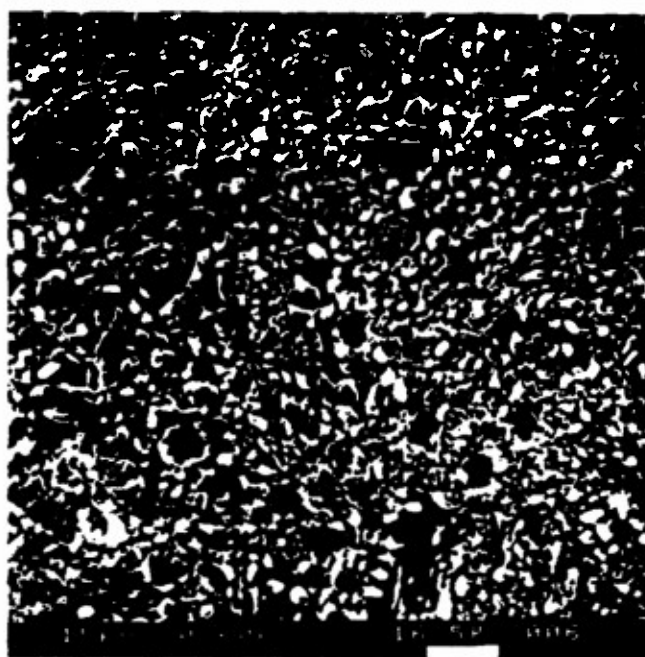


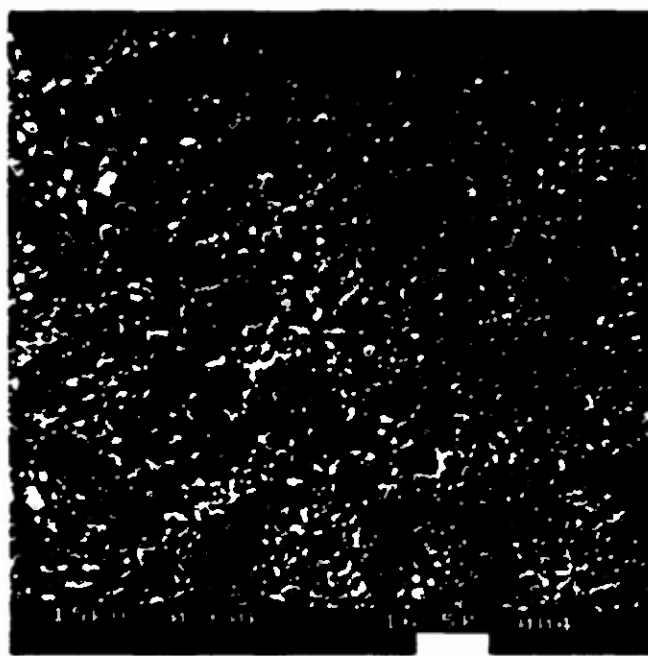
p. $t = 14.334$ ms

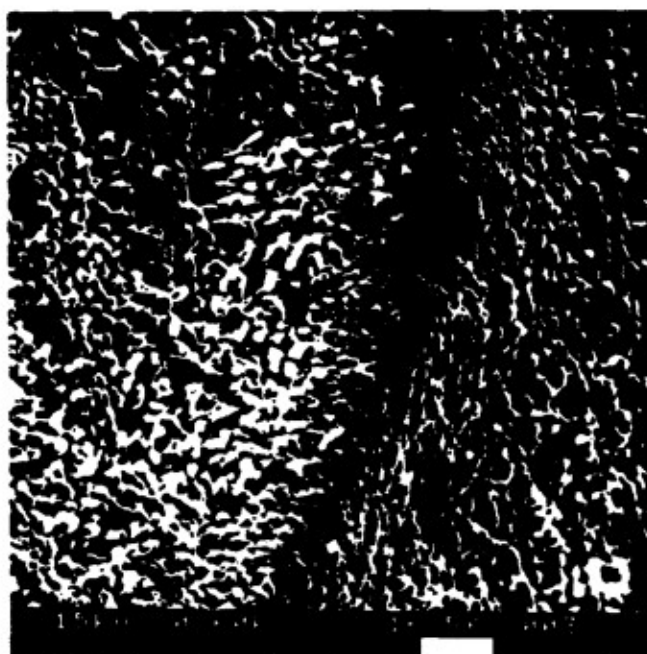


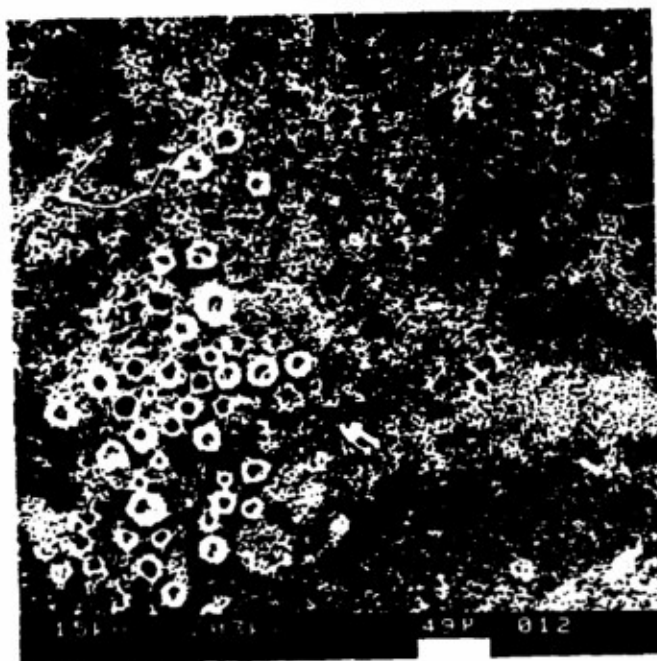












154 1071 434 812

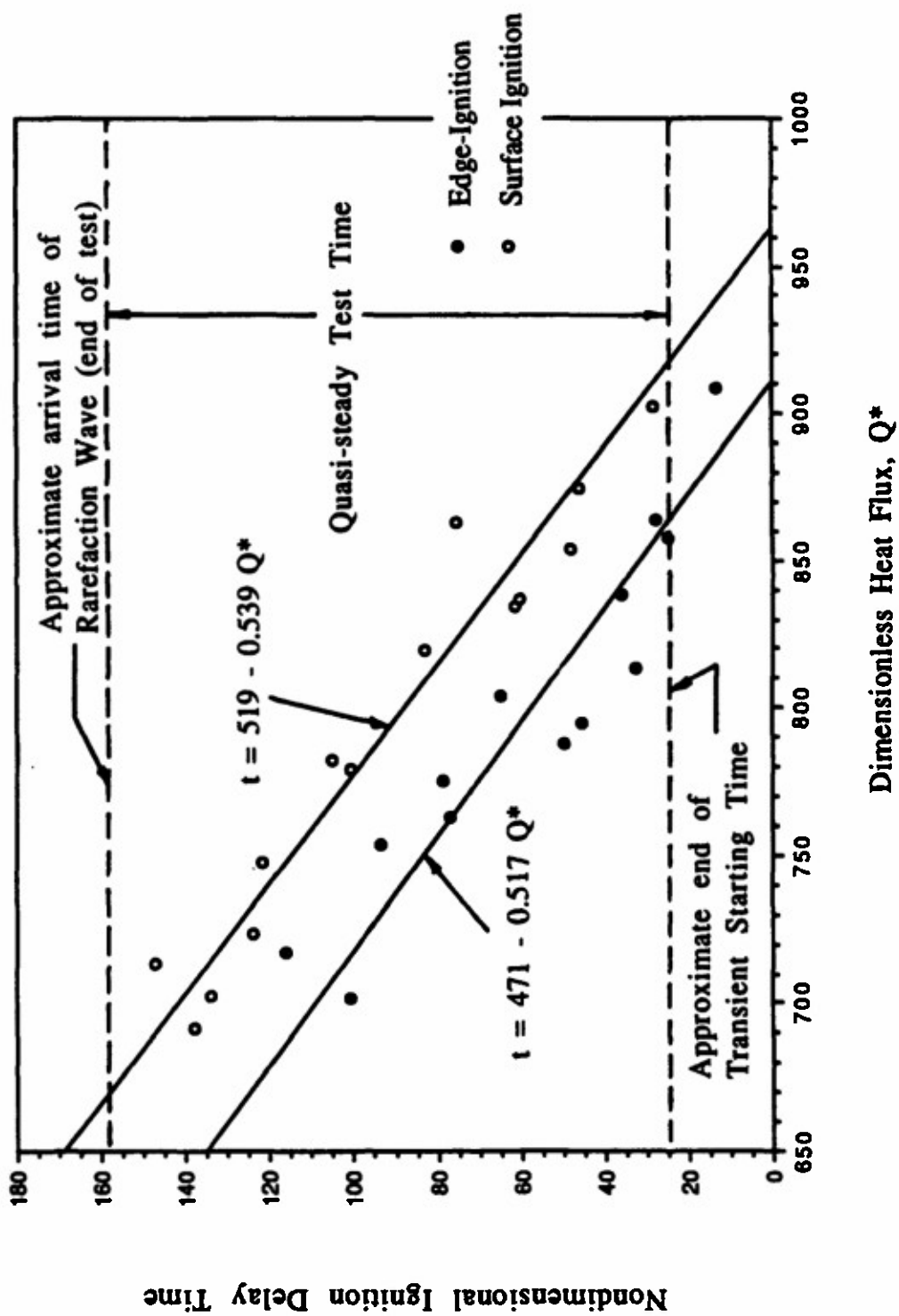
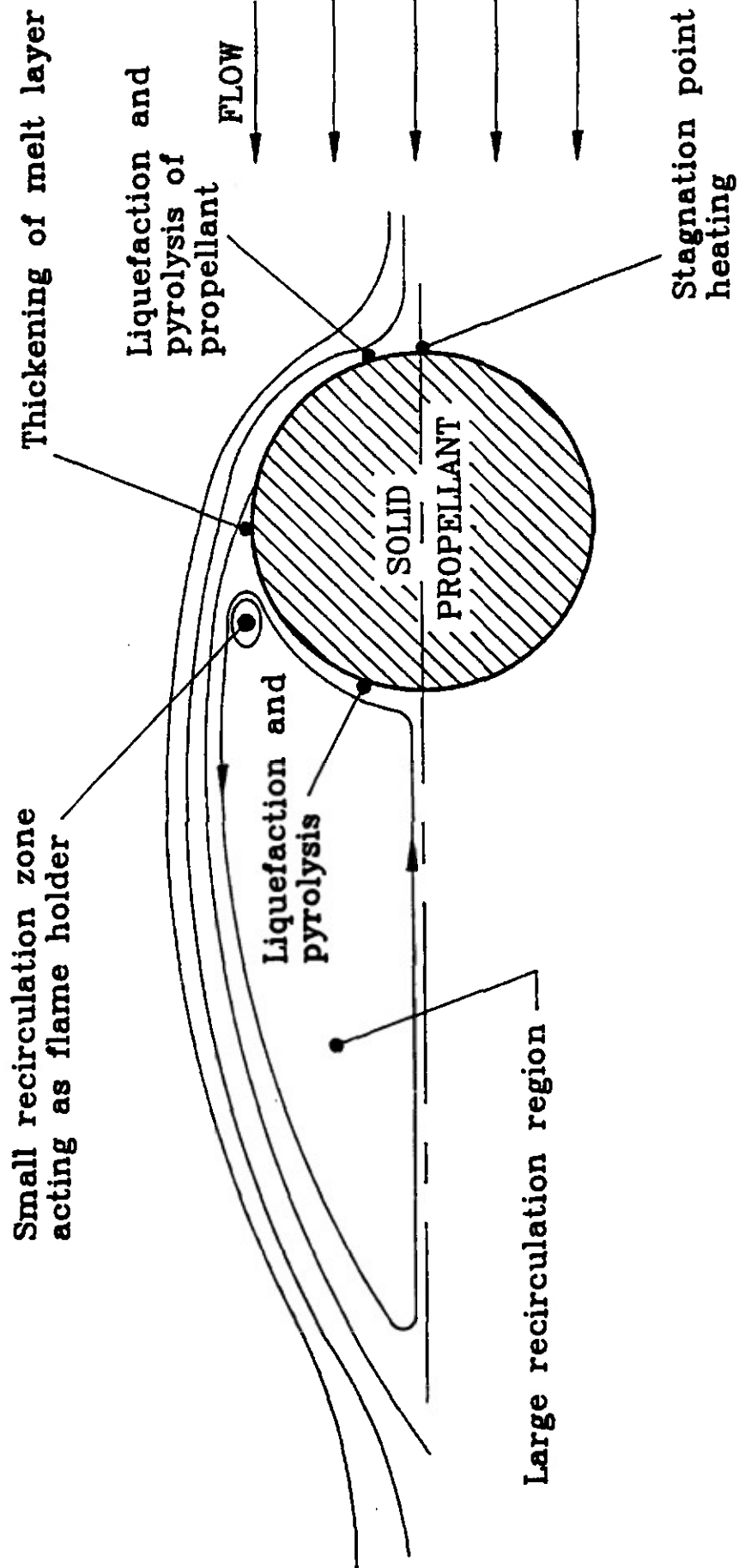


FIGURE 6 Results / Ignition Delay



Appendix H

A COMPARATIVE ANALYSIS OF THE CONVECTIVE AND RADIATIVE IGNITION PROCESSES OF XM-39 SOLID PROPELLANT*

S.J. Ritchie[#], B.L. Fetherolf[#], W.H. Hsieh[§], and K.K. Kuo[†]
Department of Mechanical Engineering
The Pennsylvania State University
University Park, PA 16802

ABSTRACT

A combined experimental and theoretical approach is applied to the study of XM-39 solid propellant ignition. The mechanisms considered are important to the processes occurring in practical ballistic systems. These are convective heat transfer into the material from a hot gaseous stream, radiative heat transfer from a hot source, and conductive heat transfer from a hot stagnant gas. Experimental measurements of ignition delay time and observations of physical characteristics for the convective and radiative ignition processes have been carried out using a shock tunnel facility and a high powered CO₂ laser, respectively. The important physical mechanisms of both types of ignition are identified and described. The differences in ignition results obtained by convective and radiative mechanisms were interpreted in terms of governing physical characteristics.

INTRODUCTION

The fundamental physical processes and chemical reactions which characterize the ignition of solid propellants in ballistic applications are difficult to determine due to the extreme temperatures, pressures, possible grain motion, geometric complexities, dynamic operating conditions, and short time scales involved. With emphasis now placed on the development of insensitive or low vulnerability munitions (LOVA)¹ and novel ignition sources for ballistic systems such as lasers, the need to understand these processes has become an extremely important issue in the development of improved propellant formulations. Gun simulator tests provide an excellent method for analyzing solid propellant ballistic performance and determining the proper igniter geometry²⁻⁵. However, simulator tests, by virtue of their complex geometry, are difficult to interpret in terms of the fundamental information which can be more easily obtained by using small-scale laboratory tests. By using simple geometries, these tests lend themselves to realistic model validation of the chemical and physical processes which are important to the ignition of the material. The small-scale tests are not without drawbacks. Most tests focus on a singular form of energetic input while striving to remove the effects of all other possible energy sources. In a gun chamber, however, the main propellant bed is conventionally ignited through a variety of mechanisms such as convection from hot primer gases, radiation from burning particles and hot primer gases, and conduction from hot impinging particles⁶. Therefore the results of several different small-scale tests would be required to characterize the ignition performance of a solid propellant to different heating conditions.

This program focuses on understanding and relating the small-scale laboratory tests which are used to examine the ignition of solid propellants subjected to thermal energetic input. This includes ignition response to radiative, convective and conductive heat transfer phenomena. The approach is taken in several steps. First, the physicochemical characteristics which govern the ignition of XM-39, an RDX-based LOVA solid propellant, when subjected to (1) convective heating, using a shock tunnel facility, and (2) radiative heating, using a CO₂ laser facility, were studied independently. The conditions chosen for each of these tests are similar to those present within a gun chamber. Secondly, an analysis has been carried out by which the results of the two different tests may be related to each other in a simple fashion. The results of this program provide, at the very least, further information into the behavior of RDX-based propellant formulations to various thermal stimuli. Additionally, the analysis may provide insight into potentially similar chemical processes despite the large differences in the physical method of thermal input.

EXPERIMENTAL METHOD

Experimentally, this project was divided into several different test programs. The first test program was performed to examine the ignition of cylindrical XM-39 solid propellant grains when subjected to predominantly convective heating from a high-temperature, high-pressure flow field. This type of flow is representative of what is found in standard gun chambers during the practical ignition process. From the literature, it has already been shown that a shock tunnel facility provides an excellent means of generating the necessary flow conditions⁷⁻¹³. Therefore, the shock tunnel facility used

*This work was performed under the sponsorship of the Army Research Office, Research Triangle Park, North Carolina, Contract No. DAALO3-87-K-0064. The support and encouragement of Dr. D.M. Mann is highly appreciated.

[#]Ph. D. Candidate

[§]Assistant Professor

[†]Distinguished Professor

previously by Birk and Caveny^{7,8} and Kashiwagi et al.⁹⁻¹² was acquired, reconstructed and used to generate the high-temperature, high-pressure flow field required for this portion of the project.

A second test was conducted to observe ignition of the same solid propellant type when subjected to laser-generated radiative heating. An existing CO₂ laser facility, especially designed to study solid propellant ignition under high-pressure conditions¹⁴⁻¹⁷, was utilized for this part of the experimental study. The laser ignition tests were designed to provide data for eventual theoretical model validation and to obtain insight into the important physical processes which occur during the ignition of nitramine-based solid propellants. The two facilities are described briefly in the following sections. More detailed descriptions of the convective¹⁸⁻²⁰ and radiative¹⁴⁻¹⁶ facilities have been given previously.

CONVECTIVE IGNITION TEST

HPCL Shock Tunnel Facility. The shock tunnel facility was designed to be as long as possible to assure longer testing times and to have large internal diameter to reduce boundary layer interaction effects on the flow properties. It is a total of 24.1 m (79 ft) long. The driver section is 9.7 m (31.8 ft) in length and the driven section is 8.5 m (27.9 ft) in length. The last 5.9 m (19.3 ft) section of the tunnel makes up the exhaust chamber for the induced flow. The inside diameter of the tunnel is approximately 9.718 cm (3.826 in.). The driver section has a maximum rating of 12.4 MPa (1800 psia) and is charged with helium gas. The driven section can be vacuumed down to pressures as low as 1.38 kPa (0.2 psia) and the test gas can be composed of any combination of oxygen and nitrogen. The tunnel is operated remotely via a test console located just outside the test cell. Firing of the tunnel is accomplished through a double burst diaphragm technique in order to achieve consistent incident shock strengths. A schematic diagram of the shock tunnel and associated diagnostics is shown in Figure 1.

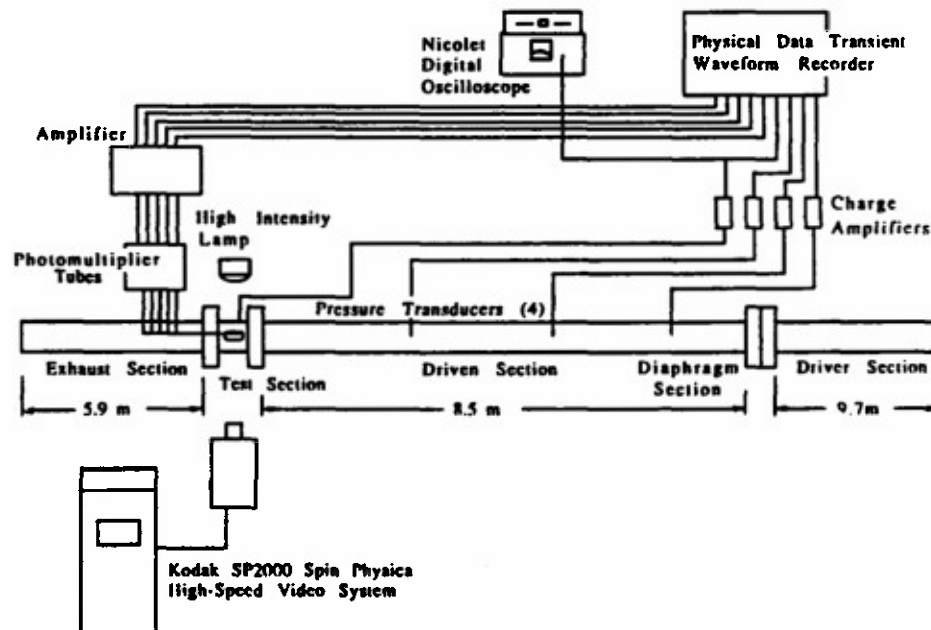


Figure 1. Schematic Diagram of Convective Ignition Shock Tunnel Test Facility and Associated Diagnostics

Convective Ignition Test Section. The test section is located at the end of the driven section and is characterized by a sudden cross-sectional area change from the 9.718 cm (3.826 in.) diameter round shock tunnel to a 2.858 cm (1.125 in.) square duct. A cut-out side view of the test section is shown in Figure 2. Quartz windows located on the top and sides of the test section (side windows not shown in the figure) provide optical access. Perforated plates are located at both the upstream entrance and downstream exit. The downstream exit plate acts as a nozzle which chokes the flow and controls the velocity of gas through the test section. The upstream perforated plate was not used by either Kashiwagi et al.⁹⁻¹² or Birk and Caveny^{7,8} in their studies. It was added to help damp out initial pressure oscillations caused by the starting transient of the flow when the shock wave passes through the test section and to act as a flow straightener.

Diagnostics. Three Kistler 601B1 pressure transducers located along the driven section of the tunnel detect the arrival of the shock wave at fixed locations and are used to measure the speed of the incident shock wave. Another Kistler 601B122 pressure transducer is located in the test section, 2.54 cm (1.0 in.) upstream of the sample, as can be seen in Figure 2. This transducer provides test section pressure information. To determine ignition delay, five RCA 1P28 photomultiplier tubes

with filters to prevent saturation are used remotely via fiber optic tubes which are mounted on the top window of the test section. High-speed visualization of the event is accomplished through the two side windows. A Kodak Spin Physics SP2000 high-speed video camera system is used with backlighting of the sample.

Test Samples. The propellant used for this study was XM-39 with a formulation of 76% RDX, 12% cellulose acetate/butyrate (CAB), 7.6% acetyl triethyl citrate (ATEC), 4% nitrocellulose (NC), and 0.4% ethyl centralite (EC). The grain geometry was cylindrical with a nominal diameter of 7 mm (0.28 in.) and length trimmed to a constant 0.74 cm (0.29 in.). For comparative purposes with the laser ignition test, the graphite coating was removed prior to testing, and the surface was polished until it was visually smooth.

The sample was mounted in the test section with the induced flow perpendicular to the length of the grain. This relatively simple grain/flow geometry was used in order to gain a more fundamental understanding of the underlying ignition mechanisms of the propellant. Mounting of the sample in the test section was accomplished by drilling a hole down the center of the cylindrical sample. A stainless steel rod is inserted through this hole and attached to end holders. The difference between the size of the test section (2.86 cm/1.125 in.) and the length of the sample (0.74 cm/0.29 in.) was occupied by inert stainless steel or teflon spacers on either side so the flow would 'see' essentially one long cylinder stretching across the entire test section. This was done to minimize end-ignition and end-burning effects from the test.

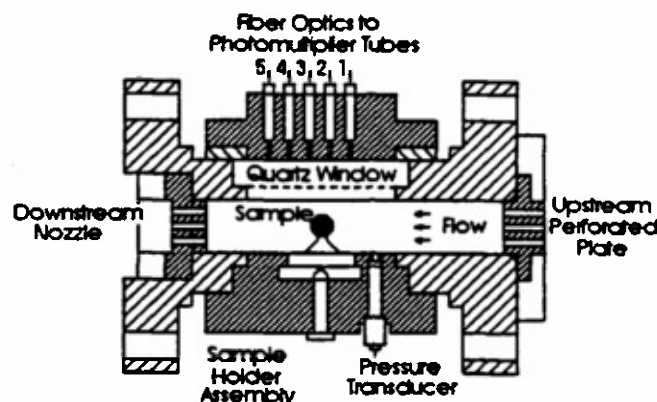


Figure 2. Cut-away Side View of Convective Ignition Shock Tunnel Facility Test Section

RADIATIVE IGNITION TESTS

CO₂ Laser Ignition Test Facility. The CO₂ laser irradiation facility is shown schematically in Figure 3. A Coherent Super 48 high-power CO₂ laser is used as the radiative energy source. This laser is capable of generating 800 watts in the continuous wave mode and 3500 watts in the pulsed mode. A mask is used to block off all but a 0.7 cm (0.28 in.) diameter portion of the laser output beam. Spatially, this unhindered portion of the laser beam exhibits a Gaussian intensity profile which is relatively uniform across the sample surface with losses of 10-15% near the edges. Heat flux generated by the laser beam at the sample location is measured using a combination of a calorimeter calibration device and a special instrument for laser time and beam intensity profile measurement²¹.

The high-pressure test chamber is designed to be operated at internal pressures up to 34.47 MPa (5,000 psi). Two long, narrow plexiglass windows located on the "front" and "back" of the circular chamber provide optical access to allow for high-speed filming of the ignition or flame spreading event. A zinc selenide window, protected from combustion products by a potassium chloride window, is mounted on the top of the chamber to allow for passage of the CO₂ laser beam. Sample insertion is accomplished through the bottom of the chamber.

Test conditions were similar to those used for the convective ignition tests. The test gas used for all radiative ignition tests was air and the pressures were in the range 1.38 to 3.79 MPa (200 to 550 psi). Heat flux rates were comparable to the data of Birk and Caverty^{7,8}. These heating rates were between 100 and 400 W/cm².

Diagnostics. Ignition delay time was measured using a silicon photodiode positioned within the high-pressure test chamber. The diode senses light emission in the visible wavelength range of 0.35 - 1.15 μ m (3500 - 11500 Å) with a peak sensitivity at 0.9 μ m (9000 Å). Data from this diode is stored on a Nicolet digital oscilloscope which is triggered by the firing of the CO₂ laser. Two types of cameras were used to film the test event and determine the ignition location and flame spread phenomena. A conventional video camera was used to record the XM-39 flame characteristics. A Spin Physics 2000 high-speed video camera (set to 500 pictures per second) was used to record ignition and flame development.

Test Samples. The XM-39 solid propellant samples for the radiative ignition test had the identical chemical formulation as the samples used in the convective ignition portion of this program. The samples were obtained in stick form, approximately 10.16 cm (4 in.) in length and 0.7 cm (.28 in.) in diameter, and were not perforated or graphite coated. These sticks were cut, by hand using a razor blade, into lengths of about .5 cm (.20 in.). These disc shapes were glued into place on the sample holder such that irradiation was on the flat end of the disc-shape.

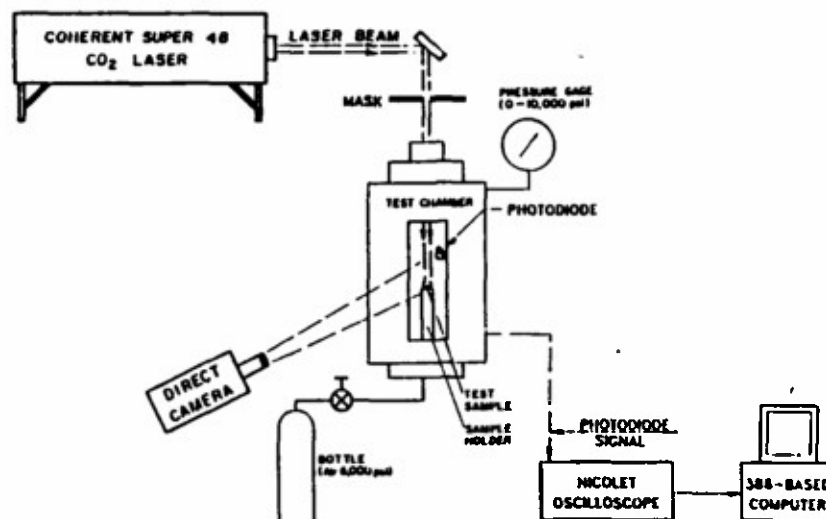


Figure 3. Schematic Diagram of Radiative Ignition CO₂ Laser Facility and Associated Diagnostics

DISCUSSION OF RESULTS AND ANALYSIS

The results of the convective and radiative ignition tests are summarized separately in the sections below. A portion of the convective ignition results obtained to date have been presented previously¹⁸⁻²⁰. A summary of convective ignition results is included for completeness. A final section is devoted to a comparative analysis of the ignition processes observed.

RADIATIVE IGNITION TEST RESULTS

Ignition Delay Time. The ignition criteria for both the radiative and convective tests had to be the same. The most easily measured parameter was the appearance of a luminous flame zone. Therefore the ignition delay time (t_{id}) for the radiative ignition test is defined as the time between the application of the laser energy and the first visible light emission. More rigorously, this value should be called the time to first light emission. This value was measured with the silicon photodiode and checked using the high-speed video image. A series of typical photodiode traces for the tests at $q'' = 200$ W/cm² and various pressures are shown in Figure 4. 'Ignition' is very easily distinguished by the sharp rise in the early stage of the event (6-7 msec). The time to first light emission at the various pressures are nearly the same even on an expanded time scale. Following this point, there are some intensity variations and after laser cutoff there exists some intensity oscillations which will be discussed in a later section. Ignition delay data are shown in Table I. Included in this table are the air pressure in the test chamber, the incident heat flux from the CO₂ laser and the ignition delay time. The data from Table I is shown on a log-log plot of the delay time versus incident heat flux (see Figure 5). The data points shown on the plot represent measurements at pressures of either 1.38 or 3.79 MPa (200 or 550 psi). Figure 5 also includes the data from the convective ignition test program in the same pressure range. This data will be described separately in later section. The correlation of the radiative ignition data is given by equation (1):

$$t_{id} = \frac{6260}{[q'']^{1.3}} \quad (1)$$

Ignition Location. Direct high-speed video of the ignition event was used to observe the first light emission location. The initial surface location of the propellant was marked using adjustable reticles on the viewing screen of the Spin Physics 2000 system. The position at which light could first be observed was compared to this surface location. The location of the first luminous reaction, measured using the described method, was in the gas-phase very near the surface. The proximity to the surface was expected due to the reasonably high-pressures under which ignition was achieved. To more

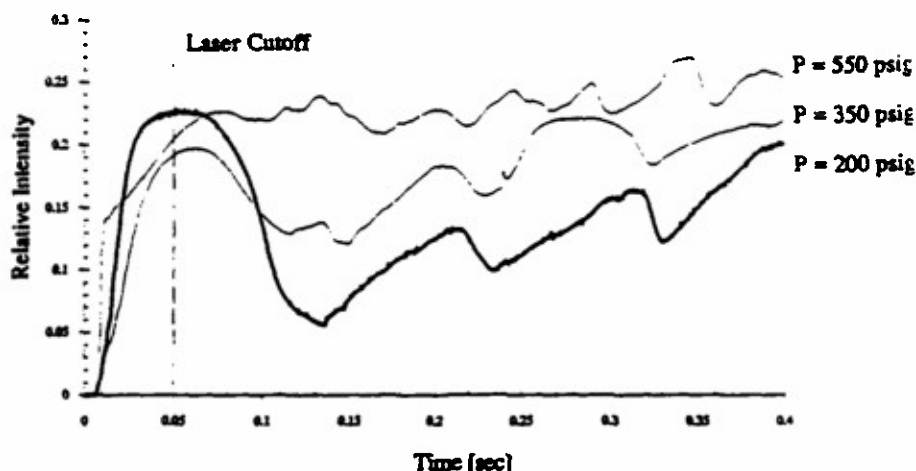


Figure 4. Photodetector Intensity Responses During Laser Ignition Tests at Various Pressure Levels
(Incident Heat Flux = 200 W/cm², Propellant Type = XM-39, Test Gas = Air)

Table I. Summary of Test Conditions and Results for Radiative Ignition Tests of XM-39 Solid Propellant in Air

Test No.	Pressure MPa (psia)	Incident Heat Flux W/cm ²	t _{id} (ms)	Test No.	Pressure MPa (psia)	Incident Heat Flux W/cm ²	t _{id} (ms)
001	1.38 (200)	130	12.35	011	1.38 (200)	200	7.8
002	2.07 (300)	130	13.18	012	3.79 (550)	375	3.25
003	3.79 (550)	130	12.39	013	1.38 (200)	375	3.40
004	1.38 (200)	190	7.0	014	1.38 (200)	375	4.30
005	1.38 (200)	200	6.5	015	3.79 (550)	375	3.50
006	2.41 (350)	200	7.1	016	3.79 (550)	130	13.2
007	3.79 (550)	200	6.1	017	1.38 (200)	130	13.6
008	3.79 (550)	200	7.6	018	3.79 (550)	250	5.2
009	3.79 (550)	200	8.5	019	1.38 (200)	250	5.3
010	3.79 (550)	200	7.6	020	1.38 (200)	250	5.6

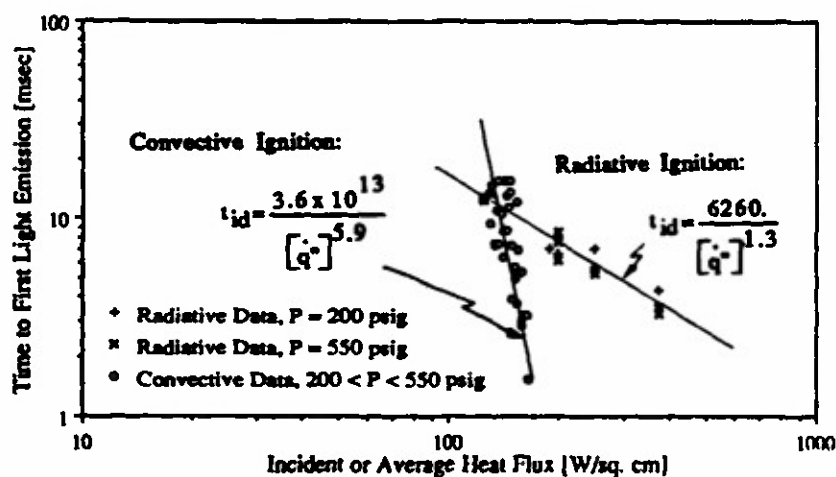


Figure 5. Radiative and Convective Ignition Delay Data in Terms of Average or Incident Heat Flux and Pressure
(Propellant Type: XM-39, Ambient Gas: Air).

accurately determine the site of the luminous reaction zone, significantly better time and spatial resolution are required than can be achieved with the Spin Physics system. There is a tradeoff between the light sensitivity of a camera system, the magnification of the image, and the framing rate employed.

Dynamic Response of Photodetector During Transition to Self-Sustained Combustion. The dynamic ignition phenomena following the onset light emission can be analyzed by considering the photodiode intensity versus time trace shown in Figure 4. At a fixed incident laser heat flux (200 W/cm^2), a change in chamber pressure significantly affects the intensity reading of the photodiode. Immediately after the onset of light emission, the photodiode intensity has the steepest rise for the highest chamber pressure of 3.79 MPa (550 psig). This is probably due to higher collision rates and associated chemical reaction rates at the higher pressure. However, the slope values do not decrease consistently with pressure. This can be explained by considering a competing mechanism. The blowing velocity at the pyrolyzing surface of the sample depends inversely on the chamber pressure. Early in the ignition process, the surface temperature at the onset of light emission is approximately independent of pressure; this can be partially justified by the independence of the light emission time with respect to pressure. Based upon the mass flux continuity at the pyrolyzing surface, the lower the gas density (chamber pressure) is, the higher the blowing velocity. As a result, the luminous gases can be ejected further upward. Therefore the photodetector intensity reading at the lower pressures could exceed the values seen when the chamber pressure is higher.

Following laser cutoff, the intensity level of the photodetector output does continue to rise to an initial maximum peak. According to the results obtained and shown in Figure 4, the time between laser cutoff and the first maximum is longest for highest chamber pressures and the shortest for the lower chamber pressure. This dependence could be due to increased gas-phase chemical reactions at the higher pressures. The chemical inertia of the reacting gas mixture is higher at higher pressures.

Following this first maximum peak, there is a significant drop in intensity levels at the lower chamber pressures. This is commonly known as a deradiation effect. The drop is because the gas-phase chemical reactions cannot generate enough energy to fully replace the external laser energy source which has been removed. At the lower pressures this is more significant for two reasons. First, the blowing velocity is higher and therefore the pyrolysis products are carried further from the sample surface. The second reason is the reduced intensity of the chemical reactions at the lower pressures, which lowers the thermal energy content of the reacting media. The effect of both these reasons is a reduction in the heat feedback to the sample surface.

For the conditions in this program, the deradiation effect was not significant enough to fully quench the ignition process. The dynamic period following this process is very interesting. At lower pressures (1.38 MPa, 200 psig), the luminous flame zone exhibits a very pronounced periodic oscillation at close to 10 Hz. As the pressure is increased to 2.41 MPa (350 psig), this periodic oscillation of 10 Hz is still noticeable but the wave contour is not as distinct. At the highest pressure tested, 3.79 MPa (550 psig), the intensity level is more or less constant, with a higher frequency of oscillation. This oscillatory or flame shedding behavior was very consistent and reproducible at the lower pressures but not so at the higher pressures.

CONVECTIVE IGNITION TEST RESULTS

Freestream Oxygen Dependency. For the tests performed in a nitrogen environment, no ignition or luminous flame was detected by either the high-speed video or the photomultiplier tube detection system. When the test gas was changed to air, ignition of the XM-39 solid propellant grain was observed for many of the imposed test conditions. A definite freestream oxidizer dependency of the ignition delay time was observed. This result substantiates previous observations by others. Birk and Caveny^{7,8} showed a similar result for HMX/PU propellant. Chang and Rocchio² have also shown that oxidizer rich igniters can reduce long ignition delays in gun simulator studies of nitramine-based propellants.

Ignition and Flame-Spread Observation. The observed ignition and flame-spread phenomena was similar for all tests in which ignition was observed. Still pictures taken from the high-speed video of a typical test were shown in Reference 18. The first evidence of luminosity was always observed in the region of boundary layer separation in a location just beyond 90° from the leading edge. The flame would spread from this location in only the downstream direction until the entire rearward surface was covered. These observations are very similar to those of Birk and Caveny^{7,8} for nitrocellulose-based propellants. It would seem that many of the important physical processes involved in the convective ignition of these different propellant types are very similar.

Ignition Delay Time. The photomultiplier tube which first recorded a signal larger than three times the average noise value was used to determine the ignition delay value. This ignition time was compared to the observed video results for clarification. In many cases, a flash of light from the sample surface could be observed very early during the test time ($< 3 \text{ ms}$). This phenomenon was also observed by Birk and Caveny^{7,8} in their study of nitrocellulose propellants. It can be explained using the following rationalization. When the incident shock wave arrives in the test section, the heating rates to the sample are very high. This has been substantiated by the heat flux data taken by Birk and Caveny^{7,8}. Gasification

of the propellant material can take place and subsequent reactions are observed. However, in tests done for this program, this momentary ignition was not always able to sustain burning for the entire test time because the heating rates decrease sharply with the onset of the quasi-steady flow through the test section. The sample, once quenched, would usually, but not always, reignite later during the steady-state convective heating period and sustain burning until the end of the test time. It is this appearance of this second luminous region which has been used to define the ignition delay time (t_{id}).

The ignition delay results from the convective ignition testing have been tabulated previously¹⁸⁻²⁰ and are plotted here with the radiative ignition results on a log-log scale as shown in Figure 5. The resulting correlation for the ignition delay versus an average heat flux is given by equation (2).

$$t_{id} = \frac{3.6 \times 10^{13}}{[\dot{q}'']^{5.9}} \quad (2)$$

The use of an average heat flux value is an attempt to display the convective ignition test results into the same form as the radiative ignition test results. In this way a comparative discussion of the two tests can be more easily carried out. This value is not meant to imply that the heating rate is uniform across the entire propellant surface. The heat flux data taken by Birk and Caveny^{7,8} distinctly show a variation in heat flux to the sample surface as a function of angular location from the leading edge. However, the average value, found using the following relationships, provides a means of qualitative comparison between the convective ignition results:

$$\bar{h} = \bar{Nu}_D \frac{k}{D} \quad (3)$$

$$\dot{q}'' = \bar{h}(T_\infty - T_s) \quad (4)$$

The average heat transfer coefficient (\bar{h}) is determined by using the Nusselt number, the conductivity of air at the 'film' temperature, and the diameter of the sample. The temperature difference was chosen to be the maximum achievable value between the initial temperature of the sample and the freestream temperature. The average Nusselt number (\bar{Nu}_D) is calculated using the following formula for flow over a cylinder²²:

$$\bar{Nu}_D = 0.26 Re_D^{0.6} Pr^{0.333} \left(\frac{Pr}{Pr_s} \right)^{.25} \quad (5)$$

The subscript (s) indicates the value of the Prandtl number evaluated at the surface temperature. This surface temperature was fixed at the initial sample temperature for all calculations.

Microscopic Analysis of Propellant Surface Characteristics. Both optical and scanning electron microscopy (SEM) analyses were performed on recovered test samples^{19,20}. The micro-photographs indicate the formation of a liquid 'melt' layer similar to that described by numerous other researchers and a number of rice-like structures are visible across the surface. There are also a number of circular holes in the surface, especially in the region where ignition was observed. These holes could represent bubbles generated by gas-producing reactions within the condensed phase or they could indicate large RDX crystals which have been ejected from the surface. The results of this study are described in greater detail along with a series of micro-photographs in the references cited.

COMPARATIVE ANALYSIS OF IGNITION RESULTS

It is clear from the plot shown in Figure 5, that the convective and radiative ignition processes have very different characteristics which control the ignition process. The approach taken here is similar to that attempted by Keller et al.¹³ for composite ammonium perchlorate solid propellants. At the lower heat fluxes where the data from the different tests collapse onto the same line, it is safe to assume that an inert heating process of the solid material dominates both processes. But as the heat flux is increased, the data follow very different trends. Consider that, if ignition were due to a surface temperature criteria and the material were to reach this temperature via an inert heating process, the slope of the curve plotted on Figure 5 would be -2.0. This would fall between the slopes of the convective and radiative data. The phenomena exhibited by both the convective and radiative results can be explained if pre-ignition gas-phase processes which are important to the ignition of XM-39 solid propellant are considered.

In the case of the radiative ignition process, gases generated by pyrolysis of the XM-39 propellant escape from the surface into a relatively low temperature ambient environment. This slows down the reactivity of the gas-phase and leads to

a 'less efficient' ignition of the material when compared to the inert heating process and the negative slope of the data is less than -2 (ie. energy is lost to the surrounding ambient gases). In the convective ignition test, the pyrolyzed gases are entrained in the relatively high-temperature boundary layer. Therefore, further heating of the gases can occur and increase subsequent chemical reactivity. Additionally, the fluid conditions around the cylindrical grain 'collect' the pyrolyzed gases in the region just beyond the separation point of the boundary layer. This increases the mixing process and the local heat feedback to the condensed material. Since the gas-phase heating and mixing effects are not considered in the average heat flux value used to plot the convective data shown in Figure 5, the convective ignition data appear to be more 'efficient' than an inert heating case and therefore display a slope of -5.9.

POSTULATION OF A GENERALIZED IGNITION DELAY CORRELATION FOR DIFFERENT MODES OF ENERGY FLUX

The major differences between the convective and radiative ignition processes are (1) the presence of hot versus cold gases adjacent to the sample surface, and (2) boundary layer flow versus stagnant conditions. It is these physical differences which must be compensated for if any comparison of the chemical processes important to the different thermal mechanisms can be made. To bridge the gap between the two different ignition processes, an intermediary ignition process should be considered. This process is associated with the ignition of XM-39 propellant subjected to conductive heating by a hot, stagnant gas at temperatures and pressures equivalent to those generated by the convective test facility. Ignition tests could be carried out under systematic variations of ambient gas temperature, oxygen mass fraction in the ambient gas mixture, and the initial propellant temperature. These data, together with those already collected, could be used to develop a more generalized correlation given below:

$$t_{LE} = \frac{C (T_{gas,ambient}, T_{initial,propellant}, Y_{Ox,ambient})}{[\dot{q}"]^n (T_{gas,amb.}, T_{init.,prop.}, Y_{Ox,amb.})} \quad (6)$$

where the exponent, n , and numerator, C , are functions of the various parameters indicated. Therefore, the values of both n and C could vary according to operating conditions. In this manner, the two different curves on Figure 5 could be represented by the same equation.

The above correlation could be extended to further include the convective ignition data by considering the flow conditions represented by dimensionless groups, such as Reynolds number and Prandtl number in the functional forms of n and C .

$$t_{LE} = \frac{C (T_{gas,ambient}, T_{initial,propellant}, Y_{Ox,ambient}, Re, Pr)}{[\dot{q}"]^n (T_{gas,amb.}, T_{init.,prop.}, Y_{Ox,amb.}, Re, Pr)} \quad (7)$$

The final empirical correlation would provide a generalized equation capable of predicting the time to first light emission time for any mode of thermal energy input.

SUMMARY AND CONCLUSIONS

The following conclusions about the radiative ignition of XM-39 LOVA propellant can be reached:

- The ignition delay time for XM-39 solid propellant has been successfully measured using a CO₂ laser facility for a variety of incident heat flux and chamber pressure conditions. This delay time, when plotted versus incident heat flux on a log-log plot, correlates to a slope of -1.3.
- There is no significant pressure dependency on the time to first light emission for XM-39 in the range of pressures between 200 and 550 psig.
- Observed gas-phase ignition is located very near the propellant surface.
- There is a deradiation effect associated with the laser cutoff; the magnitude of the resulting decay in light intensity increases with decreasing chamber pressure.
- The effect of pressure on the ignition dynamics has been observed. The light intensity oscillation is more pronounced at lower pressures.

With respect to the convective ignition of nitramine propellants, the following can be concluded:

- Convective ignition and flame spreading phenomena of XM-39 solid propellant have been successfully observed. Strong evidence of gas-phase ignition mechanism has been experimentally observed. Sustained convective ignition occurs in the region near the boundary-layer separation point.
- The presence of freestream oxidizer is very important to the ignition process. In the absence of oxidizer in the test gas, no convective ignition was observed in the range of operating conditions tested. Ignition was achieved in tests carried out in air under most operating conditions.

- The ignition delay time has been correlated to an average heat flux value and exhibits a slope of -5.9 on a log-log plot.
- Microscopic analysis of recovered propellant samples shows the formation of a liquid layer and a series of circular holes which could be representative of bubbles forming in the condensed phase. The composition of this liquid and its importance to the ignition process is still unknown and should be studied further.

Based upon the comparison between the radiative and convective ignition data, the following points can be concluded:

- Two different slopes have been identified for the light emission time versus external energy flux associated with two different modes of energy transfer. At the same heat flux value, the light emission time is shorter for convective ignition than that of radiative ignition. The reason for shorter light emission times under convective ignition is due to the hot gas environment, increased mixing of pyrolyzed gases due to shear flow, and prolonged residence times within the recirculation zone near the separation points of the boundary layer flow.
- Even though the light emission time versus heat flux curves are distinct for convective and radiative ignition, we believe that the results shown could be represented by the same equation with variable coefficient (C) and exponent (n), as long as the parameters controlling the operating conditions are properly accounted for in these two variables.

REFERENCES

1. Rocchio, J.J. (1981), "The Low Vulnerability Ammunition (LOVA) Program: A Progress Report," 1981 JANNAF Propulsion Systems Subcommittee Meeting, CPIA Publication 340.
2. Chang, L.M. and Rocchio, J.J. (1988), "Simulator Diagnostics of the Early Phase Ignition Phenomena in a 105-mm Tank Gun Chamber," Technical Report BRL-TR-2890, Ballistic Research Laboratory, Aberdeen Proving Ground, Md.
3. Stiefel, L. and Costello, J.C. (1988), "Ignition of 25mm Insensitive Propellant Charges: Studies of the Early Portion of the Pressure-Time Curve," 25th JANNAF Combustion Meeting, CPIA Publication 498.
4. Rodriguez, L.N. (1988), "Ignition/Temperature Coefficient Study for HELOVA Propellant," Report No. IHTR-1174, Naval Ordnance Station, Indian Head, Md.
5. Messina, N.A., Ingram, L.S. and Tricarico, S.A. (1988), "25mm Ballistic Simulator for XM919 Ignition System/Charge Design Studies," 25th JANNAF Combustion Subcommittee Meeting, CPIA Publication 498.
6. Varney, A.M. (1988), "Primers and Igniters," AIAA Progress in Astronautics and Aeronautics: Gun Propulsion Technology, Vol. 109, edited by L. Stiefel, pp. 1-33.
7. Birk, A. and Caveny, L.H. (1980), "Convective Ignition of Propellant Cylinders in a Developing Cross-Flow Field," MAE Report No. 1486, Department of Mechanical and Aerospace Engineering, Princeton University.
8. Birk, A. and Caveny, L.H. (1980), "Convective Ignition of Propellant Cylinders in a Developing Flowfield," AIAA Journal, Vol. 18, No. 11, pp. 1363-1370.
9. Kashiwagi, T., MacDonald, B.W., Isoda, H. and Summerfield, M. (1970), "Ignition of Solid Polymeric Fuels by Hot Oxidizing Gases," AFOSR Scientific Report #70-2935 TR.
10. Kashiwagi, T., MacDonald, B.W., Isoda, H. and Summerfield, M. (1971), "Ignition of a Solid Polymeric Fuel in a Hot Oxidizing Stream," 13th Symposium (International) on Combustion, Combustion Institute, Pitt., Pa., pp. 1073-1086.
11. Kashiwagi, T. and Summerfield, M. (1973), "Ignition and Flame Spreading Over a Solid Fuel: Non-Similar Theory for a Hot Oxidizing Boundary Layer," 14th Symposium (International) on Combustion, Combustion Institute, Pitt., Pa., pp. 1235-1247.
12. Kashiwagi, T., Kotia, G.G. and Summerfield, M. (1975), "Experimental Study of Ignition and Subsequent Flame Spread in a Hot Oxidizing Gas Stream," Combustion and Flame, Vol. 24, No. 3-4, pp. 153-160.
13. Keller, J.A., Baer, A.D. and Ryan, N.W. (1966), "Ignition of Ammonium Perchlorate Composite Propellants by Convective Heating," AIAA Journal, Vol. 4, No. 8, pp. 1358-1365.
14. Chen, D.M. (1988), "Pyrolysis, Ignition and Combustion of Solid Fuels for Ramjet Applications," Ph.D. Thesis, The Pennsylvania State University, Department of Materials Science and Engineering.
15. Kim, J.U. (1988), "Laser Ignition of Nitramine Composite Propellants," Ph.D. Thesis, The Pennsylvania State University, Department of Mechanical Engineering.
16. Kuo, K.K., Andiroghu, E. and Kamath, H. (1982), "Development and Design of a Laser Ignition Test Chamber," Final Report to the Ignition Devices Division, Naval Ordnance Station, Indian Head, Md.
17. Chen, D.M., Hsieh, W.H., Snyder, T.S., Yang, V., Litzinger, T.A. and Kuo, K.K. (1991), "Combustion Behavior and Thermophysical Properties of Metal-Based Solid Fuels," Journal of Propulsion and Power, Vol. 7, No. 2, pp. 250-257.
18. Ritchie, S.J., Hsieh, W.H. and Kuo, K.K. (1989), "Convective Ignition of LOVA Propellants Subjected to Crossflow Heating Conditions," 26th JANNAF Combustion Meeting, CPIA Publication 529, Vol. I, pp. 1-12.
19. Ritchie, S.J., Hsieh, W.H. and Kuo, K.K. (1990), "Convective Ignition Phenomena of LOVA Propellants," AIAA Paper 90-2194, AIAA/SAE/ASME/ASME 26th Joint Propulsion Conference, Orlando, FL, 16-18 July.
20. Ritchie, S.J., Hsieh, W.H. and Kuo, K.K. (1990), "Convective Ignition of LOVA Propellants," Presented at the 27th JANNAF Combustion Meeting, F.E. Warren Air Force Base, Cheyenne, Wyoming, 5-9 Nov.
21. Petherolf, B.L., Litzinger, T.A. and Kuo, K.K. (1990), "An Instrument for Measuring High-Power Laser Beam Profiles and Beam Attenuations," The Review of Scientific Instruments, Vol. 61, No. 1, pp. 7-10.
22. Zhukauskas, A. and Ambrazavichyus, A.B. (1961) International Journal of Heat and Mass Transfer, Vol. 3, No. 305, as referenced in Incropera, F.P. and Dewitt, D.P. (1985) Fundamentals of Heat and Mass Transfer, J. Wiley and Sons.